Julius-Maximilians-
UNIVERSITÄT
WÜRZBURG

UNIVERSITÄT WÜRZBURG
PHYSIKALISCHES INSTITUT
epVI

Optical study of the excited states in the semiconducting polymer poly(3-hexylthiophene) for photovoltaic applications

Dissertation zur Erlangung des
naturwissenschaftlichen Doktorgrades
der Julius-Maximilians-Universität Würzburg

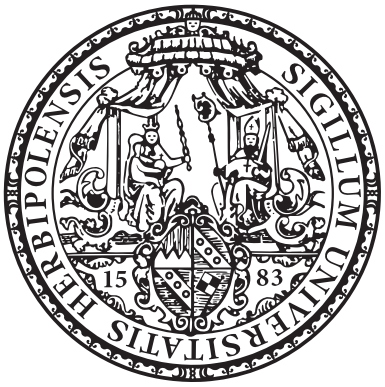

vorgelegt von

Julien François Gorenflot

aus Meaux

Würzburg 2014

Eingereicht am: 05.12.2014
bei der Fakultät für Physik und Astronomie

1. Gutachter: Prof. Dr. Vladimir Dyakonov
2. Gutachter: Prof. Dr. Tobias Hertel
3. Gutachter:
der Dissertation.

1. Prüfer:
2. Prüfer:
3. Prüfer:
im Promotionskolloquium.

Tag des Promotionskolloquiums:

Doktorurkunde ausgehändigt am:

Contents

Introduction

With the disaster of Fukushima and the resulting multiplication of programs aiming at decreasing the role of nuclear energy, the global energy problems have brutally been brought back to the front stage. In a context of global warming, for which energy production holds a large share of responsibility with more than a fourth of global greenhouse gases yearly emissions [1, p. 105], switching back to burning fossil fuels is not an option. Just as unrealistic would be a decrease in the energy demand while the majority of the world's population is still living in regions in great need for development[1].

In this context, the development of clean renewable energies is an absolute necessity. In this regard, the current situation leaves a lot of room for improvement: in 2008 renewable energies represent less than 20 % of global electricity supply (see figure 1). On the other hand, renewable sources have a potential for energy production far exceeding the current and forecasted needs of mankind [2, p. 10]. It is thus only a matter of political will to improve the situation. The current evolution of electricity production shows that such a will does exist. Indeed, according to the Intergovernmental Panel on Climate Change (IPCC) [2, p. 9]:

> "Of the approximate 300 GW of new electricity generating capacity added globally over the two-year period from 2008 to 2009, 140 GW came from [renewable energies] additions."

Among the different sources of renewable energies however, not all have the same potential and cleanliness. Hydropower currently supplies the biggest part of renewable electricity but is already used close to its full potential in many developed countries. On the other hand biomass is developing quickly and represent a solution for the coming shortage of fossil fuels, but still involves CO_2 emissions, not to mention the pressure that the production of biofuels is putting on global food resources and prices, and on the environment.

In contrast, solar energy is both abundant [2, p. 341] and produces very little greenhouse gases [2, p. 370]. In just one hour, the solar energy intercepted by the Earth exceeds the world's energy consumption for the entire year [2, p. 340]. Considering only the proportion of this energy that can actually be collected, estimations of the technical potential for photovoltaic (PV) electricity production vary from 1338 to 14778 EJ/yr [2, p. 341], depending mainly of the proportion of land considered as able to be dedicated to the energy collection.[2]

[1] 1.4 billion people do not have access to electricity in 2009 [2, p. 721]

[2] As an example a potential of 1,689 EJ was obtained considering that the suitable land area for PV deployment averages 1.67 % of total land area [2, p. 341]

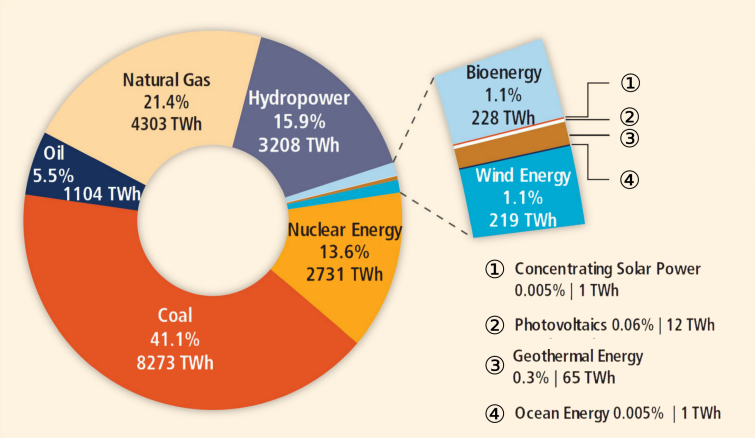

Figure 1: Share of primary energy sources in world electricity generation in 2008. Adapted from IPCC 2011 [2, p. 175]; data sources: IEA ([3] for renewable energies and [4] for fossil and nuclear).

Those numbers have to be related to the annual electricity demand which was in 2008 of 61 EJ [2, p. 184].

Moreover, from an economic point of view, the PV industry has already proven its ability to be a driving force for the economy and the semiconductors industry as the demand from the PV market led in 2008 to a massive increase of the polysilicon production capacity [2, p. 364]. Solar PV generation has grown by a factor of more than 51 between 2000 and 2011 [5, p. 41]. In 2010 only, the overall PV electricity production capacity nearly doubled with an increase of 91 % of the global capacity [5, p. 43]. Those performances are especially remarkable as they were reached in a context of global economical crisis.

The main drawback of PV electricity is its comparatively high price (see figure 2 (a)), in spite of a continuous decrease in the past decades (see figure 2 (c)). This results in a worldwide distribution of PV capabilities being function of the subsidies rather than the insolation potential as shown by the contrast between the yearly insolation and the actual production capacities of Spain, the United States and Germany on figure 2 (b).

To overcome their dependency on governmental help, the actors of PV are trying to decrease the cost of this energy. One of the answers to that has been the upscaling of manufacturing units [2, p. 364]. Another answer is the development of different technologies. A great number of PV technologies is available or in development, the laboratory performances of which are summarized in figure 3.

Among the emerging technologies, organic solar cells have undergone over the past 10 years, one of the quickest performance improvement. Besides, organic materials offer important advantages in the quest for optimal cost efficiency. Based on hydrocarbon molecules, they are an abundant resource compared to rare earth element such as tellurium used for CdTe cells [2, p. 352], or precious metals such as indium used for CIGS cells [2, p. 352]. The molecules synthesis is less demanding in energy than the purification of inorganic semiconductor to electronic grade which requires extreme temperatures. They possess high absorption coefficient which enables the use of thin films, thus using orders

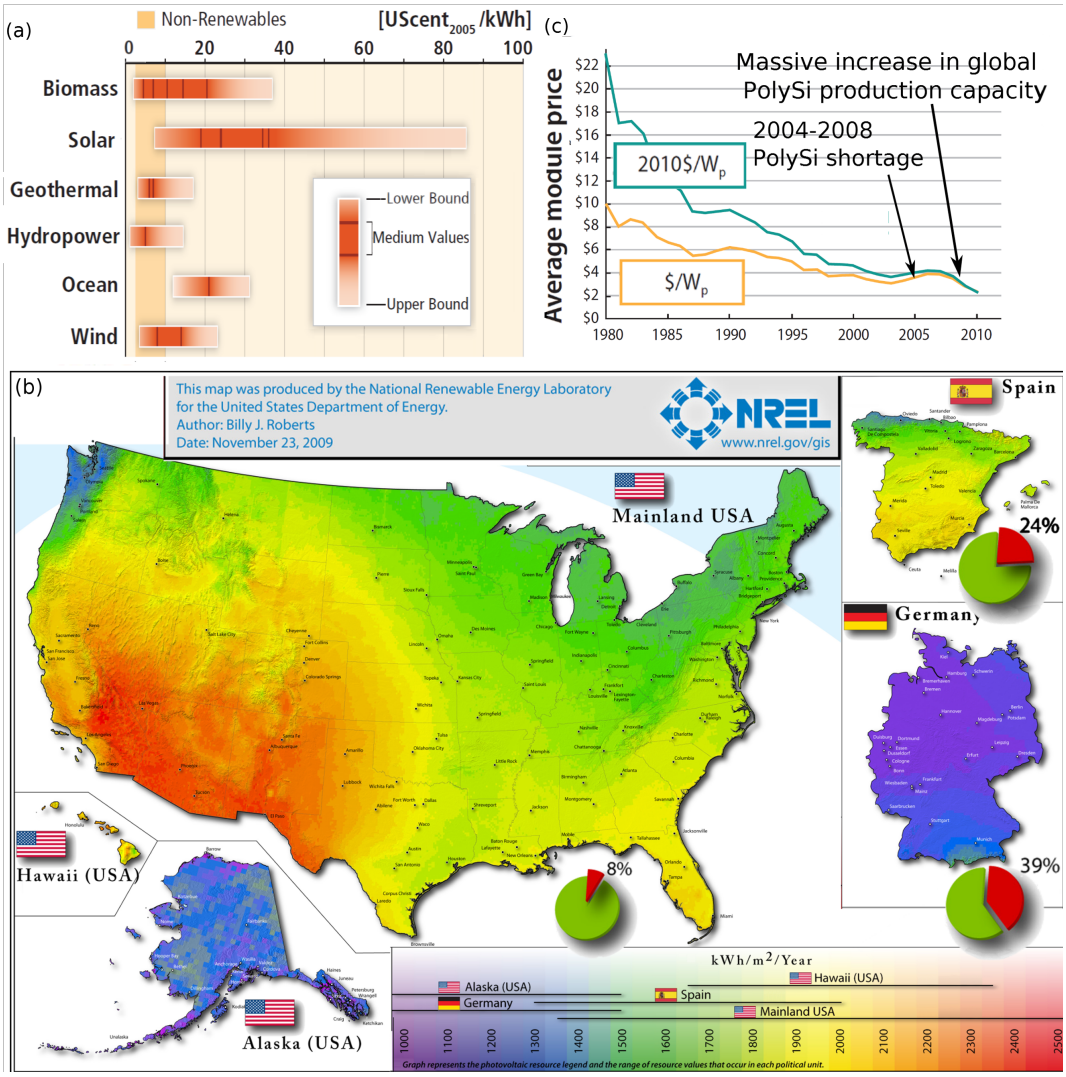

Figure 2: (a) Range in levelized cost of commercially available renewable energies technologies in comparison to non-renewable energy costs. The "medium values" for solar electricity account for (from left to right): concentrating solar power, utility-scale PV, commercial rooftop PV and residential rooftop PV. Adapted from IPCC report 2011 [2, p. 42]. (b) PV solar resource for the United States, Spain, and Germany (the pie chart represent the share of the world total production capacity in 2008). Adapted from NREL 2010 [6, p. 53]. (c) Global, average PV module prices, all PV technologies, 1984-2010 From NREL 2010 [6, p. 60] and Mint 2011 [7].

of magnitude less material than the 100 μm thick silicon solar cells, or even the μm thick thin–film solar cells [2, p. 351]. Those molecules can be tailored via molecular engineering to meet specific needs [8]. Finally, in the case of polymer–based organic solar cells which are using soluble molecules, solar panels can be produced via wet processes such as roll to roll or inkjet printing [9], which implies easy large scale- and thus cost–effective production [8].

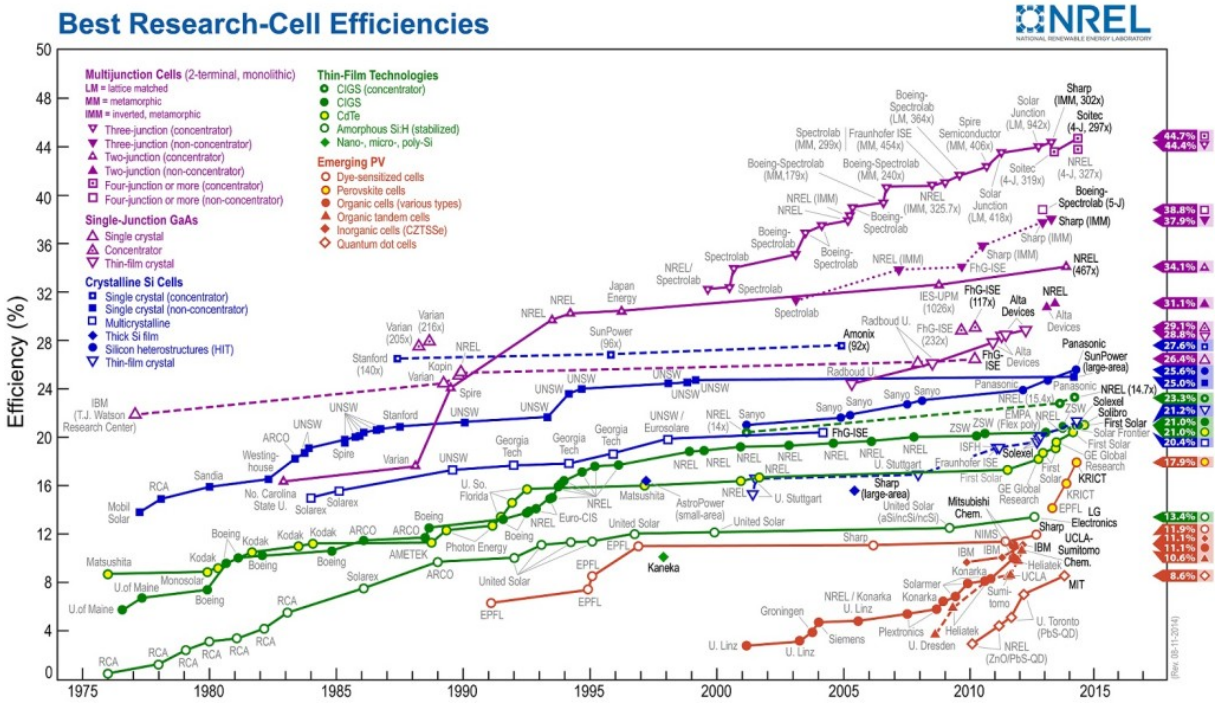

Figure 3: Best Research-Cell Efficiency. NREL, 08.2014 revision.

However, a certain number of locks have to be released before organic photovoltaics (OPV) become a viable commercial solution. One of those obstacles was, until 2008, their limited efficiency. The development of a new generation of molecules [10–16] enabled continuous improving, reaching efficiencies over 10 % in 2011 [17] comparable to some technologies already commercially available such as amorphous and nanocrystalline silicon solar cells [18]. Other issues still have to be addressed such as the long term stability of those materials upon use in PV applications [19, 20].

To solve those problems, it is mandatory to reach a perfect understanding of photogeneration in OPV. However, in contrast to what occurs in inorganic materials, charge generation in organic materials is a multisteps process. Furthermore, organic materials are intrinsically disordered materials, resulting in less crystalline films and energetically broad densities of states. Those factors contribute to make of organic materials the stage of photophysical mechanisms markedly more complex than in more traditional semiconductors, and still only partly understood.

In this dissertation, we will see how optical methods can be used in to unravel the mechanisms taking place during charge generation. Such methods present the advantage of being contact-less, thus enabling us to focus on the properties of the material itself regardless of metal/organic interfaces, and to allow for accessing not only to the densities of charged species, but also to all the kind of intermediate species that can be formed in the process of charge generation or in competition with this process. Those methods were applied on the reference material poly-3(hexylthiophene) (P3HT) and enabled us to do

important advances on its comprehension.

One of the most important peculiarities of organic semiconductors is their "excitonic" nature. It implies that light absorption generates "excitons" in which an electron and a hole are bond together. For this reason, organic solar cells active layers contain two materials, so that the difference of their electron affinity at the heterojunction acts as a driving force for separating the charges. The quantification of the energy needed for this separation has always proven challenging because the different experimental methods used to investigate a single material energy levels give quite a variety of results. After a careful analysis of the absorption and photoluminescence of P3HT to determine the nature of its excitons, we were able to quench its photoluminescence by applying an external field. The quenching is attributed to exciton dissociation. The use of the Onsager – Braun theory enable us to quantify the binding energy that is overcome. Armed with this knowledge, we are able to propose a model explaining the energy levels extracted by other method by assigning them to the different species involved in the process of charge generation. Those results are presented in chapter 4.

Another application of optical methods is to use the unique absorption spectrum of each species to investigate the occurrence of charge generation over competing processes in photoactive blends thanks to photoinduced absorption spectroscopy. We applied this method to scan new potential electron acceptors for photovoltaic applications. In combination with device, charge transport, and morphological characterization techniques, it enabled us to identify material systems for which the blend morphology was sub-optimal, either impeding the exciton to reach the heterojunction and thus to be dissociated into charges, or in the opposite enabling efficient exciton dissociation but preventing charge transport, or their extraction due to the formation of blocking layer. Those results, presented in chapter 5, highlight the necessity of finding material systems with optimal morphology in order to minimize losses.

We finally focus on the optimal morphology blend P3HT:PCBM to investigate more in detail losses due to separated charges recombination. The weakness of this recombination is largely responsible for the high quantum efficiencies reached with this blend but is still poorly understood. The analysis of photoinduced absorption spectra of neat P3HT and a P3HT:PCBM blend at different temperature enable us to identify a temperature and spectral range to specifically probe positive charges in P3HT. Transient absorption revealed that limited recombination occurs only in the blend, while recombination in neat P3HT is stronger, in agreement with the Langevin theory. Based on this knowledge we discuss the different theories proposed to explain the limited recombination in the P3HT:PCBM blend, and the role of phase separation and energetic trapping of charges. Those results are presented in chapter 6.

Prior to those result we arm the reader in chapter 1 with the theoretical background needed to get a good grasp on the discussed result. This includes a presentation of electronic transition that are monitored by the optical methods; and a description of the bulk-heterojunction structure used for polymer PV applications and of the current understanding of the mechanisms taking place in such a structure upon illumination in the peculiar case of organic semiconductors. The chapter 2 is dedicated to the experimental methods used to monitor photoluminescence, steady-state photoinduced absorption and transient absorption (TA) in the studied materials, as well as more briefly some complementary

techniques. Chapter 3 presents the reference materials P3HT as well as its blend with the fullerene derivative [6,6]-phenyl-C_{61} butyric acid methyl ester (PCBM).

Part I

Prerequisite

Chapter 1

Theoretical Background

This chapter will familiarize the reader with the fundamental concepts and theories underlying the experimental methods used in this thesis. It will also introduce to the specific properties and issues of organic materials as well as of the photovoltaic devices based on those materials.

1.1 Energy levels and electronic transitions

The experimental methods used in this thesis are based on the optical monitoring of the radiative transition between the electronic levels of the neutral or charged molecules or agglomerates of molecules. It is thus important to first present the basic rules governing the occurrence or the absence of those transition in the frame of the Born Oppenheimer approximation. We will then see the limits of this approximation and the existence of non–radiative transition which are not accessible to optical investigation but can represent a large fraction of the electronic transitions in organic semiconductors. We will finally see how agglomeration alters the spectra of molecules or monomers and enables the delocalization of the electronic excitation to form excitons. The exciton is a fundamental concept for organic electronics; its properties will thus be presented in more details.

1.1.1 Energy levels and electronic transitions in the Born–Oppenheimer (BO) approximation

Energy levels and BO approximation

In systems such as molecules or solids, interactions between the different constituents authorize those constituents positions and the system's energy to take only certain values. Under steady-state conditions, these values are the solutions of the time independent Schrödinger equation:

$$\mathcal{H}\Psi = E\Psi \tag{1.1}$$

Here, $\mathcal{H}$ is the Hamiltonian operator, Ψ the wavefunction of the system and E its energy. The Hamiltonian is the sum of the electronic and non-electronic interactions between the various components of the system. Except for the most

simple systems such as the hydrogen atom, this equation can not be solved analytically.

The BO approximation allows for decoupling the electronic and nuclear questions by considering that given their difference of mass, electrons and nuclei are moving on very different time scales. The electrons are thus viewed as interacting only with each other in a fixed potential generated by the nuclei. Similarly the nuclei are treated as vibrating in a potential given by the electronic energy level. The vibronic (nuclear or vibrational + electronic) state Ψ of the system is thus described as the product of a purely electronic wavefunction ϕ and a purely vibrational (nuclear) wavefunction χ:

$$\Psi(r_i, Q_K) = \phi \mid_{Q_K} (r_i)\chi(Q_K) \tag{1.2}$$

where r_i and Q_K are the electronic and nuclear coordinates respectively. The electronic and nuclear wavefunctions satisfy the following purely electronic and purely vibrational equations:

$$(\mathcal{H}_E + V_{Q_K}(r_i))\phi \mid_{Q_K} (r_i) = E_e \mid_{Q_K} \phi(r_i) \mid_{Q_K} \tag{1.3}$$

$$(\mathcal{H}_N + E_e(Q_K))\chi(Q_K) = E_v\chi(Q_K), \tag{1.4}$$

respectively. Here $\mathcal{H}_E$ and $\mathcal{H}_N$ are the Hamiltonian operators accounting for the electron-electron and nucleus-nucleus interactions, respectively; V_{Q_K} is the potential generated by the nuclei for a given set of nuclear coordinates Q_K. Finally E_e and E_v are the electronic and vibrational energies of the system respectively, the total energy of the system being the sum of those two.

Electronic transitions and Franck–Condon principle

Electronic transitions involve the change of the electronic, vibrational and rotational states of the system which corresponds to energies in the order of eV, tens to hundreds of meV and meV, respectively. As concerning very low energies, the rotational structures of electronic transitions can usually not be resolved except in gas phase and will not be treated here.[1]

The probability of a system in an initial state i to undergo an electronic transition to the final state f in the presence of the appropriate radiation is given by:

$$\mathcal{P}_{if} \propto |< \Psi_i \mid \mathbf{M} \mid \Psi_f >|^2 \tag{1.5}$$

where $\mathbf{M}$ is the transition dipole operator.

One interest of the BO–approximation is to give a very clear basis for understanding the so–called *selection rules* governing the electronic transitions. Indeed, using the BO–approximation and the fact that spin–orbit coupling can usually be neglected, the wave function Ψ describing the system state is simply written as the product of three independent terms: the vibrational wavefunction χ, a function ϕ_e depending only on the spatial coordinates of the electrons and a function ϕ_s depending only on the spin coordinates of the electrons: $\Psi = \phi_e\phi_s\chi$.

The transition dipole operator acts only on the spatial electron coordinates. It follows that the transition probability $\mathcal{P}_{if}$ exhibits three uncoupled dependencies over electron spin, electron coordinates, and nuclear vibrational states [21,

[1] They could theoretically be taken into account in the same way as the vibrational component, by adding a third term in the aforementioned BO approximation.

p. 23]:

$$\mathcal{P}_{if} = \underbrace{|< \phi_{e_i} \mid \mathbf{M} \mid \phi_{e_f} >|^2}_{electronic\ spatial} \quad \underbrace{|< \phi_{s_i} \mid \phi_{s_f} >|^2}_{electronic\ spin} \quad \underbrace{|< \chi_i \mid \chi_s >|^2}_{nuclear\ spatial} \tag{1.6}$$

The first meaning of this decoupling is the direct consequence of the BO–approximation: nuclear coordinates are unaffected by the electronic transition. It implies that in the common representations energy vs nuclear coordinates, or energy vs momentum, the transitions following the BO–approximation are always vertical (see figure 1.1); this is the Franck–Condon principle [22].

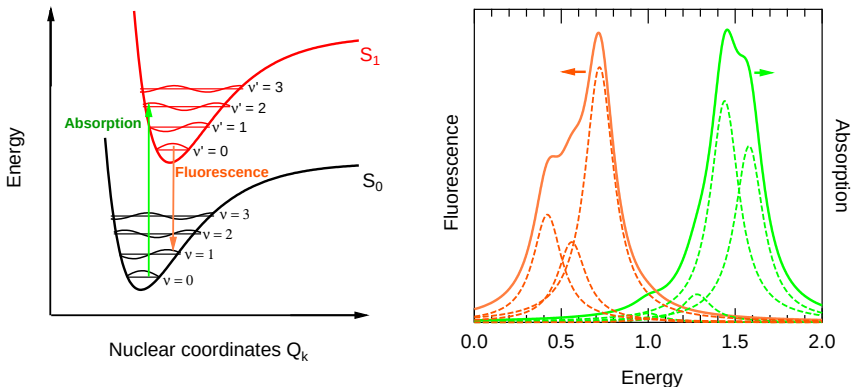

Figure 1.1: Left: Main vibronic transitions between the ground state S_0 and the first excited electronic state S_1 in a system following the BO approximation and Kasha's rule when considering only one vibrational mode. ν and $\nu\prime$ are the vibrational quantum numbers of the considered vibration mode in the ground state and excited state, respectively. Right: Corresponding absorption and emission spectra constructed from the left graph with a Lorentzian distribution line-shape (see §1.1.3) of half–width at half–maximum 100 meV (the individual vibronic transitions are represented in dotted line).

The selection rules are the second consequence of equation 1.6: any transition canceling one the three terms results in a zero transition probability, i.e. a forbidden transition:

Electronic spatial term: dipole moment. The quantity $< \phi_{e_i} \mid \mathbf{M} \mid \phi_{e_f} >$ is called *transition dipole moment*; it is responsible for the so-called symmetry rules as well as for the transition polarization. An example of these symmetry rules is that if a system has an inversion center, only transitions between states of opposite parity (odd to even or even to odd) are allowed. Other transitions have a transition dipole moment of zero and are called dipole forbidden. It results from the fact that the dipole operator is a sum of odd operators. For this reason the electronic states of a system are often named after the symmetries of their wavefunctions, using the point group formalism.

Labels A_g and B_u are the most common for conjugated polymers wavefunctions. They refer to the behavior of the wavefunction under point inversion through the chain's inversion center (g is unchanged, "gerade" and u is inverted,

"ungerade"), and under 180° rotation around any of the molecule's main axes (A is unchanged by rotation around any axis, B is inverted by at least one of these rotations).[2][3] Note, nevertheless, that the wavefunctions associated with the excited states experimentally observed are often not known precisely and are therefore simply named after their spin and by order of increasing energy (S_0 to S_n for singlets and T_1 to T_m for triplets).

Spin term: spin conservation. The spin term is zero if the initial and final states have different spins. Such a transition is said to be spin-forbidden. It is strictly forbidden as long as spin-orbit coupling is not taken into account. This coupling is nevertheless not strictly zero and transition between states of different multiplicity are experimentally observed with rates 10^3 to 10^5 times lower than those respecting the spin conservation rule [21, p. 26]. Spin-orbit coupling increases on systems including atoms of higher atomic number (such as sulfur or metals) [23, 24].

Vibrational term: Franck–Condon factor. The nuclear term is the Franck–Condon factor. Within one electronic transition, it is responsible for the relative intensity of the peaks corresponding to different quanta of vibration and thus for the vibronic structure of absorption and emission spectra. It is maximal when the overlap between the vibrational wavefunctions in the initial state and in the final state is maximal. In other words, the Franck–Condon factor is accounting for the fact that nuclei are considered immobile during the electronic transition.

If the nuclei are considered not moving during an electronic transition, they do it immediately afterwards. Thus, nuclear relaxation occurs within the time range of the nuclear vibration, i.e. 10^{-15} to 10^{-13} s [21, 25]. This relaxation normally brings the system back to the ground vibrational state of its electronic level as the fraction f_m of states having m vibrational quanta is given by [21, p. 16]:

$$f_m = e^{-mE_v/kT} \tag{1.7}$$

which gives a fraction as small as $f_1 = 3.1 \times 10^{-3}$ for the first non–fundamental level for a vibration mode energy E_v of 0.15 eV. As a results, electronic transitions in linear optics are normally always occurring from the lowest vibrational state of an electronic level [26]. This is called *Kasha's rule*. Transitions not following this rule are called *hot band* transitions.

1.1.2 Limit of the BO approximation: non radiative transitions

In the previous paragraph, we have seen the rules governing the radiative electronic transitions in optically active systems. Excited states can also return to the ground state via other decay processes. Radiative (fluorescence) and non radiative (intersystem crossing and internal conversion) decays are summarized

[2] For a system with an even number of π electrons where each molecular orbital is doubly occupied (not a radical), the ground state is usually totally symmetric (A_g) [21, p. 24].

[3] For more information about symmetries and the corresponding wavefunctions naming, the reader is referred for example to the chapters 15 and 23 of the book from Atkins and de Paula [23].

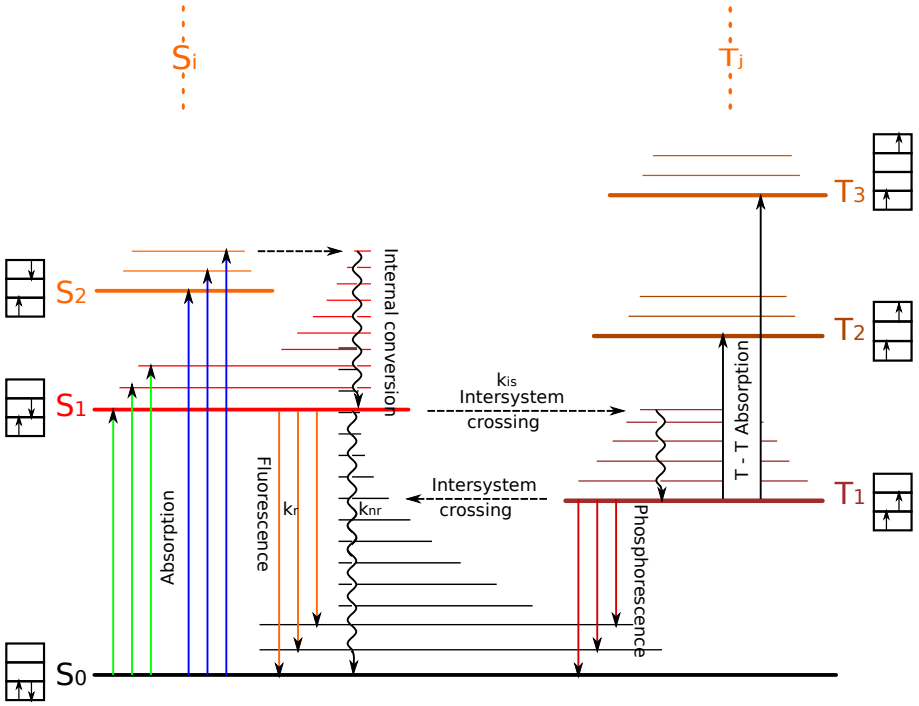

Figure 1.2: Radiative and nonradiative decay processes for systems obeying Kasha's rule. Non radiative decays are represented by wavy arrows. The dispositions of electronic spins are shown on the boxes alongside the singlet (S) and triplet (T) state designations. k_{nr}, k_r and k_{is} are the rate for non-radiative decay, radiative decay and intersystem crossing respectively. Adapted from Pope and Swenberg 1999 [21, p. 18] and Mcglynn et al. 1969 [27, p. 2]

in figure 1.2. Non radiative decays are neglected in the BO–approximation but can be predominant in real systems. In solar cells application, all those processes are in competition with charge separation.

In the frame of the BO–approximation, we consider the vibrational states as subdivisions of well separated electronic energy levels, thus not interacting with other electronic levels (see figure 1.1). This holds as long as the average energy ΔE between vibrational levels belonging to different electronic states remains bigger than the interaction energy v between those two electronic states (see Fig. 1.3), which is typically the case for isolated small molecules (less than 4 atoms) [21, p. 37].

Yet, ΔE becomes critically small when increasing the size of the molecules and thus the number of vibrational modes. Indeed a molecule with N atoms is generally expected to have $3N - 6$ normal vibration modes [23];[4] crystals, polymer (often considered as one dimensional crystals [28]) and other solids additionally exhibit intermolecular (or intermonomer) vibrational modes. It

[4]For sake of simplicity we represented only one mode (see figure 1.1). This make sense because the goal was then to describe the absorption and emission spectra, in which usually only the features associated to the vibrational mode with the largest energy quantum can be resolved [21].

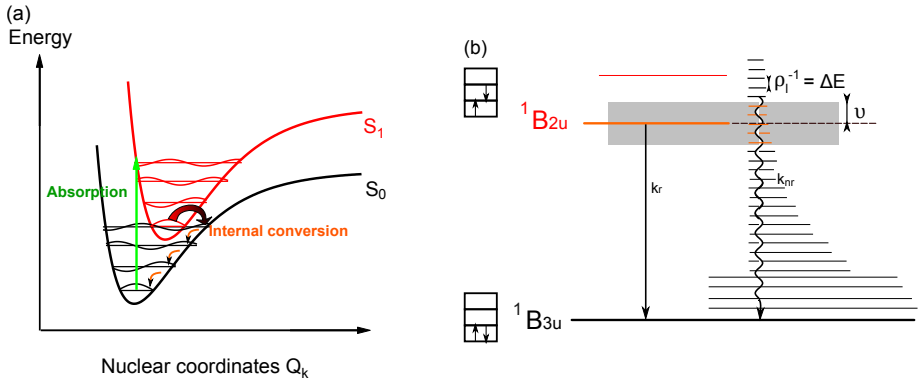

Figure 1.3: (a) Schematic representation of an internal conversion. (b) Interacting BO levels that should be considered to define the actual lowest excited state (within the grey rectangle). The actual energy level closest to the lowest vibrational level of the $^1B_{2u}$ electronic state could be obtained by linear combination of the interacting BO levels, represented in orange. For simplicity, the interaction energy v and density of vibrational levels ρ_l of the lower electronic level $^1B_{3u}$ have been set constant and the density of vibrational levels of the upper electronic level $^1B_{2u}$ has been taken very low.

follows that the vibrational modes form a quasi-continuum of vibrational levels, characterized by a density ρ_l.

As a result, the system in an excited electronic state can be written as a linear combination of the $\Delta E \times \rho_l$ interacting states shown in figure 1.3(b). Because this linear combination includes some terms from the ground electronic state (with large vibrational quantum numbers) the system can relax via vibrational relaxation (wavy arrows in figure 1.2) instead of radiative transition (straight arrows in figure 1.2) These non radiative processes can represent quite an important part of the decay, especially if the radiative transition is dipole forbidden. As an example, the fluorescence yield of benzene in a cyclohexane solution is only 0.058 [21, p. 31] [29].

1.1.3 Situation in aggregates, concepts of the exciton

Because of intermolecular interactions, the energy levels and optical properties of aggregates, substantially differ from those of isolated molecules. A consequence is the difference between the absorption spectra of molecules in solution and in films (see figure 1.4).

Those properties are especially relevant for conjugated polymers. Indeed, due to the length and relative stiffness of their backbone, the optical properties of a polymer chain can also be rendered by considering them as a 1–dimensional crystal of its monomer (with stronger interactions than for a crystal formed of separated molecules), rather than as a single molecule [28].

The changes in the optical properties of aggregates and crystals compared to isolated molecules are listed in the book from Pope and Swenberg [21, p. 39] as follow:

1. Shift of the bands.

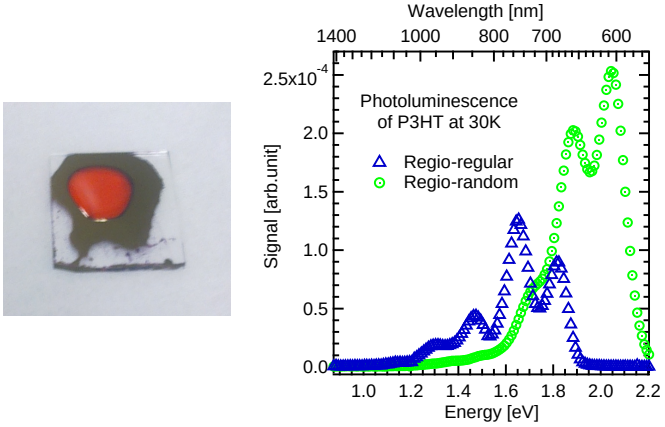

Figure 1.4: Left: Difference of absorption in aggregated (in dark purple where the solvent has evaporated) and non aggregated (in orange in colorless solvent) poly(3-hexylthiophene) (P3HT). Right: Effects of inter-molecular interactions on photoluminescence spectra of spin-coated films of P3HT: regio-random (RRa-) and regio-regular (RR-) P3HT. Adapted from Liedtke 2006 [30]

2. Splitting of spectral lines with change of polarization properties.

3. Variation of selection rules and oscillator strength.

4. Changes in the molecular vibrational frequencies and introduction of new intermolecular vibration modes.

Explaining these changes requires the introduction of one of the most important concepts of photophysics in polymers: the excitons. Several kinds of excitons can exist. We will now define them and see how they differ from the above-presented molecular excitation and how they can be derived from it.

Case of two molecules: physical dimers, excimers and exciplexes

A physical dimer is obtained when two molecules (called monomers), not chemically bound, are subject to attractive interaction promoting the exchange of charges or energy. The modeling of physical dimers is relatively simple: the dimer interaction is treated as a perturbation V_{12} ($\mathcal{H}_d = \mathcal{H}_{m1} + \mathcal{H}_{m2} + V_{12}$, with the subscripts $_d$ and $_m$ standing for dimer and monomer, respectively) affecting the energies. The systems wavefunction is thus $\Psi_d = \Psi_{m1}\Psi_{m2}$ for ground state, and $\Psi^*_{d(\pm)} = a\Psi_{m1}\Psi^*_{m2} \pm b\Psi^*_{m1}\Psi_{m2}$ for the excited state, as the excitation – symbolized by $*$ – could be bared by either of the molecules.[5] In case the two monomers are identical, the energies are given by [21, p. 41]:

$$E_{dimer} = E_{monomer1} + E_{monomer2} + W \tag{1.8}$$

$$E^*_{dimer(\pm)} = E^*_{monomer1} + E_{monomer2} + W' \pm \beta \tag{1.9}$$

$$\tag{1.10}$$

[5]In case of identical molecules, the coefficients a and b are equal ($= 1/\sqrt{2}$). In case the two molecules have different electron affinity, a term $+c\Psi_{donor+}\Psi_{acceptor-}$ can be added to account for the possibility of charge transfer between the molecules.

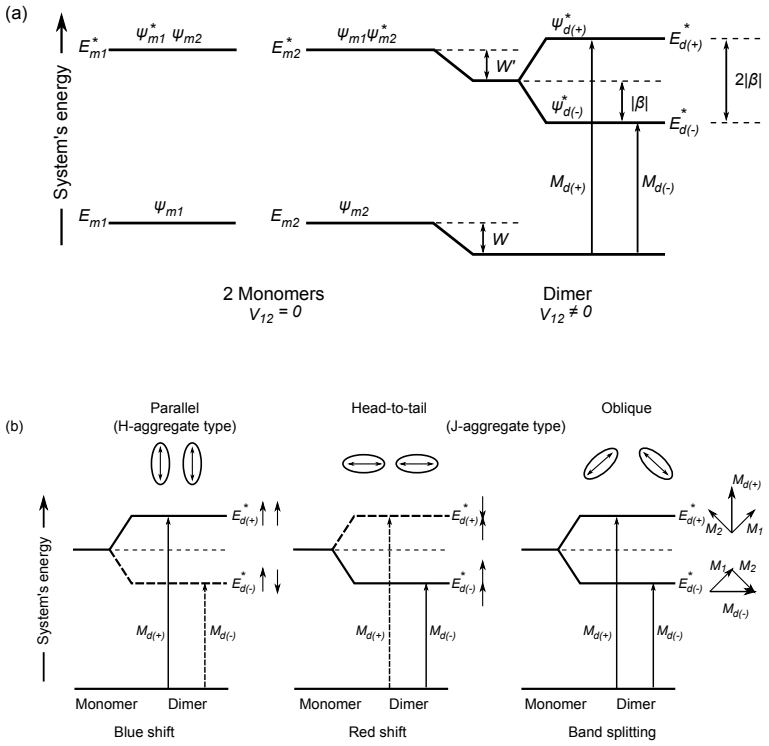

Figure 1.5: (a) Construction of the electronic energy levels of a dimer composed of two identical molecules. The energy levels and wavefunctions represented here are defined in the text. (b) Allowed transitions depend on the relative orientation of the two monomers's transition dipoles. Source: Kasha 1976 [31, pp.345-346], Pope and Swenberg 1999 [21, p.42-43].

W represents the Couloumb binding (or repulsive if $W > 0$) energy between the two monomers, W' represents the Coulombic interaction energy between the excited molecule and the not excited one and β is the resonance interaction energy between the two possible excited situations (monomer1 excited or monomer2 excited). Those energies can be visualized in figure 1.5 as well as the allowed transitions between the dimers' energy levels.

In case of identical molecules, the dimers transition dipoles moments $\mathbf{M_{d(\pm)}}$ for the absorption from the ground state are derived from the monomers ones $\mathbf{M_1}$ and $\mathbf{M_2}$ as $\mathbf{M_{d(\pm)}} = \frac{1}{\sqrt{2}}(\mathbf{M_1} \pm \mathbf{M_2})$ [21, p. 42]. Both red- and blue-shifted absorption are possible depending of the sign of $W - W'$ and of the magnitude of the energy splitting 2β. Additionally for translationally equivalent molecules, the transition moments are either parallel or anti-parallel, with consequence that for one configuration either $\mathbf{M_{d(+)}}$ or $\mathbf{M_{d(-)}} = 0$, the transition thus being dipole forbidden [21, p. 43]. This is the case for example for the absorption by delocalised P3HT polarons [32] (See § 5.2.2).

In the special case of symmetrical sandwich dimers, where the molecules lie parallel to each other, Pope and Swenberg list the following spectral properties [21, p. 46]:

1. Dimers maxima lie at lower energy than the corresponding maxima of the monomer spectrum.
2. The Franck–Condon maximum of the dimer is represented by the 0→1 transition, as compared with the 0→0 transition of the monomer.
3. The dimer spectrum is considerably broader than the monomer spectrum due to the interactions between both monomer's vibration modes.
4. There is a significant hypochroism, which means that the spectrum intensity is weaker than 2 times the intensity of the monomer spectrum.

This is observed for example when comparing the photoluminescence of regioregular P3HT to the one of regio-random P3HT where the irregularity of side–chains orientation hinders intermolecular interactions (figure 1.4(right) and more in detail in § 4.2.2).

Because molecular orbitals of higher energy states are generally more spatially extended, it is likely that two molecules interact only when one is excited ($W \geqslant 0$). The excited state of such a pair is called an *excimer* for "excitation induced dimer" (or *exciplex* if the two molecules are of different nature like at an electron donor-electron acceptor heterojunction). In the case of exciplexes, it is very likely to have a partial charge transfer with the electron being mainly located on the molecule with the stronger electron affinity and the hole on the other one [33–35].

Note that molecules energy levels hybridization is not limited to neutral excited states. A similar effect is for example observed with energy levels of polarons in P3HT (see § 1.2.3 for the definition of polarons), in which the delocalization of the polarons over two chains creates an energy level splitting [32] (see more in detail in § 5.2.2).

1-Dimensional crystal: Frenkel exciton

Similar reasoning is applied to aggregates of N molecules. The ground state Ψ is described by the product of the monomers' wavefunctions. The N excited states $\Psi^*_{(k)}$ are obtained by linear combinations of the wavefunctions Ψ'_n in which the nth molecule is excited and the others are in the ground state (tight binding approximation):

$$\Psi = \prod \Psi_n \tag{1.11}$$

$$\Psi^*_{(k)} = \sum a_n \Psi'_n \tag{1.12}$$

$$where\ \Psi'_n = \Psi^*_n \prod_{i \neq n} \Psi_i \tag{1.13}$$

$\Psi^*_{(k)}$ is called an *exciton* [21, p. 55]. It accounts for the modification of the energy levels and of the wavefunctions (compared to ground state) not only on the absorption's site but also on the surrounding (in the case of a polymer: the rest of linear chain).[6] The term *exciton* refers to both this electronic excitation

[6] For example in the case of nondegenerate polymers such as polythiophenes: "this structural relaxation is characterized by a reversal of the C—C bond length alternation to create a domain of semiquinoidal bond sequence localized over several monomer units. The magnitude of this bond length reverse is greater at the center of the exciton and progressively diminishes along the chain until an aromatic bond structure is restored." [36]

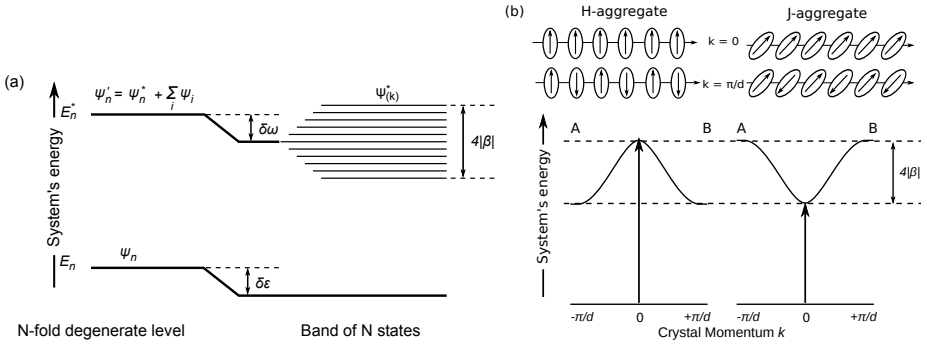

Figure 1.6: Left: electronic energy levels of 1-dimensional aggregates of molecules. $\delta\epsilon$ is the change of cohesive energy per molecule. Right: Visualization of the dispersion of the exciton energy band in 1-dimensional aggregates of molecules. State A ($k = -\pi/d$) is fully equivalent to state B ($k = +\pi/d$). In first order, only the absorptions represented by the arrows at $k = 0$ are allowed. Adapted from Geacintov and Swenberg 1978 [37, p. 255], Pope and Swenberg 1999 [21, p. 56-57] and Langner 2005 [38, p. 19].

and this local structural deformation [36].

In case all monomers are identical, and only nearest neighbours interactions are considered, the wavefunctions $\Psi^*_{(k)}$ are associated to the following energies [21, p. 55]:

$$E_{(k)} \quad = \quad E_m + \delta\omega_0 + 2\beta cos(kd) \tag{1.14}$$

where d is the lattice size and the quantity k takes N regular values between $-\Pi/d$ and $+\Pi/d$ and is related to the momentum p of the exciton by the relation $p = \hbar k$. As for dimers, β can be seen as the resonance coupling between the theoretical state Ψ'_i in which the excitation is localized on the ith molecule and the theoretical state Ψ'_{i+1} when the excitation is localized on its neighbor.

As shown in figure 1.6 (left), those energy levels correspond to the formation of an energy band. The band bending can be seen in figure 1.6 (right). Its dispersion relation is given by equation (1.14) and allows for the calculation of the effective mass m^* of the exciton:

$$(m^*)^{-1} = \frac{1}{\hbar^2}\frac{\partial^2 E(k)}{\partial k^2} \tag{1.15}$$

As an example, experimental values of $4.2{\cdot}m_e$ and $7.8{\cdot}m_e$ have been found by Matsui et al. [21, 39] for the first singlet exciton band in anthracene, for two different crystal directions (m_e being the mass of a free electron). The consequence of such high effective mass is that the exciton radius remains rather small, typically below the intermolecular distance. Such small radius excitons are called *Frenkel excitons*.

As for dimers, both red-shift and blue shift of absorption are possible. Moreover, the additional intermolecular vibration modes generally tend to make the non-radiative relaxation more favorable compared to the isolated molecules [21].

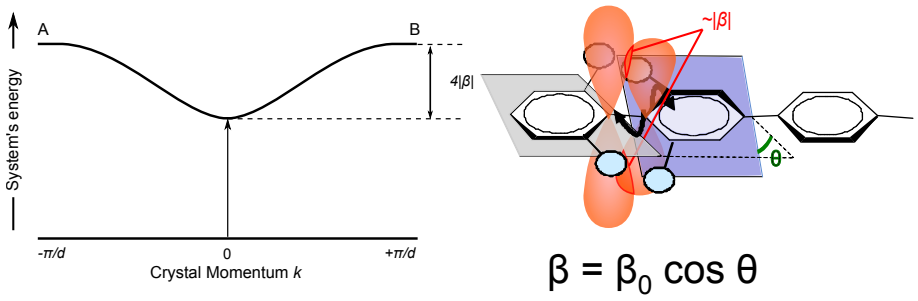

Figure 1.7: Left: the bandwidth of the excitonic energy band in a 1-dimensional aggregate of molecule is directly proportional to the resonance interaction energy of the neighboring monomers β. Adapted from Geacintov and Swenberg 1978 [37, p. 255] and Pope and Swenberg 1999 [21, pp. 56-57]. Right: In case of a polymer chain this interaction is directly connected to the torsion angle θ between neighboring monomers via the overlap of monomers' wavefunctions. This angle is controlled by two effects, the overlap of the neighbouring monomers wavefunctions (here represented in red) which is stabilizing the system and tends to decrease the angle, and the steric effect due to the side chains (represented by blue circles) which tends to increase that angle.

Polymers

As previously mentioned, a convenient way to treat the energy levels in conjugated polymers is to consider the polymers as 1-dimensional crystals. The main differences with crystals of chemically unbound monomers are: a) The hybridization of monomers also exist in the ground state. b) The interaction energy β between successive monomers is much higher, which results in the formation of broader energy bands (the bandwidth is 4β, see figure 1.6 and equation (1.14)). The resulting increased band bending means that the exciton has a much lower effective mass (see equation (1.15)), in the order of $0.1 \cdot m_e$ for poly(phenylene vinylene) (PPV) [40]. It can consequently be much further delocalized (Kirova et al. found an exciton radius of 15 Åwhich is between 2 and 3 monomer's length); that way, the first excited state in PPV has been calculated to be a *Wannier-Mott exciton* [28, 40].

Influence of the environment on polymers' excitons

The interaction energy β between neighboring monomers of a polymer is strongly influenced by the environment of the polymer. Indeed, β depends of the overlap of neighbor monomers wavefunctions which, in turn, depends on the torsion angle between successive monomers. A more compact environment will result in a smaller torsion angle θ and thus in more overlap between successive monomers wavefunction, an increased interaction energy, a decreased effective mass and more delocalized excitons (see figure 1.7) [28].

Such an effect can be experimentally forced, for example using high hydrostatic pressure, and results in a red shift of the absorption and photoluminescence spectra as pressure increases the planarity of polymers' backbone, thus increasing β and reducing the band gap [41–43]. It should nevertheless be mentioned that the enhanced inter-chain interactions under high pressure because of reduced inter-molecular distances also participates this red shift [41, 42].

Influence of disorder

Because of their size and the dispersion of their molecular weight, polymers do not form perfectly crystalline films. They cumulate intramolecular defects (torsional defects, kinks, and chemical defects) with structural defect (stacking faults, dislocations, and grain-boundaries) [44]. Depending on the side chains, they tend to form amorphous (for example MEH-PPV) to semi-crystalline (for example regio-regular P3HT) films. Nevertheless even the films of polymers forming rather crystalline structure always present some amorphous regions [45] (see also § 3.1.2).

This morphological disorder implies that important parameters such as the interchain distance, the conjugation length or the torsion angle between successive monomers of the polymer backbone strongly vary within the film. Due to the strong interactions between the polymer chains' environment and the energy levels, this structural disorder results in an energetic disorder. This disorder is accounted for by replacing the fixed energies that can be used in isolated small molecules, by a Gaussian distribution of sites energies of standard deviation σ [46–48].

This energetic disorder in turn implies that the peaks of electronic transition spectra usually exhibit some Gaussian [44, 49] line-shapes instead of the Lorentzian line-shape that would be expected in ordered systems [21].[7]

Important properties of excitons

Binding energy The binding energy is the main property that differentiates excitons from electron–hole pairs photo-generated in inorganic materials. It is the energy to overcome to separate the electron and the hole forming the exciton into charges that can be moved in opposite directions to create a current. As such it is largely responsible for the peculiarity of polymer based solar cell devices (see Section 1.2).

This binding energy is resulting from the interplay of three phenomena: Coulomb attraction (electron—hole interaction), lattice relaxation (electron—lattice interaction) and intra-ring interaction (electron—electrons interaction) [36].

The long-range Coulomb attraction potential V_C is the main factor responsible for the strong binding energy. Its most simple expression is the following:[8].

$$V_C = \frac{e^2}{4\pi\epsilon_r\epsilon_0 r} \tag{1.16}$$

Here, ϵ_r is the relative electric permitivity of the medium and r the exciton radius. Due to the very weak electric permitivity ($\epsilon_r \approx$ 2-4 compared to 12 in Silicon an 80 in TiO_2) and strong localization (nanometer scale) encountered in organic semiconductors, this potential is much higher than in inorganic semiconductors (hundreds of meV against few tens of meV).

The lattice relaxation — β being larger around the excited site results in a locally lower energy level — has an indirect effect: it is responsible for self

[7] The historical reasoning was actually the opposite: the experimental observation Gaussian line shapes in the low temperature absorption of molecular crystals submitted to single impurity inhomogeneous broadening, led Klafter and Jortner to propose a Gaussian energy distribution in 1977 [48].

[8] This expression is valid for an isotropic medium, a more realistic expression based on a 2-dimensional medium can be found in the tutorial of Kirova and Brazovskii [28]

localization [21, pp. 85-89] of the excitons and thus for a reduction of the exciton radius which has — as we have just seen — an important impact on V_C.

Intra-ring interactions are said by Brazovskii et al. [28,40] to be equivalent to a repulsive potential between the electron and the hole centered on the aromatic ring. It tends to balance the Coulomb interaction for the excitons having an even symmetry relatively to the center of the aromatic ring. This includes the lowest energy (S_1) intra-chain singlet exciton (B_u symmetry) but not the triplet (T_1 has A_g symmetry), thus explaining the lower energy of triplet states [28, 40]. This intra-ring interaction can in some cases cause the inversion of the first (B_u symmetry, optically allowed from/to the ground state) and second (A_g symmetry, optically forbidden from/to the ground state) excitons energy levels [28].

The consequences of binding energy on charge generation is discussed more detail in subsection 1.2.2. Chapter 4 is dedicated to its experimental determination in the case of P3HT.

Exciton diffusion length Excitons are able to diffuse within the polymer film. This energy transfer can take the form of a coherent motion within a prefect crystalline region (for example within the conjugation length of a polymer) or stochastic hopping from one site to another similar to charge transfer (see polaron transport in Section 1.2.3) with a hopping rate proportional to $\mid \beta \mid^2$ [21, p. 57]. The latter case is of course expected to strongly dominate in such disordered materials as conjugated polymers films [50].

Together with excitation's lifetime, the exciton diffusion constant enables to define an exciton diffusion length which is of paramount importance in solar cells application: not to be lost to recombination, an exciton has to be dissociated into free charges within that distance from where it was generated (see Section 1.2). Typical exciton diffusion lengths in conjugated polymers are found to be between 5 and 18 nm [51, 52].

Other kinds of excitons

Finally, one can not end this section about energy transitions and excitons without mentioning the existence and main properties of other kinds of excitons which also are of importance in polymer based bulk-heterojunctions:

Inter-chain excitons. As mentioned in §1.1.3, excitons can be delocalized over 2 polymer chains. In such excitons, the electron and the hole are located in 2 neighboring chains. Kirova and Brazovskii present those *inter-chain excitons* as very similar to the intra-chain ones concerning their mathematical treatment, but predict a few peculiarities with regard to their properties:

- The inter-monomer lattice distance a is replaced by the inter-chain distance d [28] which is more sensitive to environment constraints.[9]
- Higher binding energy [53]: because they have the electron and the hole centered on different polymer chains, interchain excitons are not affected

[9] See for example Webster et al. [41] for hydrostatic pressure's influence, or Jiang et al. who managed to tune the polarons' energy levels by adjusting the interchain distance by varying the alkyl side chains' length of polythiophene derivatives [32].

by intraring repulsion [28]. As this interactions is the main responsible for the energetic difference between singlet and triplets, it is predicted [28] and observed [54] that triplets and singlets energy levels are more close in inter-chain excitons [28].[10]

- Red-shifted absorption and luminescence [36,55], which is partly the direct consequence of the higher binding energy (which is shifting the excitonic levels deeper in the transport gap) but also a side effect of the higher conjugation length and the more planar structure of the better organized regions where inter-chain excitons are formed (see the example of P3HT in chapter 3). Due to these lower energy levels, inter-chain excitons are preferentially formed if the morphology enable their existence, see for example the case of P3HT in § 4.2.

- Lower luminescence yield due to the low overlap of the electron and the hole's wavefunctions which are located on different chains [28].

- Longer lifetime [28,55] and larger diffusion length [41,56]. Their ability to travel along 2 dimensions make them less vulnerable to structural defects in the film.

Moreover, as already mentioned, the absorption and photoluminescence of inter-chain excitons exhibit the same spectral differences with these of intra-chain excitons as those existing between monomers and dimers.

Charge transfer excitons and polaron pairs. Inter-chain excitons are often referred to under other names such as *polarons pair* [57], *charge transfer excitons* [21], (*coulombically bound*) *radicals pair*. In this thesis we will mention them as *inter-chain excitons* or *polaron pairs*, depending on whether we want to consider their properties of single quasi particle, or to consider them as two spatially separated charges, which they are also, although they are still energetically bound together. Note nevertheless that the equivalence of those two terms is not straightforward. For example Arkhipov and Bässler considered them as two successive steps in a process of exciton dissociation on an heterojunction's interface [58, p. 337]. The difference being that the electron and hole wavefunctions would still have a significant spatial overlap in the inter-chain exciton and not in the polaron pair which has consequences for their optical properties (for example spin-flip should be allowed in a polaron pair, and not in an inter-chain exciton). Besides, no evidence of a three-step exciton dissociation can be found in the literature. It is possible that if two distinct species exist, they are separated by an energy barrier too weak to make them practically distinguishable.

In the case of a electron donor/electron acceptor interface, the problem in commonly avoided by using the more general term of "Charge Transfer State" (CT-state) which includes the notion that a charge transfer takes place but does not specify to which extend. Especially it does not prejudge of the excitonic

[10] Such a picture was also used by Ohkita et al. to explain the difference between preferential triplet generation in blends of fullerene with polythiophenes forming amorphous films where intra-chain excited species dominate, and preferential charge generation in blends of fullerene with polythiophenes forming crystalline films where inter-chain excited species are more likely to be formed [54].

or polaron pair character of the state. For sake of clarity, the term "Charge Transfer State" will in this thesis always refer to this general heterojunction's interface state, and the term "charge transfer exciton" used by Pope and Swenberg [21] to refer to inter-chain excitons will be avoided. Note that spin-flip, and thus that inter-system crossing is expected to be facilitated in CT-states due to the weaker spin coupling between the electron and the hole [36, p. N].

Finally, the terms "excimer" and "exciplex" also refer to inter-chain excitons [36, 58]. They present the advantage of differentiating the cases where the several molecules over which the exciton is delocalized are identical (excimer) and the case where they are different (exciplex). Nevertheless, in order not to multiply the names, those terms will also be avoided here.

1.2 Bulk-heterojunction solar cells

1.2.1 Bulk-heterojunction

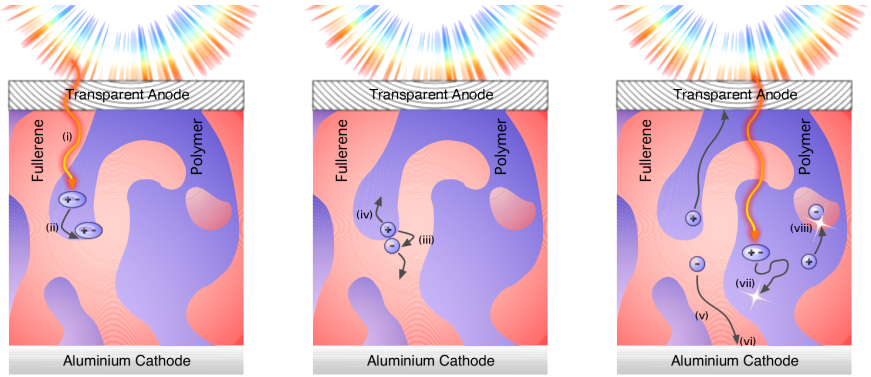

Figure 1.8: Photoinduced mechanisms in a bulk-heterojunction solar cell. Left: absorption and exciton diffusion. Center: CT-state formation and dissociation. Right: charge transport and losses. Adapted from Deibel and Dyakonov 2010 [59].

Due to the excitonic nature of the photo-excitation in organic semiconductors, photovoltaic applications require the presence of two materials with different electron affinities, so that the internal field at the electron donor–electron acceptor (D/A) heterojunction enables to split the primarily generated exciton into an electron and a hole. Moreover, a bilayer device, such as the one used for solar cells based on evaporated small molecules, is not an option for polymer based solar cells due to the too limited crystalinity of the films they form which strongly reduces the excitons diffusion length.

The bulk-heterojunction device is the answer to the double necessity for polymer based solar cells of: a) An active layer with a thickness sufficient to obtain a full absorption of the solar light, which typically means in the order of 100 nm. b) A distance to the D/A interface from any point in the bulk smaller than the exciton diffusion length which is typically in the order of 10 nm [59]. In a bulk-heterojunction, this is obtained by mixing the electron donor and the electron acceptor in solution and depositing them together (or for evaporated solar cells, by co-evaporating the two materials). Depending on the self organi-

zation properties of the blend components (miscibility, crystallization, etc.) this results either in an alloy–like active layer, with only one phase containing both materials (with or without organized structure such as interdigitation [60–62]) or in a frozen emulsion with separated phases of pure material, or more likely in something in between with some phases of pure material and some containing both materials.[11]

This self-organization approach is consistent with the concept underlying the use of conjugated polymers for solar cells, which is to produce solar energy at a reduced cost. Indeed, although studies exist for obtaining such a thin intermixing via nano-patterning method [64], such methods would probably result in a dramatic increased of the processing costs.

The working principle of bulk-heterojunction is shown in figure 1.8. (i) Light absorption in the absorber material,[12] generates an exciton. (ii) Its brownian motion has to bring it to the interface. (iii) There it can first be partly dissociated to occupy an interfacial CT-state. (iv) The two charges forming this quasi-particle being still coulombically bound, it requires one further step to dissociate them in a pair of separated charges, (v) which subsequently have to diffuse to the electrodes and (vi) be extracted to generate a photocurrent. One more constraint to the blend self-organization, is thus that it has to ensure the existence of a percolated pathway connecting any point of the active layer to the correct electrode.

Losses can occur such as (vii) recombination of the excitons before they reach the interface or (viii) recombination of free charges. In case the requirements of bulk-heterojunction (short distance to interface from any point of the active layer and percolation pathway to the electrodes) are not met, those losses can severely limit the performances of the solar cells. All those mechanisms are presented in more details in the following of this section.

1.2.2 Charge photogeneration

The D/A heterojunction ensures the dissociation of the excitons into a pair of charges free of each other attraction. As will be seen in chapter 4, the models presented here can be used to determine the binding energy of the excitons.

Exciton dissociation and CT-state formation.

As illustrated in figure 1.9, exciton dissociation is driven by the energy cascade downward from the absorber's exciton (S_1) to the excited CT-state (CT*). In addition to driving the exciton quenching, the position of the energy levels must insure that no unwanted species is energetically more favorable than the CT-state. Not meeting this condition would result in undesired "recombination" to triplet state[13] of the donor [54] (called "electron back transfer" in the usual case where the absorber is the donor), of the acceptor [65, 66] or an energy transfer [67]. Note that energy transfer is not necessarily a loss if it is followed by

[11] Phase diagrams of polymer:[6,6]-phenyl-C_{61} butyric acid methyl ester (PCBM) blends show that the fullerenes are soluble in the electron donor phase only until a certain concentration [63]. Above this limit, PCBM will usually form pure aggregates along with an alloy phase having the limit composition(although phases of pure polymer can not be excluded in actual blends because a film usually solidifies before reaching its equilibrium).

[12] Usually the electron donor.

[13] Spin flip is easier in the A+D- because spins are less strongly coupled than in an exciton.

hole back transfer to the polymer, as it has been observed in a oligophenylene—fullerene dyads [68, 69].

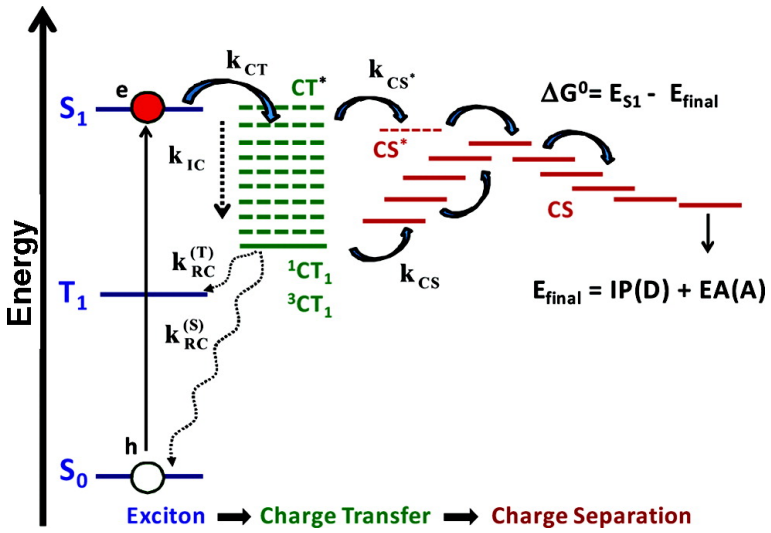

Figure 1.9: Electronic state diagram describing the photo-induced charge-carrier formation mechanism in an organic solar cell: S_0 denotes the singlet ground state of the absorber, and S_1 its first singlet excited state (excitonic state). At the D/A interface, intermolecular charge transfer leads to the occupation of a charge-transfer (CT) state, where the hole is on donor molecule(s) and the electron is on acceptor molecule(s). CT_1 is the lowest energy charge-transfer state. $CT*/CS*$ represents excited ("hot") levels of the CT/CS manifolds. The final state is a charge-separated state (CS), where the hole in the donor layer and the electron in the acceptor layer are free from each other attraction. The k_i terms indicate various competing relaxation and electron-transfer rates with $i = IC$ for Internal Conversion (see paragraph 1.1.2), RC for ReCombination ((S) to singlet, (T) to triplet state), CT for charge transfer, $CS*$ and CS for charge separation from hot and relaxed CT-states, respectively. Source: Bredas et al. 2009 [70].

Charge separation under the influence of excess energy and internal field.

The existence of interface CT-states, intermediate between the pure materials excitons and the separated charges has in the recent years been widely proven in quite a variety of material systems [36, 54, 71, 72]. Indeed, studies by Ohkita et al. have shown that — within a set of blends exhibiting excitons quenching over 70 % — charge generation efficiency (evidenced by transient absorption) could vary over 2 orders of magnitude, which was attributed to variations in the CT-states dissociation efficiency [54, 73–75]. Other studies managed to monitor the radiative recombination of CT-states and to show the invert correlation of its yield with solar cells power conversion efficiency [76] or external quantum efficiency (EQE) [77].

Two mechanisms are usually considered for the dissociation of the CT-states and are represented in figure 1.9: the dissociation of "hot CT-states" and the

dissociation of relaxed CT-states. They are associated to the rates k_{CS*} and k_{CS}, respectively.

Because of the cascade down of the energy levels between the singlet exciton and the CT-state, exciton dissociation is creating a CT-state with excess energy compared to its fundamental level. In the mechanism of "hot CT" dissociation, this excess energy is used to separate the charges further before the CT-state can relax to its fundamental level. In this mechanism, dissociation is in competition with relaxation.

The dissociation of relaxed CT-states, in contrast, would be driven by the internal electric field at the heterojunction. In that mechanism, dissociation is in competition with recombination of the CT-state.

Experimental evidences exists for both models. It is, thus, likely that both mechanisms exist and that the predominance of one over the other depends of the material system. For the "hot exciton" model, Clarke and Durrant carried out series of studies which revealed that for a same family of blends[14], the charge generation yield (estimated via transient absorption) scales exponentially with the excess energy of the primary exciton (S_1 in figure 1.9) as compared to the final separated electron-hole pair energy (taken as the sum of the acceptor's electron affinity and the donor's ionization potential, E_{final} in figure 1.9) [54,73, 74]. It appears however, that in the best performing systems, the heterojunction internal field could be enough to dissociate the CT-states without the need of any additional energy [78]. This result was obtained by Lee et al. [79] on a P3HT:PCBM blend in which they used the CT-states' absorption to generate directly some "cold CT-states" and obtained from this illumination the same internal quantum efficiency as when illuminating in the absorption region of P3HT.

Onsager-Braun model for field assisted dissociation

The modeling of field assisted dissociation enables to connect dissociation efficiency to binding energy. Different models have been developed to explain the influence of electric field on CT-state or excitons dissociation [80, 81]. Here we present the Onsager-Braun theory which has been successfully applied to a variety of cases [72, 82–84].

Onsager originally analyzed the fate of ion pairs animated by a brownian motion in their mutual attraction potential as represented in figure 1.10(a). The probability P_d of dissociation is the probability that this brownian motion brings the ions to a distance at which the coulombic attraction is smaller than the available thermal energy. This defines the "Coulomb capture radius", r_c (equation 1.18). The probability of recombination is the probability that the brownian motion brings the electron-hole distance to zero. The effect of the electric field is to bend the Coulomb attraction potential (see figure 1.10(b)), thus increasing the probability that the thermalization distance a of the electron–hole pair is beyond r_c. The resulting dissociation probability is then [36]:

$$P_d(F) = e^{\frac{-r_c}{a}} f(F) \tag{1.17}$$

$$r_c = \frac{e^2}{4\pi\epsilon_r\epsilon_0 k_B T} \tag{1.18}$$

[14] for example polythiophenes:PCBM blends in [54]

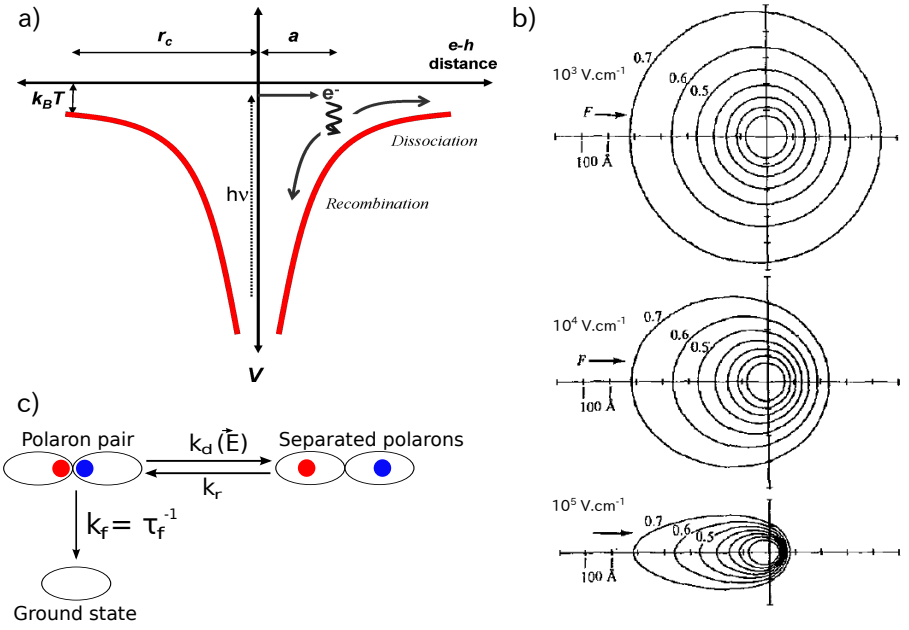

Figure 1.10: (a) Potential energy diagram summarizing Onsager theory for autoionization. The red curve illustrates the Coulomb attraction potential as a function of electron–hole ($e-h$) separation. Photoexcitation results in generation of a hot, mobile electron. This electron subsequently thermalizes at a particular distance a from the hole. If a is less than the Coulomb capture radius, r_c (as is typical for single-component organic systems), then the electron–hole pair (which we refer to herein as a charge-transfer state) can either undergo geminate recombination or dissociate into free charges. Source: Clarke and Durrant 2010 [36]. (b) Contour of constant probability for thermalized electron–hole separation for different fields and an isotropic dielectric constant $\epsilon_r = 3.02$. Source: Batt et al. 1969 [85]. (c) Competing mechanisms considered by Braun to adapt Onsager's theory with their respective rates (k_d for dissociation, k_r for reformation of the CT-state from separated charges, k_f for the decay of CT-states to the ground state).

f(F) is the field dependence term, e is the electron charge, k_B is the Boltzmann constant, T is the temperature ϵ_r is the relative dielectric constant of the surrounding medium, ϵ_0 is the permittivity of vacuum .

The Onsager theory was originally developed to describe the fate of ion pairs in gas and solutions. Its direct application to solids and especially to donor–acceptor interfaces resulted in non-realistic values for the thermalization distance [80]. Following the idea of Samoc and Williams [86], Braun proposed that this was due to a recombination condition too loose for donor–acceptor interfaces in solids. While Onsager proposed that recombination occurs only when the electron hole distance reduces to zero,[15] Braun adapted it by considering that the electron–hole distance in CT-state is so small that recombination will occur anyway, characterized by a lifetime $\tau(F)$. Dissociation is thus in kinetic

[15]Which is approximately true for ions in gas and liquids as the recombination distance is very small on the scale of the distances between the ions of a thermalized pair in such a medium.

competition with recombination. Moreover, Braun added that CT-states can be re-generated from the separated charges with a rate k_r equal to the Langevin prefactor for bimolecular recombination of separated charges [80]. As a result, the dissociation probability can be expressed as function of the rates of the competing processes (see figure 1.10(c)):

$$P_d(F) = \frac{k_d(F)}{k_f + k_d(F)} = k_d(F)\tau(F) \tag{1.19}$$

$$k_d(F) = k_r K(0) f(F) \tag{1.20}$$

For sake of simplicity, Braun considered the recombination rate $k_f = 1/\tau_f$ as field independent. Lacking accurate theory for the zero-field dissociation $k_d(0)$ [80], Braun expressed it as function of the well known Langevin recombination k_r rate (equation (1.21)) and the position $K = k_d/k_r$ of the equilibrium between dissociation and recombination for which two theories were available: for Wannier excitons (equation (1.22) from Lipnik [87, 88]) and for ion pairs (equation (1.23) from Fuoss [89, p 213]).

$$k_r = \frac{\langle\mu\rangle e}{\langle\epsilon\rangle\epsilon_0} \tag{1.21}$$

$\langle\mu\rangle$ is the spatially averaged sum of hole and electron mobilities, e the elementary charge, $\langle\epsilon\rangle$ the spatially averaged dielectric constant, and ϵ_0 the permittivity of vacuum.

$$K(0) = \left(\frac{m^* kT}{3\pi\hbar^2}\right)^{3/2} e^{-E_b/kT} \tag{1.22}$$

m^* is the reduced mass of the exciton and E_b is the binding energy of the dissociating species.

$$K'(0) = \frac{3}{4\pi a^3} e^{-E_b/kT} \tag{1.23}$$

Because the effective mass of the exciton is usually unknown, equation (1.23) is used in the vast majority of cases [72, 82–84] Besides, this formula has the advantage of introducing no other parameter than the binding energy. Indeed the ion pair separation a can be simply derived from the binding energy, which — in that case — is considered to be exclusively due to the Coulomb attraction [80]:

$$E_b = E_c = \frac{e^2}{4\pi\langle\epsilon\rangle\epsilon_0 a} \tag{1.24}$$

Finally, the field dependence $f(F)$ is taken from the original publication of Onsager [90]:

$$f(F) = K(F)/K(0) = \frac{J_1[2\sqrt{-2b}}{\sqrt{-2b}}] \tag{1.25}$$

$$\text{and } b = \frac{e^3 F}{8\pi\langle\epsilon\rangle\epsilon_0 k^2 T^2}, \tag{1.26}$$

where J_1 is the Bessel function of order 1. Interestingly enough, the initial separation r and binding energy E_b has no influence on this field dependence but only on the initial dissociation $k_d(0)$. In contrast, the dielectric constant

have an important impact which has been experimentally observed by Veldman et al. [83] in polyfluorene:PCBM blends: they observed a facilitated CT-state dissociation when increasing the PCBM content which they attributed to a change in the overall ϵ ($\epsilon_{PCBM} \approx 4$ whereas $\epsilon_{PF} \approx 3$).

When putting those equations together, one obtain the following field dependent dissociation rate $k_d(F)$ for ion pairs separation:

$$k_d(F) = \frac{3\langle\mu\rangle e}{4\pi\langle\epsilon\rangle\epsilon_0 a^3} \exp\left(-\frac{\mathbf{E_b}}{kT}\right) \frac{J_1\left(2\sqrt{-2b}\right)}{\sqrt{-2b}} \tag{1.27}$$

$$\text{with } b = e^3F/(8\pi\langle\epsilon\rangle\epsilon_0(kT)^2), \tag{1.28}$$

and for Wannier excitons dissociation:

$$k'_d(F) = \frac{\langle\mu\rangle e}{\langle\epsilon\rangle\epsilon_0} \left(\frac{m^*kT}{3\pi\hbar^2}\right)^{3/2} \exp\left(-\frac{\mathbf{E_b}}{kT}\right) \frac{J_1\left(2\sqrt{-2b}\right)}{\sqrt{-2b}} \tag{1.29}$$

$$\text{with } b = e^3F/(8\pi\langle\epsilon\rangle\epsilon_0(kT)^2). \tag{1.30}$$

In practice, internal fields are quite difficult to determine and their effect can only be speculated from the influence (or absence of influence) of external field [36, 91]. Nevertheless those models are quite important for describing the influence of external fields on CT-state dissociation and determine the binding energy of those CT-states [72]. Moreover, the model of Onsager and Braun has in some cases successfully been applied to describe the IV characteristics of solar cells [92, 93]. Finally, as will be seen in chapter 4, those models can be adapted to excitons dissociation, thus enabling to rationalize field induced photoluminescence quenching and determine excitons binding energies.

1.2.3 Charge transport and extraction

Transport of polarons in a density of localized states

The energy levels relevant for charge transportation in organic semiconductors are defined on a molecular level rather than on the whole solid. For this reason, it is usually spoken of HOMO and LUMO bands, for *Highest Occupied Molecular Orbital* and *Lowest Unoccupied Molecular Orbital*, respectively,[16] rather than valence and conduction bands.

In contrast to conduction and valence bands, LUMO and HOMO levels are localized to one molecular site (typically one molecule, a few monomers in a polymer or a few π-stacked molecules) which is physically and energetically separated from the next site. This separation is again reinforced by the polaronic effect as explained by Verlaak et al. [94]:

> "The probability for an excess charge sitting on one molecule to jump to a neighboring molecule is low in organic materials, such that those charges will (mainly electronically) polarize their environment before having made the jump, resulting in a polaron state. This polaron is even more unlikely to jump to a neighboring site since the charge is now dressed by its polarized environment."

[16] This is a generally accepted language misuse, as, literally speaking, the terms HOMO and LUMO refer to a molecular orbital and not to its energy level, and even less to a full band of energy levels.

Polarons transport is characterized by hopping between sites which are spatially localized and energetically distributed in a density of states usually assumed to be Gaussian [59, 95]. This is in contrast to crystalline semiconductors where states are usually delocalized and not so energetically dispersed, thus enabling band transport (or a combination of band and hopping transport in organic crystals). This readily explain why solution processed organic semiconductors usually exhibit much smaller mobilities than crystalline semiconductors [59].

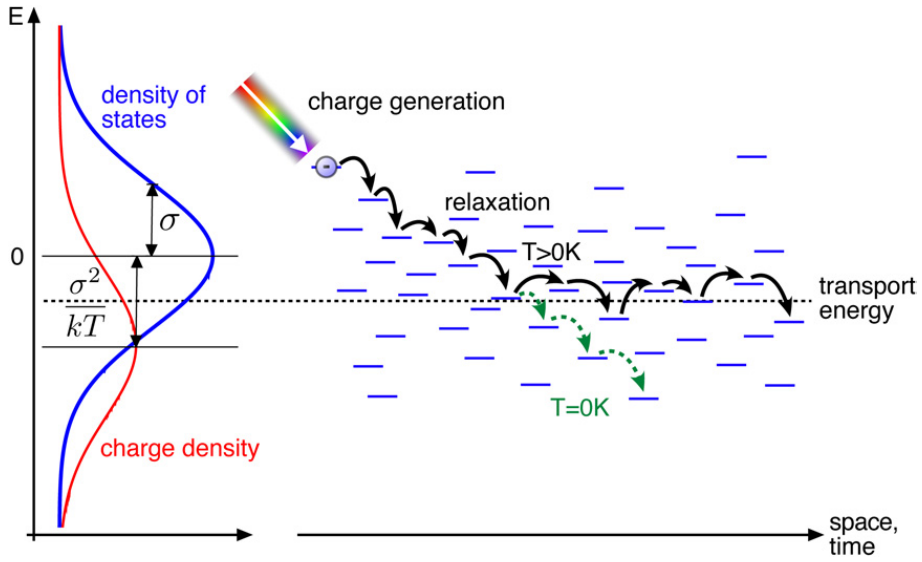

Figure 1.11: Charge transport by hopping between localized states with a Gaussian energy distribution and disorder parameter σ (blue solid line). The center of the steady-state charge distribution, also called density of occupied states distribution (red solid line), is shifted by σ^2/kT down as compared with the density of states center. Charge carriers can be photogenerated (or injected) at higher energies, followed by a relaxation of to a quasi-equilibrium. The steady-state charge transport takes place around the effective transport energy, which depends mainly on temperature and disorder. At 0 K temperature, the charge carriers relax to the deepest states where they remain trapped. Source: Deibel and Dyakonov 2010. [59]

The principle of hopping transport is schematically represented in figure 1.11. Hopping is due to a combination of tunneling and thermal activation and can be modelized by the Miller-Abrahams hopping rate ν [59, 96]:

$$\nu_{ij} = \nu_0 exp(-\gamma r_{ij}) \begin{cases} exp\left(-\frac{\Delta E_{ij}}{k_B T}\right) & \Delta E_{ij} > 0 \text{ (uphop)} \\ 1 & \Delta E_{ij} < 0 \text{ (downhop)} \end{cases} \tag{1.31}$$

Here ν_0 is the attempt-to-escape-frequency, γ the inverse localization radius, r_{ij} the distance between the localized sites i and j, ΔE_{ij} the energy offset between those two sites, k_B the Bolzmann constant and T the temperature.

A consequence is that hopping out from the states of low energy is quite unlikely, or in other words takes a long time. Those states thus act as traps. For modeling purposes, the lowest part of the density of states distribution, also

called trap distribution, is often approximated by an exponential function.

$$N(E) = \frac{N_t}{E_0} exp\left(-\frac{E}{E_0}\right). \tag{1.32}$$

Here N_t is the total density of trap states, and E_0 is the energetic disorder, which indicates the width of the density of state.

On a microscopic scale, the hopping rate can take very different values depending on whether the transport occurs within one molecule, within one morphological domain (phase, crystallite) or between two domains. For that reason, experimental methods probing local mobilities such as transient microwave conductivity (TRMC) tend to give very different results (usually the highest local mobility) from those obtained by methods probing the average macroscopic mobility (which is usually limited by the slowest of microscopic mobilities).

Charge transport can be influenced by a lot of factors such as the charge density (in case of high charge density, traps are filled and do not influence the transport anymore) or the direction (due to the molecules preferential orientation).

Morphology issues

As already mentioned, a good morphology must ensure a large D/A interface area, phases large enough to encourage polaron pairs dissociation and the existence of percolation pathway to the electrodes.

Work on solar cells processing can improve the heterojunction morphology. For example annealing is often used to increase the phase separation and the formation of domains. [36] On the opposite the use of solvents where the materials dissolve very well tends to decrease the phases size (because it prevents the formation of agglomerates in the solution). [36] The boiling point of the solvent also plays a role, as a slower evaporating solvent leaves more time for self organization of the film. Additives are also sometimes used to change the intermixing of the materials. [97] A number of example of those issues are studied in chapter 5.

Energy level alignment and extraction

Provided the heterojonction morphology enables percolated pathways to the electrode, separated charges which escape recombination are following the internal field of the device to be extracted at the desired electrode. The energy levels in a bulk-heterojunction under short circuit condition are represented in figure 1.12.

In contrast to bilayer devices where the diode behavior originates from the heterojunction, in bulk-heterojunctions, the heterojunction has no preferential direction. The diode behavior of the device is thus ensured by the asymmetry of the electrodes' workfunctions. The high work function of the anode acts as a barrier for electron's injection whereas the low work function of the cathode prevents holes injection. The alignment of the semiconductors Fermi levels with the work functions of the electrodes induces an internal field that is driving the charges to the adapted electrodes.

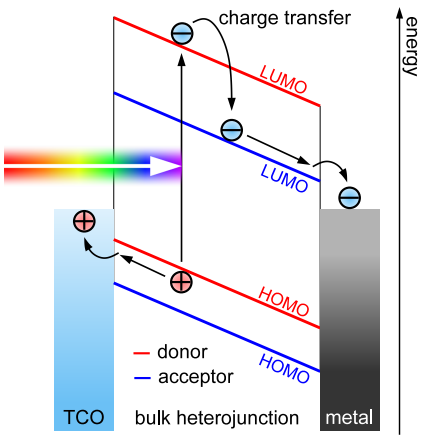

Figure 1.12: Energetics in a bulk-heterojuntion under short-circuit conditions: the slope of the LUMO and HOMO levels over the device thickness is ensured by the alignment of the semi-conductors Fermi levels with the ones of the two electrodes of different workfunction. Source: Deibel and Dyakonov 2010 [59].

A too small difference between the work functions of the electrodes can be a limiting factor for the open circuit voltage (V_{OC}) of the device. [59, 98] On the other hand too extreme workfunctions could act as extraction barriers.

Solar cells parameters

Solar cells performance is quantified using the power conversion efficiency η which is the ratio of the maximal electrical power delivered by the device over the incident radiant power P_L. This efficiency can be written in function of the parameters extracted from the current voltage characteristics of the solar cells:

$$\eta = \frac{FF j_{sc} V_{OC}}{P_L}. \tag{1.33}$$

j_{sc} is the density of current under short circuit condition, V_{OC} the open circuit voltage, and FF the fill factor defined as the ratio of the maximum obtainable power to the $V_{OC} \cdot j_{sc}$ product (see figure 1.13). Those parameters can in turn be related to physical phenomena and parameters including but not limited to the generation and recombination rates and mechanisms (mainly j_{sc} and FF), the difference between the work functions of the electrodes (V_{OC}) or the difference between the $HOMO$ of the electron donor and the $LUMO$ of the electron acceptor (V_{OC}) [59].

An other important parameter of solar cells, is its lifetime, based partly on its ability to resist aging as well as degradation due to water and oxygen. This last parameters can be improved by encapsulating the active layers.

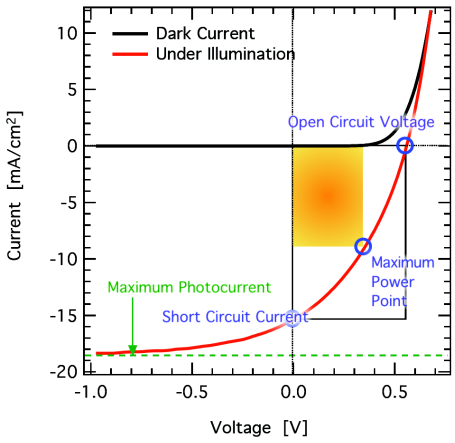

Figure 1.13: Schematic current–voltage characteristics of a solar cells. Source: Deibel and Dyakonov 2010 [59].

1.2.4 Recombination losses

Recombination losses can occur at different stages of the photocurrent generation process.

Excitons recombination.

Excitons are intrinsically unstable quasi-particle and will usually release their energy within a lifetime in the order of the nanosecond. As presented in § 1.1.2 this energy can be released as a photon (radiative recombination) — in which case it can be monitored by photoluminescence detection — or as a phonon (non radiative recombination).

The recombination of an exciton D^* back to the ground state material D is a monomolecular mechanism and the excitons density n_{exc} thus exhibits a simple exponential decay characterized by a lifetime τ in the absence of competing phenomena:

$$D^* \rightarrow D \tag{1.34}$$

$$\frac{dn_{exc}}{dt} = -\frac{n_{exc}}{\tau} \tag{1.35}$$

$$n_{exc}(t) = n_{exc,0}e^{-\frac{t}{\tau}} \tag{1.36}$$

where $n_{exc,0}$ is the initial density.

In addition to this spontaneous recombination, radiative recombination can be triggered by a photon of same energy as the one to be emitted, leading to stimulated emission. Moreover, excitons recombination can also be caused by an other excited species, which could be neutral (exciton – exciton annihilation) or charged (exciton – charge annihilation). However, such a phenomenon becomes significant only under very high density of charges and excitons, such as those found during excitation by a femtoseond laser pulse of relatively high intensity. The case of exciton-hole annihilation has been presented as being partly responsible for the sublinear dependence of the charge generation upon

varying the exciting pulse intensity in P3HT:PCBM blends [99,100]. The mechanism of exciton–hole annihilation is described by the following chemical and rate equations:

$$D^* + D^+ \rightarrow D + D^+ \tag{1.37}$$

$$\frac{dn_{exc}}{dt} = -k_{exc-hol} n_{exc} p \tag{1.38}$$

Here $k_{exc-hol}$ is the exciton–hole annihilation rate and D^+ the positively charged species of density p.

CT-states formed at the donor–acceptor interface are expected to exhibit similar recombination mechanisms, although it is less likely to be radiative due to the larger distance between the electron and the hole of those quasi particles [101, 102].

Polarons recombination.

In inorganic crystals, free charges of opposite sign, due to their high mobility, do not stay in each others vicinity long enough to result in considerable recombination rate. Recombination in such medium is thus usually occurring mainly at defect sites, although defect sites density is, in crystalline semiconductors operating devices, considerably lower than charges density. This is the case for example of Shockley, Read, Hall recombination which is a trap–mediated mechanism, dominating in conventional semiconductors. Such phenomena are sometimes also considered in organic semiconductors [103] but are not however the main effect, and can usually be neglected.

In disordered organic semiconductors on the opposite, the charge carriers mobility is very low and the Coulomb capture radius r_c (see equation (1.18)) rather large due to the low electronic permittivity. As a result, virtually any charge carrier entering in a counter–charge attraction zone will recombine before having a chance to escape. Langevin theory describes recombination in such cases [104]. A zero recombination probability is assumed for charges located outside of the capture sphere of a counter charge, and a recombination probability of one for any charge inside the capture sphere of a counter charge. [17] The recombination rate is thus limited only by the diffusion of charges into the capture spheres of their counter charges. The resulting recombination rate R is given by equation 1.39. The details of the calculation can be found in the book of Pope and Swenberg [21, p. 503].

$$R = k_{br} np \tag{1.39}$$

The Langevin recombination prefactor k_{br} is proportional to the sum of the charge carrier mobilities μ_e and μ_h for electrons and holes, respectively:

$$k_{br} = \frac{e}{\epsilon}(\mu_e + \mu_h). \tag{1.40}$$

e is the elementary charge and ϵ the dielectric constant of the composite semiconductor. It implies that for equal densities of electrons and holes, a density

[17] This assumption is valid as long as the charges mean free path is lower than the Coulomb capture radius. For narrow band semiconductors, Pope and Swenberg mention that for the condition is met until mobilities at room temperatures as high as ≈ 1 cm^{2}V^{-1}s^{-1}.

n_0 of initially generated electrons will decay as $n(t) = n_0/(1 + k_{br} n_0 t) \propto t^{-1}$ in the absence of further photogeneration.

However, a variety of experimental methods have shown that the rate of recombination of charge carriers in blends of polymers with fullerenes does not have the expected n^2 dependence (compare Eq. (1.39) with $n \approx p$). Instead, experimentally an $n^{\lambda+1}$ (equivalently $t^{-1/\lambda}$) dependence is found, where $\lambda+1$ is the apparent recombination order (see next section), usually found to be between 2.3 and 2.8 at room temperature on various polymer:fullerene blends [57, 105–107]. This issue is discussed in details in chapter 6.

Recombination order

An interesting way of characterizing recombination processes is the recombination order. The recombination order is defined as the exponent $\lambda + 1$ to which the density of the recombining species n is raised in the recombination equation:

$$R = k_\lambda n^{\lambda+1} \tag{1.41}$$

The theoretical interest of recombination order is that in case the recombination process is a single step mechanism, recombination order is characteristic of the number of individual charges or excited species involved in each recombination event. For example in the aforemention case of exciton's decay, the recombination order is one (one excited species involved), and it is two for the Langevin recombination of polarons (two charges involved, and with $n = p$, equation 1.39 becomes $R = k_{br} n^2$).

Experimentally, recombination order is interesting because if recombination is the only process occurring in the sample, the recombination order is simply related to the slope of the observed decay of the densities of recombining species in a log–log scale[18] :

$$\begin{aligned}
\frac{dn}{dt} &= -R && (1.42)\\
\Leftrightarrow \frac{dn}{dt} &= k_\lambda n^{\lambda+1} && (1.43)\\
\Leftrightarrow n(t) &= \left(n_0^{-\lambda} + t \cdot \lambda \cdot k_\lambda\right)^{-\frac{1}{\lambda}} && (1.44)\\
\Leftrightarrow \log n(t) &= -\frac{1}{\lambda} \log\left(n_0^{-\lambda} + t \cdot \lambda \cdot k_\lambda\right) && (1.45)
\end{aligned}$$

So $\log n$ as function of $\log t$ has a slope of $-1/\lambda$ for $t \gg \frac{n_0^{-\lambda}}{\lambda k_\lambda}$.

In return, one can define an experimental or apparent recombination order from the observed slope.

[18] Except for the case of an order one, where the decay is simply exponential

Chapter 2

Experimental methods

2.1 Optical methods

2.1.1 Samples

The samples used for optical investigations — with the exception of field dependent measurements — were thin films of optically active materials spin coated on large transmission bandwidth sapphire substrates. All solutions were prepared, samples spin-coated and if necessary annealed under the nitrogen atmosphere of the gloveboxes, where the water and oxygen content were kept below 10 ppm. Prepared sample where then quickly transfered into a cryostat where a high vacuum (10^{-6} to 10^{-8} mbar for the photoinduced absorption and pholuminescence setup) or a helium atmosphere (for the transient absorption setup) was quickly set. Table 2.1 gives the spin-coating parameters used as function of the main materials and solvents, every process are composed of a slow spinning step to obtain a regular surface and a quick one to eliminate the solvent in excess. This process usually enables to obtain a surface roughness in the order of magnitude of the nanometer and films thickness between 200 and 300 nm.

Table 2.1: Samples spin-coating parameters.

Material	Solvent and concentration	Parameters
P3HT 4002E and P3HT 4002E-based blends	Chlorobenzene 20-22 mg/mL	650 rpm 60s 2000 rpm 10s
	Chloroform 10-15 mg/mL	1000 rpm 20s 3000 rpm 10s
P3HT P200 and P3HT P200-based blends	Clorobenzene 20-30 mg/mL	800 rpm 30s 2000 rpm 10s

2.1.2 Absorption

UV-vis absorption spectra were recorded with a Perkin Elmer Lambda 900 spectrometer at room temperature. The spectrometer gives access for each wavelength to the fractions of reflected (R) and transmitted (T) light. The

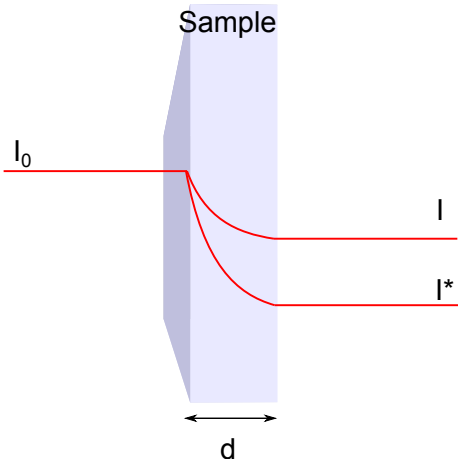

Figure 2.1: Evolution of light intensity through an absorbing sample in case of unexcited (I) and excited (I*) material.

fraction of the light absorbed by the sample being thus 1-R-T. Nevertheless absorption is usually quantified using an other quantity: the absorbance. The absorbance of a sample is defined as follow:

$$A = -\ln \frac{I}{I_0} = -\ln \frac{T}{1-R}, \tag{2.1}$$

where I and I_0 are the intensity of the light entering the sample and transmitted through it, respectively, as depicted on figure 2.1.

As can be seen in figure 2.1, the transmitted light is decreasing exponentially with the sample thickness, so does it also with the concentration of absorbing species as stated by the Beer–Lamber law (see equation (2.3)). That is the reason why absorbance is defined as a logarithm: as such, it varies linearly with the sample thickness:

$$\frac{I}{I_0} = e^{\sigma dn} \tag{2.2}$$

$$\Leftrightarrow A = \alpha d = \sigma dn \tag{2.3}$$

Here α is the absorption coefficient of the sample, σ the absorption cross section of the absorbing species and n the density of the absorbing species. An extremely important property of the Beer–Lamber law is its additivity, which implies that in the presence of several absorbing species or absorbing layers, the absorbances can simply be added. It makes it possible for example to simply substract the absorbance of the substrate from the overall absorbance of a sample, to know the absorbance of the active layer.

For two absorbing species a and b in an absorbing layer of thickness x:

$$A = A_a + A_b = (\alpha_a + \alpha_b)x \tag{2.4}$$

For two absorbing layers of thicknesses x_1 and x_2 and absorbing coefficient α_1 and α_2

$$A = A_1 + A_2 = \alpha_1 * x_1 + \alpha_2 * x_2 \tag{2.5}$$

In case of excited states characterization, we are interested in the change of absorption due to the excitation. The studied quantities are the opposite of relative change in transmission $-\Delta T/T$ in steady state absorption, and the change of optical density $-\Delta OD$ in transient absorption.

Optical density (OD) is equivalent to absorbance, however, it is usually calculated using decimal logarithm rather than a natural one:

$$OD = -\log \frac{I}{I_0} = -\log \frac{T}{1-R}, \tag{2.6}$$

If we call I^* the transmitted intensity in the excited material, the change of optical density is given by:

$$\Delta OD = OD^* - OD = -\log \frac{I^*}{I_0} + \log \frac{I}{I_0} = -log\frac{I^*}{I} \tag{2.7}$$

OD^* is the optical density in the excited sample.

On the other hand, $-\Delta T/T$ is, if neglecting the changes in reflection (or equivalently the change in I_0):

$$-\Delta T/T = -\frac{T^* - T}{T} = -\frac{I^* - I}{I_0} \cdot \frac{I_0}{I} = -\frac{I^* - I}{I} = 1 - \frac{I^*}{I} \tag{2.8}$$

T^* being the transmission through the excited material.

As a result, we have:

$$\Delta OD = -\log \frac{I^*}{I} = -\log((-\Delta T/T) - 1) = -\frac{1}{\ln 10} \cdot \ln((-\Delta T/T) - 1) \tag{2.9}$$

As $-\Delta T/T$ is very small (typically in the order of 10^{-3} or lower), the serie expansion of $ln(1-x)$ at $x = 0$ can be used and gives:

$$\Delta OD \approx \frac{1}{\ln 10} \cdot (-\Delta T/T) \approx \frac{-\Delta T/T}{2.303} \tag{2.10}$$

$-\Delta T/T$ and ΔOD are thus under this first order approximation, equivalent quantities.

2.1.3 Photoluminescence (PL)

The photoluminescence measurements were realized in the setup presented in figure 2.2. Two laser have successively been used to provide the excitation: a Melles Griot Argon Ion laser at a wavelength of 514 nm, and a solid-state laser with emission at 532 nm, both wavelengths being in the range of maximum absorption of regio-regular P3HT (see figure 2.3). No difference was observed between the spectra obtained from the two lasers. To ensure a maximal signal-to-noise ratio, the laser intensity was modulated by a mechanical chopper. The laser beam was directed onto the sample placed on the cold finger of continuous Helium-flow crysostat (Judson ST100) equiped with wide range low absorption sapphire windows. A beam-blocker was placed in the laser beam after the cryostat to ensure that potential non-absorbed part of the laser beam does not interfere with the measurement. The resulting photoluminescence was collected via a large diameter concave mirror and focused in the entrance slit of a

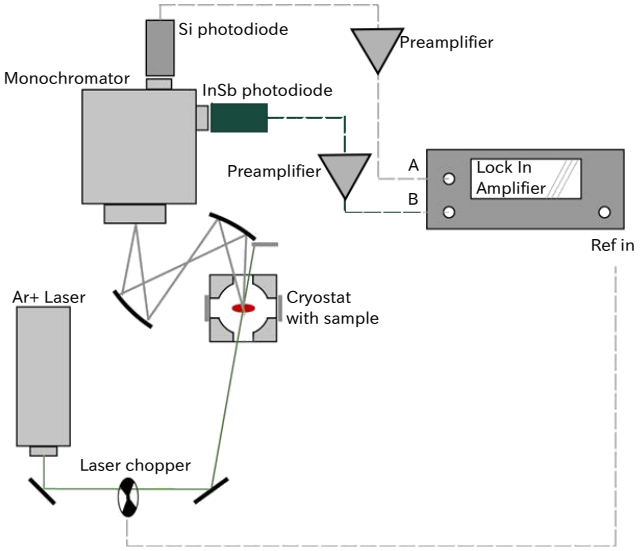

Figure 2.2: Photoluminescence spectroscopy setup. Adapted from Krantz 2008. [108]

Cornerstone 360 1/4M monochromator through another concave mirror to ensure spectral analysis. The monochromator was equipped with two photodiodes ensuring a large spectral range, a silicon photodiode for the visible and near infrared range (550 nm to 1030 nm) and a liquid nitrogen cooled InSb photodiode for far infrared (1030 nm to 5500 nm). The resulting signal was preamplified 10^5 times before being finally sent to a DSP lock-in amplifier (signal recovery 7265) for additional amplification and demodulation using the chopper frequency as a reference.

The signal was modulated at a frequency between 300 and 400 Hz. The laser power before the cryostat was set to 30 mW on a beam surface of approximately 0.1 cm^2, the low absorbance sapphire windows of the cryostat ensuring a quasi identical optical power on the sample itsef. The cryostat allowed for temperatures ranging from 3 K to 325 K with a nominal temperature stability of 50 mK. The temperature was measured directly on the film with a silicon diode temperature sensor maintained in contact with the active layer.

2.1.4 Field-dependent photoluminescence (F-PL)

Similar optical setup was used for field-dependent PL measurements. Nevertheless due to the use of non-transparent sample, the setup was adjusted so that the photoluminescence can be measured in reflexion (see figure 2.4a).

The sample used were similar to solar cells (see § 2.2) to which isolating layers was added between the active layer and the electrodes to prevent charge injection (see figure 2.4b). The material chosen as insolator was *poly(methyl metacrylate)* (PMMA) for its transparency in the visible region, its relative dielectric constant close to this of P3HT, which enables a uniform distribution of the field through the sample thickness, as well as for its ability to be solution processed from solvents in which P3HT is not soluble (namely *n-butyl acetate*),

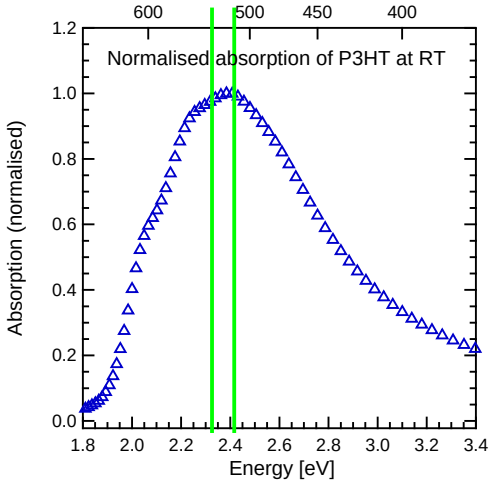

Figure 2.3: Position of the pump lasers (514 nm and 532 nm) photon energy on the absorption spectrum of P3HT. Adapted from Liedtke 2006. [30]

thus allowing for the processing of a multilayer device. The first layer of PMMA had to be annealed 10 minutes at 180 °C not to be redissolved by chlorobenzene when depositing the P3HT layer. The successive layers of the field-dependent PL sample are summarized in table 2.2. Note that the aluminium cathode also served as a mirror to reflect the photoluminescence in direction of the large collecting concave mirror.

Table 2.2: Structure of the field dependent PL sample.

Material	Role	Processing	Post treatment	Thickness
Glass	Substrate			
ITO	Transparent anode	Deposited and polished by the supplier	Patterned with photolithography	100-150 nm
PMMA	Blocking layer	Spin coated from n-butyl acetate	annealed 10 minutes at 180 °C	200 nm
P3HT	Active layer	Spin coated from chlorobenzene	annealed 10 minutes at 120 °C	80-110 nm
PMMA	Blocking layer	Spin coated from n-butyl acetate	annealed 10 minutes at 180 °C	200 nm
Al	Cathode and mirror for the PL	Thermally evaporated		80 nm

A Keithley Instrument Source-Measure-Unit (SMU) 217 was used to apply a continuous field to the sample in the reverse direction of the diode. It was also used to monitored the current and make sure that there is no short circuits. Between two measurement points, the field was set to zero and the laser blocked during 4 minutes to ensure that the sample was not getting charged. After this

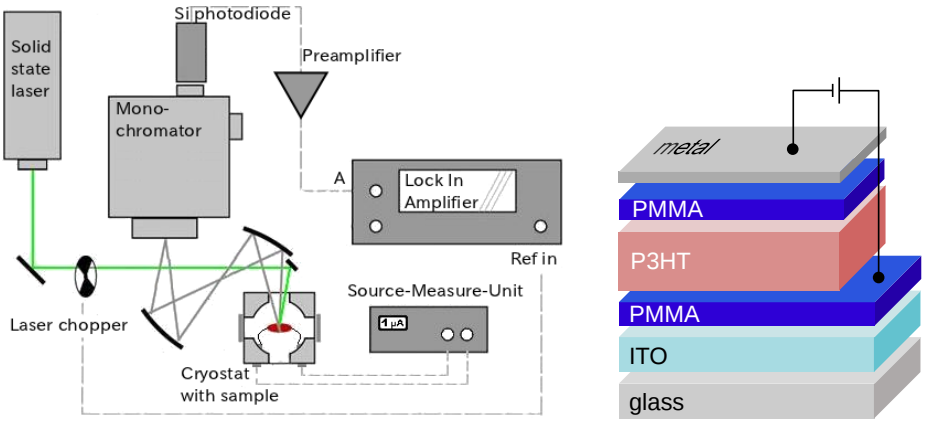

Figure 2.4: (a) Field dependent photoluminescence setup. Adapted from Krantz 2008 [108]. (b) Structure of the diod used for photluminescence.

delay, the new field was applied.

2.1.5 Steady-state photoinduced absorption (PIA)

The aim of photoinduced absorption is to detect the presence of photoexcited species via their specific absorption spectra. The photoinduced absorption spectra were recorded using a photomodulation technique whose principle is represented in figure 2.5 (a): a transmission spectrum of the sample was realized using a Xenon lamp and a monochromator while the sample is photo-excited by a chopped cw laser. As excitation source, we used the 514 nm emission of a Melles Griot Ar^+ cw laser at a power after mechanical chopping of 30 mW. Excitation and probe lights were focused onto the same point of the sample. To the exception of the probe beam, the experimental setup (excitation, collection and spectral analysis) is the same as the one used for photoluminescence and is represented on figure 2.5 (b).

The lock-in amplifier computes the in-phase S_{IP} and out-of-phase S_{OP} variation of the transmission correlated to the modulation [110]:

$$S_{IP} = \int_{period} S(t)\cos(\omega t)dt, \tag{2.11}$$

$$S_{OP} = \int_{period} S(t)\sin(\omega t)dt. \tag{2.12}$$

$S(t)$ is the output of the photodiode (containing a continuous component and a modulated component), $\omega = 2\pi f$ the angular frequency of the modulation. As the integration is over one period, the resulting signal decreases when increasing the applied modulation frequency. Interested readers are referred to the work of Epshtein et al. for a more detailed analysis of the influence of the modulation frequency on the PIA signal [110]. From those directly extracted signals, the lock-in amplifier is also calculating the phase and magnitude of the modulated signal. Because the modulation period usually exceeds the lifetime of the excited species, this technique is considered as a steady-state or quasi steady-state measurement.

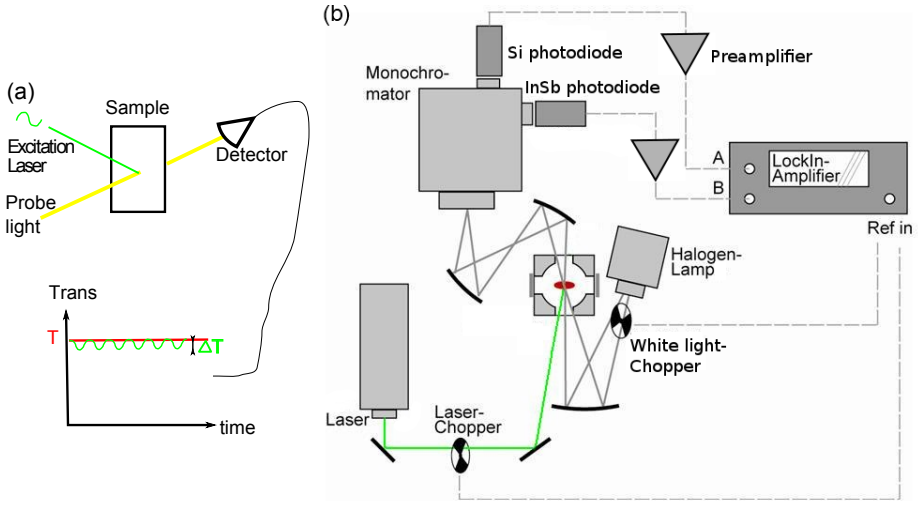

Figure 2.5: (a) Principle of the photomodulated photoinduced absorption measurement. (b) Photomodulated photoinduced absorption setup. Adapted from Liedtke 2011 [109].

The monitored quantity (that we will call *PIA signal* for sake of simplicity) is the negative differential transmission, calculated as follows:

$$\frac{-\Delta T}{T}(\lambda) = \frac{PIAPL_x(\lambda) - PL_x(\lambda)}{T(\lambda)} \tag{2.13}$$

$PIAPL_x$ is the in-phase value measured by the lock-in, PL_x is the in-phase value under photoluminescence conditions (without probe light) and T is the transmitted signal without excitation (by modulating the white light). The phase is set to zero under luminescence conditions because the extremely short lifetime of fluorescing species prevents lifetime related phase shift, thus enabling us to know and compensate the phase shift caused by the measuring system alone (due to electrical delays, and the fact that the demodulation in the lock-in amplifier is done using reconstructed sinusoids whereas the actual mechanical modulation exhibit a square-wave shape). $\Delta T/T$ is proportional to the modulated density of photoexcited species due to the Beer-Lambert law (equation (2.3)).

As shown in figure 2.6, the density of photoinduced species is a trade-off between the photoinduced generation of the absorbing species and their lifetime; indeed, species with a longer lifetime can accumulate in bigger quantities. Information about the lifetime is carried by the phase information: the density of species having extremely short lifetime follows exactly the pump light modulation without generating any out-of-phase signal (see figure 2.6(a)), whereas the density of species having a lifetime comparable to the modulation period will have an extinction delayed compared to the excitation modulation, thus generating a large out-of-phase signal (or equivalently a large phase shift, see figure 2.6(b) and (c)). Due to the higher response of long living states, it is usual to measure PIA spectra at low temperature where the longer lifetimes allow for a much stronger signal and much better resolved spectral features. Experimentally the combination of the excited species density dependence upon their life-

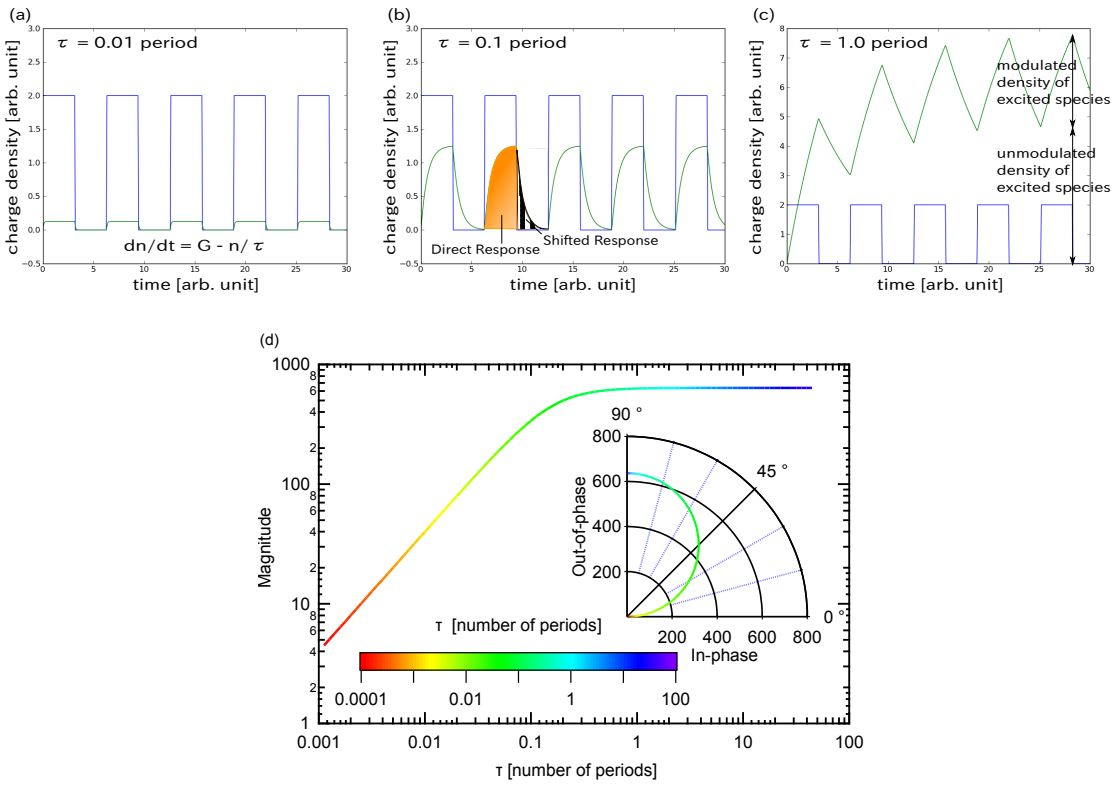

Figure 2.6: (a), (b), (c): simplified response of the density n of an excited species of defined lifetime τ (green line) to a modulated excitation G (blue line) of period T as function of the τ/T ratio. For the species with $\tau = T/100$, the density of species remains quite low and nearly perfectly in-phase. Longer lifetimes enable a larger density of species, moreover, the density of specie can not respond directly to the fast modulation, thus causing an increase of the out-of-phase signal. Finally for a lifetime close to the excitation period, the out-of-phase signal becomes dominating and a part of the density does not follow the modulation anymore and is thus not detectable with the lock-in technique. An overview of the influence of the lifetime is presented in subfigure (d).

time and the signal intensity dependence upon modulation frequency limits the observable species to those having a lifetime over approximately one microsecond. Note that the situation is different for photoluminescence measurements which are sensitive not to the density of species accumulated at a given time but to the density of radiative recombination, which is directly proportional to the amount of absorbed photons.

In addition to absorption by excited species, other phenomena can be seen in the spectra: the absorption from non-excited materials is indeed reduced by the photoexcitation, thus generating a photobleaching phenomenon in the spectral regions where ground-state absorption occurs. Similarly, stimulated emission from the excited species can be caused by the probe light. In contrast to the photoluminescence, those phenomena can not be subtracted from the overall signal using formula (2.13) and appear as negative contributions in the

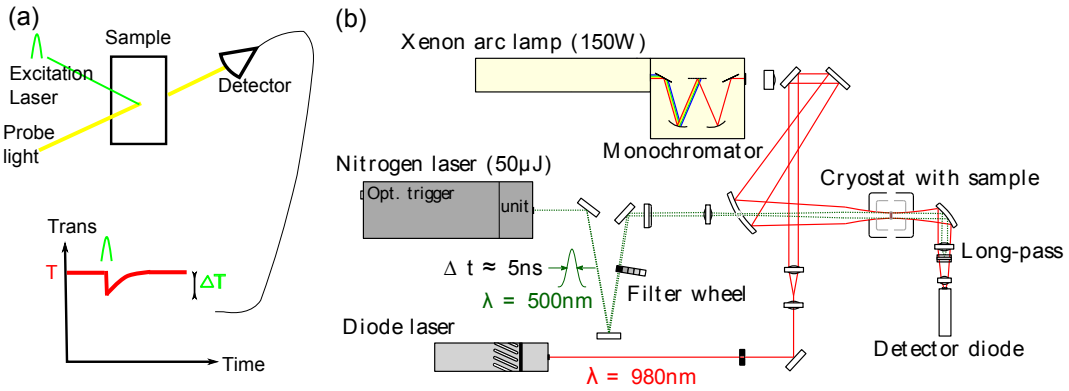

Figure 2.7: (a) Principle of the transient absorption measurement. (b) transient setup. Adapted from Kämpgen 2011 [111].

PIA spectra. In case of the presence of several types of excited species, photobleaching presents the advantage of giving an indication of the overall density of excited species.

2.1.6 Transient absorption (TA)

Transient absorption (TA) enables to directly monitor the dynamics of the excited species in the time range 10 ns to 10 ms. In addition to allowing for the monitoring of the dynamics, it enables to detect the species whose lifetime is shorter than a few microseconds, which accumulate in too little amount under steady state condition to be detected by steady state PIA.

The principle is the same as for steady state PIA except that the excitation is here provided by a 5 ns pulse of a nitrogen/dye laser at a wavelength of 500 nm and that the decay of photogenerated species following this initial excitation is directly monitored thanks to an ultrafast photodiode. The experimental setup is shown in figure 2.7. For the measurement presented here, we applied a pulse energy of 25 μJ/cm^2. The monochromatic probe light can be supplied either by a steady state infrared laser of wavelength 980nm or by a Xenon lamp coupled to a monochromator[1]. The decay of the absorption was measured using a FEMTO HCA-S-400M-IN preamplified InGaAs photodiode and recorded by a Tektronix oscilloscope synchronized with an optical trigger output provided by the pulsed laser.

In order to improve the signal-to-noise ratio, the data was obtain by averaging the response over 600 pulses in the oscilloscope. Additionally, in order to obtain a better resolution at longer time scales, where the signal becomes weaker, a polynomial fit was used to reconstruct the curve on a logarithmic scale from a number of data points increasing with time[2].

[1] More details can be found in Kaempgen 2011 [111].
[2] More details can be found in Gunz 2010 [112].

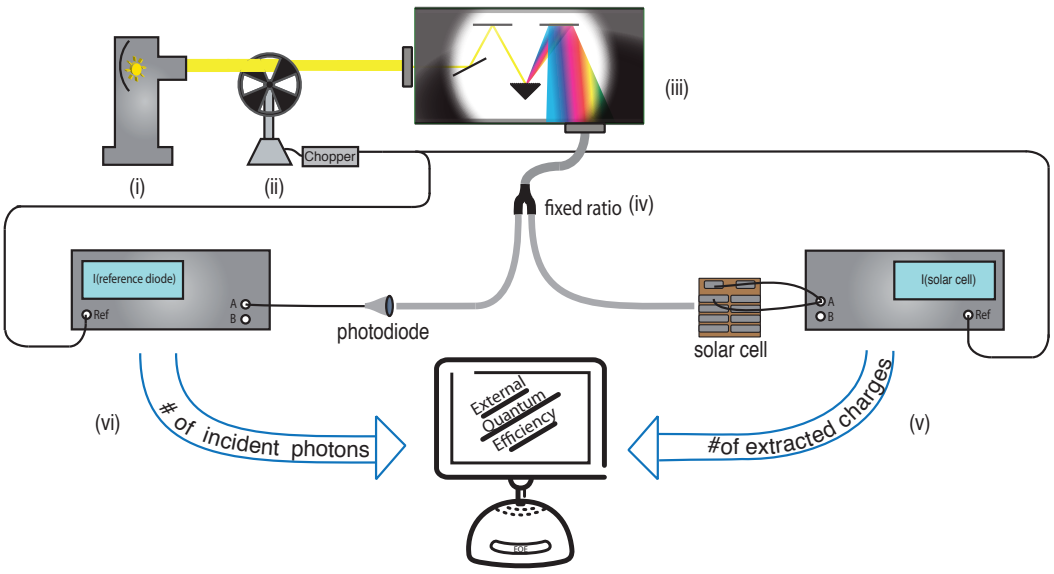

Figure 2.8: Experimental setup for the measurement of the external quantum efficiency. Source: Binder 2010 [113].

2.2 Solar cells characterization

2.2.1 Current-voltage characterization

We processed solar cells by depositing the active layer on Poly(3,4-ethylenedioxythiophene) poly(styrenesulfonate) (PEDOT:PSS) covered indium tin oxide (ITO)/glass substrates. The active layer was spin-coated as afore-mentioned (§ 2.1.1). The evaporated cathode was a Ca/Al (3/100 nm) for the solar cells and the active area was 0.5 cm^2. For current–voltage characterization we used a 300 W Xenon lamp for illumination. The intensity was adjusted to 100 $mWcm^{-2}$.

2.2.2 External quantum efficiency (EQE)

External quantum efficiency spectra were recorded by a homemade, lock-in-based setup shown in figure 2.8 equipped with a calibrated reference silicon photodiode. A 300 W Xenon lamp was applied as light source.

2.3 Other methods

Electron Spin Resonance (ESR)

ESR (modified Bruker 200D) was applied to verify the presence of spin carrying polarons. The sample was placed in a resonant cavity and cooled with a continuous flow helium cryostat, allowing a temperature range from 10 K to room temperature. The microwave absorption was measured by using lock-in, with modulation of the external magnetic field as reference. For the excitation, a white light halogen lamp guided to the microwave cavity was used. The g-

factor of ESR signals was calibrated for every measurement with a Bruker 035 M NMR-Gaussmeter and an EIP 28b frequency counter. Details about the technique can be found elsewhere. [114, 115] The ESR samples were dropcast films from 200 μl solution prepared inside a nitrogen glovebox. The resulting films were rolled up and put inside a ESR sample tubes. All samples were annealed afterwards for 10 min at 120 °C.

Time-of-flight (TOF)

Time-of-flight (TOF) measurement have been used to selectively determine the mobilities of each type of charge carrier. In TOF measurements we used a solar-cell like structure with a thicker active layer. The thickness of the films combined with the high absorption coefficient of the material used enables that a pulse of light generates excitons in the vicinity of one of the electrodes rather than in the bulk. The combined action of the field and the electrode separate charges and extract one type immediately after excitation whereas the other type of carrier drifts towards the other electrode and reaches it after a transit time t_{tr} which can be related to the mobility by the following equation:

$$\mu = \frac{d}{F t_{tr}} \tag{2.14}$$

where $d$is the active layer thickness, F the applied field, and μ the mobility of the studied charges. We processed films with thickness of approximately 2 μm resulting in applied fields in the order of 10^7 Vm^{-1}. More detail about this experiment can be found elsewhere [116].

Morphological characterization methods

Scanning electron microscopy (SEM) has been used to determine the superficial morphology of the films, whereas X-ray diffraction (XRD) was employed to address the ordering in the bulk.

X-ray diffraction measurements were carried out using a Philips PW 1729 X-ray generator. Scanning electron microscopy (SEM) measurements were carried out using a ZEISS ULTRA plus scanning electron microscope. Finally the film thicknesses were determined by a surface profilometer (Veeco).

Photoemission and inverse photoemission spectroscopies (UPS and IPES)

In photoemission spectroscopy, electrons in the material are excited by high energy photons ($h\nu$) up to the vacuum level ϕ[3] and thus emitted out of the materials. The photons' energy being higher than the difference between the vacuum level and the energy E_e[3] of the electrons in the material, the excess energy is converted in kinetic energy E_{kin} of the emitted electrons. By collecting the emitted electrons and measuring their kinetic energy, one can determine E_e.

Ultra violet photons are used in UPS, they enable to excite valence electrons to the vacuum level and thus to investigate the valence band of the molecules/films.

[3] All levels are referenced to the Fermi level E_F of a metal parallelly measured

In inversed photoemission spectroscopy (IPES), the photon beam is replaced by an electron beam of high kinetic energy. The electrons are absorbed by the film which re-emits as a photon the excess energy compared to the energy E_h of the empty state which got filled with the absorbed electron. The relation between the involved energy is the same as for direct photoemission spectroscopy, E_h can thus be computed the same way as E_e in the former case.

All UV photoemission and inverse photoemission spectroscopy measurements were performed in a UHV system VG ESCALAB equipped with an Mk II electron spectrometer at a base pressure of better than 2×10^{-10} mbar. [117] The samples were at room temperature. The He-I line of a gas discharge lamp was used for UPS. The IPES detector — a Geiger-Müller detector with SrF_2 window filled with Ar and I_2 — was used in the isochromatic mode with a fixed photon energy of about 9.5 eV. The electron beam was defocused over the sample to minimize radiation damage, and data acquisition was stopped immediately when changes in the IPES spectra occurred between two scans. [82] The measurements were carried out by Achim Schöll and Stefan Krause of the chair of experimental physics VII (formerly in the chair of experimental physics II).

Time-resolved microwave photoconductance (TRMC)

Time-resolved microwave photoconductance (TRMC) measurements were carried out by Tom J. Savenije from the Department of Chemical Engineering of the Delft University of Technology, using a custom-made liquid-nitrogen cooled microwave cavity with a resonance frequency at $\approx$ 8.4 GHz. The electric field vector of the microwaves is parallel to the substrate. Samples were photoexcited at 500 nm with a 3 ns laser pulse from an optical parametric oscillator pumped at 355 nm with the third harmonic of a Q-switched Nd:YAG laser (Vibrant II, Opotek). Photogeneration of mobile charge carriers in the sample led to an increase of the conductance, $\Delta G(t)$, and consequently to enhanced absorption of microwave power by the sample. The time-dependent change of the conductance was obtained from the normalized change in microwave power $\Delta P(t)/P$) reflected from the cavity according to:

$$\frac{\Delta P}{P} = -K\Delta G(t) \tag{2.15}$$

The geometrical dimensions of the cavity and dielectric properties of the media in the microwave cavity determine the sensitivity factor, K. From the maximum change in the conductance, ΔG_{max}, and the incident light, I_0, the parameter $\phi\Sigma\mu$ denoting the product of the charge carrier generation yield per absorbed photon (ϕ) and the sum of the electron and hole mobilities ($\Sigma\mu$) can be calculated using

$$\phi\Sigma\mu = \frac{\Delta G_{max}}{I_0\beta e F_A} \tag{2.16}$$

where β is the ratio between the broad and narrow inner dimensions of the waveguide, e is the elementary charge and F_A is the optical attenuation. For more experimental details, see references [118] and [119].

Chapter 3

Materials

Dang et al. recently published a survey entitled: *P3HT:PCBM, Best Seller in Polymer Photovoltaic Research* in which they gathered the results of 579 of the 1033 articles published between 2002 and 2010 dealing with heterojunctions based on this material system [120]. This article illustrates perfectly the front side role taken by this blend as a reference for bulk heterojunction solar cells based on the second generation of semiconducting polymers.

In the course of this thesis, P3HT:PCBM was used as a reference system for studying the properties of organic bulk heterojunctions: first P3HT alone to study the charge generation and more specifically the exciton binding energy (chapter 4); then as a comparative reference for the study of other P3HT:electron acceptor blends (chapter 5); and finally as a support for investigating charges recombination (chapter 6).

Particularly remarkable is the semi-crystalline self-organization of P3HT. This aspect is responsible for most of the peculiarities of P3HT and is presented first, together with its implications on charge transport in P3HT. The general properties of PCBM are described in the subsequent section. The last section presents the peculiar organization of those two materials when blended together which is largely responsible for the good performances of this composite for solar cells application.

3.1 Poly(3-hexylthiophene) (P3HT)

3.1.1 The molecule

Polythiophenes (PT) were first polymerised in the early 1980's [121–125]. PT quickly raised a strong interest due to their electrical properties, relative environmental stability in doped and undoped states, non-linear optical properties, and highly reversible redox switching [121]. Those promising properties led to an intensive research to overcome the main drawback of those polymers: their insolubility. Soon soluble poly(3-alkylthiophene)'s (P3AT) were developed (see figure 3.1) [126–130].

The drawback of those alkyl moieties is to break the symmetry of the thiophene ring, thus making the monomers non-equivalent unless they are assembled on a head-to-tail regio-regular configuration. Regular configuration helps the development of an organization within films or agglomerates which is — as we will

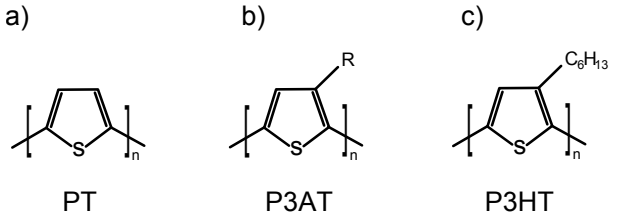

Figure 3.1: Polythiophenes' molecules: (a) unsubstituted unsoluble polythiophene (synthesized in the early 80's); (b) soluble poly(3-alkylthiophene), where R is an alkyl chain; (c) poly(3-hexylthiophene).

see — favorable for transport and optical properties (with for example a red-shift of the absorption onset in the presence of agglomerates, see figure 3.2(b)). Nevertheless obtaining a control of the polymerization process sufficient to selectively produce this configuration proved to be quite challenging. Not before 1992 was it achieved to synthesize P3RT (R being various moieties, not always alkyl) with an acceptable degree of regioregularity [121, 131–138].

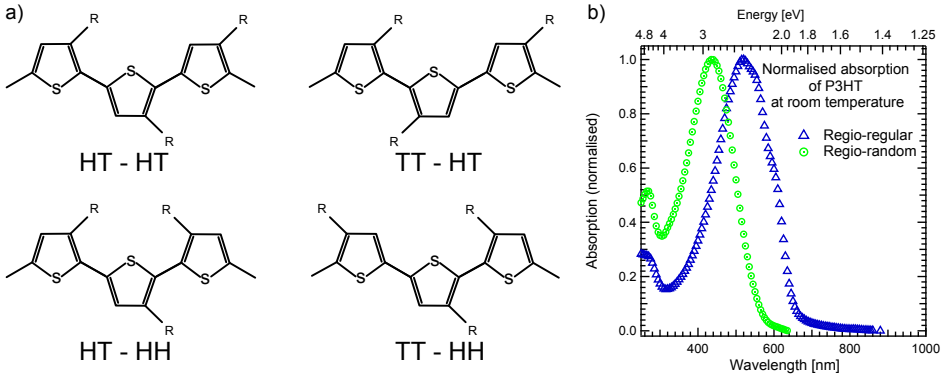

Figure 3.2: (a) Poly(3-alkylthiophene) possible configurations. Adapted from Reddinger and Reynolds 1999 [121]. (b) Corresponding films absorption spectra for the regio-regular head-to-tail and regio-random configurations. Adapted from Liedtke 2006 [30].

Those successes enabled to confirm the differences in the optical and transport properties between P3AT with regio-random configuration and those with regio-regular head-to-tail configuration. Indeed, the optical band gap of regio-regular poly(3-butylthiophene) is 1.7 eV, whereas that of random poly(3-butylthiophene) is 2.1 eV. The electrical conductivities of I_2-doped films of regio-regular poly(3-butylthiophene) have been reported as high as 1350 S·cm^{-1} while that of random poly(3-butylthiophene) exhibited a maximum of 5 S·cm^{-1} [121, 133, 134].

Subsequent studies revealed a negative correlation between the electric properties[1] and the alkyl-chains length in regio-regular P3AT [139]. On the other hand, the solubility of P3AT is increasing with the alkyl chains length, from the insoluble poly(3-methylthiophene) powders [129], via poly(3-butylthiophene) whose difficult dissolution is mentioned by Österbacka et al. [140] to poly(3-

[1] Time of flight mobilities and photocurrent in ITO/poly(3-alkylthiophene)/Al solar cells

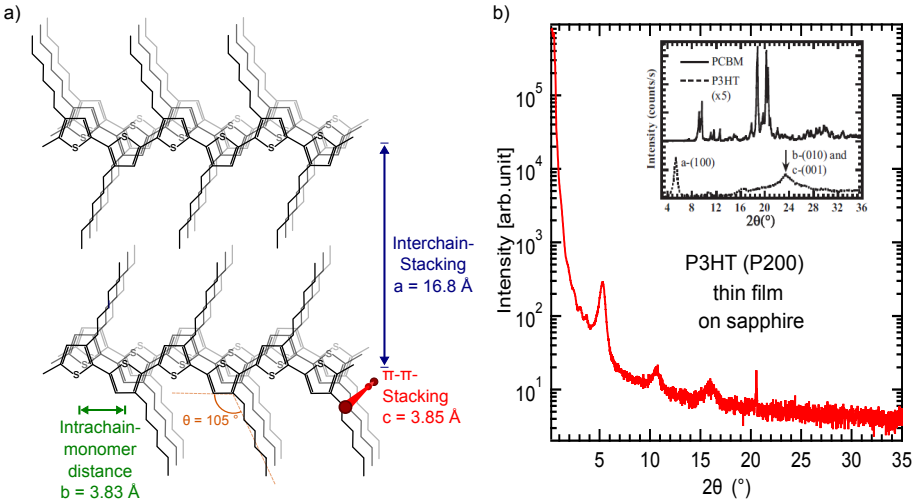

Figure 3.3: a) Structure of the P3HT crystalline regions as proposed by Prosa et al. Adapted from Kraus 2009 [142], values from Prosa et al. [141]. b) Resulting X-ray diffractogram of regio-regular head-to-tail P3HT spincoated on a sapphire substrate (annealed 10 minutes, 130°C) exhibiting peaks corresponding only to the a direction. Inset: powder X-ray diffractogram by Erb et al. [143] exhibiting the peaks corresponding to the 3 crystal parameters.

hexylthiophene) which is the P3AT with the shortest alkyl chains to be perfectly soluble in a variety of solvents. Poly(3-hexylthiophene) emerged as the best trade-of between electric properties and processability.

3.1.2 Films morphology

Crystalline structure

The reason of the good electronic and optical performances of P3AT and more specifically of P3HT lies in the peculiar ordering of their agglomerates. The crystalline structure of agglomerates of P3AT was unraveled originally by Prosa et al. in 1992 using X-ray diffraction [141]. The corresponding crystal parameters are depicted in figure 3.3a. It is characterized by a very planar configuration of the aromatic backbone and its alkyl side chains which are found to deviate of the thiophene plane by less than 1° in the case of P3HT [141]. This planarity is extended over several molecules via the alignment of successive polymers in the direction of the alkyl chains, thus forming a lamella. This extreme planarity in turn enables successive lamellae to stack in the $\pi - \pi$ direction with an inter-plane distance c equal to the distance b between the centers of successive monomers within one chain. This allows for excitations and charges to be delocalized in both the polymer chain and the $\pi - \pi$ stacking directions.

In spite of the low regioregularity of the P3AT used by Prosa et al., the determined structure was confirmed by the subsequent measurements realized on more regio-regular P3HT [143]. The XRD peaks corresponding to the inter-monomer b and $\pi - \pi$ stacking c directions are visible only in powder diffractogram, whereas films spin-coated on most commonly used substrates (glass/ITO/PEDOT:PSS [**?**]erb2005), quartz [52])typically exhibit only the peaks corresponding to the alkyl-chain di-

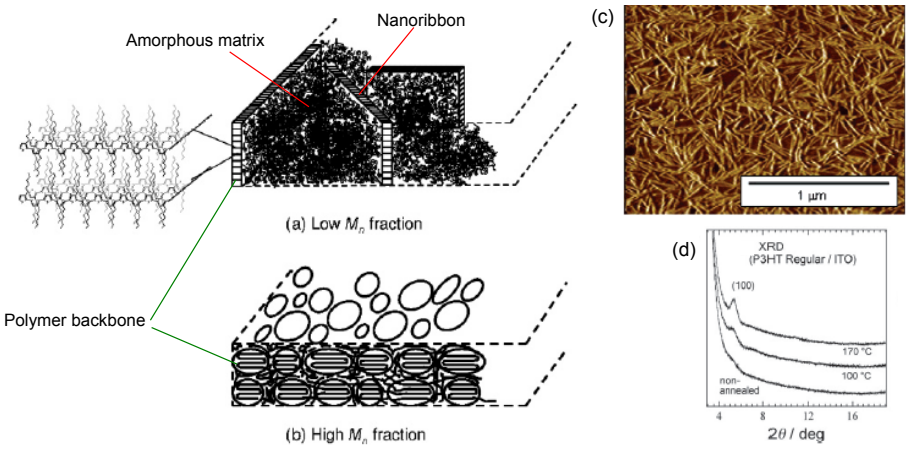

Figure 3.4: (a) and (b): simplified morphology of thin films of P3HT in the case of low M_w and high M_w polymers, respectively. Adapted from Zen et al. 2006 [145]. (c) AFM phase image of a low molecular weight P3HT thin film (Source: Zen et al. 2006 [145]). (d) XRD diffractograms of a P3HT thin film spincoated on ITO before and after annealing at different temperature. Source: Kanai et al. 2010 [146].

rection, see also figure 3.3b for sapphire substrate). This indicates a strong preferential edge-on orientation for the polymer chains relative to those substrates in which the direction a is perpendicular to the substrate.[2]

Coexistence of amorphous and crystalline regions in poly(3-hexylthiophene)

Yet, the aforementioned crystalline properties are not the rule in the whole bulk of P3HT films, in which both crystalline and amorphous domains are observed [145]. This is partly due to the imperfections of the synthesis processes which (i) enable to obtain a good but not a perfect regioregularity (typically between 90 and 99%), (ii) cannot avoid a certain dispersion in the length (or equivalently in the molecular weight M_w) of the polymer chains. A more intrinsic reason is that the first two (and last two) monomers of the chain always have a head-to-head configuration [147].

As an order of magnitude, Scharsich et al. recently found that the fraction of agglomerated molecules in solution can not exceed 55% even in a solvent where P3HT has a bad solubility (so-called *bad solvents*) [147], whereas Zen et al. measured in powders of pure P3HT a degree of crystallinity ranging from 4.5 to 18% depending on the average molecular weight of the molecules. The degree of crystallinity in films and the fraction of agglomerates in solution tends to increase with M_w [145, 147]. It can also be influenced by external conditions such as solvent quality [147][3] and temperature for solutions [148], and for films by the evaporation time of the solvent after spincoating (tunable via the boiling point or by depositing in a solvent saturated atmosphere) [147] or by annealing

[2] Face-on organization is possible on substrates functionalized via self-assembled monolayers to make them hydrophobic [144]. Organization can also be hindered in the case of very rough substrate, such as Titanium dioxyde (TiO_2) nanocrystals [52].

[3] Here, *quality* is meant as *ability to dissolve P3HT*.

the deposited film [146] (see figure 3.3(d)).[4]

The organization of amorphous and crystalline phases as presented by Zen et al. [145] is depicted in figure 3.4 in the case of molecules with high M_w (more crystalline) and low M_w (less crystalline). In both cases, the film is constituted of crystallites embedded in an amorphous matrix (see atomic force microscopy picture in figure 3.4(c) for the low M_w case). A section of those crystallites corresponds to a lamella such as represented in figure 3.3. In the case of low M_w the width of one crystallite corresponds to a fully extended polymer chain. In the case of high M_w polymer chains are longer than the crystallite width, which implies that each polymer chain is present in both the crystalline and the amorphous phase, and possibly in several crystallites or several times in the same crystallite [145]. A similar trend is found for agglomerates in solution [147].

3.1.3 Consequences on transport properties

The excellent planarity of P3HT in its crystalline form enables the conjugation length to extend as far as 29 to 40 monomers in agglomerates in *bad solvent* solutions, as determined from the absorption spectra by Scharsich et al. [147]. Moreover the regular $\pi - \pi$ stacking permits a two dimensional charge transport which allows charges to bypass structural defects. This results in very high mobilities in P3HT compared to other conjugated polymers of the same generation with for example a hole mobility measured by time-of-flight of 1.8×10^{-4} $\mathrm{cm^2V^{-1}s^{-1}}$ [116] compared to the 10^{-7} $\mathrm{cm^2V^{-1}s^{-1}}$ obtained for MDMO-PPV[5] in similar conditions [149].

Because the mobility is much lower in amorphous domains than in crystalline ones, the distribution of amorphous and crystalline phases plays an important role in charge transport properties. Indeed, field effect transistor (FET) mobilities exhibit a strong dependence upon the molecular weight of the polymer, as it has been reported to increase by 4 orders of magnitude (from 8×10^{-7} $\mathrm{cm^2V^{-1}s^{-1}}$ to 7.4×10^{-3} $\mathrm{cm^2V^{-1}s^{-1}}$) when M_w increases from 3.6 $\mathrm{kg{\cdot}mol^{-1}}$ to 27 $\mathrm{kg{\cdot}mol^{-1}}$ [145]. This exponential raise of mobility with M_w has been attributed to the phenomenon of percolation of the crystalline regions whose fraction in the film increase with M_w.[6]

Finally, the role of the amorphous phase should not be reduced to a limiting factor for mobility. Indeed, with the structure presented previously, charge transport in an ideal P3HT crystal can only take place within planes parallel to the substrate surface. As a result, transport in direction perpendicular to the substrate has to involve the amorphous segments of the polymer chains which can connect two crystalline segments having different distances to the substrate. This explains why the evolution of mobility with M_w in the perpendicular-to-substrate direction exhibits a linear dependency [151] rather than percolation-network behavior observed for FET mobilities [145].

[4] Note that the crystallization temperature is also M_w-dependent [145].

[5] Poly[2-methoxy-5-(3',7'-dimethyloctyloxy)-1,4-phenylenevinylene]

[6] Other explanation proposed by Brinkmann and Rannou was that longer chains can serve as bridges between crystalline regions [150]. But Scharsich et al. observed that the FET mobility saturates for the same M_w than the fraction of agglomerates in the solution to be spincoated [147] which speaks in favor of the explanation of Zen et al. together with the presence of a threshold for mobility, with a 3-fold mobility increase between $M_w = 4.5$ $\mathrm{kg{\cdot}mol^{-1}}$ and $M_w = 12$ $\mathrm{kg{\cdot}mol^{-1}}$ which resembles the properties of percolation networks [145].

3.1.4 Studied batches

The regio-regular P3HT used in the course of this thesis was supplied by two companies. P3HT *4002E* was synthesized by Rieke Metals, which guarantees a regioregularity of 91 to 94 %, a molecular weight of M_w between 45 and 60 kg·mol^{-1} and a content of residual impurities (Br, Ni, Zn) from the synthesis typically below 0.02%. P3HT *Sepiolid P200* was purchased from BASF which guarantees a regioregularity over 95 %, a molecular weight between 20 and 40 kg·mol^{-1} and a content of residual impurities (Fe, Pd, Sn) from the synthesis below 50 ppm. It should be noted that, in both cases, the molecular weight exceeds the molecular weight that enables to reach the maximal fraction of agglomerates in *bad solvent* found by Scharsich et al. [147]. Due to higher regioregularity and lower impurity content, *P200* tends to exhibit better ordering and a larger contribution of delocalized states in excited states spectroscopy (see § 5.2).

3.2 [6,6]-phenyl-C_{61} butyric acid methyl ester (PCBM)

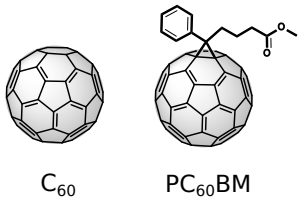

Figure 3.5: Molecules of C_{60} and PCBM.

The molecule of buckminsterfullerene C_{60} (figure 3.5 (left)) was first discovered in 1985 by Kroto, Heath, O'Brien, Curl and Smalley as the most abundant product naturally forming in a vapor of carbon obtained by laser ablation of graphite in an inert atmosphere. In addition to earning three of their inventors a Nobel prize of chemistry in 1996 [152], fullerenes and fullerene derivative have shown, since the first organic bilayer solar cell with efficiency over 1 % by Tang et al. in 1986 [153], unrivaled properties as electron acceptors for organic solar cells.

The reason for the better performances of C_{60} over other electron acceptors are still imperfectly understood. A comparative study by Imahori revealed that the use of C_{60} as electron acceptor in combination with Zinc Phtalocyanine resulted in faster electron transfer and lower charge recombination rate than with any other electron acceptor [154]. He attributed this to a smaller reorganisation energy when passing from ground state to charged C_{60} than in the other acceptors, which could be due to the large delocalization of the charge to the whole C_{60} cage[7] combined with the rigidity of the cage structure [154].

[6,6]-phenyl-C_{61} butyric acid methyl ester (PCBM) (figure 3.5 (right)) is a soluble equivalent of C_{60}. The side chains attached to the buckyball give it the ability to dissolve in most common organic solvents, thus making it usable

[7] In other acceptors, the charge is often strongly localized to the heteroatoms [154].

in solution-processed devices. Similar to its non-soluble equivalent, PCBM is strongly related to the development of organic solar cells as it has been the nearly exclusive electron acceptor used in bulk-heterojunction organic solar cells since its first synthesis in 1995 [155, 156]. In the frame of bulk-heterojunctions, its spherical shape may also be an advantage to enable molecule diffusion and self organisation within the composite medium.

3.3 P3HT:PCBM blend and solar cells applications

The review of Dennler, Scharber and Brabec [157] attributes the first encouraging P3HT:PCBM solar cell with an EQE of 76% at 550 nm to Schilinsky, Waldauf and Brabec [158]. Shortly thereafter came the first explicit mentioning of the positive effect of thermal annealing [159].

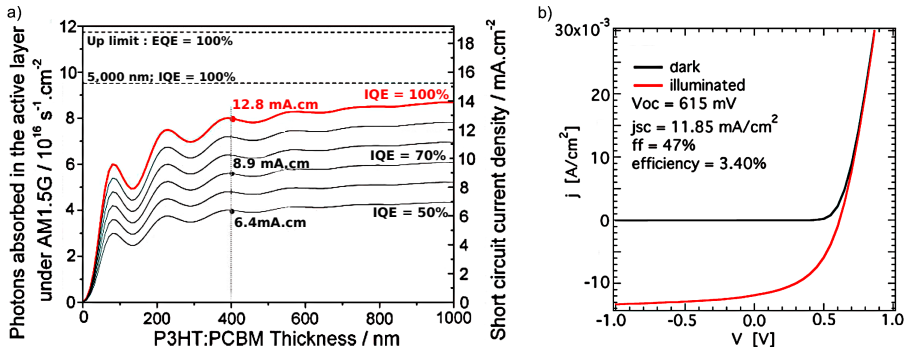

Figure 3.6: (a) Number of photons absorbed in the active layer under AM1.5G calculated by transfer-matrix formalism, for a device having the following structure: glass (1 mm)/ITO (140 nm)/PEDOT:PSS (50 nm)/P3HT:PCBM (x nm)/Al (100 nm). The right axis represents the corresponding short-circuit current density J_{sc} at various IQE, indicated in the graph. Adapted from Dennler et al., 2009 [157]. (b) IV characteristic of the best P3HT:PCBM based solar cell obtained in our group by Dr. Julia Rauh (glass/ITO(150 nm)/PEDOT:PSS(40 nm)/P3HT:PCBM 1:0.8($\approx$ 400 nm), annealed/Ca(20 nm)/Al(94 nm).

Given the matching of the blend's absorption spectrum with the solar AM1.5G spectrum and the interferences of the light within the different layers of a device, Dennler et al. [157] predicted the maximal short circuit current reachable for a glass(1 mm)/ITO(140 nm)/PEDOT:PSS(50 nm)/P3HT:PCBM/ Al(100 nm) as function of the average internal quantum efficiency (IQE) and active layer thickness (Figure 3.6 (a)). Figure 3.6 (b) shows our best solar cells obtained with this material system.[8] It has approximately the same layer thicknesses as those used in their computations and the thickness of the P3HT:PCBM layer is approximately 400 nm. The short circuit current obtained in this cell was 11.9 mA/cm^2 which corresponds, following the computations of Dennler et al., to an average IQE of more than 90 %. This illustrates perfectly well the outstanding properties of this blend.

[8] Processed by doctor Julia Rauh.

The fact that this material system is able to convert virtually every single absorbed photon into current, is due to the aforementioned very good individual performances of both materials. An additional point is that the blending of the two materials does not disturb their individual properties. In this regard, it has been shown very early that annealing plays a crucial role [159] as it is enables the individual properties of the two components to be expressed again after blending them.

Annealing of P3HT:PCBM blend has indeed been reported to improve performance by:

- Red-shifted absorption (due to crystallization of P3HT, see § 4.2) [160].
- Higher charge carriers mobility and more generally better charge carriers transport [161–163].
- Improved CT-states dissociation (lower geminate recombination) [45, 73, 75, 164].

In contrast, the exciton dissociation efficiency is slightly decreasing upon annealing as proved by an increase of photoluminescence [75], nevertheless not in proportions which are strongly detrimental to device performances.

As expected for those materials, where morphology and crystallinity plays such an essential role, changes of those two parameters upon annealing are the key factors explaining the observed annealing effects. In solution processed bulk-heterojunctions, the active layer is deposited from a solution where the 2 components are supposed to be homogeneously distributed[9] and usually gets *frozen* by the evaporation of the solvent before it can reach its solid state equilibrium morphology. As a result, the blend morphology is a metastable trade-of between the equilibrium organization of the molecules and the time it has to get close to this organization. In this context, annealing is a tool to make the molecules mobile again and thus allow the film to get closer to the equilibrium[10].

Two main film-organization related effects are reported upon annealing:

1. Crystallization of P3HT evidenced by the change in absorption and the appearing of the XRD peak[11], see figure 3.7 (left) [143].
2. Development of larger P3HT-rich and PCBM–rich domains [171] associated with the grouping of the otherwise dispersed PCBM in non-crystalline (no XRD-feature) PCBM–rich clusters[12] [143]. This enables percolation of the PCBM-rich phase and thus better photocurrents [143].

As a result, Erb et al. [143] proposed the picture reproduced in figure 3.7(b) to explain the reorganization taking place during annealing.

An important point is that the efficiency of the blend does not come from the coexistence of two but of three different phases: the PCBM-rich phase,

[9] Although agglomerates can already exist in solution in cases where one of the components is not soluble enough.

[10] The same effect can be obtain by other methods such as slow solvent evaporation [165–167], the use of non-solvents that force the agglomeration already in solution [168] and to a lower extent by the use of additive that accelerate the organization process [169, 170].

[11] Only the one corresponding to the *a* direction (see 3.3 (a)), which suggest that P3HT in blend as the same orientation relative to the substrate as pure P3HT.

[12] The non crystallinity of the PCBM–rich phase is not an universally admitted fact, with a number of paper claiming that this phase is also crystalline [45, 171].

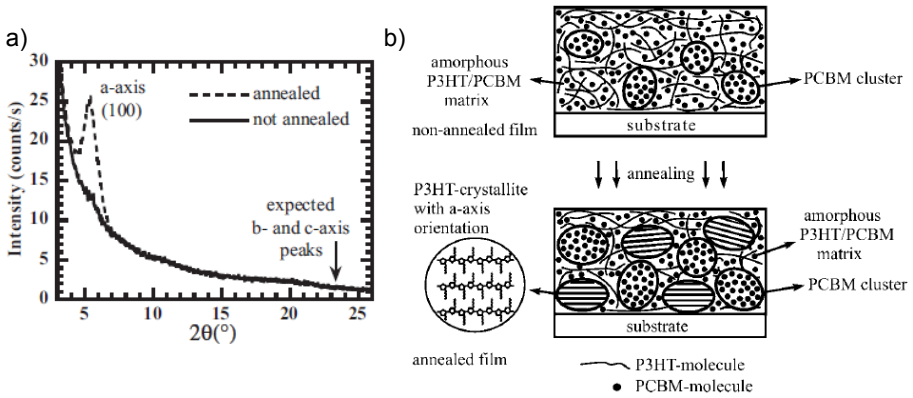

Figure 3.7: (a) Diffractogram (grazing incidence) of P3HT/PCBM composite films deposited on glass/ITO/PEDOT:PSS. Source Erb et al. 2005 [143]. (b) Associated change of the blend structure as proposed by Erb et al. Source Erb et al. 2005 [143]

the P3HT crystalline phase and the amorphous phase. Studies by Berson et al. [172] have shown that the blend can not reach its best performances without the presence of amorphous P3HT. They managed to separately process purely crystalline P3HT nanofibers and mix them with PCBM and amorphous P3HT. For 1:1 P3HT:PCBM ratio, the best performing solar cells were obtained for a ratio of 80% of crystalline P3HT and 20% of amorphous, the solar cells efficiency was found to strongly sink when increasing the crystalline P3HT ratio over this limit [172]. It was proposed that amorphous P3HT is needed in solar cell applications for vertical transport (the nanofibers tend to be lying on the substrate) [173]. Consistent result was found by study of the influence of P3HT's molecular weight on solar cells performances: Ma et al. [174] found that the best results could be obtained from P3HT benches exhibiting a relatively high chain length dispersion to insure the presence of both short chains which can initiate crystallization [175] and longer chains partly embedded in the crystallites and forming a matrix to connect the different crystallites [157].

As a summary, the P3HT:PCBM blend enables, thanks to its quite remarkable morphology, a close to unity quantum efficiency. Its main limitations are the wide energy offset between the LUMOs of P3HT and PCBM which is limiting the maximum open circuit voltage, and the insufficient absorption of P3HT in the red and infrared spectral regions. Finally the phase diagram studies by Zhao et al. [176] mention that the maximal operating temperature of a solar cell can exceed the glass transition temperature of the blend, which they found to be 40°C for a 1:1 blend. This implies that the molecules can still reorganize during solar cell operation and thus slowly degrade the device performances.

Part II

Results

Chapter 4

Exciton dissociation and binding energy in poly(3-hexylthiophene)

4.1 Introduction

In this chapter, we will bring our attention on the first bottleneck of photocurrent generation in organic solar cells: dissociating the excitons. Whereas this task does not require any special care in inorganic photoactive materials, the situation is quite different in the world of organic semiconductors. Indeed, as already discussed (§ 1.2.2) the low dielectric constant of organic materials causes the coulombic attraction (equation (1.16)) between charges of opposite sign to be stronger and to have a longer range than in inorganic materials, thus making them difficult to separate. Studies by Veldman et al. [177] claim, for example, that no proper excitons dissociation efficiency can be reached without the loss of at least 0.6 eV between the initial excitons energy E_G and the generated charges energy eV_{OC}.

To better understand this limitation, we carry out a detailed study of the binding energy E_b of the singlet excitons in the reference material poly(3-hexylthiophene). In a first part we describe the P3HT absorption and photoluminescence spectra in order to determine the nature of excitons in P3HT. We then show a method to dissociate those excitons by applying an external field F. By monitoring photoluminescence we determine the effect of F. The theoretical models by Onsager and Braun enable us to extract E_b. We discuss the representativeness of the energy obtained by this method and insert it in a larger frame by comparing it with energies obtained by photoelectron spectroscopy, and the onsets of absorption and photoconductivity.

4.2 Nature of the excitons in P3HT: absorption and emission spectra

In order to extract the binding energy of excitons in P3HT, it is first necessary to clarify their nature with the following aims: identify the kind of excitons generated upon illumination, and the excitons responsible for photoluminescence, the binding energy of which will be determined in the following of this chapters.

4.2.1 Absorption.

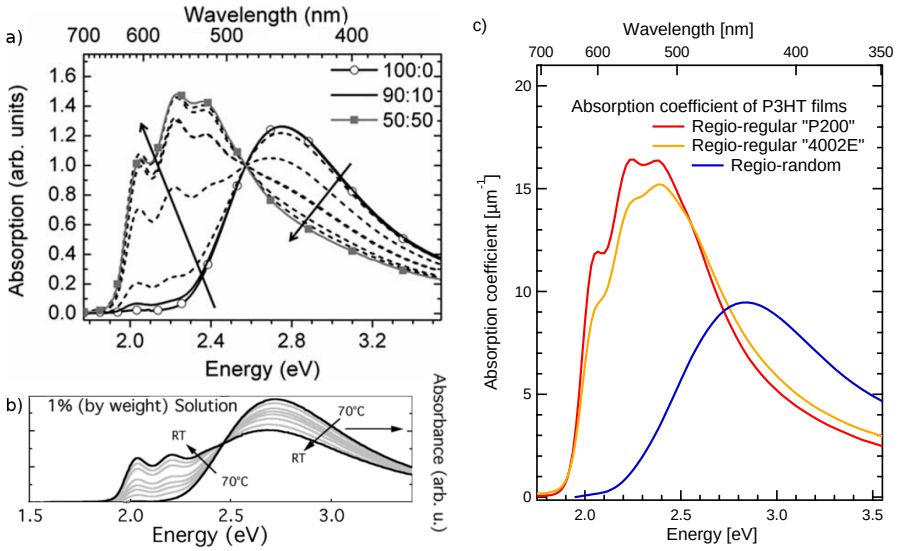

Figure 4.1: Absorption features in P3HT films and solutions: (a) Absorption spectra of P3HT in solution using as a solvent a mixture of a chloroform (CF, in which P3HT can be easily dissolved) and ethyl acetate (EtAc, in which P3HT can hardly be dissolved) for various CF:EtAc ratios. Source: Scharsich et al. 2012 [147]. (b) Absorption spectrum of P3HT in solution in isodurene at different temperatures. Source: Clark et al. 2007 [148]. (c) Absorption spectra of films of P3HT from different batches (see § 3.1.4).

As seen in chapter 3, the properties in P3HT are governed by intra- and inter-molecular interactions. This is also true for its excited species which can a priori be delocalized over the conjugation length of a single chain, or between two chains, as the distance between two monomers within a chain is quite similar — in crystalline regions — to the distance between two $\pi-$stacked chains.

By handling molecules in solution, it possible to force molecules aggregation by using solvents in which the polymer has a low solubility (see figure 4.1(a)) or by decreasing the temperature (see figure 4.1(b)), or on the opposite to prevent it, and thus to control directly which kind of interaction can or can not come into play. Those experiments carried out by Clark et al. [148] and Scharsich et al. [147] enable to identify two distinct absorption regions [44, 147, 148]:

1. Absorption of amorphous isolated coiled chains at high energies.

2. Absorption of planar chains forming weakly interacting H-aggregates at lower energies.

Interestingly, those two distinct absorption features are also found in films when comparing the absorption spectra of of regio-regular and regio-random P3HT (see figure 4.1(c)). Strikingly, the absorption spectrum of films of regio-random P3HT — where the irregular orientation of side chains prevents close stacking of the molecules — matches quite well the absorption of isolated chains in solution. Similarly, the agglomeration of films of regio-regular P3HT — where close, and locally crystalline, stacking is possible— corresponds pretty well to the absorption observed in solution for aggregates. We therefore attribute low energy and high energy absorption features to crystalline — dominated by inter-chain interactions — and amorphous — dominated by intrachain interactions— domains, respectively.

By using the absorption spectrum of regio-random P3HT films as an approx-

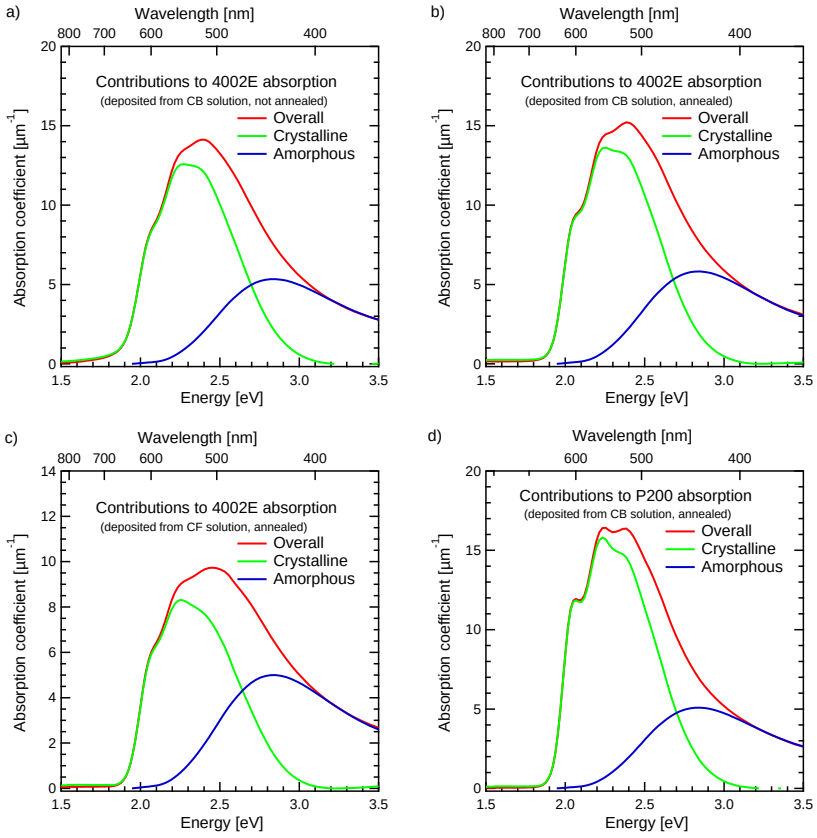

Figure 4.2: Rough estimation of amorphous and crystalline phases contribution to the absorption spectra of regio-regular P3HT films. The amorphous contribution was obtained by considering that only amorphous parts absorb at 3.2eV (see Scharsich et al. [147]), and considering that the absorption spectrum of amorphous regions is the same as the one of regio-random P3HT. This contribution was substracted to the overall absorption to obtain the contribution of the crystalline phase. Note: CF stands for chloroform and CB for chlorobenzene.

imation of the absorption of the amorphous regions in regio-regular P3HT, one can roughly estimate the contribution of the crystalline and amorphous phases to the absorption spectra of regio-regular P3HT (see figure 4.2). As expected, the contribution of the crystalline phase to absorption is larger in the material presenting the highest regioregularity: P200. We can also see that the use of a solvent with a higher boiling point (here chlorobenzene compared to chloroform) results in a larger contribution of the crystalline phase to the overall absorption. More quantitative estimations have been carried out by Clark et al. [178] and are represented in figure 4.5.

4.2.2 Photoluminescence.

The photoluminescence spectra of P3HT films are shown in figure 4.3. P3HT photoluminescence is peculiar because of its very small quantum yield (reported to be as low as 0.5% [179]) and its spectrum, characterized by a first vibronic peak having a lower intensity than the second one. Note that the predominance of the second vibronic peak over the first one is also found in the absorption spectrum (see figure 4.1), but that in contrast to luminescence yields, absorption coefficients are much stronger in regio-regular P3HT than in regio-random P3HT.

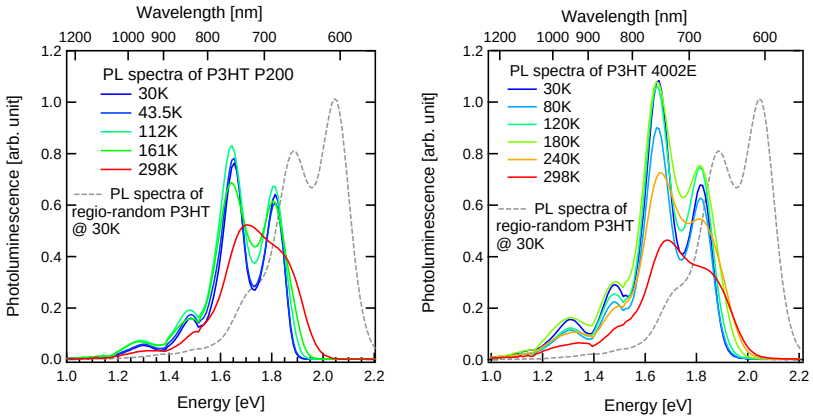

Figure 4.3: Photoluminescence spectra of the two regio-regular P3HTs used in this thesis at various temperatures (the shape of photoluminescence spectra of regio-random P3HT at 30K is also shown in dashed line for comparison).

The low-energy of PL clearly indicates a crystalline phase origin (the expected position of a photoluminescence from the amorphous part can be seen on the regio-random P3HT PL spectrum). More uncertain is the kind(s) of excitons responsible for such a peculiar spectral shape and low efficiency. Different explanation have been proposed: inversion of two first excited levels (see paragraph 1.1.3), leading to a forbidden 0–0 transition [32, 180], superposition of the spectra from two *intra-* and/or *inter-chain* species with forbidden or weakly allowed transitions [180, 181]. This last hypothesis having since then been found rather unlikely as the whole spectra was found to exhibit the same dynamics [148], excitation wavelength dependence [148] and, as we will see in § 4.3, the same field dependence.

At the present time, a model presented in 2005 by Spano [44] emerges as the one being applied with the most success to describe experimental absorption and luminescence properties of regio-regular P3HT [147, 148, 178]. An other strength of this model, is that it is based on two important peculiarities of regio-regular P3HT's crystalline organization: the short Π-stacking distance and the planarity of the polymer chains in the crystalline phase. Both result in a conjugation length as long as several tens of monomers [147].

According to this model, emission originates from *weakly interacting H-aggregates states* [44]: The compact Π-stacking observed in this materials naturally speaks in favor of interchain excited states characterised by a resonant Coulomb interchain excitonic coupling J_0. The lamellar organisation of the films implies that this aggregation is of H-type [44]. Nevertheless, theoretical works have shown that increasing the conjugation length reduces the excitonic coupling J_0 [182] which leads to the so–called *weakly interacting H–aggregates* states as presented in § 1.1.3.

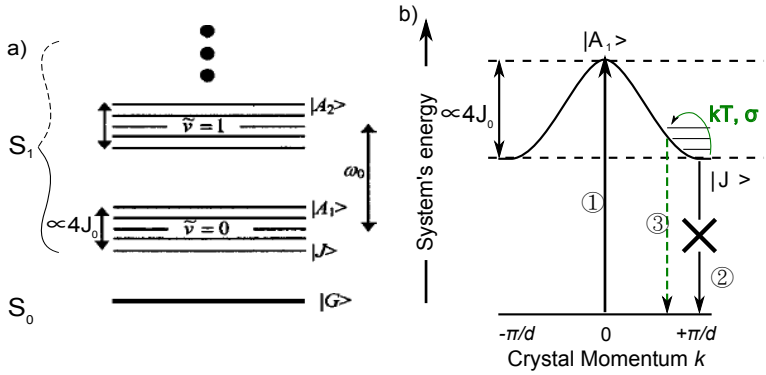

Figure 4.4: Energetic transitions in P3HT: (a) Energy-levels structure of polymer aggregates in the *weak excitonic coupling* regime. $\tilde{\nu}$ is the vibrationnal quantum number of the main vibration mode (of frequency ω_0), J_0 is the interchain excitonic coupling, $|G\rangle$, $|J\rangle$, $|A_1\rangle$ and $|A_2\rangle$ are the ground state, the initial state of the 0-0 emission, and the final states for the 0-0 and 0-1 absorption peaks, respectively. Adapted from Spano 2005 [44]. (b) Detail of the dispersion within the first excitonic band. Vertical arrows show ① the allowed 0-0 absorption, ② the forbidden 0-0 emission and ③ the blue shifted weakly allowed 0-0 emission. d is the interchain distance, kT and σ represent the temperature and energetic disorder influences, respectively.

The resulting energy levels and their consequences on electronic transitions are depicted in figure 4.4. In such H-aggregates, absorption occurs to the top of the excitonic band (transition ① in figure 4.4(b)) [148], whereas the emission is respecting Kasha's rule and thus occurs from the lowest level of this band (transition ② in figure 4.4(b)) [148]. Because the dipole moments in the lowest vibrational state of the ground state are symmetric with respect to the plane that bisects the stacking direction, absorption ① is fully allowed whereas emission ② is dipole forbiden [44]. Nevertheless, thermal disorder enables the existence of states with slightly higher energy from which emission ③ is weakly allowed [148]. With increasing thermal disorder (relatively to the bandwidth $4J_0$), emission ③ is getting more permitted and is shifting to higher energy, which results in a

blue shift and an increased intensity of the first peak relatively to the second one as observed in films of P3HT 4002E figure 4.3) upon increasing the temperature. Note that ground state levels with higher vibrational quanta have different symmetries, thus making the 0–1, 0–2, etc. transitions allowed [44].

In the frame of this model, the excitonic bandwidth $W(\propto 4J_0)$ can be directly determined from the ratio of the first and second absorption peaks [44, 147, 148, 178]. This has been done by Clark et al. [178] for series of P3HT films deposited from different solvents and annealed. The results are reproduced in figure 4.5, and illustrate how higher boiling point solvents allow for better crystallinity and thus a smaller exciton bandwidth.

The semi–empirical formula given by Clark et al. is the following [178]:

$$\frac{A_{0-0}}{A_{0-1}} \approx \left(\frac{1 - 0.24W/E_p}{1 + 0.073W/E_p} \right)^2 , \tag{4.1}$$

where E_p is the phonon energy of the main oscillator coupled to the electronic transition, which in case of P3HT is the $C = C$ symmetric stretch with an energy of 0.18 eV (as determined by Raman spectroscopy [148, 181]). Applying this formula to our measurements gives the exciton bandwidths summarized in table 4.1.[1] The exciton bandwidth follows the predicted trend, as they increase with energetic disorder.

P3HT Treat., solvent	P200 anneal., CB	4002E anneal., CB	4002E not ann., CB	4002E anneal., CF
Peaks ratio A_{0-0}/A_{0-1}	0.79	0.72	0.70	0.77
Exciton bandwidth W	68 meV	91 meV	96 meV	70 meV
Energetic disorder σ	69 mev	72 meV	78 meV	75 meV

Table 4.1: Exciton bandwidth and energetic disorder extracted for different P3HT films.

In the light of this model, it appears that, while absorption occurs in both amorphous and crystalline domains, photoluminescence is originating solely from the crystalline parts of the film. The absence of emission from the amorphous region could be due to exciton migration to the lower energy crystalline parts, or to reabsorption of the luminescence of the amorphous parts by the crystalline ones. Note that in the following of this chapter, we will focus on P3HT of the 4002E type on which the field dependent PL measurements were carried out.

4.3 Field-induced excitons dissociation

As represented in figure 4.6, the excited material is submitted to an external static electric field which is driving the two charges forming the exciton in opposite directions. The efficiency of this field-induced dissociation is controlled by monitoring the photoluminescence of the sample. Indeed, polaron pairs in which the two oppositely charges' wavefunction have no more spatial overlap

[1] The formula was applied to part of the absorption spectra due to the crystalline domains contribution (see figure 4.2).

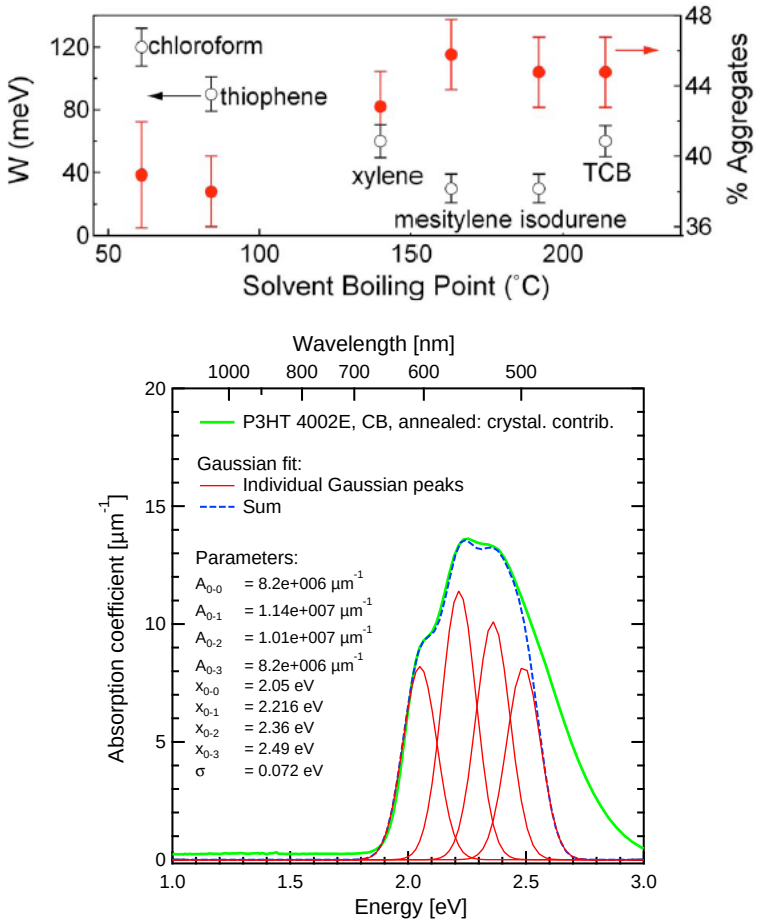

Figure 4.5: Up: Overview of the fraction of crystalline phase and exciton bandwidth W in annealed spin-coated thin films as function of the solvent boiling point. Source: Clark et al. 2009 [178]. Note: the boiling point of chlorobenzene is 132 ° C. Down: example of the Gaussian fits used to determine the relative intensity of the first vibronic transitions of the absorption of crystalline part of P3HT, here for P3HT 4002E, prepared by spincoating from chlorobenzene solution and post-annealing. A_{i-j} represent the maximal magnitude of the corresponding vibronic transitions and x_{i-j} their central energy.

(figure 4.6 (right)) are not expected to exhibit a significant radiative recombination. The experimental setup is presented in § 2.1.4.

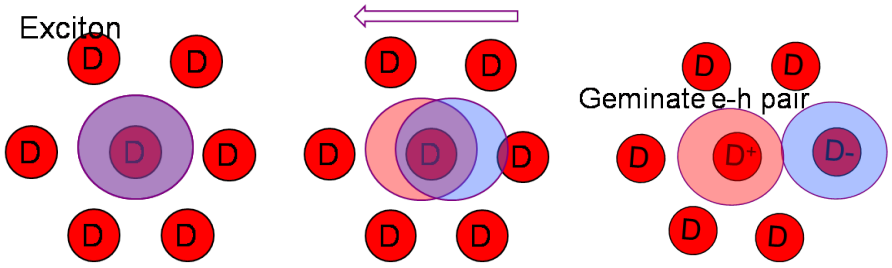

Figure 4.6: Action of an electric field (represented by the arrow) on an exciton. Note that the middle picture is a statistical representation: each exciton is actually expected to pass directly from the exciton state to the polaron pair state, with a probability depending of the applied field (see discussion § 4.6.2).

Monitored quantity

The efficiency of the exciton dissociation is quantified using the relative photoluminescence quenching $Q(F)$:

$$Q(F) = \frac{PL(F=0) - PL(F)}{PL(F=0)}, \tag{4.2}$$

where F is the applied field and $PL(F)$ the corresponding photoluminescence intensity.

Note that the use of the zero field luminescence as a reference for exciton dissociation implies that no dissociation takes place in the absence of an external field. This is not exactly true: as shown in figure 4.7 the zero field dissociation probability expected from the Braun-Onsager theory is between 10^{-11} and $5{\times}10^{-5}$ for reasonable binding energies. Nevertheless — except for the lowest binding energies under the Wannier excitons model — those values are below the sensitivity of our experimental setup.[2] Such a low dissociation could thus not be experimentally distinguished from an absence of dissociation. As a result Q(F) as defined in equation (4.2) represents in our experiment not only the PL quenching but also the exciton dissociation probability. Note that because of this sensitivity limitation, the experimental results will be presented using linear vertical scale.

Qualitative results

Spectral behavior As can be seen in figure 4.8 (left), the expected effect is indeed observed: the photoluminescence intensity decreases upon increase of the external field. The spectrum just scales down when increasing the applied field, without any apparent shift or change in peaks' relative intensity. Thanks to this property, we can measure the influence of the field on photoluminescence by simply measuring the intensity of the main peak at 730 nm (1.7 eV). Moreover,

[2]Noise level between 0.01 and 0.5 % of the maximal signal depending of the experimental conditions.

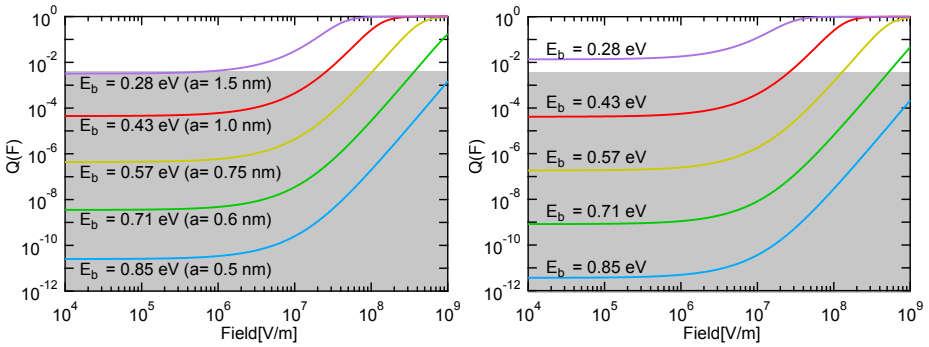

Figure 4.7: Field induced dissociation as predicted by the Braun Onsager theory for different binding energies, the grey area represent the experimentally unaccessible regions. Left: initial dissociation from the ion-pair model (with parameters from table 4.2). Adapted from Mack 2009 [183, p. 37]. Right: initial dissociation from the Wannier exciton model (with parameters from table 4.3, see section 4.4 for more details about the used parameters).

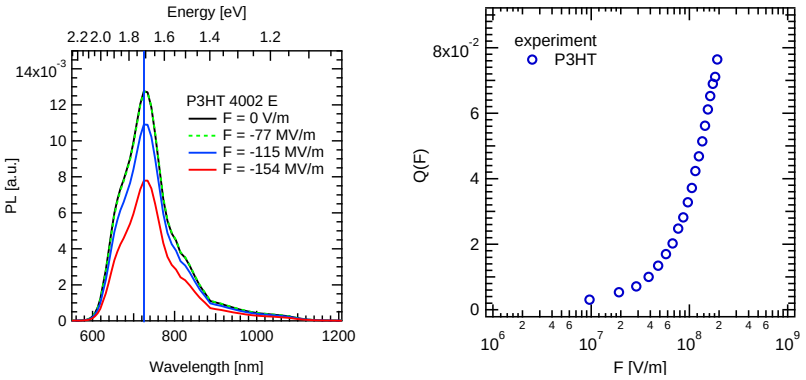

Figure 4.8: Left: Pure F-dependent PL spectra. The vertical line represent the wavelength 730 nm at which the F-dependent PL was measured in the following. Right: Field dependence of the photoluminescence measured at 730 nm.

the stability of the spectral shape confirms the idea of a direct transfer from a radiative state to a non-radiative state rather than a progressive distortion of the exciton. Indeed, a progressive distortion of the exciton would result in a quenching of the luminescence as the overlap between the wavefunctions of the hole and the electron are decreasing; but this type of quenching should be accompanied by a modification of the remaining photoluminescence spectrum (Stark shift) in contrast with our experimental results.

Quenching Figure 4.8 (right) shows the field-dependent quenching of the main peak of P3HT's photoluminescence measured at 730 nm. Albeit the quenching is very clear, it appears to be limited. The first reason is that it was not possible to apply higher fields without irreversibly damaging the sample. A second reason is that even in cases where the saturation of the quenching can be obtained, this one never reaches 100% [102, 184–187].

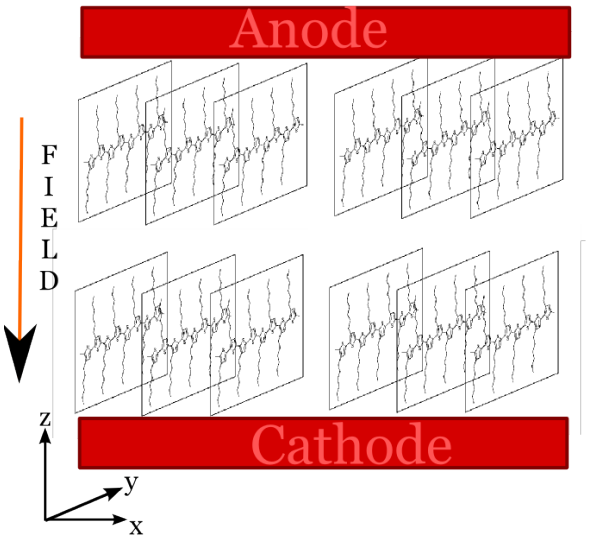

Figure 4.9: Schematic representation of the crystalline region of the P3HT layer unaffected by the electronic field.

The fact that the saturation of the photoluminescence quenching is not reached obliges us to speculate about its value before trying to quantitatively fit the data. Depending on the value we assume for the saturation of the quenching, different values of binding energies could be extracted. We chose to focus our interest on the lower limit of possible exciton binding energy, by carrying out quantitative fits under the assumption that quenching remains limited to 9 %.

It is important to notice that there is good reasons to think that the quenching could indeed saturate at such low values. Indeed, as explained previously (see § 3.1.2) and represented in figure 4.9, polymer chains in crystalline P3HT orientate preferentially parallel to the substrate, *standing* on their side chains. As a result, both intra-chain and interchain excitons extend on a direction perpendicular to the applied field. Adding to this — as explained in § 4.2.2 — that PL is originating only from the crystalline domains of the film, only excitons in crystals not perfectly following the natural stacking pattern are likely to be dissociated by the applied field.[3] This would explain that quenching efficiency saturates at rather low percentages.

4.4 Quantitative results: connecting quenching to binding energy.

To extract the exciton binding energy from the observed PL field-dependence, we adapted the models presented in the theoretical part (§ 1.2.2) by replacing

[3]Note that a planar configuration of the device would solve this problem but the large distance between the electrode would not allow for applying sufficient fields to obtain exciton dissociation. Additionally, the field would not be uniform in all the layer thickness.

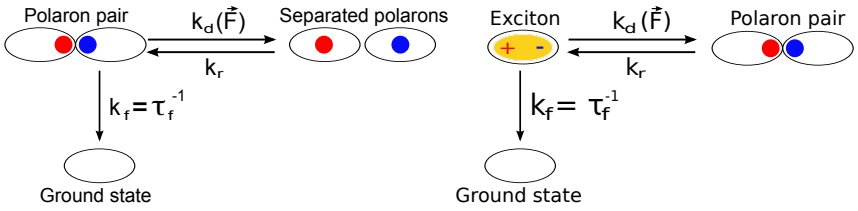

Figure 4.10: Dissociation model adapted from CT-states to excitons dissociation. Left: original competing mechanisms considered by Braun for CT-states dissociation. Right: Adapted scheme relevant for exciton dissociation.

CT-state by excitons and separated polarons by polaron pair (discussed more in details in § 4.5.2) as depicted in figure 4.10. As a result, the excitons dissociation probability is expected to be governed by the competition between dissociation and their recombination as expressed by equations 1.19 and 1.20.

Considering that the excitons recombination rate k_f is field independent and equal to the invert of the zero-field excitons lifetime τ_f, the whole field-dependence is beard by the dissociation rate $k_d(F)$. The goal of the different models is thus to express the magnitude and field dependence of this parameter.

4.4.1 Braun-Onsager model for ion pairs separation

The Braun-Onsager model for ion pairs dissociation is detailed in § 1.2.2. According to this model, the dissociation rate k_d is given by equation 1.27.

With the exciton radius and binding energy being directly related, exciton dissociation is thus controlled by 5 parameters: the zero-field exciton lifetime τ_f, the relative dielectric constant of the medium $\langle\epsilon\rangle$, the sum of electron and hole mobilities $\langle\mu\rangle$, the temperature T and of course the binding energy E_b. The number of variables can be reduced to 4 by grouping $\langle\mu\rangle$ and τ_f via the use of a reduced dissociation rate $\kappa_d = k_d/\langle\mu\rangle$ which is then independent of $\langle\mu\rangle$:

$$P_d(F) = Q(F) = \frac{k_d(F)}{k_d(F) + k_f} = \frac{\kappa_d(F)}{\kappa_d(F) + \langle\mu\rangle\tau_f} \tag{4.3}$$

Chosen parameters and their influence

Among those parameters, the binding energy is the one we are trying to determine. The others are known from different experiments, the values used are presented in table 4.2. As explained by Deibel et al. [188] and Veldman [189], the charge motion associated to exciton dissociation takes place on a local scale, as such, the relevant mobilities to quantify it is the local mobility of crystalline phases, which does not take into account the macroscopic limitations such as grain boundaries or amorphous domains.

The dependence of the dissociation upon those parameters is shown in the following.

Mobility lifetime product Thanks to time resolved photoluminescence studies, zero-field singlet exciton lifetime τ_f is a rather well known parameter expected to be between 0.4 ns [190] and 0.66 ns [191]. Time resolved microwave conductivity (TRMC) on the other hand enables to extract the local mobility of

Parameter	Utilized Value
$\langle\mu\rangle \cdot \tau_f$	5×10^{-16} m^2/V
$\langle\epsilon\rangle$	3.4
T	300 K

Table 4.2: List of the parameter values used for fitting the PL-quenching with the Braun-Onsager theory for ion pairs dissociation. From Mack, 2009 [183, p. 37]

charges. Using this method, Grzegorczyk et al. have determined a mobility of 1×10^{-6} m^2/V/s, which gives us a factor in the range of (4 to 6.6)$\times10^{-16}$ m^2/Vs.

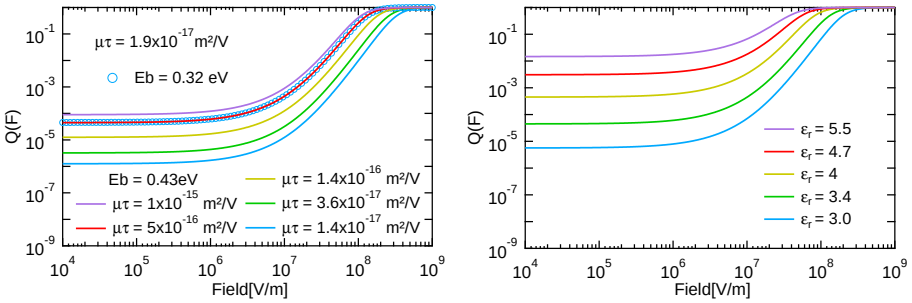

Figure 4.11: Left: F-PL quenching for different values of the $\langle\mu\rangle \cdot \tau_f$ product including the expected range of 4 to 6.6$\times10^{-16}$ m^2/V and range that would be obtained using macroscopic mobilities (1.4 to 2.6$\times10^{-17}$ m^2/V). Other parameters from table 4.2. Right: F-dependent PL quenching for different values of $\langle\epsilon\rangle$ calculated using the following parameters from table 4.2 and $a = 1$ nm (E_b then varies with $\langle\epsilon\rangle$ between 0.26 and 0.48 eV, see equation (1.24)).

The influence of the parameter $\langle\mu\rangle \cdot \tau_f$ on the quenching curves is relatively weak. Nevertheless using macroscopic mobilities (in the range of 1.8 – 4 $\times10^{-8}$m^2/Vs) instead of local ones would result in a underestimation the $\langle\mu\rangle \cdot \tau_f$ factor of more than one order of magnitude and thus an underestimation of the binding energy as high as 0.11 eV.

Relative dielectric constant The crucial influence of the dielectric constant on field induced dissociation is confirmed by the simulation depicted on figure 4.11(right). As can be seen, even small variations of $\langle\epsilon\rangle$ causes an important change in the field dependence of photoluminescence. In contrast to $\langle\mu\rangle \cdot \tau_f$ and E_b, $\langle\epsilon\rangle$ has influence on both the initial dissociation (equation (1.23)), the relative field dependence (equation (1.25)) and —in the ion pair model— on the definition of the binding energy itself (equation (1.24)).[4] The values represented in figure 4.11(right) are typical for organic semiconductors and correspond to the range obtained by Breselge et al. [192] by varying the side chains in PPV polymers. The relative dielectric constant of P3HT is 3.4.

[4] In other models, the binding energy is not necessarily restricted to the Coulomb interaction.

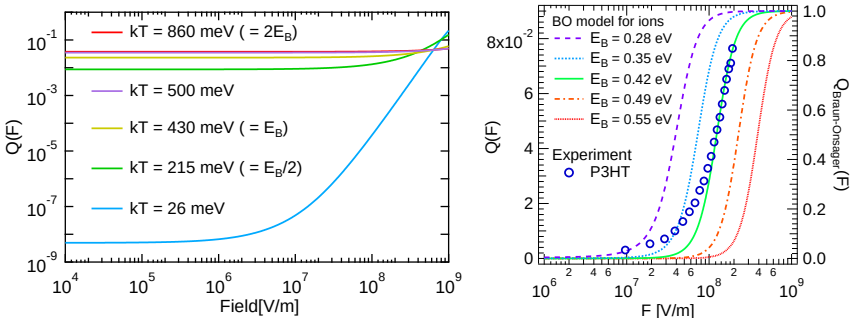

Figure 4.12: Left: F-dependent PL quenching for different values of kT calculated using the following parameters: $\langle\epsilon\rangle = 3.4$, a = 1 nm ($E_b = 0.43$ eV) and $\langle\mu\rangle \cdot \tau_f = 5{\times}10^{-20}$ m^2/V. Right: Comparison of the field-induced photoluminescence quenching in P3HT 4002E with the model of Onsager-Braun for ions dissociation. For the numerical value of fit parameters, see table 4.2.

Thermal energy Because all parameters are strongly dependent upon temperature,[5] simulating the quenching with only a different T parameter can not represent the actual behavior to expect upon changing the temperature. Nevertheless it can give an idea of the dissociation of "hot excitons", in case this additional energy can be used to help dissociation. In that case "kT" does not represent the ambient temperature anymore but the additional energy of the absorbed photon compared to the absorption threshold. Dissociation of hot excitons should not be in competition with recombination to the ground state, but with the much quicker vibrational relaxation, which is expected to occur in the 10^{-15} to 10^{-13}s timescale. As a result, we diminish the $\langle\mu\rangle \cdot \tau_f$ product to $5{\times}10^{-20}$ m^2/V for this simulation.[6]

The results are shown in figure 4.12(left). Thermal energy has two effect on the dissociation. On the one hand it increases the thermally assisted zero-field dissociation (see equation (1.23)), secondly it decreases the effects of the field on dissociation (see equation (1.25)) to such an extent that for an excess thermal energy of 500 meV, the PL quenching barely exhibits any field dependence for experimentally reachable electric fields. Interestingly, this excess thermal energy is the one we apply on P3HT whose absorption onset occurs at 1.85 eV and is illuminated with a laser of energy 2.32 eV.

Binding energy One can see from equation (1.27), that $k_d(F)/k_d(F=0)$ is independent of E_b. E_b thus only affects the absolute value of the quenching, via the zero-field dissociation [80]. Graphically — as can be seen in figure 4.7 (left) — it means that the quenching curves just scales with the E_b. Although the zero field quenching is not experimentally reachable, this scaling of the curve implies that E_b can still be determined from the field at which a given quenching, say 50%, is reached. Quantitatively, this influence of E_b is quite important as the field required to reach a given quenching increases by nearly two orders of magnitude when increasing the binding energy from 0.28 eV to 0.85 eV.

[5] See for example chapter 6 for the influence of temperature on mobilities

[6] As expected, using the recombination time instead of this relaxation time results in a full quenching even at zero field.

Results of the fits

The comparison of experimental data with the model of Braun-Onsager for ion pair dissociation is depicted on figure 4.12(right) in the hypothesis that the maximum quenching is reached at 9% (already discussed in § 4.3). The values used for the fit parameters are those reported in table 4.2. With them, we extract a minimum binding energy E_b of 0.42 +/- 0.02 eV equivalent to an exciton radius a = 1 +/- 0.1 nm which corresponds to 2.65 monomers in the polymer chain direction (much smaller than the conjugation length which extends to several tens of monomers, see chapter 3) or 2.65 chains in the π-stacking direction.

4.4.2 Braun-Onsager model for Wannier excitons dissociation.

The version of the Braun-Onsager theory for Wannier excitons is much more rarely used than the one for ion pair dissociation. A reason is that the former is using effective mass of the exciton, which is not directly accessible by the experiment. Nevertheless, as seen in § 4.2, the absorption and emission spectra of P3HT are well known and models exist to describe the band structure of their excitons from those spectra, allowing to extract their effective mass.

Compared to the model used for dissociation of ion pairs, only the prefactor for the dissociation rate is changing, as the equilibrium constant $K(F = 0)$ describing the balance between dissociation and reformation of the excitons is now given by equation (1.22) instead of equation (1.23). The resulting dissociation is governed by equation (1.29).

As a result, the exciton dissociation is controlled by the same parameters as in the Braun-Onsager model for ion pairs dissociation, to which is added the effective mass of the excitons.

Determination of the effective mass of the exciton, and comparison with the Braun-Onsager model for ion pairs dissociation,

Using the model from Spano [44], we have determined for the luminescing excitons of crystalline P3HT 4002E annealed a bandwidth W of 91 meV (see table 4.1). The dispersion relation given by equation (1.14) for the excitonic band, one can determine the effective mass of the exciton from equation (1.15) as being:

$$(m^*)^{-1} = \frac{2\beta d^2}{\hbar^2} = \frac{W d^2}{2\hbar^2}, \tag{4.4}$$

where d is the interchain distance in the π-stacking direction (3.85 Å), $\beta = W/4$ is the interchain interaction. This gives us a value of $m^* = 1.03{\times}10^{-29}$ kg or $11.3{\cdot}m_e$, where m_e is the mass of a free electron. This high effective mass is the direct consequence of the weak interchain coupling[7] predicted by Beljonne et al. for large conjugation lengths [182]. It should be noticed that m^* is the effective mass in the π-stacking direction. The effective mass in the intra-chain direction would in contrast be expected to be very low due to very strong inter-monomer

[7] As a comparison, excitons in anthracene with a similar exciton bandwidth but a 2 times larger intermolecular distance have an effective mass in the order of $8{\cdot}m_e$ in the [010] direction [21, 39, 193].

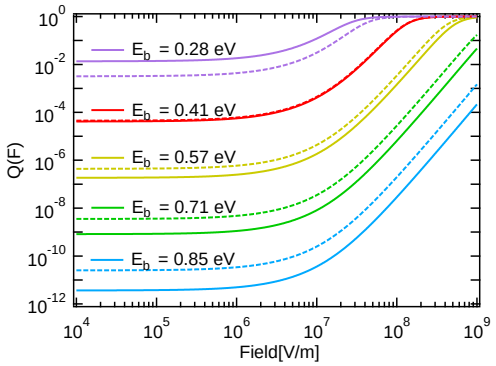

Figure 4.13: Comparison of the exciton dissociation predictions of Braun Onsager theory for ion pairs (dashed lines) and for Wannier excitons (solid lines) with the parameters summarized in tables 4.2 and 4.3

coupling. As an example, Moses et al. use for MEH-PPV an effective mass of $0.1 \cdot m_e$ [81].

With the effective mass determined, we now possess a full set of parameters to simulate (or fit) the exciton dissociation. Those parameters are summarized in table 4.3.

Parameter	Utilized Value
$\langle \mu \rangle \cdot \tau_f$	1.9×10^{-17} m^2/V
$\langle \epsilon \rangle$	3.4
T	300 K
m^*	1.03×10^{-29} kg $= 11.3 \cdot m_e$

Table 4.3: Parameter values used for fitting the PL-quenching with the Braun-Onsager model for Wannier exciton dissociation.

The comparison of the simulations following this model to those using the model of ion pairs separation (see figure 4.13) reveals that both models are nearly equivalent for binding energies around 400 meV but that the Wannier excitons dissociation seems to exhibit a stronger dependence on their binding energy.

Influence of the parameters

The influence of the different parameters on the dissociation efficiency (or equivalently PL quenching) is depicted on figure 4.14. As can be seen, the trends are the same as for the model for ion pair separation, with the notable difference that the dielectric constant has nearly no influence on the zero-field dissociation. Zero-field dissociation is mainly influenced by the effective mass of the excitons. Note that the vertical scale employed here is smaller than this of figure 4.13; indeed all those parameters have a reduced influence compared to the influence of the binding energy. An important point is that the dissociation occurs at notably lower fields for excitons having a larger effective mass. This implies that for the highly anisotropic P3HT, dissociation will occur first in the direction of higher effective mass, which is, here, the π-stacking direction.

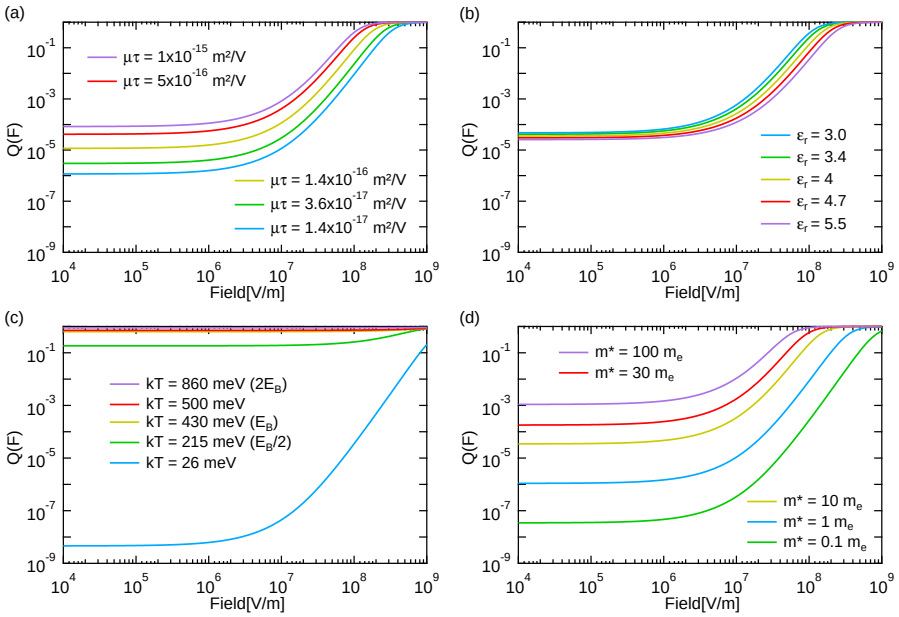

Figure 4.14: Influence of the parameters on the field-induced dissociation efficiency for the model of Onsager Braun for Wannier excitons dissociation. (a) $\langle\mu\rangle \cdot \tau_f$. (b) $\langle\epsilon\rangle$. (c) kT. (d) m^*. Except for (c), the parameters used are those of table 4.3 with a binding energy of 0.43eV. For the thermal energy dependence (c) a $\langle\mu\rangle \cdot \tau_f$ product value of 5×10^{-20} m^2/V was used as the dissociation of hot excitons is in competition with their relaxation to the lowest excited state instead of their recombination to ground state.

Results of the fits

Figure 4.15 shows the comparison between the experimental data for PL quenching and the predictions from the Onsager Braun model for Wannier exciton dissociation. As can be seen, the observed quenching corresponds to a binding energy E_b of 0.42 +/- 0.02 eV. Interestingly this is the same energy that was found with the BO model for ion pairs dissociation which indicates that the excitons probably have a rather strong ion-pair character. If considering that the binding energy is only due to Coulombic interaction, the exciton radius a, calculated with equation (1.24), is 1 nm, corresponding to 2.65 polymer chains. Note that in this model the binding energy is not necessarily due to Coulombic interaction only (it could for example include a difference of polaronic relaxation energy between the exciton and the pair of polarons obtained after dissociation), as a result a is only an indicative value. If we consider that the polaronic effect should be larger in the polaron pair than in the exciton, then the actual Coulombic interaction in the exciton should exceed the extracted binding energy, and thus the exciton radius should be smaller than the aforementioned value (see figure 4.16 and § 1.1.3).

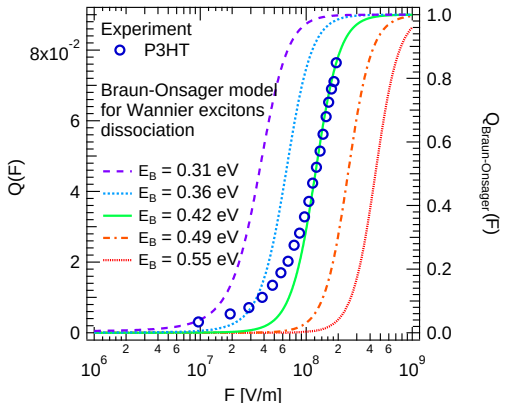

Figure 4.15: Comparison of the field-induced photoluminescence quenching in P3HT 4002E with the model of Onsager-Braun for Wannier excitons dissociation. For the numerical value of fit parameters, see table 4.3.

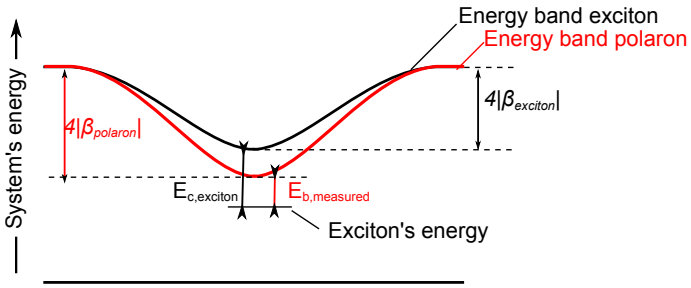

Figure 4.16: Illustration of the possible difference between binding energy and Coulomb attraction energy due to polaronic relaxation. $E_{c,exciton}$ represent the Coulomb attraction energy of the exciton and $E_{b,measured}$ the measured binding energy, the difference being due to the difference between the interchain interaction $\beta_{polaron}$ in polarons and $\beta_{exciton}$ in excitons.

4.4.3 Summary of the results

The results of fits carried out using the Onsager–Braun theory for ion pair separation, and Wannier excitons dissociation, respectively, are summarized in table 4.4. Although, the model for Wannier excitons dissociation may be theoretically more adapted to the case, it presents the disadvantage of requiring to know the effective mass of the exciton, which is usually not directly accessible by the experiment. However, as can be seen here, the model describing ion pair separation leads to the same result. The weak point of this model being that the value obtained for the dissociation efficiency strongly depends on the dielectric constant, which much thus be known with high precision.

Model	Fitting to the experiment	Binding energy
Braun-Onsager for ion pairs	ok	0.42 eV
Braun-Onsager for Wannier exc.	ok	0.42 eV

Table 4.4: Binding energy extracted from the PL-quenching using the different models.

4.5 Interpretation: what is this binding energy? The greater perspective.

In this section, a set of complementary methods is used to enable us to access additional information on the energy levels relevant for solar cells application. The results presented in that section have been obtained together with collaborators within the chair of experimental physics VI as well as from the chair of experimental physics VII (formerly in the chair of experimental physics II). They have been published, together with the PL quenching results in [82].

4.5.1 Results from other experimental techniques

Absorption

The onset of absorption gives the lower limit of the spectrum that can be collected in solar cells application (if neglecting the absorption by excited species which can occur at lower energies but represent very small amount of light due to the relatively low density of those species). In the case of P3HT, this onset is found to occur at 1.85 eV as can be seen in figure 4.17.

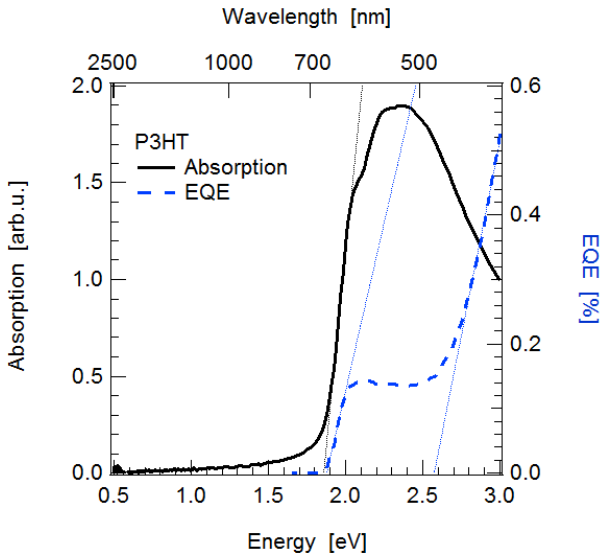

Figure 4.17: Absorption (solid line) and EQE (dashed line) of P3HT thin films. The thin lines show how the onsets of the respective spectra were determined. The onset of the spectrally resolved photocurrent, the EQE, starts just above the absorption onset of 1.86 eV. The major photocurrent contribution, however, is seen at the energy of 2.6 eV, which corresponds to the transport gap extracted in figure 4.18. Adapted from Deibel et al. 2010 [82].

Photoemission and inverse photoemission spectroscopies

Photoemission spectroscopy uses highly energetic photons (UPS and XPS) or electron (IPES) beams to ionize a material and determine the energy levels of the resulting charged media (see experimental methods, § 2.3).

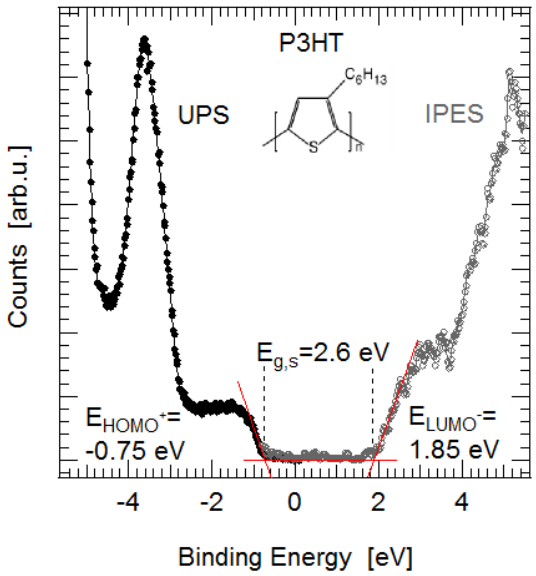

Figure 4.18: UPS (black) and IPES (gray) spectra of a 70-nm-thick P3HT film on ITO/glass. Measured data are plotted as points, the straight lines are 5 point averages. The transport levels were derived from the band onsets as indicated by the lines. The transport gap is 2.6 eV. The molecular structure of P3HT is shown in the inset. Source: Deibel et al. 2010 [82].

As discussed by Krause et al. in Ref. [117], using the onset of the UPS spectra gives the upper limit of the energy of the final state formed by electron emission which is a relaxed free positive polaron. This is the upper limit of the HOMO of P3HT positive polarons (HOMO+). Equivalently, the onset of the IPES spectra gives us the lower limit of the LUMO band of negative P3HT polarons (LUMO-).

The result found for P3HT are displayed in figure 4.18, the HOMO+ band is found at -0.75 eV relatively to the Fermi level of the co-measured metal and the LUMO- band at +1.85 eV, which gives us a transport gap of 2.6 eV.

External Quantum Efficiency

The importance and role of those two gaps is clarified by the result of spectrally dependent photocurrent measurement in a solar cell. The EQE spectrum of pure P3HT photodiodes is shown in figure 4.17. With increasing photon energy, one can see a small photocurrent threshold at the same energy as the onset of absorption corresponding to a very small charge generation efficiency which we tentatively attribute to defect states or to dissociation at the interface with the electrodes. At a photon energy of c.a. 2.6 eV a stronger threshold of the photocurrent takes place, and this in spite of a decreasing absorption. This energy corresponds quite nicely to the transport band gap as measured by PES.

Our interpretation is that the excitons generated by such high energy photons have enough thermal energy to overcome their binding energy and dissociate into polarons. An important point is that we do not associate the photons'

absorption to a direct transition to a state where charges are separated. The transition is rather associated with the generation of a hot S_1 exciton with a higher vibrational quantum number,[8]. Due to this additional energy, the exciton has the possibility of dissociating into a pair of separated polarons which will subsequently participate in the photocurrent (see also figures 4.12 and 4.14 (c) where high kT enables zero field dissociation and virtually no field dependence). Nevertheless this dissociation is in competition with the relaxation to the lowest vibrational level of the S_1 vibronic state which occurs in the time scale of the molecular vibration (10^{-15} to 10^{-13} s [21]).[9] As such this dissociation is still relatively inefficient, which explains the EQE remaining below one percent.

4.5.2 Global picture

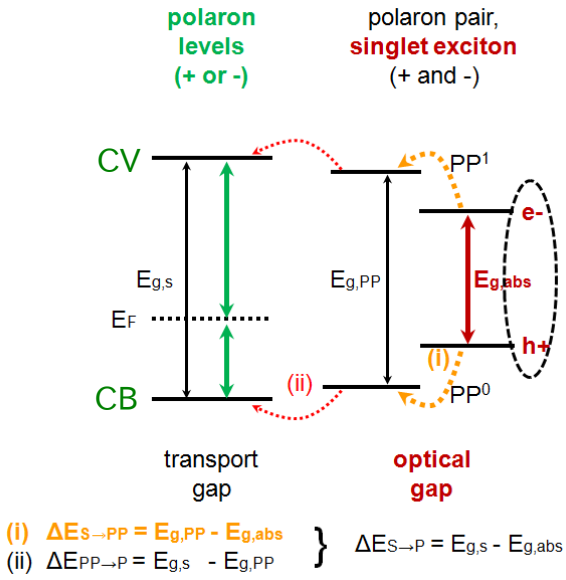

Figure 4.19: Schematic representation of the energy levels in P3HT. S, P, PP stand for singlet exciton, polaron pair and separated polarons, respectively. The following colors indicate the method used to determine the energies: yellow for field dependent PL quenching, green for photoemission spectroscopy and dark red for absorption spectroscopy. Adapted from Deibel et al. 2010 [82].

To explain our findings, we proposed for the exciton's dissociation in pure P3HT a two steps mechanism similar to what is observed in blends.[10]

a) As seen in § 4.2 the absorption of photons having an energy above the absorption gap $E_{g,abs}$ is generating an interchain exciton.

b) If supplied in an energy $\Delta E_{S\rightarrow PP}$ this exciton can dissociate in a polaron pair, in which the two opposite charges have no wavefunction overlap anymore.

[8]This quantum number would be at least 3 for the main vibration mode, according to the decomposition of absorption spectrum shown in figure 4.5

[9]See also theoretical part, § 1.1.1

[10]See theoretical part, § 1.2.2

Energy	[eV]	Methods
$E_{g,abs}$	$1.85 - 1.88$	absorption - EQE
$E_{g,s}$	$2.58 - 2.61$	EQE - PES/IPES
$\Delta E_{S \to PP}$	$\geq 0.42 - 0.46$	field dependent PL
$\Delta E_{PP \to P}$	$\leq 0.24 - 0.28$	calculated
$\Delta E_{S \to P}$	≈ 0.7	calculated

Table 4.5: Experimentally determined energy levels of the conjugated polymer P3HT.

Therefore they can not recombine radiatively; for this reason, their formation can be detected by the reduction of the exciton photoluminescence. Another possibility is that transition from this intermediate level to the ground state is optically forbidden. The minimal value for $\Delta E_{S \to PP}$ is found to be 0.42 eV. Although those polarons can not recombine radiatively, they are still bound together and can therefore not participate in the photocurrent, as can be seen by the absence of raise of the EQE when increasing the photon's energy over 2.2-2.4 eV (figure 4.17).

c) To participate in the photocurrent charges must be excited at least until the HOMO+ and LUMO- levels, for holes and electrons, respectively, as determined by photoemission spectroscopy (figure 4.18). Those two levels define a transport gap $E_{g,transport}$ of 2.6 eV. As evidenced by photocurrent measurements, excitons generated with an energy higher than this transport gap have chances to overcome their binding energy and dissociate into free charges which can subsequently be extracted of the device. From there we can conclude that the total binding energy of the exciton is 0.7 eV and the upper limit for the binding energy of the polaron pair is 0.28 eV. The determined energy levels are summarized in figure 4.19 and table 4.5.

4.6 Discussion

4.6.1 Total binding energy

Why such high binding energy?

With a value of 0.7 eV, the total binding energy found for P3HT is much higher than this found by Krause et al. in 2008 by the same method (comparing photoemission spectroscopy and the absorption onset) in evaporated small organic molecules [117]. This can be attributed to the absence of long range order in solution-processed films in comparison with evaporated ones which limits the possibility of large radius excitons, especially in the interchain direction, thus increasing the binding energy. As a matter of fact, perfectly crystalline conjugated polymers such as the polydiacetylene synthesized by Yee and Chance have been found to exhibit a binding energy of 0.4 eV [11] closer to the one of organic semiconductors based on small molecules [194].

Additionally theoretical work by Kirova and Brazovskii predicts larger binding energy for interchain excitons as compared to intrachain ones due to the absence of an intramonomer repulsion in interchain excitons which is reducing the binding energy of intrachain excitons (see theoretical part 1.1.3) [28].

[11] Determined from the difference between the onsets of absorption and photoconductivity.

The 0.7 eV determined are actually rather close to the theoretical value of 0.6 eV found by van der Horst et al. from density functional theory calculation on polythiophene [195]. Using electroabsorption measurements, Liess et al. also estimated 0.6 eV as a lower value for binding energy in poly(3-octylthiophene) films [196]. Nevertheless those two studies did not involve regioregular polythiophene, as a result it is not unexpected to find a slightly higher energy in our case.

Comparison with the P1/P2 polaronic transitions as detected by photoinduced absorption

As we will see in the next chapter (§ 5.2), the photoinduced absorption spectra of P3HT polarons is characterized by two absorption peaks P_1 and P_2, which are traditionally associated to the two sub-bandgap transitions shown on figure 4.20 which are known to verify $E_g = P_2 + 2P_1$,[12] where E_g is the optical bandgap of the polymer [140]. In the light of our energy model, it could seem contradictory that polarons have transitions over the optical gap, and not over the polaron gap that we have determined. However, it is not. Indeed, whereas the P_1 transition of a positive polaron corresponds to a hole going deeper in the HOMO band, the P_2 transition in contrast, corresponds to an electron passing from the polaronic HOMO level (actually SOMO as it was "single occupied") to the polaronic LUMO level, and thus to the formation of an electron-hole pair, or more correctly: an exciton. As such it it expected that this transition is lowered of E_b compared to the transport gap, which make it correspond to the optical gap lowered of the polaron relaxation energy ($\approx P_1$) if we consider that the exciton binding energy is the same in a charged polymer as in the neutral polymer.

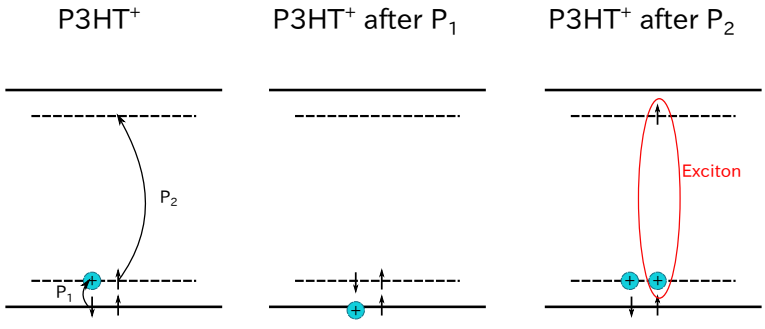

Figure 4.20: Formation of an exciton in $P3HT^+$ polaron by P_2 absorption.

Nevertheless the fact that the exciton binding energy would be the same in neutral polymer chain and in the charged one is surprising, as for example in the case of a positive polaron, the electron constitutive of the exciton is feeling the attraction from two holes. Possibly this additional coulombic attraction energy is then compensated by the repulsion between the two holes.

[12] E_g 1.85 eV, P_2 ≈1.25 eV, P_2 ≈0.3 eV

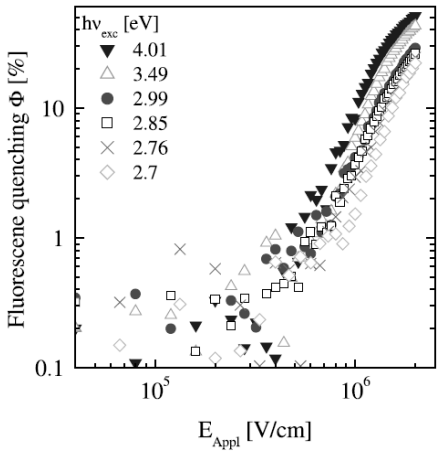

Figure 4.21: Field induced photoluminescence quenching of ladder-type poly(paraphenylene) (MeLPPP) for different excitation wavelengths. Source: Hertel et al. 2002 [185].

4.6.2 Field induced PL quenching

In contrast to absorption and photoemission spectroscopies, where the initial and final states are clearly identified in a relatively stable system, field dependent photoluminescence quenching addresses the composition of the system in a dynamic configuration: namely just after excitation. In the following, we will try to clarify the nature of the species present before and after field-induced dissociation as well as the possible mechanisms leading to the formation of the latter and quenching of the former. We will finally discuss the relevance of using PL to monitor exciton quenching in P3HT where radiative recombination is known for concerning less than 1% of the excitons [32, 191].

Initial state: "hot" or "relaxed" excitons?

To explain that the exciton binding energy extracted from F-PL quenching is lower than the one obtained by PES, we invoke that the final state in F-PL quenching is a still coulombically bound polaron pair, whereas the final state in PES is an unbound polaron. Why should the difference not be in the initial state? Indeed, the photon energy of the exciting laser used for F-PL quenching is much higher than the absorption onset. Actually, when adding the F-PL binding energy (at least 0.42 eV) to the photon's energy (2.32 eV), one finds an energy of 2.74 eV which is rather close to the transport gap as determined from PES.

Nevertheless, the comparison can not be done so easily. Indeed, as mentioned by Clarke and Durrant [36], dissociation of hot excitons would be in competition not with their recombination but with their relaxation which is much quicker (in the order of 10^{-15} to 10^{-13} s). This means that much higher fields would be necessary to overcome the binding energy within such a short lifetime (see for example figure 4.12). Reciprocally, for this dissociation to occur at the observed fields, the binding energy would need to be extremely small (and thus

not comparable with this obtained by PES anymore). Moreover, even in the case of a very small binding energy, the dissociation efficiency would be at best in the range of 50 %. Indeed, dissociation requires the hopping of one charge to a neighbor molecule, thus its rate can not excess the hopping rate which is typically in the range of 10^{13} s^{-1} [188]. Although this limitation of the maximal quenching is not incompatible with the results we obtained with P3HT, results obtained for other polymers speak against this hypothesis, with for example a quenching reaching 80 % in MDMO-PPV.

For a definitive answer about the possible dissociation of "hot" excitons, it would be interesting to compare dissociation of excitons of different "hotness", which is to say generated from photons of different energies. This was done by Hertel et al. on methyl-substituted ladder-type poly(para-phenylene) (MeLPPP) by varying the excitation energy over 1.3 eV [185]. The result is displayed in figure 4.21. An increase of the dissociation efficiency with the excitation energy is indeed seen. However, the observed change is rather small and would correspond to a change of binding energy of only few tens of meV which is within the range of precision we can reach when determining the binding energy. As a result one can conclude that the "hotness" of the generated exciton plays a role which is not precisely understood, but that it is on the order of a correction rather than the main mechanism.

Nature of the final state

The nature of the state formed upon field-induced dissociation is also a non trivial question. In contrast to blends, where the existence of a stable CT-state is rather well established [36], it is a priori unsure whether a relatively stable state results from the field-induced exciton dissociation in pure material. One could for example imagine that the distance between the exciton electron and hole is continuously increasing with the applied field, thus lowering the overlap of the two wavefunctions and with it the photoluminescence yield. Nevertheless the absence of distortion of the PL spectra under field (see figure 4.8) speaks in favor of a discrete transition between two species, one emitting and the other not.

The examination of the higher excited states of regio regular polythiophenes also reinforces this hypothesis: Two photon absorption spectroscopy measurements by Sakurai et al. indeed enable to detect the presence of the second excited state of regioregular poly(3-octyl)thiophene [24]. The A_g symmetry of this state impedes direct electronic transition from or to the ground state, which implies that it can neither participate to one photon absorption nor in photoluminescence. Moreover, the onset of its absorption is starting around 0.35 eV above the onset of one photon absorption[13] which corresponds rather well to the binding energy we measured.

One question remains though: why should an applied field promote the formation of this state. The answer is this time brought by the theoretical work from Van der Horst et al. who calculated the electron-hole probability of radius in those two excitons [197]. It reveals that the ^1A_g exciton exhibits a much more pronounced charge transfer character than this of the ^1B_u exciton, thus explaining its field induced formation.

[13] attributed to a transition from the ground state to the first excited state which is of B_u symmetry.

Dissociation mechanism: discussion of the fitting models

The comparison of the experimental results with the models for Onsager-Braun for ion pair (figure 4.12(right)) and Wannier excitons (figure 4.15) dissociation show that the two models seem to render very well the experimentally observed behavior. The slight mismatch observed at lower fields might be understood under the reasonable assumption of a distribution of binding energies due to the disorder inherent to those materials (an energetic disorder of $\sigma = 72$ meV was measured from the absorption spectrum of this material, see table 4.2). A constant shift due to the built-in voltage in the device could also cause such a distortion, but this hypothesis does not resist quantitative evaluation as it would correspond to a built-in voltage of approximately 10 V.

The fact that both versions of the Onsager Braun model give an identical value for the binding energy is a good indication that the excitons of P3HT indeed have a rather strong charge transfer character. As the dissociation rate exhibits different temperature dependences in the two versions of the model (see equations (1.27) and (1.29)), it would be quite interesting to study the influence of temperature on the field induced PL quenching. Nevertheless, if the experiment is feasible, the modeling remains at the moment critical due to the lack of information concerning the variation of the parameters with temperature, as especially the behavior of the excitons lifetime τ_f is not precisely known.

Despite their good agreement with the experimental observation, criticism can be formulated against the models from Onsager and Braun. Braun mentioned already in his original paper that a more accurate analysis should take into account a distribution of exciton radii (or binding energies) [80], which was implemented by Mihailetchi et al. [93]. Nevertheless, such an analysis requires to add a distribution of exciton radii whose shape is quite difficult to know experimentally; for this reason, we chose to remain on the original model which presents the advantage of containing only experimentally accessible parameters, to the cost of a less good fitting and a resulting binding energy which is only the average one.

Another critical point concerns the adaptation of the Onsager-Braun to neat material exciton dissociation. Indeed, this model was initially developed to model the dissociation of ion pairs into free ions. In that view, it is quite meaningful that the pair reformation coefficient k_r is given by the Langevin prefactor for the recombination of separated charges. The logic is much less obvious in the case of excitons whose "dissociation" — as we have just seen — actually corresponds to a transition to their S_2 (^1A_g) exciton level, which exhibits a much larger charge transfer character. For this reason, different models were tried which do not invoke the Langevin recombination such as the model from Kirova and Brazovskii [28, 81] or Emilianova and Arkhipov [184]. Nevertheless, those two models fail to describe the observed behavior as they both exhibit a too steep raise of the quenching ratio upon raising the electric field. This question is still an open issue, nevertheless, the good agreement between the determined energy and the energy separating the ^1B_u and the more strongly charge separated ^1A_g states in regioregular poly(3-octylthiophene) speaks in favor of the validity of the transposition of the OB model from polaron pairs to excitons. A possible explanation would be that due to the rather large radius of the ^1A_g exciton, the two charges move within this radius and recombine on a way which is similar to free charges but with local mobilities.

Representativeness of photoluminescence in P3HT

There is an open issue concerning how representative of the excitons is photoluminescence in a material in which less than 1 % of the excitons undergo radiative recombination. Piris et al. [191] managed to use transient absorption (TA) to probe excitons lifetime in pure P3HT as well as in blends with PCBM. In pure P3HT, they extracted from this TA, probed at 0.9 eV, an excitons lifetime of 200 ps whereas the time constant of PL was 600 ps. Similarly the exciton quenching by addition of PCBM was different in both cases, which enabled them to extract a diffusion constant one order of magnitude smaller from the transient absorption than from the PL. This speaks in favor of the presence of two kinds of excitons, and it is thus unsure whether those two kind of excitons have the same binding energy.

The problem of the representativeness of photoluminescence could be answered in the future by monitoring via field dependent photoinduced absorption whether or not the PL quenching is correlated to an increase of the polaron density or if the increase of polaron density exhibits a different field dependence. Nevertheless field-dependent photoinduced absorption remains a technically challenging task.

4.7 Conclusion

As a summary, the present study has proven that the field dependence of photoluminescence could be used as a tool to address the exciton binding energy of semiconducting polymers. The expected photoluminescence quenching is indeed observed and models exist that offer a relatively good match to the experimental data and enable to extract the binding energy.

Although it was originally developed to describe the dissociation of ion pairs into free charges, the Onsager-Braun theory has proven to be the most able to render the experimental observation. Evaluation of the experimental results resulted in a binding energy of 0.42 eV. Moreover, the theoretical description of P3HT fluorescent exciton enables to determine the effective mass of this quasiparticle, and thus to apply the variant of the Onsager-Braun theory relevant for Wannier exciton dissociation. This model gave an estimation of the binding energy of 0.42 eV identical to the one obtained with the ion-pair model. This result seems to indicate a rather strong charge-transfer character of the interchain exciton in P3HT.

The comparison of the results of PL-F quenching to energy levels obtained from absorption and photoemission spectroscopiy and confirmed by excitation energy dependent photoconductivity measurements, enables to draw a global picture of the energy levels relevant for photovoltaic applications in regio regular P3HT. As presented in Physical Review B [82], this analysis reveals the presence of a transport gap having an energy 0.7 eV higher than the optical gap. The difference is the total binding energy of the exciton, which is the energy to provide for the dissociation of exciton into free charges. The field-dependent PL quenching in turn reveals the presence of an intermediate excited state presenting a charge transfer character larger than the one of the primary S_1 exciton (of B_u symmetry). By comparison with two photon absorption measurements from Sakurai et al. [24] and theoretical work by van der Horst et al. [197] this

intermediate state was attributed to the S_2 excited level (of A_g symmetry).

However, the exciton binding energy is far from being a closed topic. Technical and theoretical issues such as the incomplete PL quenching and influence of polymer chains orientation relatively to the field, the influence of photon's thermal energy, the representativeness of fluorescing excitons among the P3HT excitons, the temperature dependence of field induced dissociation, are still opened for further investigation. Experiments have been proposed to address those points which are not out of reach.

This work serves as a base for further research on the field dependent photoluminescence which is going on and was since then applied with success to other material systems such as PPV derivatives and their blends with PCBM [72].

Chapter 5

Charges generation and transport

5.1 Introduction

5.1.1 Motivation

While the previous chapter was dedicated to the use of absorption and emission spectroscopy to characterize the primary excitation in P3HT, in this chapter we will demonstrate how the absorption spectroscopy of excited species in photovoltaic blends can be used to monitor the generation of charges and intermediate species upon photoexcitation and thus identify the strengths and weaknesses of new material systems.

As detailed in § 1.2, photocurrent generation in organic solar cells requires to go through a certain number of steps. This complex process leads to the existence of a several bottlenecks. Although those steps seem to be successfully passed in P3HT:PCBM, whose solar cells EQE exceeds 80% [59], it is important to identify potential limitations for the design of new materials (with absorption matching the solar spectrum better, or enabling larger open-circuit voltages) which might not initially exhibit such optimal blend structure and photophysical properties as P3HT and PCBM.

In the frame of the SolarNtype European Research Training Network, I had the opportunity to work on novel electron acceptors that could be an alternative to PCBM. Extensive photophysical studies as well as charge transport, devices and morphological characterizations enabled me to pinpoint a certain number of obstacles that can hinder the photocurrent generation in bulk-heterojunctions solar cells.

This chapter includes a short presentation of a selection of studied molecules. Follows a description of the spectral signatures of the different excited species in P3HT which can be used to determine the fate of photoexcitation via photoinduced absorption spectroscopy. The two last sections present, on some examples, the issues of blend morphology and charge transport in bulk-heterojunction structures, respectively, as well as how PIA and PL spectroscopies can help pinpointing those problems.

5.1.2 Studied molecules

The aim of the SolarNtype European Research Training Network was the design, synthesis and evaluation of electron acceptor materials as alternatives to PCBM. The underlying idea was that in contrast to electron donors, for which a variety of possibilities have been successfully experimented [11,59,156,198,199], only a few efficient alternatives to fullerene derivatives as electron acceptor have been reported. Those alternatives being mainly inorganic —such as ZnO nanocrystals [200]— or polymeric [201], although conjugated molecules such as perylene-3,4:9,10-bis(dicarboximide) have been long known for their good electron accepting properties [202, 203]. Within the SolarNType network, a certain number of molecules were synthesized in partner laboratories, whose structures are presented in figure 5.1.

Rylene derivatives, terrylene-3,4:11,12-bis(dicarboximide) (TDI) and perylene-3,4:9,10-bis(dicarboximide) (PDI), were synthesized in the Max Planck institute for Polymer Research in Mainz following the methods previously presented by Nolde et al. [204]. TDI was studied extensively in blend with P3HT. For comparison purposes we carried out additional investigations on blends of PDI with P3HT as well as blends of TDI with poly[2-methoxy-5-(2-ethylhexyloxy)-p-phenylene vinylene] (MEH-PPV). Both TDI and PDI have electron affinities — related to their lowest unoccupied molecular orbital (LUMO) — of 3.7 eV (determined from cyclic voltammetry presented by Lee et al. [205] using the method presented by Pron et al. [206]), making them potential acceptors for higher energy electrons from P3HT (LUMO = - 3.3 eV). Additionally, TDI has a rather low bandgap which gives it an absorption band between 600 and 800 nm, interestingly complementing the one of P3HT (see figure 5.2).

Phtalocyanines derivatives are well known dye molecules counting for approximately 25% of all artificial organic pigments [207]. In the field of organic

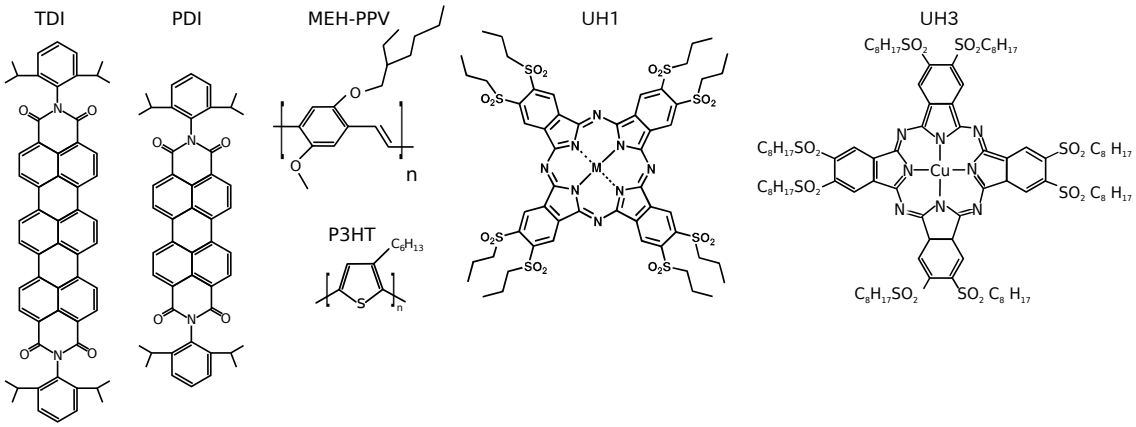

Figure 5.1: Chemical structure of the studied materials: from the left to the right, the two rylene derivative electron acceptors from Max Planck Institute for Polymer Research perylene-3,4:9,10-bis(dicarboximide) (PDI) and terrylene-3,4:11,12-bis(dicarboximide) (TDI), the two reference electron donors poly[2-methoxy-5-(2-ethylhexyloxy)-p-phenylene vinylene] (MEH-PPV) and poly(3-hexylthiophene) (P3HT) and the two sulfonyl-fonctionalized copper phthalocyanine electron acceptors from Universidad Autónoma de Madrid (UH1 and UH3).

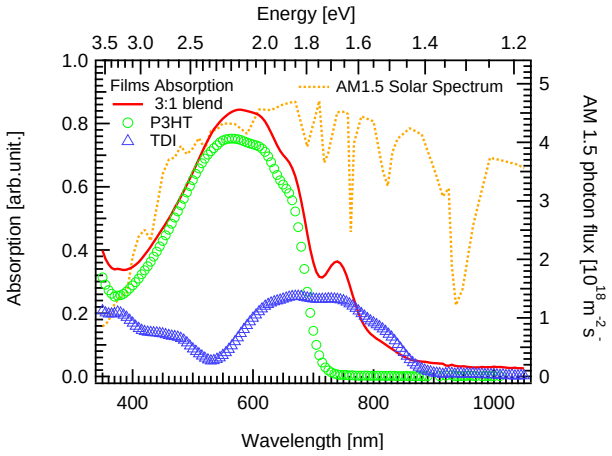

Figure 5.2: Absorption spectra of pristine P3HT thin film (◯), pristine TDI thin film (△) and 3:1 P3HT:TDI blend film (continuous line) together with the AM1.5 solar spectrum (dotted line, right axis).

electronics, metal-phtalocyanines have been use as early as in 1986 as the electron donor of the first bilayer organic solar cell to reach the 1% efficiency [153] and are still regularly used, for solar cells [208, 209], field effect transistor [210], or light emitting diods [211] applications.

In the Universidad Autónoma de Madrid, copper phtalocyanine (CuPC) were functionalized with sulfonyl groups bearing alkyl side chains, which make them soluble and electron acceptor. We were supplied in molecules with alkyl side chains of two different sizes and thus different solubility. UH1 has rather short side chains (3 carbon atoms) and is thus soluble only in small concentrations, whereas UH3 having longer side chains can be more easily dissolved in organic solvents. Both UH1 and UH3 exhibit a very strong absorption band at 700 nm, which is complementary to the one of P3HT.

5.2 Characteristic features of P3HT PIA spectra

We use PIA to monitor the excited species photogenerated in donor–acceptor heterojunctions. As a result, we will first spend some time identifying the characteristic features of the different species.

5.2.1 Features: number of species

Reference spectra Figure 5.3 shows the reference PIA spectra and polar plot of P3HT and P3HT:PCBM 1:1 blends at 30 K. Those spectra are expected to be representative of the absorption of neutral species (pure P3HT) and charged species (blend) of P3HT, respectively. Indeed the contribution of PCBM excited species to photoinduced absorption is usually found to be very weak, and thus negligible if occurring in the same region as the absorption of the excited species

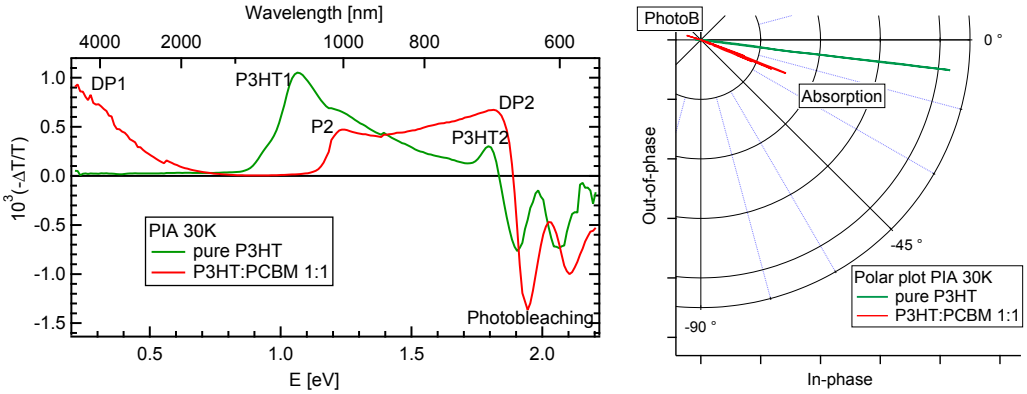

Figure 5.3: PIA spectra and polar plot of films of pure P3HT (green) and P3HT:PCBM (red) at 30 K (P3HT P200). Note: for the polar plot, the in-phase and out-of-phase signals are used without normalization to the samples transmission (see equation (2.13)) in order not to overweight the spectral regions where the signal is weak.

of P3HT. This is indeed the case as PCBM anions absorption have been found to occur around 1.2 eV [109, p. 56] and this of PCBM triplets around 1.7 eV [212].

The absorption from excited species in pure P3HT is characterized by one broad main absorption peak, labeled *P3HT1* on figure 5.3 and taking its maximal value at approximately 1.05 eV, as well as a thin secondary peak centered 1.8 eV and labeled *P3HT2* on figure 5.3. In the P3HT:PCBM blend spectrum, three peaks are to be recognized: a broad peak at low energy labeled *DP1*, and two partly superposing peaks labeled *P2* and *DP2* whose maxima occur at 1.25 and 1.85 eV, respectively.

One can notice that the onset of the photobleaching occurs at higher energies in the blend than in pure P3HT, which could at a first sight be surprising knowing that the onset of absorption occurs at the same energy in those two systems. An other striking difference is the phase of the PIA signal: if this one is relatively stable over one spectrum (just being shifted by 180° in photobleaching as compared with absorption), it is much smaller in the pure P3HT case, thus indicating a shorter lifetime of the species (see § 2.1.5).

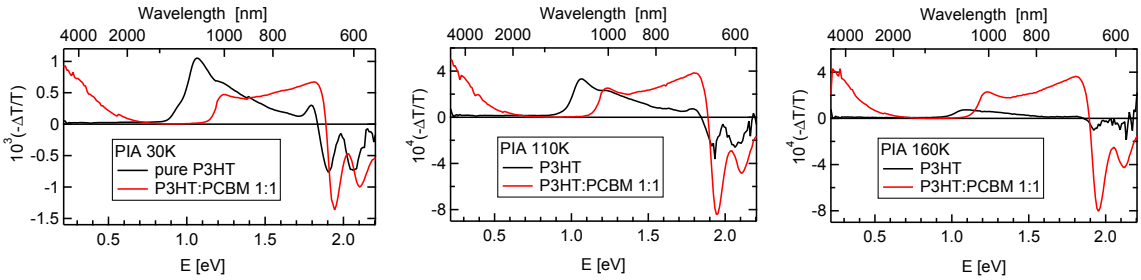

Figure 5.4: Temperature dependence of the PIA spectra of P3HT and P3HT:PCBM 1:1 (P3HT P200).

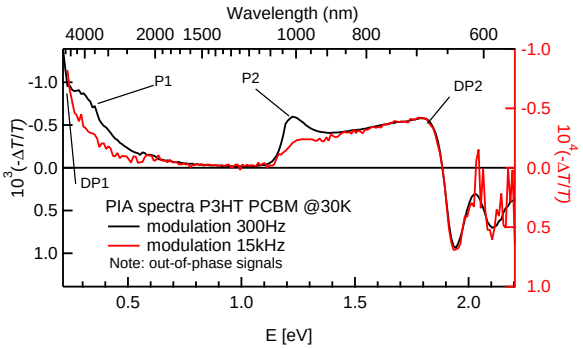

Figure 5.5: Comparison of the *P1, P2* and *DP1, DP2* peaks of the photoinduced absorption spectra of a P3HT:PCBM 1:1 upon changing the modulation-frequencies (P3HT P200). Note: in contrast to the usual PIA spectra (see equation (2.13), those spectra were constructed from the out-of-phase signal, indeed when the species lifetime is comparable to the modulation period, as it is the case at f =15 kHz, the signal is nearly entirely out-of-phase (see figure 2.6).

Dependences and distinction of the different features Additionally to their different phase, excited species in pure P3HT and in P3HT:PCBM can also be distinguished by the temperature dependence of their absorption (Figure 5.4). If both spectra lose in intensity when increasing the temperature, the PIA of pure P3HT vanishes already at lower temperatures than this of the blend which remains detectable up to room temperature. This is consistent with the expected shorter lifetime of the species observed in pure P3HT that was already indicated by the smaller phaseshift of their photoinduced absorption.

PIA spectra also enables to distinguish different excited species within the blend. Figure 5.5 show the PIA spectra of a P3HT:PCBM 1:1 blend under two different modulation frequencies. As expected the PIA signal is much lower under high frequency modulation, but one can see that the $P2$ peak is much more quenched, until nearly disappearing, by an increase of the modulation frequency, which is not the case of the $DP2$ peak. Moreover one can see that the low energy peak actually contains two components, the lowest energy — labeled $DP1$ in figure 5.5 — is quenched like $DP2$, whereas the one with a bit higher energy — labeled $P1$ in figure 5.5 — is nearly totally quenched, similarly to $P2$.

A number of studies have shown that $P1$ and $P2$ always exist together[1] and exhibit the same dependence upon external stimuli (variation of the excitation modulation frequency [140], of the excitation intensity [140], of the temperature [140], isolation of the chains in an inert polystyrene matrix [140]); moreover photoinduced absorption detected magnetic resonance (PADMR) studies showed that they share the same resonance g factor slightly different of this found for $DP1$ and $DP2$ [140]. $P1$ and $P2$ are thus considered as two absorption features originating from the same excited species. Similarly $DP1$ and $DP2$ are found to be due to a unique excited species, distinct of the one causing the $P1$ and $P2$ PIA bands [140, 179].

[1] Not only under photoexcitation, but also under I^- doping [140]

Presence of the blends features in pure P3HT Examination of the low energy regions of the PIA spectra of pure P3HT reveals that the $P1$ and $DP1$ peaks also exist in the pure material. Moreover, one can see in figure 5.6 that this low energy photoinduced absorption in pure P3HT has the same phaseshift as the phaseshift of the PIA in the blend, which is quite different from the phaseshift of the other features of pure P3HT PIA spectrum. This indicates that the excited species responsible for the $P1$ and $DP1$ absorption are also formed in the pure material, with a very weak efficiency though.

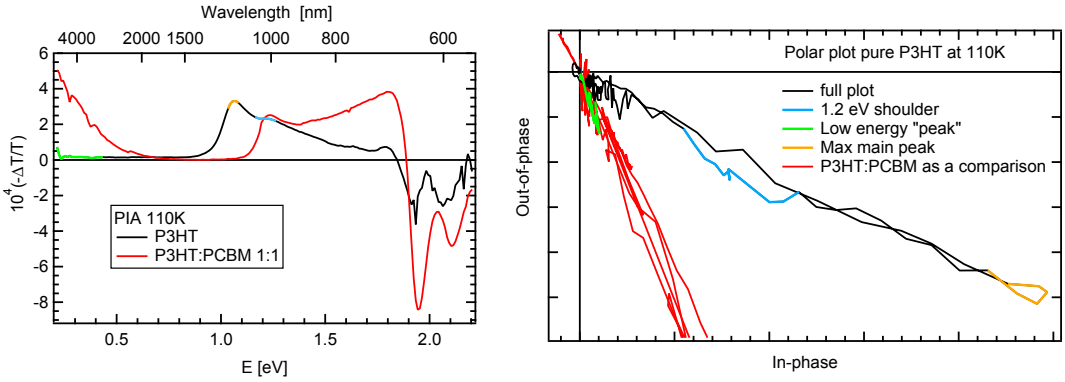

Figure 5.6: Phase of the different features of the PIA spectra of pure P3HT compared to the phase of the P3HT:PCBM 1:1 blend (P3HT P200).

5.2.2 Identification of the species

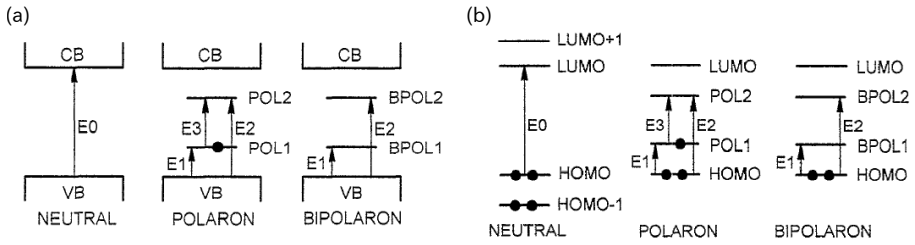

Figure 5.7: Electronic transitions associated with the $P1$ and $P2$ absorptions. (a) One electron band model of charged conjugated polymers and olygomers. Source: Maud 1999 [213]. (b) Molecular orbital description of neutral and charged oligomers. Source: Maud 1999 [213].

Blends: charged species. A variety of measurement enables to undoubtedly attribute the $P1/P2$ and $DP1/DP2$ absorption bands to polarons in P3HT. Indeed $P1$ and $P2$ are also obtained upon doping with I^- or $FeCl_4^-$ instead of photoexcitation [24, 140] and the $DP1$ and $DP2$ have been detected on FET structures in the accumulation regime using charge modulation spectroscopy[2] [214, 215]. Moreover those two pairs of bands where found to be associated to a spin 1/2 using photoinduced absorption detected magnetic resonance [32].

[2]Modulation of the gate voltage.

The $P1$ and $P2$ absorptions correspond well to the intragap transition characteristics for the polarons of conjugated polymers as initially predicted by Fesser et al. [216] from a one electron band model in polyacetylene and since then observed in virtually every conjugated polymers. This model predicts that

> "removal of an electron from the top of the valence band (VB) results in the formation of a radical cation (polaron) which is characterised by the appearance of two new levels inside the band gap. The lower level, $POL1$ [see figure 5.7(a)], is occupied by one electron and three electronic transitions, $E1$, $E2$ and $E3$, lower in energy than that of the neutral [molecule] are predicted." [213]

Note that this scheme is consistently predicted by both solid state physics one electron band model and quantum chemistry molecular orbital approaches (see figure 5.7(b)). In the case of oligothiophenes:

> "the transition $E2$, involving promotion of an electron from the HOMO to $POL2$ ($BPOL2$) involves levels of identical symmetry. [...] Such transitions are expected to have only a very small oscillator strength or they are strictly forbidden." [213]

As a result the observed transitions $P1$ and $P2$ are associated to the predicted ones $E1$ and $E3$, respectively. Note that the transition $E0$ that is responsible for the onset of ground state absorption is still possible in the polarons. This might partly explain why the photobleaching starts at higher energies in P3HT:PCBM than in pure P3HT (see figure 5.3).[3] Note also that in this model, $P1$ is directly related to the polaron relaxation energy E_r [32].

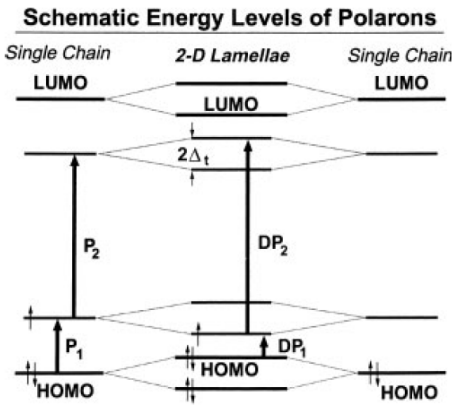

Figure 5.8: Model for the gap energy levels and related allowed optical transitions of intrachain polarons and delocalized polaron excitations. $2\Delta_t$ is the DP level splitting and the relation $E(DP_1) + E(DP_2) = E(P_1) + E(P_2)$ holds. Source: Jiang et al. 2002 [32].

Important differences between the $P1/P2$ peaks and the $DP1/DP2$ are that the latter are absent in solution [214], not or weakly detected in doping

[3] Another explanation is that the actual onset of photobleaching in the blend is hidden by the upper energy tail of the DP2 peak, indeed PADMR spectra (reproduced on figure 5.9(a)) shows that the DP2 peak extends over the onset of the photobleaching [32].

induced absorption[4] [24,140], quenched by embedding the polythiophene chains in an inactive polystyrene matrix [140], that the $DP1$ peak position is very sensitive to the polymer chains environment (solvent used, alkyl-chain length in P3ATs, hydrostatic pressure) [32, 140] and that they do not exist in regio-random P3HT[5] [32, 140]. For these reasons they are attributed to interchain delocalized polarons.

Figure 5.8 shows the formation of the DP1/DP2 levels by hybridization of the energy levels of two neighbor polymer chains. This is the same principle as the exciton dimerization presented in the theoretical part (§ 1.1.3). This readily explains the observed dependence of the $DP1$ peak position upon stacking conditions [32,140]: by decreasing the stacking distance (decrease of the alkyl-chain length in P3ATs, use of higher boiling point solvent, high hydrostatic pressure) the interchain interaction β is increased and thus the dimer splitting (labeled Δ_t in figure 5.8), which in turns shifts $DP1$ to lower energies.

Pure P3HT: neutral species. Regarding now the pristine material, in contrast to the PIA features of the blend, the peaks observed in pure P3HT are much less clearly identified. The distinction between the two peaks $P3HT1$ and $P3HT2$ (see figure 5.3) itself is unsure. Indeed, the region of weaker photoinduced absorption at approximately 1.7 eV corresponds quite well to P3HT's photoluminescence (see figure 4.3). As such, it could be that this *hole* in the absorption spectrum is actually due to the opposite contribution of stimulated emission. Although the early studies by Jiang et al. [32] claimed that no stimulated emission could be detected in pure regioregular P3HT, this was contradicted by most of the recent ultrafast spectroscopy studies [99, 164, 191] the latest of which even observed stimulated emission in P3HT:PCBM blends at very early times [99,191]. This implies that the $P3HT2$ peak might actually be a tail of the $P3HT1$ peak, just separated by a region where stimulated emission is compensating the photo-induced absorption.

The nature of the $P3HT1$ peak is also an ongoing debate. In most of the conjugated polymers, including regio-random P3HT [32,140], the main distinctive feature or pure polymer is a broad triplet peak. If the early studies from Valdeny et al. [32,140] claimed that this was not the case in regioregular P3HT, some of their arguments have since then been contradicted.

The theoretical argument was that the very planar organization of regioregular P3HT films was detrimental to triplet formation. Nevertheless as we saw before (§ 3.1.2), an important fraction of the regioregular P3HT films is constituted of amorphous regions where the planar configuration of the polymer chains is not the rule. Moreover it is usually considered [23] that sulfur atoms are heavy enough so that nuclear–electron spin coupling enhances inter-system crossing.

The main experimental argument was for Jiang et al. [32] the non-detection of species having a spin 1:

> "Using PADMR at $H_{1/2}$ that corresponds to g=5.1 of triplet species, long live spin 1 excitation *have not* been found in RR-P3HT films." [32]

As a matter of fact, Sakurai et al. indeed observed triplet emission in regioregular

[4] Large interstitial ions may actually isolate the polymer chains from each other [140].
[5] In regiorandom P3HT, the random organization of the side chains prevents π-stacking.

poly(3-octylthiophene) only when breaking the ordering by embedding the conjugated polymer in a polyethylane matrix [24], or by electroluminescence. However, spin 1 species have since then been clearly observed in regioregular P3HT films using photoluminescence detected magnetic resonance (PLDMR) [217].

The arguments that remain in favor of the non-triplet nature of the excited species causing the $P3HT1$ PIA peak is its dynamics: indeed this peak is known for being associated to relatively short living species (the peak extinguishes within microsecunds to tens of microseconds even at temperatures so low as a few tens of kelvins) which do not decay monomolecularly and exhibit a sublinear dependence upon light excitation intensity [32]. This is in contrast with the triplet peak observed by Jiang et al. in regiorandom P3HT [32], or to the one observed in regioregular poly(3-ocrylthiophene) by Sakurai et al. which exhibited a lifetime of 30 ms at 77 K, although its spectral shape and position was exactely the same as this observed in regioregular P3HT [24].[6] An other argument used by Ohkita et al. [54,57] is that the dynamics of this peak remains unchanged when measured under O_2 atmosphere, which strongly contrast with triplet peaks, such as these observed in the polythiophenes that do not present any interchain organization (including regio-random P3HT) [54, 57].

As a result, some publications describe this peak as being due to triplets [177, Supporting informations] [24,218] whereas others consider it as due to interchain singlet excitons [32, 140] or coulombically bound polaron pairs [54, 57] (which could also include some pairs with spin 1, as the ones detected by Sperlich et al. using PLDMR [217]).

More generally accepted is the interchain character of the excited species causing the $P3HT1$ PIA peak. Indeed groups in favor of the singlet nature of the excited species noticed that this peak is disappearing upon embedding the polymer chain in a polystyrene matrix [140], while groups in favor of its triplet nature claim that the position of the peak, quite red-shifted compared to the peak observed in solution, is due to an agglomeration effect similar to the one observed for the ground states absorption [177, Supporting information] (see also § 4.2). Also clear is the neutral character of this excited species as it was never observed upon doping [24,140], charge modulation [214,215] and that PADMR studies could not associate it with a spin 1/2 [32, 140, 219]. In this thesis we thus will limit ourself to define it as a neutral excited species.

5.2.3 Comparision of P3HT P200 and P3HT 4002E

Figure 5.9 shows the differences between the PIA spectra of P3HT 4002E and P200 as well as the *historical* P3HT used by Valdeny et al. [32,140] to identify the spectroscopic features associated with the polymer's excited species. The most striking difference is the clear presence of the polaron peaks in the *historical* spectrum which is not clearly present in the two modern materials. The formation of polarons in *historical* P3HT could be due to the bigger amount of impurities remaining from the synthesis, as these impurities could act as dissociation centers on the excitons. The synthesis of P3HT having improved in the ten years following those early studies, modern spectra exhibit only a shoulder at the position of the $P2$ polaron peak. By comparing the spectra of P3HT 4002E and P3HT P200, one can notice that the shoulder associated with the

[6] Nevertheless it could be that Sakurai et al. observed only the long-lived tail of the decay.

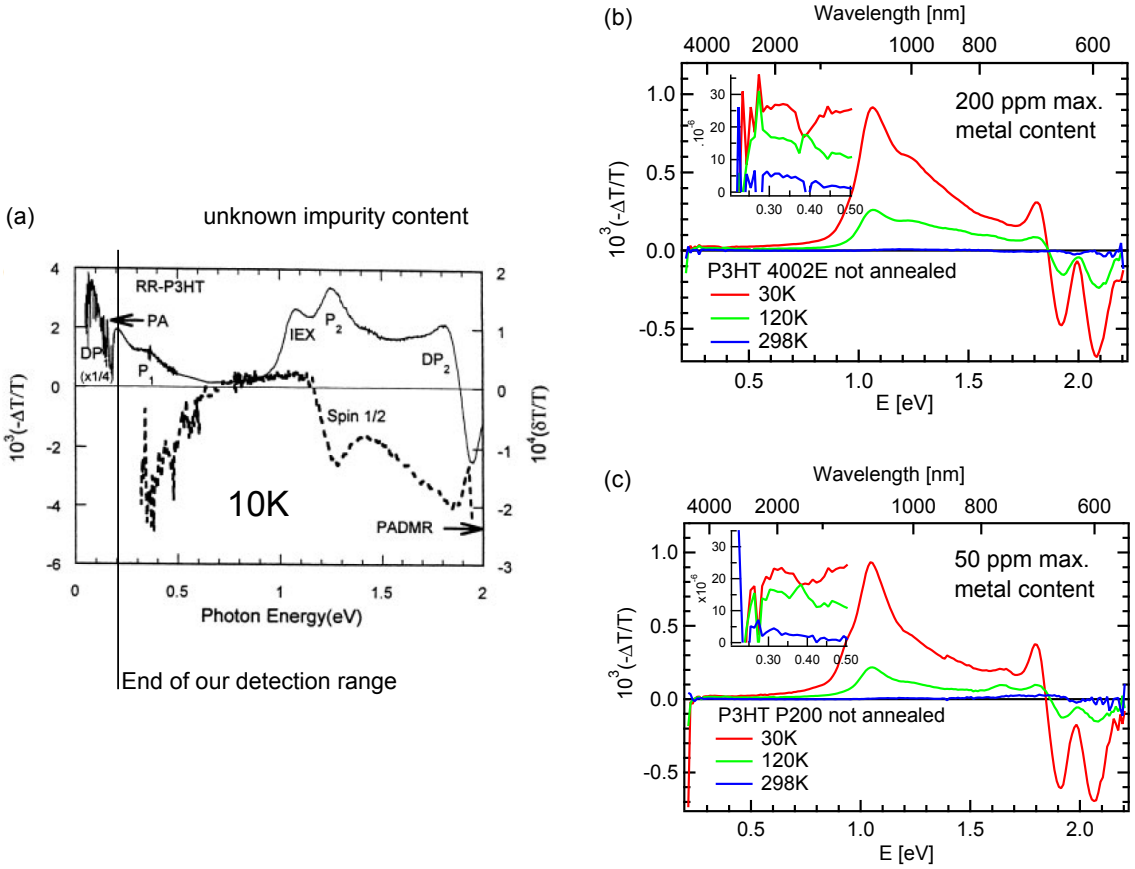

Figure 5.9: Comparison of the PIA spectrum of the historical P3HT used by Valdeny et al. [32,140,219] with the spectra of modern P3HT P200 and 4002E used in this thesis. (a) PIA and PADMR spectra of historical P3HT at T = 10 K. Source: Korovyanko et al. [219]. (b) and (c) PIA spectra at different temperatures of P3HT 4002E and P200, respectively. The insets represent the low energy features on a different scale.

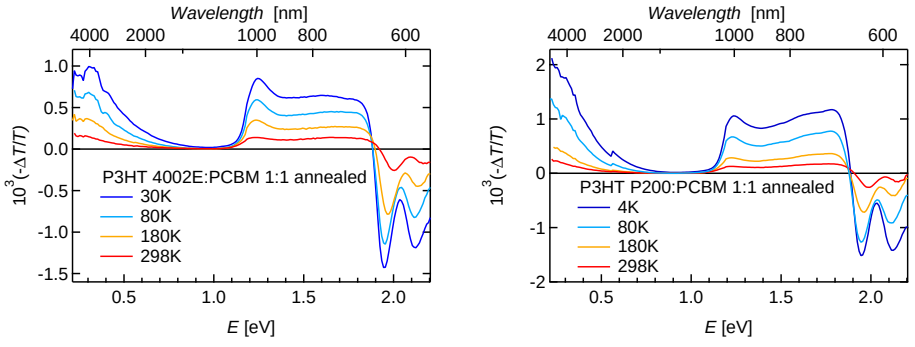

Figure 5.10: Comparison of the PIA spectra of the P3HT:PCBM 1:1 annealed blend based on P3HT 4002E and P3HT P200.

$P2$ polaron peak at 1.25 eV is more clear in the 4002E, which once again corresponds rather well to the larger concentration of impurities present in P3HT 4002E as compared to P3HT P200 (200 ppm in 4002E compared to 50 ppm in P200, see § 3.1.4).

Figure 5.10 shows the spectra of P3HT:PCBM 1:1 annealed blend with P3HT 4002E and P3HT P200. As expected from the stronger regioregularity of the P3HT P200, supposed to result in a better crystalline structure, the absorption attributed to delocalized polarons ($DP1$ and $DP2$) is much larger in the P200:PCBM blend than in the 4002E:PCBM blend.

5.3 Application to photoactive material systems characterization: phase separation in P3HT:CuPC blends

In bulk-heterojunction solar cells, the blend structure depends on the self organization properties of the two components. This structure should ensure close intermixing of the phases so that an heterojunction interface is always within reach of the primarily photogenerated excitons, which have a limited diffusion length. On the other hand it is necessary that a percolated pathway exist from any point in the acceptor phase to the cathode and from any point in the donor phase to the anode so that the charges can be extracted from the device. Depending on the processing condition and the affinity of the two components for each other, several situations can occur as represented in figure 5.11. In this section we will present those question based on the example of the molecules UH1 and UH3 (see figure 5.1) synthesized in the Universidad Autónoma de Madrid.

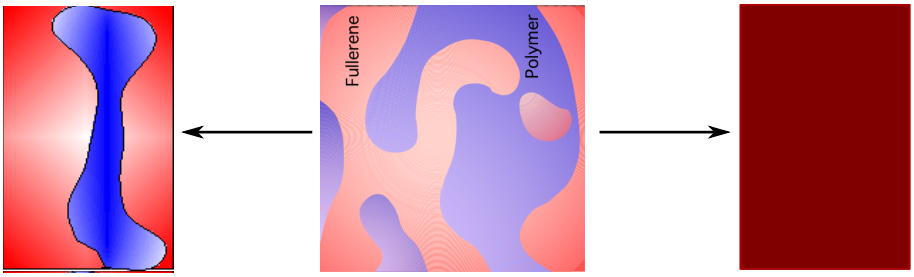

Figure 5.11: Possible blend morphologies. Left: Total demixion of the two components: all generated charge carrier will reach their electrode but most of excitons will not dissociate because no interface within diffusion range. Center: Ideal situation: excitons can reach an interface, and separated charges can diffuse to the electrodes (adapted from Deibel et al. 2010 [59]). Left: No demixion, all excitons will be dissociated but charges have very little chances to find a pathway to an electrode.

5.3.1 Excessive phase separation: problem of excitation harvesting

Due to its low solubility, UH1 is expected to quickly agglomerated when deposited on a sample. This leads to the formation of phases of big dimensions as

seen by scanning electron microscopy (SEM) (figure 5.12) with a phase size in the shortest direction of approximately 230 nm, which is largely exceeding the exciton's diffusion length in organic materials which is in the order of 10 nm.

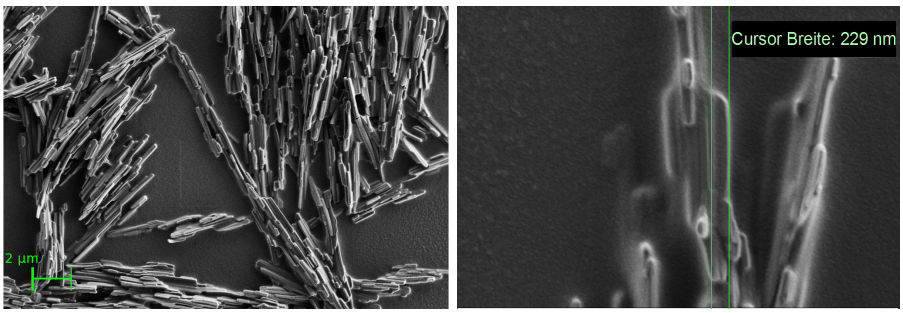

Figure 5.12: SEM pictures of a P3HT:UH1 blend.

The consequence of this excessive phase separation is that the excitons generated by light absorption have little chances to reach an interface and thus to be dissociated. As a result, most of them will recombine giving a photoluminescence nearly as intense in the blend as in neat P3HT, as shown in figure 5.13 (left). Similarly the PIA spectrum at low temperature (figure 5.13 (right)) is clearly dominated by the absorption of excited species typical of pure P3HT, although a weak polaron absorption peak can also be seen at low energies. Note: the negative peak at 1.65 eV corresponds to CuPC absorption and can thus be attributed to photobleaching.

The influence of processing conditions on solar cell performances is in agreement with previous observations. Indeed the use of solvents with a low boiling temperature such as chloroform enables to obtain better solar cells performances than solvents with higher boiling points such as chlorobenzene (figure 5.14 (b)). Low boiling temperature solvents evaporated quickly after deposition, the blend is thus expected to be "frozen" in an intermediate morphology before reaching full phase separation. Similarly, annealing has a negative impact on solar cells performances as it is expected to enable the molecules to reorganize further and thus to form bigger phases (figure 5.14 (a)). Processing optimization enables to strongly enhance the solar cells performances. However, those performances remain too low for application.

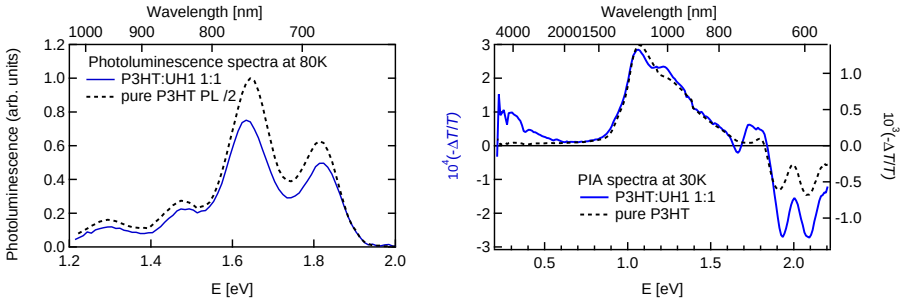

Figure 5.13: PL and PIA spectra of a P3HT:UH1 1:1 blend (continuous line) as well as neat P3HT (dashed line) shown for comparison.

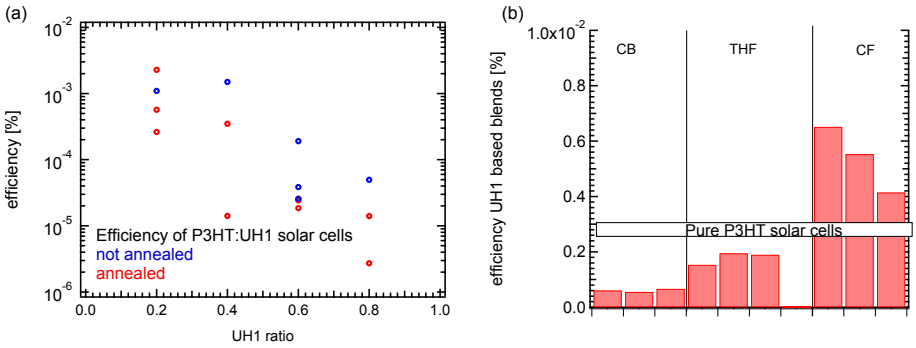

Figure 5.14: P3HT:UH1 solar cells. (a) Efficiency of the processed solar cells as function of the acceptor ratio and annealing (150°C, 60 minutes). Each point represents one cell. (b) Efficiency of solar cells based on P3HT:UH1 films processed from different solvents. Each bar represent a solar cell. CB stands for chlorobenzene (boiling point 132°C), CF for chloroform (boiling point 62°C) and THF for tetrahydrofurane (boiling point 66°C).

5.3.2 Insufficient phase separation: problem of charge transport.

On the opposite, the blend of P3HT with UH3 exhibits a perfect quenching of P3HT's photoluminescence (figure 5.15 (a)), and this even with a lower content of UH3 (P3HT:UH3 4:1 weight ratio). This quenching is even superior to what is usually seen for example in P3HT:PCBM, the reference blend. This tends to indicate the formation of very small phases, or possibly even the absence of separation of the two components of the blend. The PIA results confirm excitons quenching as the 1.05 eV peak due to the absorption of pure P3HT excitons (triplets or delocalised excitons) is completely quenched (figure 5.15 (b)). More generally the PIA spectrum of this blend is quite typical of polarons in P3HT as they can be seen for example in P3HT:PCBM blend (see figure 5.15 (c)) with the two additional features of CuPC: the photobleaching at 1.65 eV and the peak at 1.75 eV.

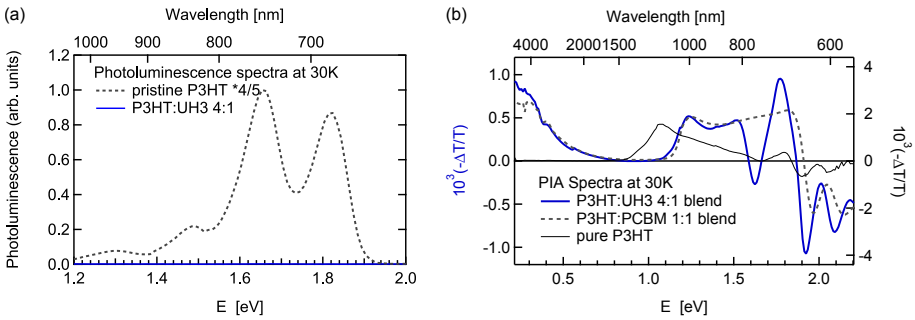

Figure 5.15: PL (a) and PIA (b) spectra of a P3HT:UH3 4:1 blend (continuous line) as well as neat P3HT and P3T:PCBM (b) for comparison.

However, solar cells based on the P3HT:UH3 blend also exhibit efficiencies limited to the order of 10^{-3} %. The efficiency of the PL quenching pinpoints

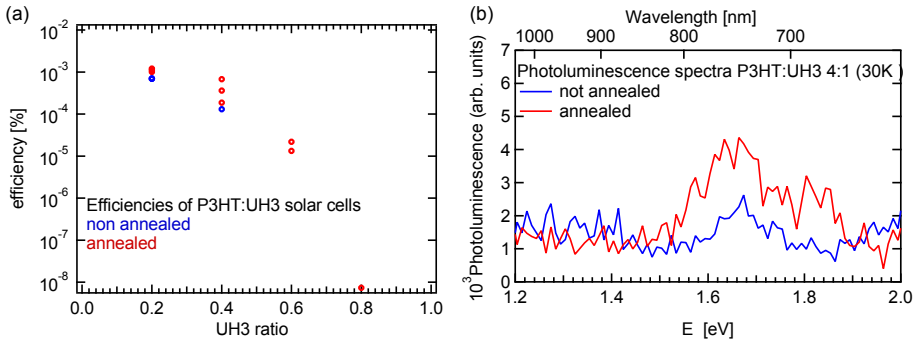

Figure 5.16: P3HT:UH3 solar cells. (a) Efficiency of the processed solar cells as function of the acceptor ratio and annealing (150°C, 60 minutes). Each point represents one cell. (b) Photoluminescence spectra of unannealed and annealed films of P3HT:UH3 blend.

a lack or a too small of phase separation, which allows for a perfect excitons quenching but hinders the percolation and thus the existence of continuous pathway for charges to the electrodes. Those charges are thus lost to recombination. The variations of the solar cells performances upon varying the processing conditions is in agreement with this hypothesis. In contrast to what happens with UH1 based solar cells, no positive effect can be seen when using a solvent with lower boiling point. Moreover, annealing enhances the performances, while slightly decreasing the photoluminescence quenching (figure 5.16) which indicates the formation of small domains of pure P3HT. However, the photoluminescence remains much lower than in P3HT:PCBM blends, it is thus likely that the domains size still does not enable percolation. Finally the best solar cells are obtained for rather thin layers (around 70 nm which contrasts with the optimal thickness around 200 nm for P3HT:PCBM solar cells) which is consistent with the hypothesis of a percolation problem.

5.4 Charge transport and extraction: the case of TDI

Among the two materials provided by the Max Planck Institute for Polymer Research in Mainz, we chose to focus our study on TDI which was more promising due to the complementarity of its absorption spectrum with this of P3HT, and to use PDI mainly for comparison. In contrast with TDI, PDI has a larger band gap and its main absorption peak is located between 530 and 535 nm [204] which is in the same spectral region as P3HT. We expect both PDI and TDI to have the same ability to attract the electrons from associated polymer, because they have the same LUMO level. Films were deposited from chloroform solutions, various blend ratios were tested, weight ratio for P3HT:TDI between 3:1 and 4:1 appeared to give the best results regarding photoluminescence quenching and PIA signal intensity as well as solar cells efficiency. The absorption spectrum of a 3:1 blend is shown in figure 5.2; it corresponds to the superposition of the pristine materials absorptions. All the results reproduced in this section have been reported by us in the peer reviewed journal Synthetic Metals in 2012 [220].

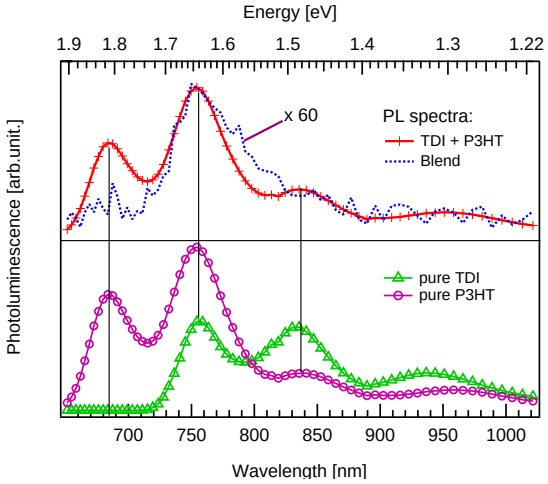

Figure 5.17: Sum of photoluminescences of P3HT and TDI in a 4:1 ratio (see Eq. 5.1) (+), actual photoluminescence spectrum of the blend (dotted line) and photoluminescence spectra of the pristine materials (P3HT: ◯, TDI: △). The curves represented here were measured at 30 K, temperatures up to 300K give quite similar results in terms of quenching.

5.4.1 Excitation harvesting and charge generation in TDI

PL spectra of pristine P3HT, TDI and P3HT:TDI (ratio 4:1) blend films were recorded. Both pristine materials show characteristic PL (see figure 5.17). In order to better visualize the quenching contribution, we calculated the photoluminescence that a 4:1 P3HT:TDI blend would have in the absence of this quenching, according to the following expression:

$$PL_{calc}(\lambda) = \frac{4}{5} \times PL_{P3HT}(\lambda) + \frac{1}{5} \times PL_{TDI}(\lambda) \tag{5.1}$$

where PL_{P3HT} is the PL of the pure P3HT and PL_{TDI} the one of pure TDI. This PL is represented by the symbol (+) in figure 5.17. In contrast to the pristine materials, the blend exhibited very weak luminescence, the magnitude of the highest peak being only 1.7% of the calculated one. As a comparison, we obtained 4.1% residual luminescence with a P3HT:PCBM 1:1 blend under the same conditions (see table 5.1).

This luminescence quenching suggests that most of the primary photogenerated excitons are converted into non-emitting excited species before they radiatively recombine, which was reported to occur within 1 ns after excitation in pure P3HT [191] (see also § 6.2). Moreover the shape of the remaining luminescence roughly corresponds to the calculated one which indicates that the primary excited species are indeed the same ones as in the pristine materials. Nevertheless, one can notice that the peak at 680 nm which corresponds exclusively to PL from P3HT (see figure 5.17) is more quenched than the peaks in the spectral region where both materials are luminescing. This implies that P3HT excitons are a bit more efficiently quenched than TDI excitons. This difference can be explained in terms of charge affinity of the two materials if we consider — as will be shown below — that this PL quenching is due to exciton

dissociation into charges at the heterointerface. In case of P3HT excitons, the electron is attracted by the very electronegative TDI molecule as expected from the significant LUMO offset. In contrast, TDI excitons would be dissociated by the hole transfer to the P3HT, which is a bit less favorable, as expected from the lower HOMO offset between both materials (table 5.1). Another possible reason would be that excitons in P3HT can reach the heterojunction interface more easily than those in TDI, either because of superior exciton diffusion coefficient or lower average distance to travel.

Further insight of the fate of those excitons can be obtained by studying the photo-induced absorption spectrum of the P3HT:TDI blend, which is shown in figure 5.18a. This spectrum clearly exhibits the characteristic absorption for P3HT localised (P1 and P2) and delocalised (DP2) polarons (see § 5.2.2). Those peaks can also be seen in other blends involving the formation of P3HT+ polarons such as P3HT:PCBM (dotted line shown for comparison).

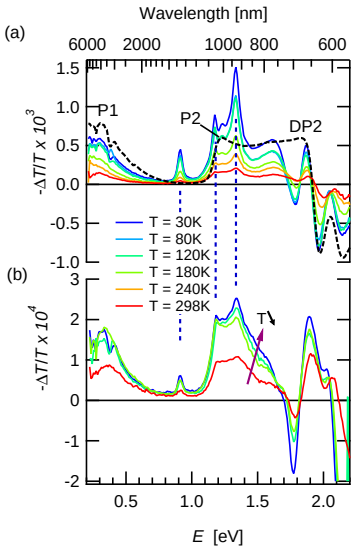

Figure 5.18: (a) Photoinduced absorption spectra of a P3HT:TDI blend at various temperatures (continuous lines) and P3HT:PCBM blend at 30K (dotted line). (b) Photoinduced absorption spectra of a MEH-PPV:TDI blend at various temperatures.

In addition to those P3HT features are the 0.91 eV, 1.17 eV and 1.33 eV peaks. Similar peaks, though blue shifted by 0.4 eV, were already mentioned for PDI [221] and attributed to PDI negative radical anions (0.4 eV is also difference between the HOMO-LUMO gaps of TDI and PDI respectively, the same blue-shift can also be found in absorptions and photoluminescence) [204]. The position of those peaks appeared to be quite stable with temperature, as well as by varying the donor:acceptor ratio or the donor molecule. We also observed them at the same position when using MEH-PPV as a donor (see figure 5.18b). For all those reasons, we attribute those peaks to TDI anions.

Those features, characteristic for charged species, are a strong indication that the initially generated excitons are efficiently separated into positive P3HT polarons and negative TDI anions. Efficient charge generation has also been reported in various polythiophene:PDI blends [222]. An additional indication is

given by the absence of the peak at 1.05 eV. This peak is a very clear feature in pure P3HT and has been ascribed to neutral excited species in pure P3HT (see § 5.2.2); it is totally missing in blends.

Those spectra also confirm that absorption indeed occurs in both materials as seen by the P3HT photobleaching from 1.9 to 2.2 eV (also seen in P3HT:PCBM) and one negative peak that we attribute to TDI photobleaching at 1.78 eV (corresponding to the maximum of the second absorption peak of TDI).

Figure 5.19 shows the ESR measurements which confirm the presence of photoinduced charges in blends of TDI or PDI with P3HT. A single ESR line was observed, which exhibited resonance features such as g-factor, linewidth and saturation under high microwave power conditions (inset in figure. 5.19) quite typical for positive P3HT polarons as in P3HT:PCBM blends [115]. However no signal of the negative TDI or PDI polaron was detected. We assume that this signal might have similar resonance features as the P3HT polaron and is superimposed by the more intense P3HT polaron spectrum.

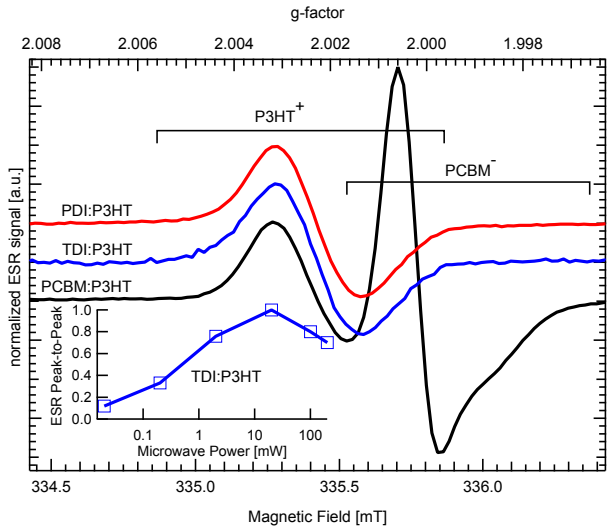

Figure 5.19: Normalized ESR spectra of P3HT blended with TDI, PDI and PCBM measured at 100 K with a microwave power of 20 mW and white light illumination. The inset shows the microwave saturation behavior of the peak-to-peak signal intensity of the P3HT:TDI blend.

5.4.2 Solar cells and EQE

Using the P3HT:TDI blend as an active layer, we were able to produce diodes. Nevertheless the photovoltaic response of the devices remained quite below our expectations. A typical current voltage characteristic is shown in figure 5.20. The open circuit voltage remained comparable to what can be observed in P3HT:PCBM cells (see Table 5.1), but the photocurrent was very low which contrasts quite strongly with the charge generation observed by PIA and EQE. Additionally the photocurrent is exponentially increasing when getting away from the open circuit voltage, which results in a low fill factor and suggests a

field dependent generation, and is here again in contrast with the aforementioned good charge generation properties.

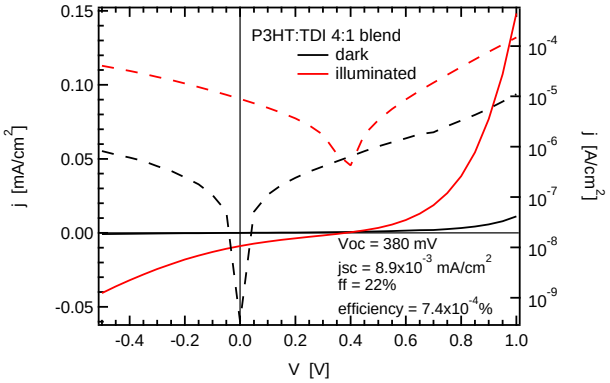

Figure 5.20: Current–voltage characteristics of a P3HT:TDI solar cell with 0.5 cm^2 active area in dark and under halogen lamp 100 $mWcm^{-2}$ illumination represented on linear (left axis, continuous lines) and logarithmic (right axis, dotted line) current scale.

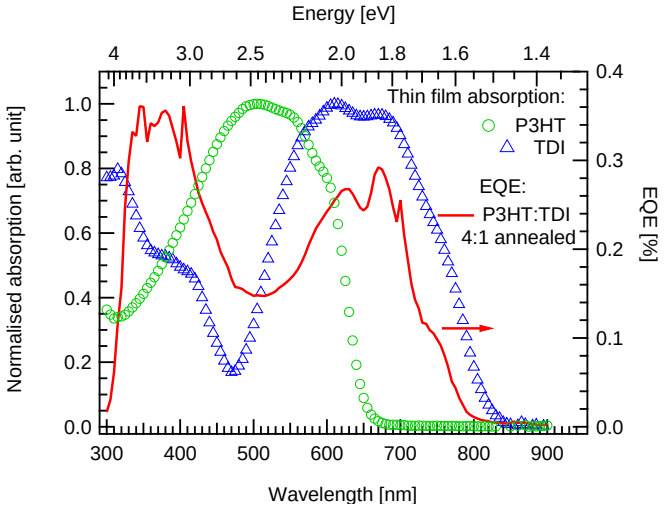

Figure 5.21: EQE spectrum of 4:1 P3HT:TDI blend (continuous line, left axis), normalised absorption spectra of pristine P3HT thin film (◯) and pristine TDI thin film (△)

The EQE spectrum of those solar cells is shown in figure. 5.21. It reveals that the charges generated at 500 nm (as shown by the PIA and ESR measurements) — and more generally in the spectral region where mainly P3HT is absorbing — are not well extracted. In contrast, in the regions where mainly or even only TDI is absorbing (above 680 nm), the EQE is higher. In fact, the EQE spectrum looks quite similar to the absorption spectrum of pure TDI with a distortion in favour of the UV region. This overweighting of the UV-regions could be due to the fact that photons of the UV region could generate excitons with

enough thermal energy to overcome their binding energy and split into charges even without the assistance of an heterojunction, similar to what occurs in pure P3HT diodes with photons of energy over 2.6 eV (see § 4.5.1 and Ref. [82]).

5.4.3 Influence of the energy levels

In order to rule out the possibility of an energy level mismatch between the electron donor and the electron acceptor, we reproduced the experiments changing one of the components of the blend in order to obtain blends with higher HOMO levels offsets. This offset is indeed rather small in the P3HT:TDI blend which might leave some possibilities of energy transfer from P3HT to TDI which has a smaller band gap. Such a change should also increase the driving force for charge separation. Nevertheless, it should be noted that none of the photoluminescence measurements revealed the occurrence of an energy transfer which should have caused enhanced TDI luminescence in the blend. To increase the HOMO offset, two approaches were considered: using an electron donor with higher HOMO level in a MEH-PPV:TDI blend, and using an electron acceptor with lower HOMO level in a P3HT:PDI blend (see HOMO offsets in table 5.1). The blends were studied in following ratios: 2:1 for MEH-PPV:TDI and 3:1 for P3HT:PDI. Although PIA measurements are not quantitatively comparable from one spectrum to the next, general trends can be extracted from them.

Table 5.1: Summary of the donor:rylene blends performances.

blend	ratio[b]	Energy levels [eV][a]		Excit. harvest.	Charge separat.	
		ΔHOMO	ΔLUMO	PL quench.	PIA[c]	ESR[d]
P3HT:TDI	4:1	0.4	0.2	≈ 98%	1	1
P3HT:PDI	3:1	0.4	0.5	≈ 97%	≈ 8.8	2-3
PPV:TDI	2:1	0.8	0.4	> 99%	≈ 1.5	NA
P3HT:PCBM[e]	1:1	0.4	0.9	≈ 96%	≈ 5	≈ 10

blend	ratio[b]	Solar cells			
		V_0 [V]	j_{sc} $[mA/cm^2]$	fill fact.	efficiency
P3HT:TDI	4:1	0.39	1.6×10^{-2}	33%	1.0×10^{-3}%
P3HT:PDI	3:1	0.39	2.3×10^{-2}	25%	1.4×10^{-3}%
PPV:TDI	2:1	0.74	0.12	26%	1.6×10^{-2}%
P3HT:PCBM[e]	1:1	0.62	10.33	57%	3.63%

[a] Calculated from cyclovoltametry measurements shown in [205] using the method presented in [206] plus data from [223] and [199] [b] Ratio providing the best efficiencies [c] integrated P1 peak at room temperature, normalized to the P1 peak of the P3HT:TDI blend [d] Integrated ESR signal, relatively to P3HT:TDI, at 100K [e] Samples prepared from chlorobenzene solution

The results of these studies are summarized in table 5.1. Both blends exhibited a very good harvesting of the primary excitons, characterized by a high quenching of the materials photoluminescence. In the MEH-PPV:TDI blend, the remaining photoluminescence was even below the limits of detection except at the lowest temperature (30 K), though pristine MEH-PPV has the strongest luminescence of the studied materials. The charge generation measurements (PIA and ESR) and current–voltage characteristics revealed an absence of cor-

relation between the photophysically measured charge generation and the device performances. Indeed, although the use of PDI instead of TDI results in a clear enhancement of charge generation (see table. 5.1), both P3HT:PDI and P3HT:TDI based solar cells exhibit a very similar performance, which is a good indication of a process preventing the charges from being extracted, independently of their concentration. In contrast, the MEH-PPV:TDI blend which exhibits smaller P1 peak (see figure. 5.18b) enabled us to process solar cells with a short circuit current one order of magnitude higher than the P3HT:rylene blends.

5.4.4 Charge transport

Possible intrinsic limitations regarding electron transport in TDI were investigated by time-of-flight photoconductivity measurements. Due to excessive roughness of pristine TDI films, no working device could be processed from them. Measurements were thus carried out on P3HT:TDI blends. They revealed an electron mobility between 1.07×10^{-3} $cm^2s^{-1}V^{-1}$ and 2.37×10^{-3} $cm^2s^{-1}V^{-1}$ (figure 5.22 (a)) for electric fields ranging from 3.3×10^7 Vm^{-1} to 4.0×10^7 Vm^{-1}. This value is nearly one order of magnitude larger than our measurements of the electron mobility with the same method in pristine P3HT and comparable to the electron mobilities obtained in P3HT:PCBM with excess of PCBM [116]. We therefore attribute it to electron transport through TDI.

The hole mobility on the same sample was found to range from 2.95×10^{-5} $cm^2s^{-1}V^{-1}$ to 6.92×10^{-5} $cm^2s^{-1}V^{-1}$ for fields between 6.7×10^6 Vm^{-1} and 3.3×10^7 Vm^{-1}. As represented in figure 5.22 (b), this is one order of magnitude lower than in pure P3HT. This is expected in blends compared to pure samples as a percolated pathway is longer than a straightforward way in a bulk, we therefore attribute this mobility to holes transported in P3HT. Such decrease has also been observed when blending P3HT with PCBM although to a lower extent [116], which suggest a less favorable morphology in the P3HT:TDI blend than in P3HT:PCBM.

5.4.5 Morphology and charge extraction

X-ray diffraction pattern (see figure 5.23) revealed in the bulk of the P3HT:TDI 3:1 sample the same feature as in the typical stacked layer of pure P3HT with a characteristic distance in the (100) direction of $\lambda/2\sin(\theta) = 17.1$ $\mathring{A}$ comparable to 16.8 $\mathring{A}$ found in literature [141]. This feature reveals an undisturbed P3HT-lamellae formation which is an indication of the presence of a pure P3HT phase in the blend.

Scanning electron microscopy performed on pristine TDI as well as P3HT:TDI 1:1 and 4:1 blends is represented in figure 5.24. The images are consistent with the afore-mentioned phase separation as they exhibit two very different kind of structures. Needle-like structures are present in the pure TDI as well as in the blends and were already observed in PDI [224, 225]. Their size is decreasing with the ratio of TDI. We therefore attribute those needles to pure TDI phases. Between the needles: a flat surface, the level of which is increasing with the ratio of P3HT to finally leave just a few needles emerge in the 4:1 ratio. We attribute this feature to the P3HT phase. It should be noted that the propor-

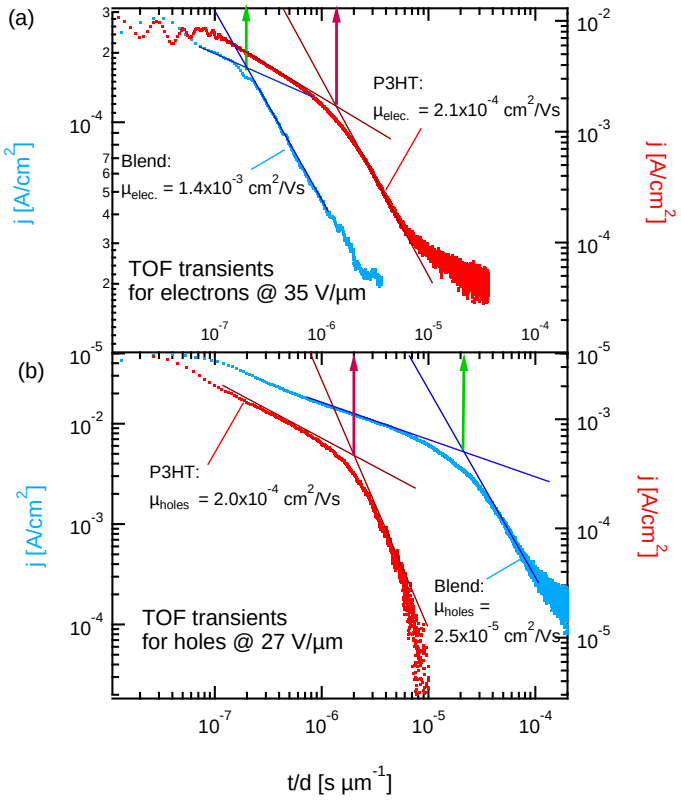

Figure 5.22: (a) Electron and (b) hole current transients for the neat P3HT and P3HT:TDI 4:1 blend. The time scale has been normalised to the thickness of the sample, the arrow thus represents the transit times t_{tr} divided by the films thicknesses, which is to say the time required by charges to travel 1 μm.

tion of TDI visible at the surface of the 4:1 sample is much lower than 20 %, suggesting a non homogeneous distribution of the materials in the bulk. Finally a third kind of feature has to be mentioned: pure TDI also forms a flat surface on the substrate which differs from the P3HT surface by its larger roughness. Although it can be observed only in the pure TDI film, this layer could also be present in the P3HT:TDI under the P3HT.

Those images also make clear why a ratio of at least 3:1 is necessary to obtain good photophysical properties. In the 1:1 ratio, a big part of the TDI needles are not covered by the P3HT phase, thus making it impossible for the TDI excitons to reach a donor:acceptor interface, resulting in a strong remaining TDI photoluminescence in case of a 1:1 ratio. It also explains the problem of making devices using pure material where needles height typically reaches several hundred nanometers, which is an obstacle to the evaporation of an electrode as thin as 50 nm required for time of flight measurements.

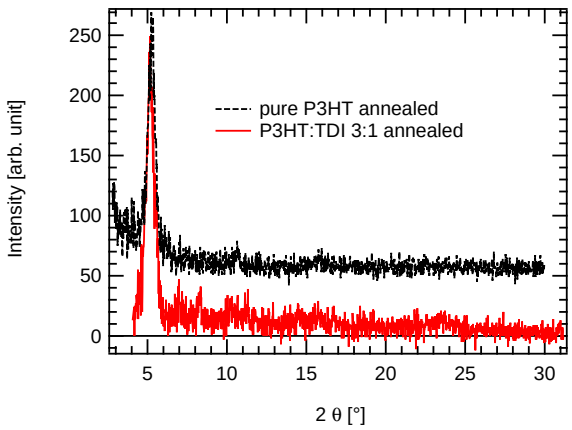

Figure 5.23: X-ray diffraction by a P3HT:TDI 3:1 (continuous line) sample and pristine P3HT reference in dotted line (with a vertical offset for clarity).

5.4.6 Discussion

The most remarkable observation resulting from our studies is the mismatch between the very good properties of terrylene-3,4:11,12-bis(dicarboximide) as electron acceptor and electron transporter in P3HT:TDI blends and the poor performances of the solar cells processed from the same blend. Photo-induced absorption and electron spin resonance measurement concomitantly show that illuminating a P3HT:TDI blend with a 500 nm light results in the generation of separated charges.

The comparisons of P3HT:TDI and P3HT:PDI blends confirms that charge generation, although less efficient than in P3HT:PCBM, is not the main problem of P3HT:xDI blends. Indeed, while P3HT:PDI blends exhibit a charge generation efficiency several times higher than the one of P3HT:TDI as proven by ESR and PIA measurements, the solar cells performances of those two blends are almost identical.

The measurements of time of flight mobilities in the P3HT:TDI blend enabled to rule out transport problems by revealing an electron mobility quite comparable to the one of PCBM. This is consistent with the high local mobilities reported in literature on crystaline PDI. [226]

At first sight, the morphology appears to be also rather well adapted to solar cells application: phase separation does occur, as proven by the XRD measurements and SEM images. Moreover, the PL quenching seems to indicate a rather optimal phase size: too small phases would result in a total PL quenching (as for MEH-PPV:TDI blends, shown in table 5.1, or P3HT:UH3 blends in § 5.3.2) whereas excessive phase separation would prevent PL–quenching (see the example of UH1 in § 5.3.1). None of these situation is observed with P3HT:TDI blends.

The EQE spectrum of P3HT:TDI shows that very little photocurrent is originating from the P3HT absorbing regions, where the maximum of the EQE would be expected by comparison with P3HT:PCBM cells and the absorption spectra. We know that charges are generated in that spectral region because that is where the samples are excited in the PIA experiment. We propose that

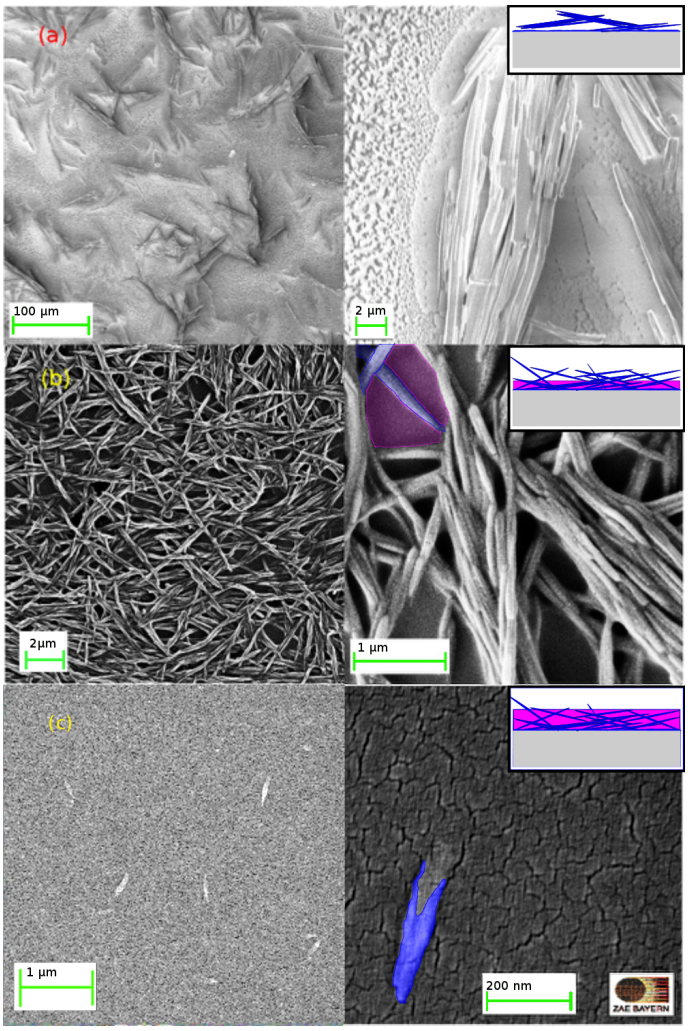

Figure 5.24: SEM pictures of following materials spincoated on sapphire substrates: pure TDI (a) and P3HT:TDI blends with weight ratio 1:1 (b) and 4:1 (c). The size of the needles is visibly decreasing when increasing the ratio of P3HT. The cracks visible on the 4:1 blend are due to a thin layer of gold deposited on the organic layer for imaging. Schematics in the inset represent the suggested bulk structures with blue representing TDI, fuchsia representing P3HT.

a thin pure TDI layer — similar to the ones observed on pure TDI samples— could be formed close to the substrate in the P3HT:TDI blend. This layer could efficiently prevent the holes in P3HT from reaching the anode. This assumption is consistent with the observation of a TDI layer on the substrate by SEM imaging of the pure TDI sample. This layer could also be present in the blend, even if not observable because lying under the P3HT. Such vertical segregation have been reported — to a lower extend — in P3HT:PCBM blends, where the PCBM is found to be much more abundant close to the substrate that at the surface of the film [227]. We suggest that the extent of this phenomena in P3HT:TDI results in the ITO cathode being efficiently sealed by a TDI layer.

This is also consistent with the low solubility of TDI, which thus tends to deposit first during the solvent evaporation process, whereas the P3HT can just have its concentration increasing in the remaining solution.

The higher quantum efficiency in the spectral regions where only TDI absorbs can be explained by pristine material photovoltaic effect: the hot excitons are generated, separated and extracted within the TDI phase without the assistance of P3HT due to thermally assisted dissociation and the energetic disorder inherent to organic semiconductors. This is consistent with the SEM measurements that revealed that some TDI needles can reach the surface of the blend, thus being in contact with the anode. Photoluminescence studies also demonstrated that the contribution of TDI in the remaining luminescence in the blend is higher than the one of P3HT, proving that some excitons can remain in the TDI phase long enough for recombination to occur.

To evaluate the magnitude that charge dissociation can reach in a pure material, we processed pure P3HT solar cells. The EQE of those cells reached a maximum of 4.3×10^{-3}, similar to the P3HT:TDI solar cells whose EQE reaches a maximum of 3.7×10^{-3}. Another interesting point is the shape of the EQE spectrum: in contrast to a system in which the charge separation would be driven mainly by the heterojunction, the highest energy peaks are quite overweighted relatively to the absorption, which is a sign that the driving energy for charge separation could be excess energy of the "hot" excitons generated through absorption of photons having an energy over the absorption gap (see also chapter 4 and Ref. [82]).

This hypothesis is also in agreement with the low hole mobility observed in the P3HT:TDI sample. Indeed, in a TOF experiment, all the countercharges are immediately extracted. In a solar cells, holes would probably recombine when reaching the electron-rich TDI layer. In the TOF experiment this recombination can not occur, holes are thus eventually extracted but the necessity to cross the TDI layer before reaching the anode makes it much slower.

A last indication of the formation of this TDI layer was obtained by the processing of a bilayer solar cell in which a layer of P3HT was deposited under a layer of TDI thanks to the use of 2 different solvents (chlorobenzene and dichloromethane, respectively). Those cells enabled a much higher open circuit voltage (550mV), possibly indicating the open-circuit voltage is limited by space charge in the bulk-heterojunction cells. Nevertheless, due to intrinsic limitation of bilayers (rather poor charge generation), this structure did not notably allow for a better efficiency than the bulk-heterojunction. We suggest that this problem could be solved by the use of devices with inverted structure (anode as top electrode).

A possible reason why this phenomenon does not appear in MEH-PPV:TDI solar cell is that in contrast with MEH-PPV, regio regular P3HT has a crystalline structure. Because of this tendency to crystallize, both P3HT and TDI crystallizations are in competition thus applying some mechanical constraints on each other which may push some TDI under the P3HT containing part until forming this hole blocking layer.

5.5 Conclusions and outcome

The study of alternative electron acceptors enabled us to pinpoint a number of limiting factors in photocurrent generation. Although all molecules enable the conversion of primary excitons into charges, as revealed by the PIA spectra, critical morphology issues were found to prevent efficient current generation. Both P3HT:UH1 and P3HT:UH3 blends self organization resulted in morphology not favorable for solar cells applications. While the earlier tends to form too big phases, which impede efficient excitons harvesting, the latter lacked the minimum phase separation necessary for establishing percolation pathways from the donor (resp. acceptor) phase to the anode (resp. cathode).

In TDI, we found an organic material exhibiting some very interesting properties regarding its use as electron acceptor in blend with P3HT. Good charge generation and transport together with an absorption band complementary to the one of P3HT were demonstrated, promising good photovoltaic properties to the P3HT:TDI blend. Nevertheless, the solar cells produced using this blend as active layer resulted in low performances. In agreement with our morphology investigations, we present two explanations. In the case of MEH-PPV:TDI, we propose that the photocurrent is severely limited by the too small phase separation similar to what was observed in P3HT:UH3. In P3HT:TDI solar cells, the formation of a thin layer of pure TDI along the ITO electrode seems to prevent hole extraction.

By enabling to evaluate exciton collection and charge generation, optical characterization brins crucial knowledge on the strengths and limitations of new blends. In combination with transport and morphology studies, it enables to determine the causes of limited performances and thus to send a precious feed back to the laboratories synthesizing new molecules. In parallel to this work, our collaborators of Max Planck institute managed to synthesize perylene derivatives overcoming the identified problem: by replacing the N-substitution of PDI derivative by a core substitution, they managed to limit rylene agglomeration and to improve solar cell performances [228]. As a result one could expect that core-substituted TDI derivative also exhibit a morphology more compatible with solar cell applications, thus enabling the quite promising potential of those acceptors to be used in good performing solar cells collecting a wider range of the solar spectra.

Chapter 6

Bimolecular Recombination

6.1 Introduction

In chapter 4, field dependent PL studies enabled us to uncover the binding energy of pure P3HT, which is the main reason why P3HT alone can not be used for photovoltaic applications and has to be accompanied by an electron acceptor material. In chapter 5, we have identified, thanks to PIA spectroscopy, a number of bottlenecks and limitations to photocurrent generation and extraction, that exist when adding an electron acceptor to P3HT in a bulk-heterojunction structure. We saw that obtaining a morphology that allows for both an efficient exciton harvesting and an obstacle–free charge transport and extraction could prove quite challenging. In this last chapter, we will see that even when the blend morphology meets the aforementioned conditions, obtaining high performance solar cells is not straightforward. Indeed, if applying the Langevin theory such as presented in § 1.2.4 to the mobilities of P3HT and PCBM (on the order of the 10^{-4} cm^2/Vs) and the average relative dielectric constant of the blend (typically 3.5), almost 85% of charge carriers should recombine nongeminately within the time required for charge extraction in organic solar cell devices (typically 100 ns [57, 59]). However, this does not happen and charges actually do survive until extraction can occur, with external quantum efficiencies over 80 % being the rule in P3HT:PCBM based bulk-heterojunction solar cells.

As a matter of fact, experimental observations in blends, obtained by various transient methods [57, 106, 107], strongly differ from what would be expected applying Langevin theory alone: recombination rates are found to be quite lower and associated to relatively high apparent recombination orders.[1] In order to unravel the possible causes for such a discrepancy, we used time resolved photoinduced absorption — more simply called transient absorption (TA) — to monitor the dynamics of separated charges recombination. By avoiding the injection and extraction related perturbations, this methods enable us to focus on recombination alone. Recombination dynamics were monitored in neat P3HT and in a P3HT:PCBM blend in a range of temperatures.[2]

The study will be presented as follow: in section 6.2, we determine from a

[1] See definition in § 1.2.4.

[2] For the experiments carried out in this chapter, we used exclusively P3HT "P200 Sepiolid" synthesized by BASF (See § 3.1.4).

bibliographical study, as well as temperature dependent PIA spectra, the correct temperature range and wavelength to observe specifically separated charges. We then briefly treat the problem of the quantification of charges density from the observed absorption. Section 6.4 presents the experimental results and compare them with the results expected from Langevin theory. In section 6.5 we discuss the possible sources of the differences observed between, on the one hand Langevin theory and experimental observation in neat P3HT, and on the other hand the recombination experimentally observed in the blend. Finally, in section 6.6, we discuss the generality of our finding in the light of a recent paper by Guo et al. [57] which presented the possibility of the existence and detection of two different kinds of polarons in P3HT:PCBM blends, presented there as exhibiting different transport and recombination modes.

6.2 Monitored species

Literature femto- and transient absorption studies

In complement to section 5.2 which was dedicated to the species observable in P3HT (neat or blended with PCBM) using steady-state PIA, we present here the shorter living species that do not accumulate enough to be detected in steady state mode, but might —or not— be observed in transients. Especially important for us are the species which can be detected in the times ranging form 10 ns to 10 ms, which is the range of detection of our TA setup.

Table 6.1: Excited species detectable in transient and femtosecond absorptions.

Species	Typical lifetime and decay way	Spectral feature
Singlet radiative excitons	660 ps in pure P3HT [191] 40–70 ps in P3HT:PCBM [191]	Detected by time resolved PL. Causes stimulated emission at 1.6–1.8 eV [99, 191]. Quenched by PCBM [191].
Singlet non radiative excitons	200 ps in pure P3HT [191] 20–60 ps in P3HT:PCBM [191]	Mainly 0.8–1.1 eV but extending over 1.35 eV [191, 229]. Quickest vanishing species, quenched by PCBM [191].
Coulombically bound electron–hole pairs	Monomolecular decay within 2 ns [99]	1.45–1.65 eV
Separated charges .	Hundreds of ns to hundred μs [57]. No decay before 3 ns [99]. Bimolecular to higher orders[a].	1.1–1.9 eV [191, 229] + below 0.8 eV [191]

[a] Guo et al. differentiate a bimolecular decay at 1.77 eV attributed to charges undergoing trap–free transport, and a higher order one at 1.25 eV attributed to charges undergoing trap–rich transport [57], this will be discussed in section 6.6

Table 6.1 lists the species that have been reported in literature, together with their temporal detection range and spectral features (the lifetimes presented have all been measured at room temperature).

Among those excited species, only the separated charges should be visible at room temperature in the time range relevant for transient absorption. However, the typical lifetime attributed to electron–hole pairs is in the order of the nanosecond at room temperature in pure material, and could thus extend

to our measurement range at lower temperatures. Moreover, in contrast to P3HT:PCBM blends, very little report exist concerning transient absorption in neat P3HT. Such article usually report that no signal can be seen in neat regio-regular P3HT [54]. As we will see in section 6.4, this is true only at room temperature where the decays are too quick to be observed in the 10 ns to 10 μs time range.

The challenge of polarons monitoring in neat P3HT

As presented in § 5.2.1 (figure 5.6), charges can be detected in steady-state in neat P3HT in spite of the relatively low exciton's dissociation efficiency. The formation of charges is confirmed by ultrafast spectroscopy studies by Piris et al. who detected charge formation with an efficiency as high as 15% in neat P3HT [191]. In a nutshell, separated polarons can be detected in neat P3HT in both steady-state and ultra fast transient spectroscopies. However, attempts to monitor those charges at room temperature in the time range relevant for charge extraction in solar cells application (which is to say over 100 ns) failed to detect any signal in neat P3HT [54], which contrasts with strong signal observed in P3HT:PCBM [54, 57]. The reason for this absence of detection was that polarons recombination in neat P3HT would occur too quickly "within instrumental response function" [54]. To overcome this first obstacle, we performed measurements at temperatures ranging from 30 K to 300 K to increase the lifetime of polarons. We observed that signal was detectable in pure P3HT until a temperature of 250 K (see figure 6.2(a)).

Another difficulty is to address exclusively polarons absorption. Indeed, unlike ultrafast spectroscopy [191] and steady-state PIA (see § 5.2), TA can not be used to probe the spectral region further than the near-infrared (until 1400 nm) where only polarons have absorption features (at wavelength over 1500 nm). More precisely, in our case, transient absorption was probed at 980 nm which corresponds to the maximum of the so–called $P2$ polarons peak (see inset in figure 6.1 or § 5.2.2 for more details). In this spectral region, polarons are not the only transient species liable to absorb. Especially the neutral species which are responsible for the main absorption peak in neat P3HT at 30 K (see § 5.2.2) have a strong absorption coefficient in that spectral region. Note that this problem does not exist in the blend as the density of the neutral species in P3HT:PCBM blends decays on the sub-nanosecond scale even at low temperatures [229].

To distinguish between the potential absorbing species, we performed temperature dependent steady-state PIA studies. The results of those measurement are reproduced in figure 6.1. It shows that the absorption from neutral species (main peak at 1.05 eV) is continuously decreasing when increasing the temperature. As a matter of fact, the contribution of neutral species to absorption at 1.25 eV becomes vanishing above 142 K thus leaving only the $P2$ absorption peak due to polarons whose maximal is at 1.25 eV. It is therefore safe to assume that between 142 and 250 K, polarons are the only absorbing species at 980 nm for the blend in the time range 10^{-8} to 10^{-4} s. We conclude that above 140 K, the absorption at 980 nm is representative of the polaron density in both pristine P3HT and P3HT:PCBM blend.

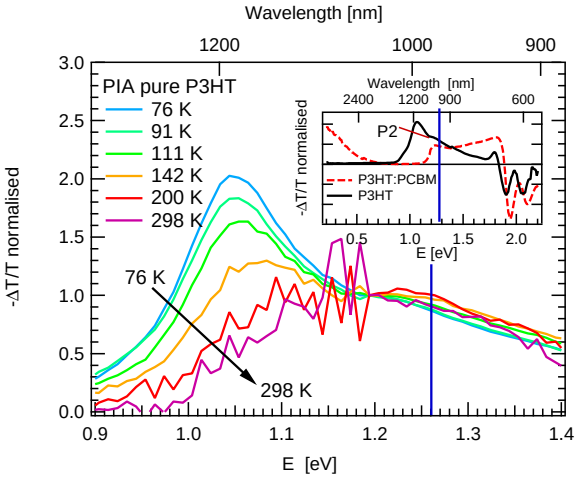

Figure 6.1: Temperature dependent steady-state PIA spectra of neat P3HT (normalized to its value at 1.2 eV). The blue line indicates the probe wavelength used for TA; above 140 K, absorption at this wavelength is proportional to the density of polarons in both P3HT and P3HT:PCBM. Inset: Steady-state PIA spectra of neat P3HT (continuous black line) and P3HT:PCBM blend (broken red line) at a temperature of 30 K.

6.3 Quantification of the density of charges

In order to extract physical parameters from the transients, it is necessary to determine the density of charges represented by those absorptions and thus to know the absorption coefficient of polarons, or equivalently their absorption cross section. At the excitation wavelength of 500 nm, 10.3% of incident light was reflected by the P3HT:PCBM sample. 3.6% was transmitted, yielding an upper limit for the average density of generated excitons of 1.8×10^{18} cm^{-3} at a pulse energy of 25 μJ/cm^2.

By solving the rate equations described by Howard et al. [99] including the nonlinear losses due to polaron–exciton annihilation [100] at high excitation intensity and a Gaussian exciton generation term representing the laser pulse, we estimated the number of generated positive polarons to be $(7.8\pm2.0)\times10^{17}$ cm^{-3} in P3HT:PCBM, with a polaron–exciton annihilation rate of $(1.7\pm0.7)\times10^{-7}$ cm^3/s obtained from excitation intensity dependence of the initial change of optical density ΔOD_0. From the corresponding ΔOD, the absorption cross section of P3HT polarons at 980 nm was evaluated to $(1.9\pm0.5)\times10^{-16}$ cm^2. The details of the resolution of the rate equations system and the determination of the absorption cross section σ_{hole} can be found elsewhere [111, pp. 29–38].

6.4 Transient absorption results

The transient decay of the change in optical density of neat P3HT and the P3HT:PCBM blend is shown in Fig. 6.2. The initial change of optical density ΔOD_0 at 10 ns, including geminate recombination [229] and exciton–polaron annihilation [99], is virtually temperature independent—only slightly lowered

for temperatures approaching 300K due to nongeminate losses starting to set in already before. For both neat P3HT and the blend, the decay dynamics beyond 10 ns are due to nongeminate recombination, with an increasing recombination rate for higher temperatures. In agreement with the previous work of Ohkita et al. in 2008 [54], the decay in pure P3HT is too quick to be observed at room temperature but remains visible until temperatures as high as 250 K.

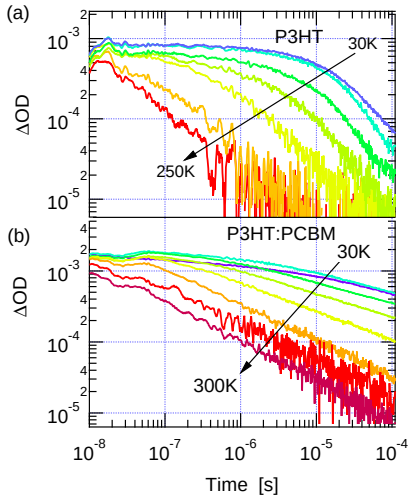

Figure 6.2: (a) Transient absorption decays in P3HT for different temperatures. (b) Transient absorption decays in P3HT:PCBM (solid line)

6.4.1 Neat P3HT

In order to gain a deeper understanding of the polaron dynamics, we compared the experimental decays to simulations based on continuity equations. In the absence of any external contributions (injection or photoexcitation from the ground state) for $t > 0$, the continuity equation describing the polaron density n becomes

$$\frac{dn}{dt} = -R \tag{6.1}$$

Although bimolecular Langevin recombination (Eq. 1.39) is the expected loss mechanism for separated polarons, we also considered monomolecular decay [59]. The sum of a monomolecular and a bimolecular terms perfectly fitted the decay observed in neat P3HT for temperatures below 140 K, whereas at higher temperatures the decays were purely bimolecular. The latter finding is in total agreement with the assignment of the transient absorption in neat P3HT to polarons at temperatures above 140 K and to a sum of contributions from polarons and neutral species at lower temperatures (see § 6.2). These neutral species could be triplets excitons [231], interchain singlet excitons [32] or polaron pairs [99] (discussed more in details in § 5.2.2).

Strikingly, the recombination of polarons in neat P3HT exhibits the same bimolecular behaviour as predicted by Langevin theory. The recombination prefactor k_{br} obtained from the fits in Fig. 6.3(a) yields a sum of mobilities

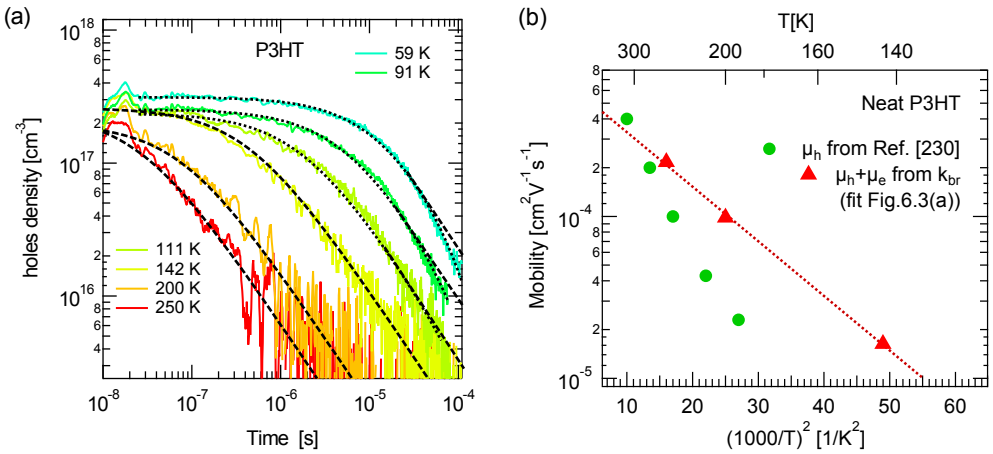

Figure 6.3: (a) Decay of the density of charges in P3HT corresponding to the transients of figure 6.2(a) for different temperatures (solid lines). The fits in dashed lines correspond to bimolecular Langevin recombination and the fits in dotted lines account for a mono- and bimolecular contributions. The asymptotes that would corresponding to a purely bimolecular decay are shown for comparison for 111 K, 91 K and 59 K (dashed lines). (b) Sum of mobilities extracted from the Langevin recombination fit using Eq. 1.40, compared to experimental hole mobilities from Ref. [230]. The dashed line is a fit of $\mu \propto \exp(2\sigma/3k_BT)^2$, yielding standard deviations of the Gaussian DOS of 36.6 meV for neat P3HT.

(Eq. 1.40), shown in Fig. 6.3(b), which is in the same range as the experimental time-of-flight mobilities [230]. This indicates that recombination of free polarons in neat P3HT follows the Langevin theory, and that the relevant charge carrier mobility is the macroscopic (intermolecular) instead of the local one (measured by microwave conductivity [100]). Indeed, the activation energy of recombination extracted from the temperature dependence of k_{br} is as high as 75 meV, one order of magnitude higher than the 6.6 meV observed for the local mobility in P3HT:PCBM blends [229]. In the frame of a Gaussian disorder model, we determined from Fig. 6.3(b) a DOS standard deviation of 36.6 meV for $\mu_h + \mu_e$. Previously, a value of 56 meV was found by Mauer et al. using time of flight [230] which may be due to thicker films resulting in different film morphology and more dispersive charge transport on the micrometer scale than in the mesoscopic scale relevant for recombination.

6.4.2 Blend

While the dynamics of the charge recombination in neat P3HT follow the Langevin theory, the transient absorption in the P3HT:PCBM blend exhibits a much slower decay (Fig. 6.2b), similar to previous reports [57, 106, 107]. It is characterized by a reduced recombination rate in combination with a high apparent recombination order. This high apparent recombination order can be seen from the slope of the experimental curves, which as shown in figure 6.4(a), exhibits a much more gentle slope than expected for a second order decay.

More quantitatively, the apparent recombination order can be obtained by fitting the curves using the equation (1.41) for general order recombination. As

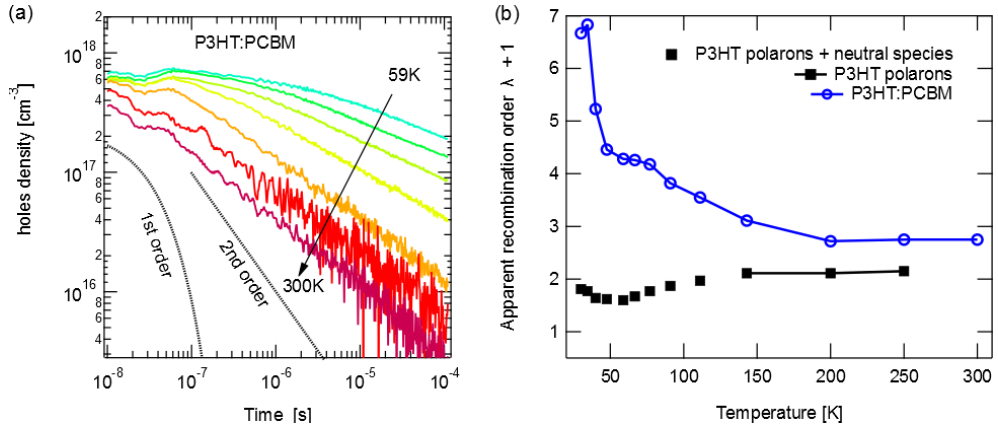

Figure 6.4: (a) Transient absorption decays in P3HT:PCBM (solid line). Typical shape of mono- and- bimolecular decays (dotted lines). (b) Apparent recombination order as function of temperature for neat P3HT and blend.

shown in figure 6.4(b), the extracted orders exceed the value of 2 already at room temperature, increasing to about 7 at 30 K. Those fits should be considered as purely mathematical and empirical fits. Indeed, with such high orders, it is excluded that the recombination order reflects the actual number of particles involved in the recombination mechanism.

6.5 Possible sources for the different recombination behavior of P3HT:PCBM compared to P3HT and Langevin theory

The fact that non-Langevin recombination is observed only in the blends and not in neat P3HT is a finding of prime importance. Indeed, it confirms the applicability of Langevin's theory to organic semiconductors (neat P3HT), and indicates the existence of an additional effect that enables the charges to survive long enough in the blend so that they can be extracted, thus making this blend usable for photovoltaic applications. It also suggests that the presence of two materials or maybe two phases as observed in blends of P3HT with PCBM (see § 3.3) plays a major role in protecting the charges from a quick Langevin recombination.

However, the mechanism of this protection can so far only be speculated. In the following we will examine four possible reasons and see how they seem to be — or not to be — in agreement with the experimental observations.

6.5.1 Geometrical reduction factor

The idea underlying the geometrical reduction factor is that, due to the existence of a strong phase separation, electrons and holes can meet — and thus recombine — only at the interface between an electron acceptor domain (here a pure PCBM domain) containing only negatively charged polarons, and an electron donor domain (here a pure P3HT domain) containing only positively charged polarons.

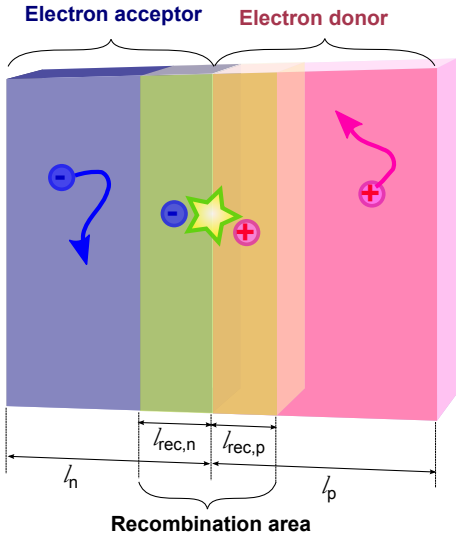

Figure 6.5: Schematic view of the polarons recombination in a bilayer: $l_{rec,n}$ and $l_{rec,p}$ represent the width of the recombination area and in the electron acceptor and electron donor regions, respectively; l_n and l_p correspond to the total width of those regions.

Taking the extreme case of a bilayer can help to understand qualitatively what is to be expected in such cases. In a system such as the one represented in figure 6.5, polarons located in the vicinity of the interface[3] are expected to undergo a normal Langevin recombination, which is to say to recombine with a rate proportional to their own density multiplied by the density of recombining partners. If we consider that the event of having charges diffusing from outside this recombination area is more likely than having a polaron in the recombining area finding a recombining partner within its coulomb radius (because the density of charges remain relatively small), then recombination should not significantly affect the density in the neighborhood of the interface compared to the rest of the volume. Thus:

$$R_{rec.area} = k_{br} n_{rec.area} p_{rec.area} = k_{br} np \tag{6.2}$$

On the other hand, no recombination is expected in the rest of the volume. As a result the total recombination rate becomes:

$$R = R_{rec.area} + R_{volume} = x \cdot k_{br} np + (1 - x) \cdot 0 = x \cdot k_{br} np \tag{6.3}$$

where x is the proportion of the volume located in the recombination area, and de facto the geometrical reduction factor. A more detailed analysis could be done by considering that the local recombination rate does not pass from zero to $k_{br}np$ when entering the recombination but actually increases progressively from a distance to the interface of one Coulomb radius to a distance of zero, as a bigger part of the coulomb radius sphere would be located in the part of the system where counter–charges can be encountered. However, as long as the polarons diffusion is sufficient to avoid local depletion at the interface, this should still result in a geometrical reduction factor.

[3] i.e. the region going from the interface, to one Coulomb capture radius away from it

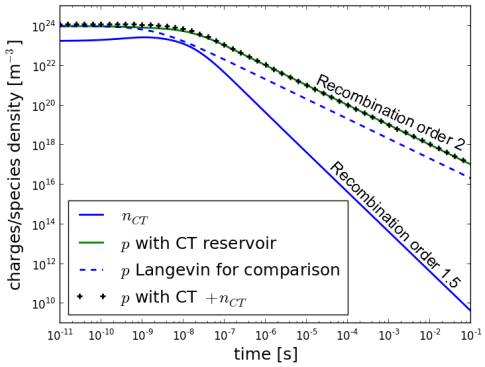

Figure 6.6: Numerical simulation of the decay of polarons density, with and without taking into account CT-states reformation and redissociation (from equations (6.5)).

6.5.2 Reservoir of CT–states redissociating into polarons

Another hypothesis, is that polarons might upon "recombination" form a new coulombically bound polaron pair or interface exciton ("CT–state" for generality) instead of directly returning the system to its ground state. This CT–state could in turn either geminately recombine to ground state, or dissociate again into a new pair of separated polarons. In such a situation, the rate equations describing the system would become (without taking into account the initial generation term, as we consider times were this step is over):

$$\frac{dn}{dt} = -k_{br}np + k_{diss}n_{CT} \tag{6.4}$$

$$\frac{dn_{CT}}{dt} = k_{br}np - k_{diss}n_{CT} - \frac{n_{CT}}{\tau_{CT}} \tag{6.5}$$

with n_{CT} the density of the CT–states, k_{diss} the rate of dissociation of those CT–states into polarons and τ_{CT} the time constant of CT–states geminate recombination.

To study the effects that such a mechanism would have, we simulated those rate equations for realistic values. The lifetime of CT–states (inverse of $k_{diss}+1/\tau$) has been taken as 0.8 ns in the order of magnitude observed in literature [99, 232]. $1/\tau$ has been taken 4 times smaller than k_{diss} to account for the very good dissociation efficiency in P3HT:PCBM blend. Finally the recombination rate k_{br} for separated polarons has been taken equal to the Langevin rate (equation 1.40) with $\epsilon = 3\epsilon_0$ and $\mu_e = \mu_h = 4.10^{-4}$ cm^2/V/s.

The initial densities of separated polarons were set to 10^{18} cm^{-3} corresponding to the initial density obtained in our transients. The initial density of CT–state has been taken 5.5 times smaller than the density of separated polarons, in agreement with measurements from Howard et al. [99] who detected in annealed P3HT:PCBM blends the ultrafast initial formation of 15% of bounded polaron pairs for 85% of separated polarons.

The results are shown in figure 6.6. As can be seen the decay of p exhibits the same slope as when CT–states redissociation is not taken into account. The only difference being that the characteristic kink occurs at later times which

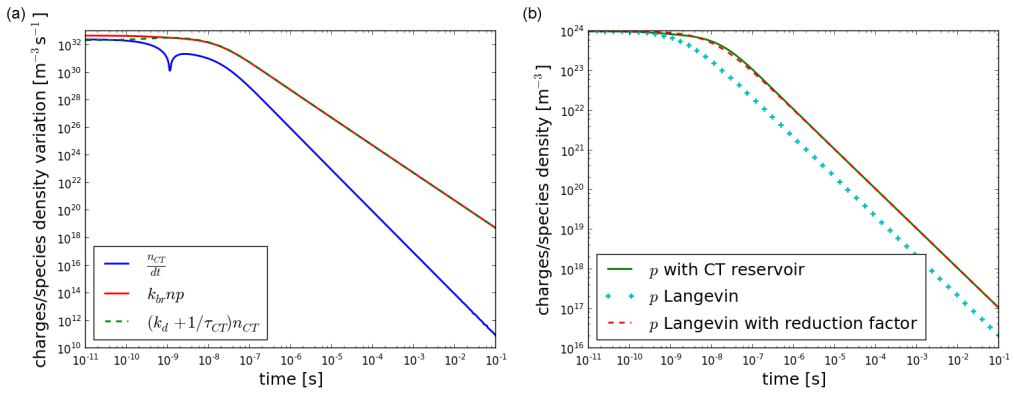

Figure 6.7: Verification of the quasi-static hypothesis for the effect of CT–states reservoir: (a) Comparison of $\frac{dn_{CT}}{dt}$ (blue line) with the CT–states formation (red line) and disappearing (green line) rates. (b) Comparison of the evolution $p(t)$ given by the equations 6.4 and 6.5 (full line) and its approximation by a reduction factor in the Langevin rate equation (equation 6.9, dotted line).

corresponds to a same recombination order but a reduced prefactor. Notably n_{CT} decreases more quickly than p with an apparent recombination order of 1.5 and remains negligible in comparison to p. As a result, even if both separated and bound charges were detected together, $p+n_{CT}$ would follow the same trend as p (see figure 6.6). Note that other initial values were also tried, all giving the same results in terms of apparent recombination orders.

This result can also be obtained analytically under the assumption that the variation of the density of CT–states dn_{CT}/dt is slow compared to other relevant parameters. In this case, the system can be considered at every instant in quasi equilibrium. Thus:

$$\frac{dn_{CT}}{dt} \approx 0 \quad = \quad k_{br}np - k_{diss}n_{CT} - \frac{n_{CT}}{\tau_{CT}} \tag{6.6}$$

$$\Leftrightarrow k_{br}np \quad \approx \quad (k_{diss} + 1/\tau_{CT})\, n_{CT} \tag{6.7}$$

$$\Leftrightarrow n_{CT} \quad \approx \quad \frac{k_{br}}{k_{diss} + 1/\tau_{CT}} np \tag{6.8}$$

$$\Rightarrow \frac{dn}{dt} \quad \approx \quad -k_{br}\left(1 - \frac{k_{diss}}{k_{diss} + 1/\tau_{CT}}\right) np \tag{6.9}$$

Figure 6.7(a), shows that the aforementioned hypothesis is verified: at times exceeding 1 ns, the variation of the density of CT–states (dn_{CT}/dtin blue) is negligible in comparison with the rates of their formation ($k_{br}np$ in red) and disappearing ($k_d + 1/\tau_{CT}$ in green), which practically compensate each other as expected from equation 6.6.

As a result, the effect of intermediate CT–states (if they exist) can be reasonably accounted by a constant reduction factor $k_{red,CT} = 1 + \frac{k_{diss}}{k_{diss}+1/\tau_{CT}}$ in the Langevin rate equation 1.39, as shown in figure 6.7. It can thus not be responsible for the experimentally observed change of recombination order.

Concerning the likeliness of such a phenomena, a study by Lee et al. [79] suggests that CT–states can dissociate without additional thermal energy. Moreover, CT–states formed not from excitons but from separated polarons have 3/4

chances of being triplet and thus to not undergo recombination to ground state, which also speaks in favor of their subsequent redissociation.

6.5.3 Carrier concentration dependent mobility

Alternatively, it was proposed that carrier concentration dependent mobility could be responsible for the high apparent recombination order. This hypothesis was considered by Rauh et al. who carried out simultaneous measurements of n and μ. They concluded that the variation of μ with the charge carrier concentration alone was insufficient to fully explain the observed decays for P3HT:PCBM at $T < 300$ K [233].

6.5.4 Reservoir of not-recombining "trapped" charges

Finally, it is likely that energetically trapped charges play a different role in a phase separated system like P3HT:PCBM than in an homogeneous one like neat P3HT.

Indeed, taking into account the density of trap charge carriers leads to the following rewritten form of the recombination rate in a homogeneous medium:

$$R_{homogeneous} = k_{br,cc} n_c p_c + k_{br,ct} n_c p_t + k_{bt,tc} n_t p_c, \tag{6.10}$$

where the index c stands for conducting (mobile) charge carriers and t for trapped ones, with $n = n_c + n_t$ and $p = p_c + p_t$. Compared to Eq. (1.39), only the $n_t p_t$ term is missing, which means that both equation are practically equivalent in case of a low density of traps, as observed in neat P3HT [234].

On the other hand a composite system such as P3HT:PCBM contains domains where only one of the blends components is present (see section 3.3). Charges trapped in those domains can not be reached by their counter charges which are restricted to the other phase, and R is further reduced to:

$$R_{phas.sep.} = k_{br,cc} n_c p_c. \tag{6.11}$$

We stress that in any case, the recombination mechanism is still bimolecular, and the order should actually be two if expressed as function of the density of charges actively participating at a given time. Nevertheless, trying to express R as function of the total density of charges can result in higher apparent recombination orders, as shown by the successful modelizations of power law decays by models accounting for the immobilization of charges occupying levels in the deeper energy tail of an exponential density of states [105]. However, we note that no model has so-far explained the evolution of apparent recombination orders with temperature.

6.6 Possibility of selectively probing different kind of polarons in P3HT:PCBM

In 2010, Guo et al. published an article suggesting that not all positive polarons may be affected by trap-limited transport [57]. By carrying out TA measurements at two different wavelengths on an annealed P3HT:PCBM blend, they observed two different behaviors. When probing at 980 nm, they observed a

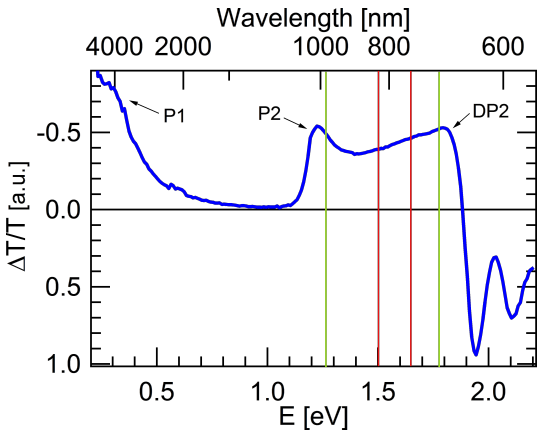

Figure 6.8: Steady-state PIA spectrum of annealed P3HT:PCBM (1:0.8) at T=30K. The two green lines show the wavelengths 1000 nm and 700 nm at which transient absorption decays were measured by Guo et al. [57]. We also carried out measurements at those two wavelengths (more precisely 982 nm and 700 nm), additional measurements were carried out at 750 and 825 nm (red lines).

slow "high order" decay similar to the one we described in the previous section, which they attributed to the recombination of polarons following a "trap limited transport". However, when probing at 700 nm, they observed a second order decay which they attributed to polarons following a "trap-free transport". Such a result forces us to wonder what we actually probe at 980 nm. Does this method give us access to the whole or just a part of the density of polarons? This section is dedicated to checking the existence or the absence of those two transport —and thus recombination— modes.

The two wavelengths chosen by Guo et al. are shown on a steady-state P3HT:PCBM PIA spectrum on figure 6.8. They roughly correspond to the maxima of the so–called P2 (980 nm) and DP2 (700 nm) peaks which are traditionally associated to intrachain polarons in amorphous P3HT domains (P2) and 2-dimensional polarons in the crystalline P3HT domains (DP2) (see § 5.2.2). This is consistent with the two different transport modes, as a broader energetic distribution is expected in amorphous domain due to polymer chain alignment defects.

6.6.1 Comparison with other contactless transient probing techniques

However, no trace of this trap–free transport has been found when monitoring transient decays of polarons densities by method not sensitive to the polarons absorption wavelength. On the opposite, other methods always show polarons density decays exhibiting apparent recombination orders higher than 2 in P3HT:PCBM [91, 106, 235]. In this regard, the study we carried out in association with the Delft University of Technology is of particular relevance. In this study, we compared the transients obtained by transient absorption, and those obtained by time-resolved microwave photoconductance (TRMC) [236]. TRMC being — in the same way as TA — an eletrodeless measurement, it was

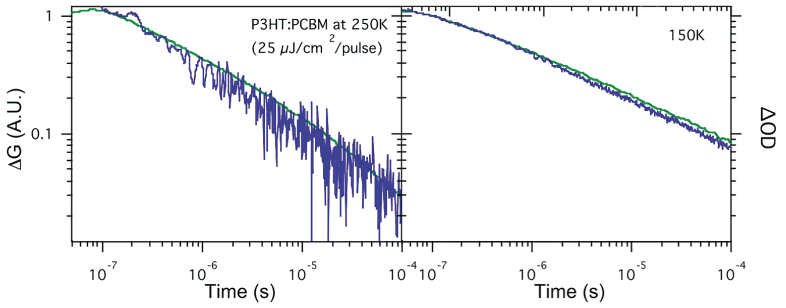

Figure 6.9: TA (blue) and TRMC (green) transients recorded on excitation at $\lambda = 500$ nm with a fluence of 25 μJ/cm^2/pulse. The amplitudes of the traces were normalized at 100 ns and plotted in a log–log representation with the y-axis ranging over 2 orders of magnitude. Adapted from Savenije et al. 2011 [236]

possible to carry out the TA and TRMC measurements on identical samples, thus insuring the comparability of the transients.

As written in the experimental section (§ 2.3), the change of microwave conductance probed by TRMC, is proportional to the product of the density of conductive species, times their mobility; or in the case of several conductive species, the sum of their mobility × density products (equation 2.16). As such it is supposed to be sensitive to the density of both kind of positive polarons, with probably the ones following a defect–free motion overweighted due to their higher mobility.

Remarkably, not only did the curves of TRMC and TA exhibit similar behavior, but they totally superposed when normalized at 100 ns[4] and this for a range of temperature between 150 and 300 K[5]. This result is reproduced in figure 6.9.

Between other consequences, the perfect superposition of both transients seems to indicate that the TA at 982 nm is representative for all polarons, unless the polarons at 700 nm exhibit a notably lower mobility which would be unexpected considering their supposed defect–free transport mode. Another possibility would be that those polarons exhibit a high mobility mainly in the direction perpendicular to the substrate,[6] as the electric field vector of the microwaves is parallel to the substrate [236].

6.6.2 Comparison of the decays at different wavelengths

After extending our setup by adding to it a white light coupled to a monochromator as a source of probing light (see § 2.1.6), we were able to reproduce the experiment of Guo et al. [57].

The results of those first measurements are shown in figure 6.10(a) and (b) in a timescale from 30 ns to 100 μs. As can be seen, very little difference exist between the two measurements. This is not in contrast with Guo et al. findings,

[4]Response time of the instruments with a certain security margin.

[5]Which is also the temperature range studied in the article of Guo et al. [57].

[6]Which is extremely unlikely according to what we know of P3HT chains preferential stacking on a substrate, see § 3.1.

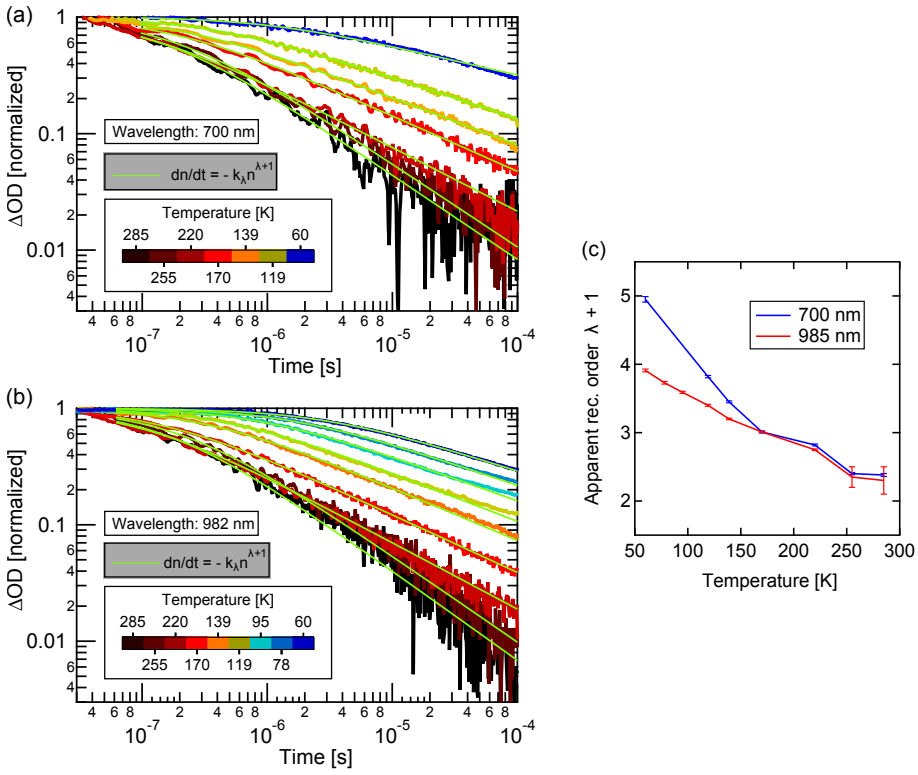

Figure 6.10: (a) Normalised transient absorption decays of annealed P3HT:PCBM blend film upon 25 μJ/cm^2 excitation on a timescale from 30 ns to 100 μs and temperatures between 60K and 285K probed at 700 nm (a) and 982 nm (b) respectively. Empirical general order fit of those transients (green lines).(c) Apparent recombination orders extracted from the general order empirical fits depicted on ((a) and (b)).

as they also mentioned the similarity of both measurements in the early stage (until 10 μs in their case). However, while Guo et al. attributed those decays to a trap-free recombination[7] characterized by a recombination order of two, our measurements clearly show the setting of a slower recombination which exhibits higher apparent recombination orders at both wavelengths.

More quantitatively, the apparent recombination orders can be extracted by applying a general recombination order fit (equation 1.45). As can be seen in figure 6.10(c), the fits are quite good and result in apparent recombination orders which are (1) very similar in their value and temperature dependence for both wavelengths, (2) largely exceeding 2. We thus reject the attribution of those early stage decays to "trap–free bimolecular recombination".

Expanding the scale until 1 ms (figure 6.11), which is the scale used by Guo et al., brings no change at 982 nm but reveals the appearance of a second kink in the decays measured at 700 nm. As shown, the decay after this kink could be interpreted as a second order. However, as the kink appears close to the end of the time window, it is uncertain if the decay curve has reaches a stable

[7]Preceding trapping for the polarons absorbing at 1000 nm.

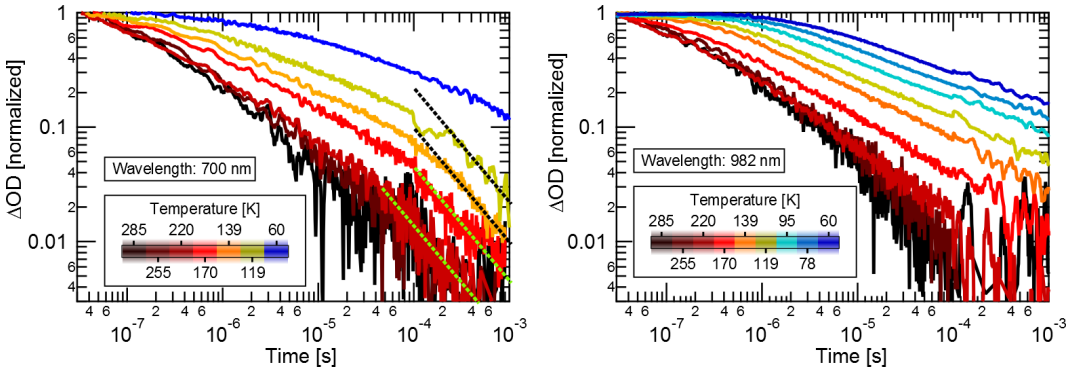

Figure 6.11: Transient absorption decays of annealed P3HT:PCBM blend film probed at 700 nm and 982 nm upon 25 μJ/cm^2 excitation on a timescale from 30 ns to 1 ms and temperatures between 60K and 285K; the dashed lines show the slope expected after the kink for a second order recombination (note that a purely bimolecular recombination should exhibit a plateau before the kink, and not a started decay as seen here).

asymptote or if the slope is still evolving.

Thanks to the use of wider time and temperature range, as well as the use of additional wavelength within the $DP2$ peak (750 and 825 nm, see figure 6.8), we were able to better resolve this second kink and the subsequent evolution of the density of polarons. As shown in figure 6.12, it can clearly be seen at 700 nm for the temperatures 60 K and 119 K, that the second order decay previously observed is actually only the transitory slope of a decay which is subsequently accelerating, without reaching an asymptote. Such a trend is characteristic of monomolecular dynamics. The same can be seen at 750 and 825 nm where it can be seen for temperatures as high as 130 K.

For higher temperatures, it is extremely likely that such a phenomenon also occurs, and that only the weakness of the signal at those temperatures prevents us from undoubtedly identifying the second kink. As a result, we assume that the decay observed by Guo et al. was not a trap–free second order recombination, but rather the onset of an unidentified monomolecular phenomena. Interestingly, such a monomolecular decay also takes place at 982 nm, though it starts at later time, which explains why it could not be observed by Guo et al.

Based on those observation, we can say, in contrast to the first conclusions obtained by Guo et al., that trap–limited recombination appears to govern the dynamics of non-geminate recombination for all wavelengths. However, the difference observed by Guo et al. between the decays of the $P2$ and $DP2$ peaks intensity indeed exists. This difference is caused by a monomolecular decay that comes in addition to the previously mentioned high apparent order recombination. The nature of this decay is still unclear. In particular, it is not known if it is due to a second polaron recombination mechanism exhibiting monomolecular dynamics (with different time constants for the polarons absorbing in the $DP2$ and $P2$ regions) or to another excited species exhibiting a monomolecular decay (and whose absorption spectra would correspond to the $DP2$ peak).

The monomolecular decay of polaron density could be due for example to

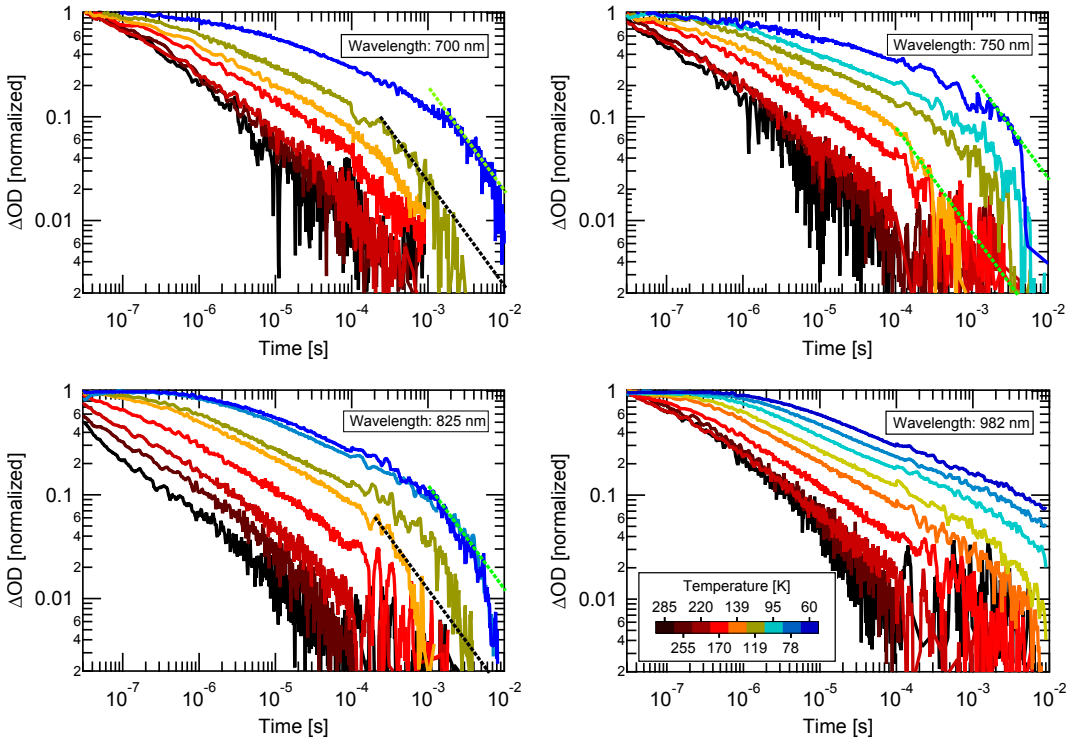

Figure 6.12: TA decays of annealed P3HT:PCBM at 700, 750, 825 and 982 nm upon 25 μJ/cm^2 excitation on a timescale from 30 ns to 10 ms and temperatures between 60K and 285K; the dashed lines show the slope expected after the kink for a second order recombination.

the existence of a deep monoenergetic trap level from where charges would be released monomolecularly with a time constant τ_r. This release of trapped charges would be the limiting factor of their recombination, thus causing a monomolecular decay. The recombination rate would thus be:

$$\frac{dp}{dt} = -k_\lambda p^\lambda - \frac{p}{\tau_r} \tag{6.12}$$

where λ and k_λ are the polarons empirical recombination order and prefactor,respectively.

In case of 2 absorbing species — the second of which could be for example triplet excitons of one of the materials having a density n_t, an absorption cross section σ_t and a lifetime τ_t — the absorption would be:

$$A = d\sigma p + d\sigma_t n_t \tag{6.13}$$

$$A(t) = d\sigma \left(p_0^{-\lambda} + t \cdot \lambda \cdot k_\lambda\right)^{-\frac{1}{\lambda}} + d\sigma_t n_{t0} e^{-t/\tau_t} \tag{6.14}$$

where d is the thickness of the sample, p_0 and n_{t0} the initial densities of positive polarons and triplets.

As seen in figure 6.13, both models can relatively well reproduce the experimental decays. The exact nature of this monomolecular decay is thus still an open question.

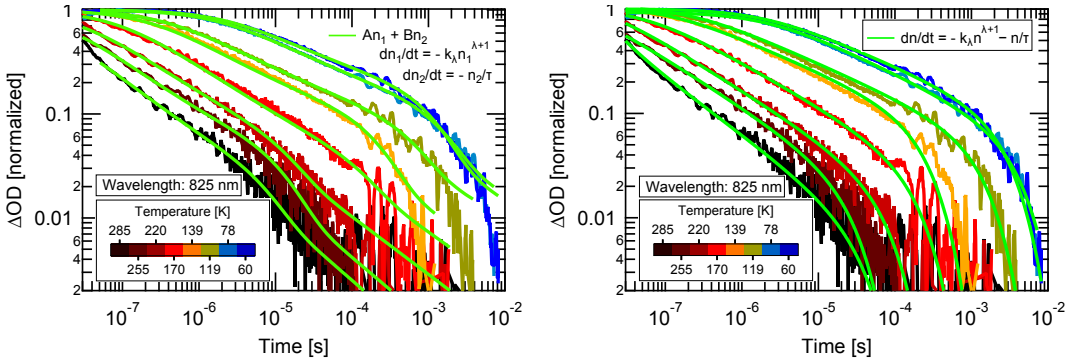

Figure 6.13: Fitting of the experimental TA decay at 825 nm by curves representing the expected decays for polarons + geminately recombining species (left) and polarons exhibiting order $\lambda + 1$ + monomolecular decays (right, adapted from Kämpgen 2011 [111, p. 47]).

6.7 Conclusions

The high order decay of the density of polarons in organic semiconductor blends, and in particular in the reference blend P3HT:PCBM, has been a long standing interrogation as well as a key point of BHJ solar cells efficiency, as decays conform to Langevin's prediction would be too quick to enable efficient charge extraction.

Thanks to a comprehensive analysis of the steady state absorption spectra of P3HT and P3HT:PCBM, we determined a temperature range where the photoinduced absorption can be used to monitor exclusively the density of polarons in both pure P3HT and the blend. We use transient absorption to monitor the nongeminate polaron decay in P3HT and P3HT:PCBM blend following an initial photoexcitation.

The comparison of the transients obtained in pristine P3HT and in P3HT:PCBM reveals that — in contrast with what is observed in the blend— polarons density decay in pure P3HT follows the Langevin theory both qualitatively (2nd order decay) and quantitatively (mobilities calculated from the experimental Langevin prefactor are quite consistent with what is usually measured in pure P3HT). This perfect agreement between the theory and the experiment brings us two crucial informations: First, it confirms that Langevin type bimolecular recombination leads to a too quick decay of polarons densities for applications in solar cells, thus pointing out the importance of the high order decay observed in the blend. Second, it suggests that the presence of several materials or phases is the main reason for the slow decay observed in the blend.

After considering several possibilities, we propose an interplay of phase separation and energetic trapping to be the cause of the high order decays observed in the blend: phase separation prevents trapped charge carriers from participating in the recombination process, which results in a stronger dependence of the recombination order upon the distributions of free and trapped charge carriers, respectively. Phase separation can additionally yield a geometrical reduction factor. Moreover, dissociation of coulombically bound polaron pairs can also lower the recombination rate. Clearly, quantitative modeling—being

both mathematically appropriate and physically representative—remains challenging. In terms of the solar cell performance, we expect that phase separation protects trapped charges from recombination, thus enabling lesser losses and an enhanced photocurrent in the coarse grained blend morphology of P3HT:PCBM as compared to finely intermixed blends. Those results have been published in the Journal of Applied Physics [237].

Following a publication by Guo et al. [57] revealing the existence in P3HT:PCBM of different two of polarons — one of which claimed to undergo trap-free transport and recombination —, we undertook additional research to check the applicability of our finding to the non-geminate recombination of those different kind of polarons. Comparison of TA (probed at 982 nm) and TRMC measurements showed a perfect match between the transients measured by both methods. Especially, no indication of trap–free second order recombination could be found in the TRMC transients. Those two methods should a priori not be sensitive to the same polarons, the absorption at 982 nm being attributed by Guo et al. to polarons located in amorphous parts of the blend, thus less mobile, whereas TRMC is more sensitive to the charges with the highest mobility. As a result the fact that both TRMC and TA perfectly superpose, speaks in favor of the generality of the slow–decay observed at 982 nm. This comparative study has been published in the Journal of Physical Chemistry Letters in 2011 [236].

Reproducing the TA measurements of Guo et al. at 700 nm we confirmed that, in contrast to their observation, trap–limited recombination is also observed at 700 nm. Moreover, the decay at 700 nm that they attributed to trap–free bimolecular recombination was found to be most likely the onset of a monomolecular decay coming additionally to the aforementioned trap–limited recombination. This monomolecular decay was also found at all the wavelengths studied within the $DP2$ peak, a similar decay but shifted to later times was also found at 982 nm.

The nature of this kink being still in need for clarification, it is not known yet whether two different kind of polarons are indeed present in the blend, or if the two features $P2$ and $DP2$ are due to polarons only and polarons plus something else, respectively. Nevertheless we are now sure that all the polarons detected by transient absorption undergo trap–limited recombination and that this trap–limited recombination is made possible thanks to the presence of two materials and do not exist in the pristine polymer's films. These findings represent an important step in our understanding of non–geminate recombination in organic semiconductors.

Summary

In the course of this dissertation, we have presented the interest of using spectroscopic methods to unravel the physics of polymer semiconductors in photovoltaic applications. Applying photoluminescence and photoinduced absorption spectroscopy to the reference system P3HT:PCBM has enabled us to study the major steps of photocurrent generation in organic bulk heterojunctions, from excitons generation to charges extraction and loss mechanisms and thus to improve the understanding of those mechanisms.

The exciton binding energy, is the first obstacle to overcome for photocurrent generation in organic solar cell and the reason for the use of two materials, whose heterojunction act as a driving force for charge separation. We developed an original photoluminescence-detected field-induced exciton quenching method to investigate this energy. Absorption and photoluminescence spectra of pure P3HT show that, while both amorphous and crystalline domains participate in absorption, the energy is then transferred to the crystalline domains, from where the photoluminescence is exclusively originating. The field dependence of this photoluminescence showed that an energy of no less than 420 meV is necessary to split excitons into non photon–emitting species. Comparing those results with energy levels obtained by absorption and photoelectron spectroscopies,[8] confirmed that the formation of those species is only a first step toward dissociation into free charges. Indeed, photoemission spectroscopy and the onset of photocurrent upon increasing the photon energy in a pure P3HT solar cell, concomitantly show that the energy level of a pair of free polarons is located 0.7 eV above the one of the exciton. The comprehensive analysis of those results originating from those different method enable us to draw a global picture of the states and energies involved in free polarons generation in pure material. This work has been widely acknowledged by the scientific community, published in Physical Review B in 2010 [82] and presented in national [238] and international [239] conferences.

The spectroscopy of excited states is used to detect the presence of wanted species (charges) and potentially unwanted neutral species upon photoexcitation. As such, it offers us the possibility to qualify the efficiency of charge generation and, if any, identify the competing processes and the generation of unwanted species. In the frame of the European Marie Curie Research Network SolarNType,[9] this possibility was used — in combination with morphological, charge transport and devices characterizations — to study a number of new donor–acceptor blends. Thanks to those techniques, we were able to not only

[8] Collaboration with the chair of experimental physics VII.

[9] Marie-Curie RTN "SolarNTyp" Contract No. MRTN-CT-2006-035533.

quantify the potential of those blends, but also to provide the chemist laboratories with a precious and detailed feedback on the strengths and weakness of the molecules, regarding charge generation, transport and extraction. The detailed study of terrylene-3,4:11,12-bis(dicarboximide) as electron acceptor for solar cells application was published in the peer review journal Synthetic Metals and was chosen to illustrate the cover page of the issue [220].

Finally, in the last chapter, we have used time resolved photoinduced absorption to improve the understanding of the charge carrier loss mechanisms in P3HT:PCBM active layers. This comprehension is of prime importance because, the fact that this recombination is far weaker than expected from the Langevin theory, enable polarons to travel further without recombining and thus to build thicker and more efficient devices. A comprehensive analysis of steady-state PIA spectra of pure P3HT, indicates that probing at 980 nm at a temperature between 140 and 250 K enables to monitor specifically polaron densities in both neat P3HT and P3HT:PCBM. Applying this finding to transient absorption enabled us to monitor, for the first time, the bimolecular recombination in pure P3HT, and to discover that — in sharp contrast with the blend — this recombination was in agreement with the Langevin theory. Moreover, it enables us to pinpoint the important role played by the existence of two materials and of energetical traps in the slow recombination and high recombination orders observed in the blend. This work has been published in the Journal of Applied Physics. [237]

Those new insights in the photophysics of polymer:fullerene photoactive layers could have a strong impact on the future developement of those materials. Consistent measurements of the binding energy of excitons and intermediate species, would enable to clarify the role played by excess thermal energy in interfacial states dissociation [54, 73–75, 240]. Better understanding of blends morphology and its influence on solar cells parameters and in particular on recombination could enable to reproduce the conditions of limited recombination on material systems offering some promising performances but with only limited active layer thicknesses [240]. However, due to the number of parameters involved, further experimentation is required, before we can reach a quantitative modeling of bimolecular recombination.

Zusammenfassung

In der vorliegenden Arbeit wurden die zugrundeliegenden Mechanismen, die während der Photostromgeneration in Polymer:Fulleren-Solarzellen stattfinden, von der Exzitonengeneration bis zur Ladungsträgerextraktion, mittels spektroskopischer Methoden untersucht.

Nach der Absorption eines Photons ist die Exzitonenbindungsenergie das erste zu überwindende Hindernis, um einen Photostrom in organischen Halbleitern zu generieren. Diese begründet die Notwendigkeit, zwei unterschiedliche Halbleitermaterialien zu implementieren, deren energetischer Offset die treibende Kraft für Exzitonentrennung am Heterogrenzfläsche bildet. Zur Erforschung dieser Energie haben wir eine neuartige Methode entwickelt, mit welcher wurden Einfluss eines elektrischen Feldes auf die Exzitonen durch Photolumineszenzmessungen quantifizieren können. Aus Absorptions- und Photolumineszenzspektren ist ersichtlich, dass im reinen P3HT sowohl amorphe als auch kristalline Bereiche zur Absorption beitragen. Daraufhin erfolgt ein anschließender effektiver Energietransfer zu den kristallinen Domänen, der durch die ausschließlich in diesen Bereichen auftretende Photolumineszenz nachgewiesen wird. Diese Exzitonen sind als *interchain excitons* bekannt, die bereits bei 0.42 eV; in nicht emittierende Spezies dissoziiert werden können, wie unsere feldabhängigen Photolumineszenzmessungen zeigen. Mit Hilfe komplementärer Methoden konnten wir nachweisen, dass diese Dissoziation nur ein erster Schritt zur Generation freier Ladungsträger ist. So konnte durch Photoelektronenspektroskopie [10] und Messungen der externen Quanteneffizienz gezeigt werden, dass die Erstellung freier Ladungsträger 0.7 eV benötigt. Die zusammenführende Analyse dieser Ergebnisse ermöglicht die Erstellung eines umfassenden Bildes der für die Photostromgeneration relevanten Energieniveaus in reinem P3HT. Desweiteren wurden die Ergebnisse dieser Arbeit national [238] als auch international [239] auf Konferenzen präsentiert und im Jahr 2010 in Physical Review B [82] publiziert. Die Tatsache, dass diese bereits über 50 mal zitiert wurden, verdeutlicht die große Bedeutung der erlangten Resultate.

Durch die Verwendung der Quasi-Steady-State-Spektroskopie angeregter Spezies können unter Beleuchtung erwünschte (Ladungsträger) und unerwünschte (neutrale) Zustände detektiert werden. Im Rahmen des EU-Projekts "SolarNType",[11] wurden dazu mehrere, als Elektronenakzeptor dienende, Moleküle teilnehmender Institutionen untersucht. Mit Hilfe unserer spektroskopischen Methode und durch ergänzende Messungen des Ladunsträgerstransports sowie der Morphologie und Strom-Spannungs-Charakteristiken der Solarzellen waren wir im Stande,

[10] In Kollaboration mit dem Lehrstuhl für experimentelle Physik VII.
[11] Marie-Curie RTN "SolarNTyp"; Contract No. MRTN-CT-2006-035533.

nicht nur das Potential dieser Moleküle zu beurteilen, sondern auch unseren Projektmitarbeitern detaillierte und wertvolle Informationen über die Stärken und Schwächen der von ihnen synthetisierten Materialien zu geben. Die detaillierte Untersuchung von terrylene-3,4:11,12-bis(dicarboximide) als Elektronenakzeptor, welche wir für das Max-Planck-Institut in Mainz erstellten, wurde im Jahr 2012 in *Synthetic Metals* publiziert und für die Titelseite ausgewählt. [220]

Im letzten Abschnitt werden die Ergebnisse transienter photoinduzierter Absorptionsmessungen diskutiert, welche zur Bestimmung der Rekombination freier Ladunsträger in P3HT:PCBM-Mischschichten durchgeführt wurden. Diese Rekombination ist dafür bekannt, nicht der Langevin-Theorie zu folgen, was für Solarzellen von großer Bedeutung ist. Anstelle von Rekombination zweiter Ordnung nach der Langevin-Theorie, rekombinieren Ladungsträger in dieser Materialkombination unter höherer Ordnung und einem starken zusätzlichen Reduktionsfaktor. Dies hat zur Folge, dass die Ladungsträger weiter diffundieren können, was die Erstellung dickerer und daher effizienterer Solarzellen ermöglicht. Durch umfassende Analysen der P3HT Quasi-Steady-State-Spektren wurde ein spektraler sowie thermischer Bereich identifiziert, in dem in reinem P3HT ausschließlich Polaronen für die Absorption verantwortlich sind. Die Verwendung dieser Ergebnisse in transienten Absorptionsmessungen ermöglichte es erstmals, das Rekombinationsverhalten in reinen sowie mit PCBM gemischten P3HT-Schichten zu vergleichen. Es zeigt sich, dass die Abnahme der Ladungsträgerdichte in reinem P3HT der Langevin-Theorie perfekt folgt. Demzufolge scheint die beobachtete limitierte Rekombination in gemischten P3HT:PCBM-Schichten aus der Präsenz zweier unterschiedlicher Materialien zu resultieren. Nach der Betrachtung mehrerer möglicher Mechanismen kommen wir zu dem Schluss, dass eine Kombination von energetischem Trapping und Phasenseparation für dieses Verhalten verantwortlich ist. Diese Ergebnisse wurden im Jahr 2014 in *the Journal of Applied Physics* publizierrt.

Die erlangten neuen Einblicke in die photophysischen Eigenschaften von Polymer:Fulleren-Mischschichten besitzen große Bedeutung für die weitere Entwicklung in diesem Bereich. Systematische Messungen der Bindungsenergien von Exzitonen sowie Polaronenpaaren scheinen eine vielversprechende Methode zu sein, die Bedeutung der Exzitonen-Überschussenergie für die Photostromgeneration zu verstehen. [54, 73–75, 240] Ein besseres Verständnis der Mischungsmorphologie sowie ihren Einfluss auf die bimolekulare Rekombinationsdynamik bahnt den Weg zur Steigerung der Leistung in vielversprechenden Materialsystemen, die bisher durch die limitierte Dicke der Solarzellen eingeschränkt ist. [240] Allerdings bedingt die große Anzahl an Faktoren, die in diesen Rekombinationsmechanismen eine Rolle spielen, weitere fundierte experimentelle Ergebnisse, bevor eine quantitative Modellierung der Prozesse erreicht werden kann.

Bibliography

[1] B. Metz, O. R. Davidson, P. R. Bosch, R. Dave, and L. A. Meyer, editors. *Climate Change 2007: Mitigation. Contribution of Working Group III to the Fourth Assessment Report of the Intergovernmental Panel on Climate Change*. Cambridge University Press, Cambridge, United Kingdom and New York, NY, USA., 2007.

[2] O. Edenhofer, R. Pichs-Madruga, Y. Sokona, K. Seyboth, P. Matschoss, S. Kadner, T. Zwickel, P. Eickemeier, G. Hansen, S. Schloemer, and C. von Stechow, editors. *Renewable Energy Sources and Climate Change Mitigation, Special Report of the Intergovernmental Panel on Climate Change*. Cambridge University Press, Cambridge, United Kingdom and New York, NY, USA, 2011.

[3] I. E. A. (IEA), editor. *Energy Balances of non-OECD Countries 2010*. OECD Publishing, Paris, France, 2010.

[4] I. E. A. (IEA), editor. *World Energy Outlook 2010*. OECD Publishing, Paris, France, 2010.

[5] R. Gelman. 2011 Renewable Energy Data Book. Technical report, National Renewable Energy Laboratory (NREL), Golden, CO., October 2012, revised 2013.

[6] K. Ardani and R. Margolis. 2010 Solar Technologies Market Report. Energy Efficiency & Renewable Energy (EERE). Technical report, National Renewable Energy Laboratory (NREL), Golden, CO., November 2011.

[7] P. Mint. Photovoltaic Manufacturer Shipments, Capacity, & Competitive Analysis 2010/2011. Technical Report Report NPS-Supply6, Palo Alto, CA: Navigant Consulting Photovoltaic Service Program., 2011.

[8] K. L. Chopra, P. D. Paulson, and V. Dutta. Thin-film solar cells: an overview. *Progress in Photovoltaics: Research and Applications*, 12:69, 2004.

[9] F. C. Krebs. Fabrication and processing of polymer solar cells: A review of printing and coating techniques. *Sol. Ener. Mat. Sol. Cells*, 93:394, 2009.

[10] E. Wang, L. Wang, L. Lan, C. Luo, W. Zhuang, J. Peng, and Y. Cao. High-performance polymer heterojunction solar cells of a polysilafluorene derivative. *Appl. Phys. Lett.*, 92(3):033307, 2008.

[11] S. Park, A.Roy, S.Beaupre, S.Cho, N.Coates, J.S.Moon, M.Leclerc, K.Lee, A. Heeger, and D.Moses. Bulk heterojunction solar cells with internal quantum efficiency approaching 100%. *Nat. Phys.*, 3:297, may 2009.

[12] Y. Zou, A. Najari, P. Berrouard, S. Beaupré, B. Réa Aïch, Y. Tao, and M. Leclerc. A thieno[3,4-c]pyrrole-4,6-dione-based copolymer for efficient solar cells. *J. Am. Chem. Soc.*, 132(15):5330–5331, 2010. PMID: 20349958.

[13] H.-Y. Chen, J. Hou, S. Zhang, Y. Liang, G. Yang, Y. Yang, L. Yu, Y. Wu, and G. Li. Polymer solar cells with enhanced open-circuit voltage and efficiency. *Nat. Phys.*, 3:649, 2009.

[14] Y. Liang, Y. Wu, D. Feng, S.-T. Tsai, H.-J. Son, G. Li, and L. Yu. Development of new semiconducting polymers for high performance solar cells. *J. Am. Chem. Soc.*, 131(1):56–57, 2009.

[15] Y. Liang, D. Feng, Y. Wu, S.-T. Tsai, G. Li, C. Ray, and L. Yu. Highly efficient solar cell polymers developed via fine-tuning of structural and electronic properties. *J. Am. Chem. Soc.*, 131(22):7792–7799, 2009.

[16] J. Hou, H.-Y. Chen, S. Zhang, R. I. Chen, Y. Yang, Y. Wu, and G. Li. Synthesis of a low band gap polymer and its application in highly efficient polymer solar cells. *J. Am. Chem. Soc.*, 131(43):15586–15587, 2009.

[17] R. F. Service. Outlook brightens for plastic solar cells. *Science*, 332:293, 2011.

[18] M. A. Green, K. Emery, Y. Hishikawa, W. Warta, and E. D. Dunlop. Solar cell efficiency tables (version 42). *Progress in Photovoltaics: Research and Applications*, 21(5):827–837, 2013.

[19] D. M. Tanenbaum, M. Hermenau, E. Voroshazi, M. T. Lloyd, Y. Galagan, B. Zimmermann, M. Hosel, H. F. Dam, M. Jorgensen, S. A. Gevorgyan, S. Kudret, W. Maes, L. Lutsen, D. Vanderzande, U. Wurfel, R. Andriessen, R. Rosch, H. Hoppe, G. Teran-Escobar, M. Lira-Cantu, A. Rivaton, G. Y. Uzunoglu, D. Germack, B. Andreasen, M. V. Madsen, K. Norrman, and F. C. Krebs. The isos-3 inter-laboratory collaboration focused on the stability of a variety of organic photovoltaic devices. *RSC Adv.*, 2:882–893, 2012.

[20] M. Jørgensen, K. Norrman, S. A. Gevorgyan, T. Tromholt, B. Andreasen, and F. C. Krebs. Stability of polymer solar cells. *Adv. Mater.*, 24(5):580–612, 2012.

[21] M. Pope and C. E. Swenberg. *Electronic Processes in Organic Crystals and Polymers*. Oxford University Press, USA, 2nd edition, 1999.

[22] H. Mustroph and S. Ernst. Das Franck-Condon-Prinzip. *Chemie in unserer Zeit*, 45(4):256–269, 2011.

[23] P. Atkins and J. de Paula. *Atkins' Physical Chemistry*. Oxford University Press, 7^{th} edition, 2002.

[24] K. Sakurai, H. Tachibana, N. Shiga, C. Terakura, M. Matsumoto, and Y. Tokura. Experimental determination of excitonic structure in polythiophene. *Phys. Rev. B*, 56:9552–9556, 1997.

[25] F. Hirayama, T. Gregory, and S. Lipsky. Fluorescence from highly excited-states of some aromatic molecules in solution. *J. Phys. Chem.*, 58(10):4696–4697, 1973.

[26] M. Kasha. Characterization of electronic transitions in complex molecules. *Discuss. Faraday Soc.*, 9:14–19, 1950.

[27] S. P. McGlynn, T. Azumi, and M. Kinoshita. *Molecular spectroscopy of the triplet state*. Englewood Cliffs, N.J. : Prentice-Hall, 1969.

[28] S. Brazovskii and N. Kirova. Physical theory of excitons in conducting polymers. *Chem. Soc. Rev.*, 39:2453–2465, 2010.

[29] I. Berlman. *Handbook of fluorescence spectra of aromatic molecules*. Academic Press, 1965.

[30] M. Liedtke. *Optische Untersuchung photogenerierter Zustände in konjugierten Polymeren und Polymer-Fulleren Gemischen*. Diplomarbeit, Physikalisches Institut der Julius-Maximilians-Universität Würzburg, 2006.

[31] M. Kasha. Molecular excitons in small aggregates. In B. Dibartole, editor, *Spectroscopy of the Excited State*. Plenum Press, New York, 1976.

[32] X. Jiang, R. Österbacka, O. Korovyanko, C. P. An, B. Horovitz, R. A. J. Janssen, and Z. V. Vardeny. Spectroscopic studies of photoexcitations in regioregular and regiorandom polythiophene films. *Adv. Funct. Mater.*, 12:587, 2002.

[33] S. Yang, X. Zhang, Y. Hou, Z. Deng, and X. Xu. Charge carriers at organic heterojunction interface: Exciplex emission or electroplex emission? *J. Appl. Phys.*, 101:096101, 2007.

[34] R. Huenerbein and S. Grimme. Time-dependent density functional study of excimers and exciplexes of organic molecules. *Chem. Phys.*, 343:362, 2008.

[35] S. A. Jenekhe and J. A. Osaheni. Excimers and exciplexes of conjugated polymers. *Science*, 265:765–767, 1994.

[36] T. M. Clarke and J. R. Durrant. Charge photogeneration in organic solar cells. *Chem. Rev.*, 110(11):6736–6767, 2010.

[37] N. Geacintov and C. Swenberg. Magnetic field effects in organic spectroscopy. In M. Lumb, editor, *Luminescence spectroscopy*. Academic Press, 1978.

[38] A. P. Langner. *Wachstum und optische Anregung in dünnen Tetracenfilmen auf einkristallinen Oberflächen*. PhD thesis, Mathematisch-Naturwissenschaftlichen Fakultät der Rheinischen Friedrich-Wilhelms-Universität Bonn, 2005.

[39] A. Matsui and Y. Oeda. Density of states and the exciton band structure in crystalline anthracene. In *6th Mol. Cryst. Symp.*, pages 41–44, Schoss Elmau, Germany, 20-25 May 1973.

[40] N. Kirova, S. Brazovskii, and A. Bishop. A systematic theory for optical properties of phenylene-based polymers. *Synth. Met.*, 100(1):29 – 53, 1999.

[41] S. Webster and D. Batchelder. Absorption, luminescence and Raman spectroscopy of poly(p-phenylene vinylene) at high pressure. *Polymers*, 37(22):4961 – 4968, 1996. Symposium commemorating the 35th anniversary of Polymer.

[42] E. Olejnik, S. Singh, B.Pndit, V. Morandi, J. Holt, C. X. Sheng, and Z. V. Vardeny. Optical probes of MEH-PPV films at high hydrostatic pressure. In *MAR10 Meeting of The American Physical Society*, 2010.

[43] N. Kirova. New insight to excitons in optically active polymers. Presented in the University of Würzburg, 28-07-2011, July 2011.

[44] F. C. Spano. Modeling disorder in polymer aggregates: The optical spectroscopy of regioregular poly(3-hexylthiophene) thin films. *J. Chem. Phys.*, 122:234701, 2005.

[45] T. J. Savenije, J. E. Kroeze, X. Yang, and J. Loos. The effect of thermal treatment on the morphology and charge carrier dynamics in a polythiophene-fullerene bulk heterojunction. *Adv. Funct. Mater.*, 15:1260, 2005.

[46] G. Schönherr, R. Eiermann, H. Bässler, and M. Silver. Dispersive exciton transport in a hopping system with gaussian energy distribution. *Chem. Phys.*, 52:287, 1980.

[47] R. Hesse, W. Hofberger, and H. Bässler. Absorption spectra of disordered solid tetracene and pentacene. *Chem. Phys.*, 49(2):201 – 211, 1980.

[48] J. Klafter and J. Jortner. Urbach rule in the optical spectra of crystalline and amorphous organic-solids. *Chem. Phys.*, 26(3):421 – 430, 1977.

[49] E. Knapp. Lineshapes of molecular aggregates, exchange narrowing and intersite correlation. *Chem. Phys.*, 85(1):73 – 82, 1984.

[50] S. T. Hoffmann, H. Bässler, J.-M. Koenen, M. Forster, U. Scherf, E. Scheler, P. Strohriegl, and A. Köhler. Spectral diffusion in poly(*para* -phenylene)-type polymers with different energetic disorder. *Phys. Rev. B*, 81:115103, Mar 2010.

[51] M. Theander, A. Yartsev, D. Zigmantas, V. Sundström, W. Mammo, M. R. Andersson, and O. Inganäs. Photoluminescence quenching at a polythiophene–C60 heterojunction. *Phys. Rev. B*, 61:12957, 2000.

[52] A. Huijser, T. J. Savenije, A. Shalav, and L. D. A. Siebbeles. An experimental study on the molecular organization and exciton diffusion in a bilayer of a porphyrin and poly(3-hexylthiophene). *J. Appl. Phys.*, 104:034505, 2008.

[53] R. Jakubiak, C. J. Collison, W. C. Wan, L. J. Rothberg, and B. R. Hsieh. Aggregation quenching of luminescence in electroluminescent conjugated polymers. *J. Phys. Chem. A*, 103(14):2394–2398, 1999.

[54] H. Ohkita, S. Cook, Y. Astuti, W. Duffy, S. Tierney, W. Zhang, M. Heeney, I. McCulloch, J. Nelson, D. D. C. Bradley, and J. R. Durrant. Charge carrier formation in polythiophene/fullerene blend films studied by transient absorption spectroscopy. *J. Am. Chem. Soc.*, 130:3030, 2008.

[55] I. D. W. Samuel, G. Rumbles, and C. J. Collison. Efficient interchain photoluminescence in a high-electron-affinity conjugated polymer. *Phys. Rev. B*, 52:R11573–R11576, Oct 1995.

[56] S. W. Thomas, G. D. Joly, and T. M. Swager. Chemical sensors based on amplifying fluorescent conjugated polymers. *Chemical Reviews*, 107(4):1339–1386, 2007.

[57] J. Guo, H. Ohkita, S. Yokoya, H. Benten, and S. Ito. Bimodal polarons and hole transport in poly(3-hexylthiophene):fullerene blend films. *J. Am. Chem. Soc.*, 132:9631, 2010.

[58] V. I. Arkhipov, I. I. Fishchuk, A. Kadashchuk, and H. Bässler. *Photophysics of Molecular Materials*, chapter 6, Charge Transport in Disordered Organic Semiconductors, page 261. WILEY-VCH Verlag GmbH & Co. KGaA, Weinheim, 2006.

[59] C. Deibel and V. Dyakonov. Polymer–fullerene bulk heterojunction solar cells. *Rep. Prog. Phys.*, 73:096401, 2010.

[60] A. C. Mayer, M. F. Toney, S. R. Scully, J. Rivnay, C. J. Brabec, M. Scharber, M. Koppe, M. Heeney, I. McCulloch, and M. D. McGehee. Bimolecular crystals of fullerenes in conjugated polymers and the implications of molecular mixing for solar cells. *Adv. Funct. Mater.*, 19:1173, 2009.

[61] N. C. Cates, R. Gysel, Z. Beiley, C. E. Miller, M. F. Toney, M. Heeney, I. McCulloch, and M. D. McGehee. Tuning the properties of polymer bulk heterojunction solar cells by adjusting fullerene size to control intercalation. *Nano Lett.*, 9:4153, 2009.

[62] A. Baumann, T. J. Savenije, D. H. K. Murthy, M. Heeney, V. Dyakonov, and C. Deibel. Influence of phase segregation on recombination dynamics in organic bulk-heterojunction solar cells. *Adv. Funct. Mater.*, 21(9):1687—-1692, 2011.

[63] J. Y. Kim and C. D. Frisbie. Correlation of Phase Behavior and Charge Transport in Conjugated Polymer/Fullerene Blends. *J. Phys. Chem. A*, 112:17726, 2008.

[64] D. Cheyns, K. Vasseur, C. Rolin, J. Genoe, J. Poortmans, and P. Heremans. Nanoimprinted semiconducting polymer films with 50 nm features and their application to organic heterojunction solar cells. *Nanotechn.*, 19:424016, 2008.

[65] J. J. Benson-Smith, L. Goris, K. Vandewal, K. Haenen, J. V. Manca, D. Vanderzande, D. D. C. Bradley, and J. Nelson. Formation of a ground-state charge-transfer complex in polyfluorene//[6,6]-phenyl-C61 butyric acid methyl ester (PCBM) blend films and its role in the function of polymer/PCBM solar cells. *Adv. Funct. Mater.*, 17:451, 2007.

[66] J. J. Benson-Smith, H. Ohkita, S. Cook, J. R. Durrant, D. D. C. Bradley, and J. Nelson. Charge separation and fullerene triplet formation in blend films of polyfluorene polymers with [6,6]-phenyl C61 butyric acid methyl ester. *Dalton Trans.*, pages 10000–10005, 2009.

[67] J. J. M. Halls, J. Cornil, D. A. dos Santos, R. Silbey, D.-H. Hwang, A. B. Holmes, J. L. Brédas, and R. H. Friend. Charge- and energy-transfer processes at polymer/polymer interfaces: A joint experimental and theoretical study. *Phys. Rev. B*, 60:5721, 1999.

[68] T. I. Hukka, T. Toivonen, E. Hennebicq, J.-L. Brédas, R. A. J. Janssen, and D. J.Beljonne. Pathways for resonant energy transfer in oligo(phenylenevinylene)–fullerene dyads: An atomistic model. *Adv. Mater.*, 18(10):1301–1306, 2006.

[69] P. A. van Hal, R. A. J. Janssen, G. Lanzani, G. Cerullo, M. Zavelani-Rossi, and S. D. Silvestri. Two-step mechanism for the photoinduced intramolecular electron transfer in oligo(p-phenylene vinylene)-fullerene dyads. *Phys. Rev. B*, 64:075206, 2001.

[70] J.-L. Brédas, J. E. Norton, J. Cornil, and V. Coropceanu. Molecular understanding of organic solar cells: The challenges. *Acc. Chem. Res.*, 42:1691, 2009.

[71] K. Vandewal, L. Goris, I. Haeldermans, M. Nesladek, K. Haenen, P. Wagner, and J. Manca. Fourier-transform photocurrent spectroscopy for a fast and highly sensitive spectral characterization of organic and hybrid solar cells. *Thin Solid Films*, 516:7135, 2008.

[72] J. Kern, S. Schwab, C. Deibel, and V. Dyakonov. Binding energy of singlet excitons and charge transfer complexes in MDMO-PPV:PCBM solar cells. *physica status solidi (RRL) – Rapid Research Letters*, 5(10-11):364–366, 2011.

[73] T. M. Clarke, A. M. Ballantyne, J. Nelson, D. D. C. Bradley, and J. R. Durrant. Free Energy Control of Charge Photogeneration in Polythiophene/Fullerene Solar Cells: The Influence of Thermal Annealing on P3HT/PCBM Blends. *Adv. Funct. Mater.*, 18(24):4029–4035, 2008.

[74] T. Clarke, A. Ballantyne, F. Jamieson, C. Brabec, J. Nelson, and J. Durrant. Transient absorption spectroscopy of charge photogeneration yields and lifetimes in a low bandgap polymer/fullerene film. *Chem. Comm.*, pages 89–91, 2008.

[75] P. E. Keivanidis, T. M. Clarke, S. Lilliu, T. Agostinelli, J. E. Macdonald, J. R. Durrant, D. D. C. Bradley, and J. Nelson. Dependence of Charge Separation Efficiency on Film Microstructure in Poly(3-hexylthiophene-2,5-diyl):[6,6]-Phenyl-C61 Butyric Acid Methyl Ester Blend Films. *J. Phys. Chem. C*, 1(4):734–738, 2010.

[76] T. Offermans, P. A. van Hal, S. C. J. Meskers, M. M. Koetse, and R. A. J. Janssen. Exciplex dynamics in a blend of π-conjugated polymers with electron donating and accepting properties: MDMO-PPV and PCNEPV. *Phys. Rev. B*, 72(4):045213, 2005.

[77] C. Yin, T. Kietzke, D. Neher, and H.-H. Horhold. Photovoltaic properties and exciplex emission of polyphenylenevinylene-based blend solar cells. *Appl. Phys. Lett.*, 90:092117, 2007.

[78] T. G. J. van der Hofstad, D. Di Nuzzo, M. van den Berg, R. A. J. Janssen, and S. C. J. Meskers. Influence of Photon Excess Energy on Charge Carrier Dynamics in a Polymer-Fullerene Solar Cell. *Adv. Ener. Mater.*, 2(9):1095–1099, 2012.

[79] J. Lee, K. Vandewal, S. R. Yost, M. E. Bahlke, L. Goris, M. A. Baldo, J. V. Manca, and T. V. Voorhis. Charge transfer state versus hot exciton dissociation in polymer-fullerene blended solar cells. *J. Am. Chem. Soc.*, 132(34):11878–11880, 2010.

[80] C. L. Braun. Electric field assisted dissociation of charge transfer states as a mechanism of photocarrier production. *J. Chem. Phys.*, 80(9):4157, 1984.

[81] D. Moses, J. Wang, A. J. Heeger, N. Kirova, and S. Brazovski. Singlet exciton binding energy in poly(phenylene vinylene). *P. Nat. Acad. Sci.*, 98:13496, 2001.

[82] C. Deibel, D. Mack, J. Gorenflot, A. Schöll, S. Krause, F. Reinert, D. Rauh, and V. Dyakonov. Energy levels and exciton binding energy in the conjugated polymer poly(3-hexyl thiophene). *Phys. Rev. B*, 81:085202, 2010.

[83] D. Veldman, Ö. Ipek, S. C. J. Meskers, J. Sweelssen, M. M. Koetse, S. C. Veenstra, J. M. Kron, S. S. van Bavel, J. Loos, and R. A. J. Janssen. Compositional and electric field dependence of the dissociation of charge transfer excitons in alternating polyfluorene copolymer/fullerene blends. *J. Am. Chem. Soc.*, 130:7721, 2008.

[84] T. Offermans, S. C. J. Meskers, and R. A. J. Janssen. Monte-Carlo simulations of geminate electron-hole pair dissociation in a molecular heterojunction: a two-step dissociation mechanism. *Chem. Phys.*, 308:125, 2005.

[85] R. H. Batt, C. L. Braun, and J. F. Hornig. Field and temperature dependent recombination in anthracene. *Appl. Opt.*, 8(S1):20–24, Jan 1969.

[86] M. Samoc and D. F. Williams. Photoconductivity in crystals of charge-transfer complex anthracene–tetracyanobenzene. *J. Chem. Phys.*, 78(4):1924–1930, 1983.

[87] A. A. Lipnik. Binding and Decay of the Mott Exciton by Phonons and Impurity Centers. *Soviet Physics-Solid State*, 3(8):1683–1689, 1962.

[88] A. A. Lipnik. Certain Characteristics of the Process of Pair Coupling to form an Exciton and Exciton Dissociation by Phonons - Effect of these Processes on the Behavior of Nonequilibrium Carriers. *Soviet Physics-Solid State*, 6(4):823–827, 1964.

[89] M. Fuoss and F. Accascina. *Electrolytic Conductance*. Interscience, New York, 1959.

[90] L. Onsager. Deviations from Ohm's law in weak electrolytes. *J. Chem. Phys.*, 2:599, 1934.

[91] M. Mingebach, S. Walter, V. Dyakonov, and C. Deibel. Direct and charge transfer state mediated photogeneration in polymer–fullerene bulk heterojunction solar cells. *Appl. Phys. Lett.*, 100(19):193302, 2012.

[92] D. E. Markov, E. Amsterdam, P. W. M. Blom, A. B. Sieval, and J. C. Hummelen. Accurate measurement of the exciton diffusion length in a conjugated polymer using a heterostructure with a side-chain cross-linked fullerene layer. *J. Phys. Chem. A*, 109:5266, 2005.

[93] V. D. Mihailetchi, L. J. A. Koster, J. C. Hummelen, and P. W. M. Blom. Photocurrent generation in polymer-fullerene bulk heterojunctions. *Phys. Rev. Lett.*, 93:216601, 2004.

[94] S. Verlaak, D. Beljonne, D. Cheyns, C. Rolin, M. Linares, F. Castet, J. Cornil, and P. Heremans. Electronic structure and geminate pair energetics at organic/organic interfaces: The case of pentacene/C60 heterojunctions. *Adv. Funct. Mater.*, 19:3809, 2009.

[95] H. Bässler. Charge transport in disordered organic photoconductors — A monte carlo simulation study. *Phys. Stat. Sol. B*, 175:15, 1993.

[96] A. Miller and E. Abrahams. Impurity conduction at low concentrations. *Phys. Rev.*, 120:745, 1960.

[97] S. Albrecht, W. Schindler, J. Kurpiers, J. Kniepert, J. C. Blakesley, I. Dumsch, S. Allard, K. Fostiropoulos, U. Scherf, and D. Neher. On the Field Dependence of Free Charge Carrier Generation and Recombination in Blends of PCPDTBT/PC70BM: Influence of Solvent Additives. *J. Phys. Chem. Lett.*, 3(5):640–645, 2012.

[98] C. M. Ramsdale, J. A. Barker, A. C. Arias, J. D. MacKenzie, R. H. Friend, and N. C. Greenham. The origin of the open-circuit voltage in polyfluorene-based photovoltaic devices. *J. Appl. Phys.*, 92:4266, 2002.

[99] I. A. Howard, R. Mauer, M. Meister, and F. Laquai. Effect of morphology on ultrafast free carrier generation in polythiophene:fullerene organic solar cells. *J. Am. Chem. Soc.*, 132:14866, 2010.

[100] A. J. Ferguson, N. Kopidakis, S. E. Shaheen, and G. Rumbles. Dark Carriers, Trapping, and Activation Control of Carrier Recombination in Neat P3HT and P3HT:PCBM Blends. *J. Phys. Chem. C*, 115(46):23134–23148, 2011.

[101] K. Vandewal, A. Gadisa, W. D. Oosterbaan, S. Bertho, F. Banishoeib, I. V. Severen, L. Lutsen, T. J. Cleij, D. Vanderzande, and J. V. Manca. The Relation Between Open-Circuit Voltage and the Onset of Photocurrent Generation by Charge-Transfer Absorption in Polymer:Fullerene Bulk Heterojunction Solar Cells. *Adv. Funct. Mater.*, 18:1616, 2008.

[102] M. Hallermann, S. Haneder, and E. D. Como. Charge-transfer states in conjugated polymer/fullerene blends: Below-gap weakly bound excitons for polymer photovoltaics. *Appl. Phys. Lett.*, 93:053307, 2008.

[103] R. C. I. MacKenzie, C. G. Shuttle, M. L. Chabinyc, and J. Nelson. Extracting Microscopic Device Parameters from Transient Photocurrent Measurements of P3HT:PCBM Solar Cells. *Adv. Ener. Mater.*, 2(6):662–669, 2012.

[104] P. Langevin. Recombinaison et mobilités des ions dans les gaz. *Ann. Chim. Phys.*, 28:433, 1903.

[105] J. Nelson. Diffusion-limited recombination in polymer-fullerene blends and its influence on photocurrent collection. *Phys. Rev. B*, 67:155209, 2003.

[106] A. Foertig, A. Baumann, D. Rauh, V. Dyakonov, and C. Deibel. Charge carrier concentration and temperature dependent recombination in polymer–fullerene solar cells. *Appl. Phys. Lett.*, 95:052104, 2009.

[107] C. G. Shuttle, R. Hamilton, J. Nelson, B. C. O'Regan, and J. R. Durrant. Measurement of charge-density dependence of carrier mobility in an organic semiconductor blend. *Adv. Funct. Mater.*, 20(5):698–702, 2010.

[108] J. Krantz. *Photolumineszenzeigenschaften organischer Halbleiter abhängig von Donator:Akzeptor-Verhältnis und elektrischem Feld.* Diplomarbeit, Physikalisches Institut der Julius-Maximilians-Universität Würzburg, 2008.

[109] M. Liedtke. *Optische Spektroskopie an Fullerenen als Akzeptoren in organischen Solarzellen.* PhD thesis, Physikalisches Institut der Julius-Maximilians-Universität Würzburg, 2011.

[110] O. Epshtein, G. Nakhmanovich, Y. Eichen, and E. Ehrenfreund. Dispersive dynamics of photoexcitations in conjugated polymers measured by photomodulation spectroscopy. *Phys. Rev. B*, 63:1252061, 2001.

[111] A. Kämpgen. *Spectrally and Temporally Resolved Photoinduced Absorption in Organic Solar Cells.* Master's thesis, Physikalisches Institut der Julius-Maximilians-Universität Würzburg, June 2011.

[112] M. Gunz. *Zeitaufgelöste Photoinduzierte Absorption in organischen Solarzellen.* Diplomarbeit, Physikalisches Institut der Julius-Maximilians-Universität Würzburg, Juni 2010.

[113] M. Binder. *Ladungstransferzustände in organischen Solarzellen.* Diplomarbeit, Physikalisches Institut der Julius-Maximilians-Universität Würzburg, Juli 2010.

[114] A. Sperlich, M. Liedtke, J. Kern, H. Kraus, C. Deibel, S. Filippone, J. L. Delgado, N. Martín, and V. Dyakonov. Photoinduced C70 radical anions in polymer:fullerene blends. *physica status solidi (RRL) – Rapid Research Letters*, 5(3):128–130, 2011.

[115] K. Marumoto, N. Takeuchi, T. Ozaki, and S. Kuroda. ESR studies of photogenerated polarons in regioregular poly(3-alkylthiophene)-fullerene composite. *Synth. Met.*, 129:239, 2002.

[116] A. Baumann, J. Lorrmann, C. Deibel, and V. Dyakonov. Bipolar charge transport in poly(3-hexyl thiophene)/methanofullerene blends: A ratio dependent study. *Appl. Phys. Lett.*, 93:252104, 2008.

[117] S. Krause, M. B. Casu, A. Schöll, and E. Umbach. Determination of transport levels of organic semiconductors by UPS and IPS. *New J. Phys.*, 10(8):085001, 2008.

[118] J. E. Kroeze, T. J. Savenije, M. J. W. Vermeulen, and J. M. Warman. Contactless Determination of the Photoconductivity Action Spectrum, Exciton Diffusion Length, and Charge Separation Efficiency in Polythiophene-Sensitized TiO2 Bilayers. *J. Phys. Chem. B*, 107(31):7696–7705, 2003.

[119] A. Huijser, T. J. Savenije, J. E. Kroeze, and L. D. A. Siebbeles. Exciton diffusion and interfacial charge separation in meso-tetraphenylporphyrin/tio2 bilayers: Effect of ethyl substituents. *J. Phys. Chem. B*, 109(43):20166–20173, 2005.

[120] M. T. Dang, L. Hirsch, and G. Wantz. P3HT:PCBM, Best Seller in Polymer Photovoltaic Research. *Adv. Mater.*, 23(31):3597–3602, 2011.

[121] J. R. Reddinger and J. R. Reynolds. Molecular enineering of pi-conjugated polymers. *Advances in Polymer Science*, 145:73, 1999.

[122] P. Kovacic and K. N. McFarland. Polymerization of aromatic nuclei. XIX. Polymerization of thiophene by aluminum chloride. *Journal of Polymer Science: Polymer Chemistry Edition*, 17(7):1963–1976, 1979.

[123] T. Yamamoto, K. Sanechika, and A. Yamamoto. Preparation of thermostable and electric-conducting poly(2,5-thienylene). *Journal of Polymer Science: Polymer Letters Edition*, 18(1):9–12, 1980.

[124] J. W.-P. Lin and L. P. Dudek. Synthesis and properties of poly(2,5-thienylene). *Journal of Polymer Science: Polymer Chemistry Edition*, 18(9):2869–2873, 1980.

[125] G. Koßmehl and G. Chatzitheodorou. Electrical conductivity of poly(2,5-thiophenediyl)-AsF5-complexes. *Die Makromolekulare Chemie, Rapid Communications*, 2(9-10):551–555, 1981.

[126] K. Jen, R. Oboodi, and R. L. Elsenbaumer. Processible and Environmentally Stable Conducting Polymers. *Polymeric Materials: Science and Engineering*, 53:79, 1985.

[127] R. Elsenbaumer, K. Jen, and R. Oboodi. Processible and environmentally stable conducting polymers. *Synth. Met.*, 15(2–3):169–174, 1986. Proceedings of the Workshop on Conductive Polymers.

[128] M.-A. Sato, S. Tanaka, and K. Kaeriyama. Soluble conducting polythiophenes. *J. Chem. Soc., Chem. Commun.*, pages 873–874, 1986.

[129] S. Hotta, S. D. D. V. Rughooputh, A. J. Heeger, and F. Wudl. Spectroscopic studies of soluble poly(3-alkylthienylenes). *Macromolecules*, 20(1):212–215, 1987.

[130] M. Lemaire, D. Delabouglise, R. Garreau, A. Guy, and J. Roncali. Enantioselective chiral poly(thiophenes). *J. Chem. Soc., Chem. Commun.*, pages 658–661, 1988.

[131] R. D. McCullough and R. D. Lowe. Enhanced electrical conductivity in regioselectively synthesized poly(3-alkylthiophenes). *J. Chem. Soc., Chem. Commun.*, pages 70–72, 1992.

[132] R. D. McCullough and S. P. Williams. Toward tuning electrical and optical properties in conjugated polymers using side-chains: highly conductive head-to-tail, heteroatom functionalized polythiophenes. *J. Am. Chem. Soc.*, 115(24):11608–11609, 1993.

[133] R. D. McCullough, R. D. Lowe, M. Jayaraman, and D. L. Anderson. Design, synthesis, and control of conducting polymer architectures: structurally homogeneous poly(3-alkylthiophenes). *The Journal of Organic Chemistry*, 58(4):904–912, 1993.

[134] T. A. Chen and R. D. Rieke. The first regioregular head-to-tail poly(3-hexylthiophene-2,5-diyl) and a regiorandom isopolymer: nickel versus palladium catalysis of 2(5)-bromo-5(2)-(bromozincio)-3-hexylthiophene polymerization. *J. Am. Chem. Soc.*, 114(25):10087–10088, 1992.

[135] T. A. Chen, R. A. O'Brien, and R. D. Rieke. Use of highly reactive zinc leads to a new, facile synthesis for polyarylenes. *Macromolecules*, 26(13):3462–3463, 1993.

[136] T.-A. Chen, X. Wu, and R. D. Rieke. Regiocontrolled Synthesis of Poly(3-alkylthiophenes) Mediated by Rieke Zinc: Their Characterization and Solid-State Properties. *J. Am. Chem. Soc.*, 117(1):233–244, 1995.

[137] X. Wu, T.-A. Chen, and R. D. Rieke. Synthesis of Regioregular Head-to-Tail Poly[3-(alkylthio)thiophenes]. A Highly Electroconductive Polymer. *Macromolecules*, 28(6):2101–2102, 1995.

[138] M. R. Andersson, D. Selse, M. Berggren, H. Jaervinen, T. Hjertberg, O. Inganaes, O. Wennerstroem, and J.-E. Oesterholm. Regioselective polymerization of 3-(4-octylphenyl)thiophene with FeCl3. *Macromolecules*, 27(22):6503–6506, 1994.

[139] K. Takayama, M. Kaneko, S. Pandey, W. Takashima, and K. Kaneto. Photocarrier generation in regioregular poly(3-alkylthiophene)photovoltaic cells. *Synth. Met.*, 121(1–3):1565 – 1566, 2001. Proceedings of the International Conference on the Science and Technology of Synthetic Metals.

[140] R. Österbacka, C. P. An, X. M. Jiang, and Z. V. Vardeny. Two-dimensional electronic excitations in self-assembled conjugated polymer nanocrystals. *Science*, 287:839, 2000.

[141] T. J. Prosa, M. J. Winokur, J. Moulton, P. Smith, and A. J. Heeger. X-ray structural studies of poly(3-alkylthiophenes): an example of an inverse comb. *Macromolecules*, 25:4364, 1992.

[142] H. Kraus. *Optisch detektierte Magnetresonanzspektroskopie an organischen Halbleitern.* Diplomarbeit, Physikalisches Institut der Julius-Maximilians-Universität Würzburg, 2009.

[143] T. Erb, U. Zhokhavets, U. Gobsch, S. Raleva, B. Stühn, P. Schilinsky, C. Waldauf, and C. Brabec. Correlation between structural and optical properties of composite polymer/fullerene films for organic solar cells. *Adv. Funct. Mater.*, 15:1193, 2005.

[144] D. H. Kim, Y. Jang, Y. D. Park, and K. Cho. Layered molecular ordering of self-organized poly(3-hexylthiophene) thin films on hydrophobized surfaces. *Macromolecules*, 39(17):5843–5847, 2006.

[145] A. Zen, M. Saphiannikova, D. Neher, J. Grenzer, S. Grigorian, U. Pietsch, U. Asawapirom, S. Janietz, U. Scherf, I. Lieberwirth, and G. Wegner. Effect of molecular weight on the structure and crystallinity of poly(3-hexylthiophene). *Macromolecules*, 39(6):2162–2171, 2006.

[146] K. Kanai, T. Miyazaki, H. Suzuki, M. Inaba, Y. Ouchi, and K. Seki. Effect of annealing on the electronic structure of poly(3-hexylthiophene) thin film. *Phys. Chem. Chem. Phys.*, 12:273–282, 2010.

[147] C. Scharsich, R. H. Lohwasser, M. Sommer, U. Asawapirom, U. Scherf, M. Thelakkat, D. Neher, and A. Köhler. Control of aggregate formation in poly(3-hexylthiophene) by solvent, molecular weight, and synthetic method. *Journal of Polymer Science Part B: Polymer Physics*, 50(6):442–453, 2012.

[148] J. Clark, C. Silva, R. H. Friend, and F. C. Spano. Role of intermolecular coupling in the photophysics of disordered organic semiconductors: Aggregate emission in regioregular polythiophene. *Phys. Rev. Lett.*, 98(20):206406, May 2007.

[149] S. M. Tuladhar, D. Poplavskyy, S. A. Choulis, J. R. Durrant, D. D. C. Bradley, and J. Nelson. Ambipolar charge transport in films of methanofullerene and poly(phenylenevinylene)/methanofullerene blends. *Adv. Funct. Mater.*, 15:1171, 2005.

[150] M. Brinkmann and P. Rannou. Effect of molecular weight on the structure and morphology of oriented thin films of regioregular poly(3-hexylthiophene) grown by directional epitaxial solidification. *Adv. Funct. Mater.*, 17(1):101–108, 2007.

[151] C. Goh, R. J. Kline, M. D. McGehee, E. N. Kadnikova, and J. M. J. Fréchet. Molecular-weight-dependent mobilities in regioregular poly(3-hexyl-thiophene) diodes. *Appl. Phys. Lett.*, 86:122110, 2005.

[152] R. H. Smalley. Discovering the fullerenes. *Rev. Mod. Phys.*, 69:723, 1997.

[153] C. W. Tang. Two-layer organic photovoltaic cell. *Appl. Phys. Lett.*, 48:183, 1986.

[154] H. Imahori. Creation of fullerene-based artificial photosynthetic systems. *Bulletin of the Chemical Society of Japan*, 80(4):621, 2007.

[155] J. C. Hummelen, B. W. Knight, F. LePeq, and F. Wudl. Preparation and characterization of fulleroid and methanofullerene derivatives. *J. Org. Chem.*, 60:532, 1995.

[156] G. Yu, J. Gao, J. C. Hummelen, F. Wudl, and A. J. Heeger. Polymer photovoltaic cells: enhanced efficiencies via a network of internal donor-acceptor heterojunctions. *Science*, 270:1789, 1995.

[157] G. Dennler, M. C. Scharber, and C. J. Brabec. Polymer-fullerene bulk-heterojunction solar cells. *Adv. Mater.*, 21:1323, 2009.

[158] P. Schilinsky, C. Waldauf, and C. J. Brabec. Recombination and loss analysis in polythiophene based bulk heterojunction photodetectors. *Appl. Phys. Lett.*, 81:3885, 2002.

[159] F. Padinger, R. S. Rittberger, and N. S. Sariciftci. Effects of postproduction treatment on plastic solar cells. *Adv. Funct. Mater.*, 13:85, 2003.

[160] D. Chirvase, J. Parisi, J. C. Hummelen, and V. Dyakonov. Influence of nanomorphology on the photovoltaic action of polymer–fullerene composites. *Nanotechn.*, 15:1317, 2004.

[161] G. Li, V. Shrotriya, Y. Yao, and Y. Yang. Investigation of annealing effects and film thickness dependence of polymer solar cells based on poly(3-hexylthiophene). *J. Appl. Phys.*, 98:043704, 2005.

[162] V. D. Mihailetchi., H. X. Xie, B. de Boer, L. J. A. Koster, and P. W. M. Blom. Charge transport and photocurrent generation in poly(3-hexylthiophene): Methanofullerene bulk-heterojunction solar cells. *Adv. Funct. Mater.*, 16(5):699–708, 2006.

[163] M. Reyes-Reyes, K. Kim, and D. L. Carroll. High-efficiency photovoltaic devices based on annealed poly(3-hexylthiophene) and 1-(3-methoxycarbonyl)-propyl-1-phenyl-(6,6)C_{61} blends. *Appl. Phys. Lett.*, 87:083506, 2005.

[164] I.-W. Hwang, D. M., and A. J. Heeger. Photoinduced carrier generation in P3HT/PCBM bulk heterojunction materials. *J. Phys. Chem. C*, 112:4350–4354, 2008.

[165] P. Vanlaeke, G. Vanhoyland, T. Aernouts, D. Cheyns, C. Deibel, J. Manca, P. Heremans, and J. Poortmans. Polythiophene based bulk heterojunction solar cells: Morphology and its implications. *Thin Solid Films*, 511–512:358, 2006.

[166] V. D. Mihailetchi, H. Xie, B. de Boer, L. M. Popescu, J. C. Hummelen, P. W. M. Blom, and L. J. A. Koster. Origin of the enhanced performance in poly(3-hexylthiophene): [6,6]-phenyl C_{61}-butyric acid methyl ester solar cells upon slow drying of the active layer. *Appl. Phys. Lett.*, 89:012107, 2006.

[167] G. Li, Y. Yao, H. Yang, V. Shrotriya, G. Yang, and Y. Yang. "Solvent annealing" effect in polymer solar cells based on poly(3-hexylthiophene) and methanofullerenes. *Adv. Funct. Mater.*, 17:1636, 2007.

[168] A. J. Moule and K. Meerholz. Controlling morphology in polymer-fullerene mixtures. *Adv. Mater.*, 20:240, 2008.

[169] J. Peet, C. Soci, R. C. Coffin, T. Q. Nguyen, A. Mikhailovsky, D. Moses, and G. C. Bazan. Method for increasing the photoconductive response in conjugated polymer/fullerene composites. *Appl. Phys. Lett.*, 89:252105, 2006.

[170] W. Wang, H. Wu, C. Yang, C. Luo, Y. Zhang, J. Chen, and Y. Cao. High-efficiency polymer photovoltaic devices from regioregular-poly(3-hexylthiophene-2,5-diyl) and [6,6]-phenyl-c[sub 61]-butyric acid methyl ester processed with oleic acid surfactant. *Appl. Phys. Lett.*, 90(18):183512, 2007.

[171] X. Yang, J. Loos, S. Veenstra, W. J. H. Verhees, M. M. Wienk, J. M. Kroon, M. A. J. Michels, and R. A. J. Janssen. Nanoscale morphology of high-performance polymer solar cells. *Nano Lett.*, 5(4):579, 2005.

[172] S. Berson, R. D. Bettignies, S. Bailly, and S. Guillerez. Poly(3-hexylthiophene) Fibers for Photovoltaic Applications. *Adv. Funct. Mater.*, 17:1377, 2007.

[173] L. Valentini, D. Bagnis, and J. M. Kenny. Nanofibrillar self-organization of regioregular poly(3-hexylthiophene) and [6,6]-phenyl C 61 -butyric acid methyl ester by dip-coating: a simple method to obtain efficient bulk heterojunction solar cells. *Nanotechn.*, 20(9):095603, 2009.

[174] W. Ma, J. Y. Kim, K. Lee, and A. J. Heeger. Effect of the molecular weight of poly(3-hexylthiophene) on the morphology and performance of polymer bulk heterojunction solar cells. *Macromolecular Rapid Communications*, 28(17):1776–1780, 2007.

[175] R. C. Hiorns, R. de Bettignies, J. Leroy, S. Bailly, M. Firon, C. Sentein, A. Khoukh, H. Preud'homme, and C. Dagron-Lartigau. High Molecular Weights, Polydispersities, and Annealing Temperatures in the Optimization of Bulk-Heterojunction Photovoltaic Cells Based on Poly(3-hexylthiophene) or Poly(3-butylthiophene). *Adv. Funct. Mater.*, 16:2263, 2006.

[176] J. Zhao, A. Swinnen, G. Van Assche, J. Manca, D. Vanderzande, and B. V. Mele. Phase Diagram of P3HT/PCBM Blends and Its Implication for the Stability of Morphology. *J. Phys. Chem. B*, 113(6):1587–1591, 2009.

[177] D. Veldman, S. C. J. Meskers, and R. A. J. Janssen. The energy of charge-transfer states in electron donor–acceptor blends: Insight into the energy losses in organic solar cells. *Adv. Funct. Mater.*, 19:1939, 2009.

[178] J. Clark, J.-F. Chang, F. C. Spano, R. H. Friend, and C. Silva. Determining exciton bandwidth and film microstructure in polythiophene films using linear absorption spectroscopy. *Appl. Phys. Lett.*, 94(16):163306, 2009.

[179] X. Jiang, Y. Harima, K. Yamashita, Y. Tada, J. Oshita, and A. Kunai. Doping-induced change of carrier mobilities in poly(3-hexylthiophene) films with different stacking structures. *Chem. Phys. Lett.*, 364:616, 2002.

[180] S. Kobayashi, T. Takenobu, S. Mori, A. Fujiwara, and Y. Iwasa. Fabrication and characterization of C60 thin-film transistors with high field-effect mobility. *Appl. Phys. Lett.*, 82:4581, 2003.

[181] P. Brown, D. Thomas, A. Köhler, J.-S. K. J.S. Wilson, C. Ramsdale, H. Sirringhaus, and R. Friend. Effect of interchain interactions on the absorption and emission of poly(3-hexylthiophene). *Phys. Rev. B*, 67:064203, 2003.

[182] D. Beljonne, J. Cornil, R. Silbey, P. Millie, and J. L. Bredas. Interchain interactions in conjugated materials: The exciton model versus the supermolecular approach. *J. Chem. Phys.*, 112(10):4749–4758, 2000.

[183] D. Mack. *Exzitonenbindungsenergie in konjugierten Polymeren.* Diplomarbeit, Physikalisches Institut der Julius-Maximilians-Universität Würzburg, 2009.

[184] V. I. Arkhipov, E. V. Emilianova, and H. Bässler. Quenching of excitons in doped disordered organic semiconductors. *Phys. Rev. B*, 70:205205, 2004.

[185] D. Hertel, E. V. Soh, H. Bässler, and L. J. Rothberg. Electric field dependent generation of geminate electron-hole pairs in a ladder-type p-conjugated polymer probed by fluorescence quenching and delayed field collection of charge carriers. *Chem. Phys. Lett.*, 361:99, 2002.

[186] T. M. Smith, J. Kim, L. A. Peteanu, and J. Wildeman. Electric Field Effects on Internal Conversion: An Alternative Mechanism for Field-Induced Fluorescence Quenching of MEH-PPV and Its Oligomers in the Low Concentration Limit. *J. Phys. Chem. C*, 111:10119, 2007.

[187] V. Singh, A. K. Thakur, S. S. Pandey, W. Takashima, and K. Kaneto. Evidence of photoluminescence quenching in poly(3-hexylthiophene-2,5-diyl) due to injected charge carriers. *Synth. Met.*, 158(7):283 – 286, 2008.

[188] C. Deibel, T. Strobel, and V. Dyakonov. Origin of the efficient polaron pair dissociation in polymer–fullerene blends. *Phys. Rev. Lett.*, 103:036402, 2009.

[189] D. Veldman. *Charge Generation in Molecular Materials. Photophysics of Organic Photovoltaics.* PhD thesis, Technische Universiteit Eindhoven, 2008.

[190] P. E. Shaw, A. Ruseckas, and I. D. W. Samuel. Exciton Diffusion Measurements in Poly(3-hexylthiophene). *Adv. Mater.*, 20:3516, 2008.

[191] J. Piris, T. Dykstra, A. Bakulin, P. van Loosdrecht, W. Knulst, M. Trinh, J. Schins, and L. Siebbeles. Photogeneration and ultrafast dynamics of excitons and charges in P3HT/PCBM blends. *J. Phys. Chem. C*, 113:14500, 2009.

[192] M. Breselge, I. V. Severen, L. Lutsen, P. Adriaensens, J. Manca, D. Vanderzande, and T. Cleij. Comparison of the electrical characteristics of four 2,5-substituted poly(p-phenylene vinylene) derivatives with different side chains. *Thin Solid Films*, 511:328, 2006.

[193] A. Matsui, K. Tomioka, Y. Oeda, and T. Tomotika. Exciton band structure of crystalline anthracene. *Surface Science*, 37(0):849 – 854, 1973.

[194] K. C. Yee and R. R. Chance. Synthesis and properties of a new polydiacetylene: Poly[1,6-di(n-carbazolyl)-2,4-hexadiyne]. *Journal of Polymer Science: Polymer Physics Edition*, 16(3):431–441, 1978.

[195] J.-W. van der Horst, P. A. Bobbert, M. A. J. Michels, and H. Bässler. Calculation of excitonic properties of conjugated polymers using the Bethe-Salpeter equation. *J. Chem. Phys.*, 114:6950, 2001.

[196] M. Liess, S. Jeglinski, Z. V. Vardeny, M. Ozaki, K. Yoshino, Y. Ding, and T. Barton. Electroabsorption spectroscopy of luminescent and nonluminescent π-conjugated polymers. *Phys. Rev. B*, 56:15712–15724, 1997.

[197] J.-W. van der Horst, P. A. Bobbert, P. H. L. de Jong, M. A. J. Michels, G. Brocks, and P. J. Kelly. *Ab initio* prediction of the electronic and optical excitations in polythiophene: Isolated chains versus bulk polymer. *Phys. Rev. B*, 61:15817–15826, 2000.

[198] C. R. McNeill, A. Abrusci, J. Zaumseil, R. Wilson, M. J. McKiernan, J. H. Burroughes, J. J. M. Halls, N. C. Greenham, and R. H. Friend. Dual electron donor/electron acceptor character of a conjugated polymer in efficient photovoltaic diodes. *Appl. Phys. Lett.*, 90:193506, 2007.

[199] W. S. Shin, S. C. Kim, S.-J. Lee, H.-S. Jeon, M.-K. Kim, B. V. K. Naidu, S.-H. Jin, J.-K. Lee, J. W. Lee, and Y.-S. Gal. Synthesis and photovoltaic properties of a low-band-gap polymer consisting of alternating thiophene and benzothiadiazole derivatives for bulk-heterojunction and dye-sensitized solar cells. *Journal of Polymer Science Part A: Polymer Chemistry*, 45(8):1394, 2007.

[200] S. Oosterhout, M.M.Wienk, S. van Bavel, R. Thiedmann, L. J. Koster, J. Gilot, J. Loos, V. Schmidt, and R. Janssen. The effect of three-dimensional morphology on the efficiency of hybrid polymer solar cells. *Nat. Mater.*, 8:818, 2009.

[201] C. R. McNeill, J. J. M. Halls, R. Wilson, G. L. Whiting, S. Berkebile, M. G. Ramsey, R. H. Friend, and N. C. Greenham. Efficient Polythiophene/Polyfluorene Copolymer Bulk Heterojunction Photovoltaic Devices: Device Physics and Annealing Effects. *Adv. Funct. Mater.*, 18:2309, 2008.

[202] G. Horowitz, F. Kouki, P. Spearman, D. Fichou, C. Nogues, X. Pan, and F. Garnier. Evidence for n-type conduction in a perylene tetracarboxylic diimide derivative. *Adv. Mater.*, 8:242, 1996.

[203] A.-Y. Jen, Y. Liu, Q.-S. Hu, and L. Pu. Efficient light-emitting diodes based on a binaphthalene-containing polymer. *Appl. Phys. Lett.*, 75(24):3745, December 1999.

[204] F. Nolde, W. Pisula, S. Muller, C. Kohl, and K. Mullen. Synthesis and self-organization of core-extended perylene tetracarboxdiimides with branched alkyl substituents. *Chem. Mater.*, 18:3715, 2006.

[205] S. K. Lee, Y. Zu, A. Herrmann, Y. Geerts, K. Müllen, and A. J. Bard. Electrochemistry, spectroscopy and electrogenerated chemiluminescence of perylene, terrylene, and quaterrylene diimides in aprotic solution. *J. Am. Chem. Soc.*, 121(14):3513–3520, 1999.

[206] A. Pron, P. Gawrys, M. Zagorska, D. Djurado, and R. Demadrille. Electroactive materials for organic electronics: preparation strategies, structural aspects and characterization techniques. *Chem. Soc. Rev.*, 39:2577–2632, 2010.

[207] G. Löbbert. Phthalocyanines. In *Ullmann's Encyclopedia of Industrial Chemistry*. Wiley-VCH Verlag GmbH & Co. KGaA, 2000.

[208] A. Opitz, B. Ecker, J. Wagner, A. Hinderhofer, F. Schreiber, J. Manara, J. Pflaum, and W. Brütting. Mixed crystalline films of co-evaporated hydrogen- and fluorine-terminated phthalocyanines and their application in photovoltaic devices. *Org. Electron.*, 10(7):1259 – 1267, 2009.

[209] I. Bruder, J. Schöneboom, R. Dinnebier, A. Ojala, S. Schäfer, R. Sens, P. Erk, and J. Weis. What determines the performance of metal phthalocyanines (MPc, M = Zn, Cu, Ni, Fe) in organic heterojunction solar cells? a combined experimental and theoretical investigation. *Org. Electron.*, 11:377, 2010.

[210] G. Chaidogiannos, F. Petraki, N. Glezos, S. Kennou, and S. Nešpůrek. Low voltage operating OFETs based on solution-processed metal phthalocyanines. *Applied Physics A: Materials Science & Processing*, 96:763–767, 2009.

[211] M. Ichikawa, K. Kobayashi, T. Koyama, and Y. Taniguchi. Intense and efficient ultraviolet electroluminescence from organic light-emitting devices with fluorinated copper phthalocyanine as hole injection layer. *Thin Solid Films*, 515(7-8):3932, 2007.

[212] R. V. Bensasson, E. Bienvenüe, C. Fabre†, J.-M. Janot, E. J. Land, S. Leach, V. Leboulaire, A. Rassat, S. Roux, and P. Seta. Photophysical properties of three methanofullerene derivatives. *Chemistry – A European Journal*, 4(2):270–278, 1998.

[213] J. Maud. Optical transitions in oligothiophene radical cations (positive polarons): a semi-empirical study. *Synth. Met.*, 101(1–3):575 – 578, 1999. International Conference on Science and Technology of Synthetic Metals.

[214] H. Sirringhaus, P. J. Brown, R. H. Friend, M. M. Nielsen, K. Bechgaard, B. M. W. Langeveld-Voss, A. J. H. Spiering, R. A. J. Janssen, E. W. Meijer, P. Herwig, and D. M. de Leeuw. Two-dimensional charge transport in self-organized, high-mobility conjugated polymers. *Nature*, 401:685, 1999.

[215] P. J. Brown, H. Sirringhaus, M. Harrison, M. Shkunov, and R. H. Friend. Optical spectroscopy of field-induced charge in self-organized high mobility poly(3-hexylthiophene). *Phys. Rev. B*, 63(12):125204, Mar 2001.

[216] K. Fesser, A. R. Bishop, and D. K. Campbell. Optical absorption from polarons in a model of polyacetylene. *Phys. Rev. B*, 27:4804–4825, Apr 1983.

[217] M. Liedtke, A. Sperlich, H. Kraus, A. Baumann, C. Deibel, M. J. M. Wirix, J. Loos, C. M. Cardona, and V. Dyakonov. Triplet exciton generation in bulk-heterojunction solar cells based on endohedral fullerenes. *J. Am. Chem. Soc.*, 133(23):9088–9094, 2011.

[218] S. D. Oosterhout, L. J. A. Koster, S. S. van Bavel, J. Loos, O. Stenzel, R. Thiedmann, V. Schmidt, B. Campo, T. J. Cleij, L. Lutzen, D. Vanderzande, M. M. Wienk, and R. A. J. Janssen. Controlling the morphology and efficiency of hybrid ZnO:Polythiophene solar cells via side chain functionalization. *Adv. Ener. Mater.*, 1:90–96, 2011.

[219] O. J. Korovyanko, R. Österbacka, X. M. Jiang, Z. V. Vardeny, and R. A. J. Janssen. Photoexcitation dynamics in regioregular and regiorandom polythiophene films. *Phys. Rev. B*, 64:235122, Nov 2001.

[220] J. Gorenflot, A. Sperlich, A. Baumann, D. Rauh, A. Vasilev, C. Li, M. Baumgarten, C. Deibel, and V. Dyakonov. Detailed study of n,n'-(diisopropylphenyl)-terrylene-3,4:11,12-bis(dicarboximide) as electron acceptor for solar cells application. *Synth. Met.*, 161(23–24):2669 – 2676, 2012.

[221] R. Gomez, D. V. R. Blanco, C. Seoane, J. L. Segura, and R. A. J. Janssen. Energy and electron transfer in a poly(fluorene-alt-phenylene) bearing perylenediimides as pendant electron acceptor groups. *Macromolecules*, 40:2760, 2007.

[222] S. Shoaee, Z. An, X. Zhang, S. Barlow, S. R. Marder, W. Duffy, M. Heeney, I. McCulloch, and J. R. Durrant. Charge photogeneration in polythiophene–perylene diimide blend films. *Chem. Comm.*, page 5445, 2009.

[223] Y. Li, Y. Cao, J. Gao, D. Wang, G. Yu, and A. J. Heeger. Electrochemical properties of luminescent polymers and polymer light-emitting electrochemical cells. *Synth. Met.*, 99:243, 1999.

[224] J. Zhou, Y. C. Zhou, J. M. Zhao, C. Q. Wu, X. M. Ding, and X. Y. Hou. Carrier density dependence of mobility in organic solids: A Monte Carlo simulation. *Phys. Rev. B*, 75(15):153201, 2007.

[225] J. L. Li, M. Kastler, W. Pisula, J. W. F. Robertson, D. Wasserfallen, A. C. Grimsdale, J. S. Wu, and K. Mullen. Organic bulk-heterojunction photovoltaics based on alkyl substituted discotics. *Adv. Funct. Mater.*, 17:2528, 2007.

[226] C. W. Struijk, A. B. S. J. E. J. Dakhorst, M. van Dijk, P. Kimkes, R. B. M. Koehorst, H. Donker, T. J. Schaafsma, S. J. Picken, A. van de Craats, J. M. Warman, H. Zuilhof, and E. J. R. Sudhölter. Liquid crystalline perylene diimides: Architecture and charge carrier mobilities. *J. Am. Chem. Soc.*, 122:11057, 2000.

[227] M. Campoy-Quiles, T. A. M. Ferenczi, T. Agostinelli, P. G. Etchegoin, Y. Kim, T. D. Anthopoulos, P. N. Stavrinou, D. D. C. Bradley, and J. Nelson. Morphology evolution via self-organization and lateral and vertical diffusion in polymer: fullerene solar cell blends. *Nat. Mater.*, 7:158, 2008.

[228] V. Kamm, G. Battagliarin, I. A. Howard, W. Pisula, A. Mavrinskiy, C. Li, K. Müllen, and F. Laquai. Organic solar cells: Polythiophene: Perylene diimide solar cells – the impact of alkyl-substitution on the photovoltaic performance. *Adv. Ener. Mater.*, 1(2):137–137, 2011.

[229] W. J. Grzegorczyk, T. J. Savenije, T. E. Dykstra, J. Piris, J. M. Schins, and L. D. Siebbeles. Temperature-Independent Charge Carrier Photogeneration in P3HT-PCBM Blends with Different Morphology. *J. Phys. Chem. C*, 114(11):5182–5186, 2010.

[230] R. Mauer, M. Kastler, and F. Laquai. The Impact of Polymer Regioregularity on Charge Transport and Efficiency of P3HT:PCBM Photovoltaic Devices. *Adv. Funct. Mater.*, 20:2085, 2010.

[231] P. A. van Hal, M. P. T. Christiaans, M. M. Wienk, J. M. Kroon, and R. A. J. Janssen. Photoinduced electron transfer from conjugated polymers to TiO2. *J. Phys. Chem. B*, 103:4352, 1999.

[232] J. Guo, H. Ohkita, H. Benten, and S. Ito. Charge generation and recombination dynamics in poly(3-hexylthiophene)/fullerene blend films with different regioregularities and morphologies. *J. Am. Chem. Soc.*, 132:6154, 2010.

[233] D. Rauh, C. Deibel, and V. Dyakonov. Charge density dependent nongeminate recombination in organic bulk heterojunction solar cells. *Advanced Functional Materials*, 22(16):3371–3377, 2012.

[234] J. Schafferhans, A. Baumann, A. Wagenpfahl, C. Deibel, and V. Dyakonov. Oxygen doping of P3HT:PCBM blends: Influence on trap states, charge carrier mobility and solar cell performance. *Org. Electron.*, 11:1693, 2010.

[235] C. G. Shuttle, B. O'Regan, A. M. Ballantyne, J. Nelson, D. D. C. Bradley, and J. R. Durrant. Bimolecular recombination losses in polythiophene: Fullerene solar cells. *Phys. Rev. B*, 78:113201, 2008.

[236] T. J. Savenije, D. H. K. Murthy, M. Gunz, J. Gorenflot, L. D. A. Siebbeles, V. Dyakonov, and C. Deibel. Absence of postnanosecond charge carrier relaxation in poly(3-hexylthiophene)/fullerene blends. *The Journal of Physical Chemistry Letters*, 2(12):1368–1371, 2011.

[237] J. Gorenflot, M. C. Heiber, A. Baumann, J. Lorrmann, M. Gunz, A. Kämpgen, V. Dyakonov, and C. Deibel. Nongeminate recombination in neat P3HT and P3HT: PCBM blend films. *J. Appl. Phys.*, 115(14):144502, 2014.

[238] J. Gorenflot, D. Mack, D. Rauh, S. Krause, C. Deibel, A. Schöll, F. Reinert, and V. Dyakonov. Energetics of excited states in the conjugated polymer poly(3-hexylthiophene). In *DPG Frühjahrstagung 2010*, CPP20:10, Regensburg, Germany, 2010. Deutsche Physikalische Gesellschaft.

[239] J. Gorenflot, D. Mack, D. Rauh, S. Krause, C. Deibel, A. Schöll, F. Reinert, and V. Dyakonov. Energetics of excited states in the conjugated polymer poly(3-hexylthiophene). In *International Conference of Synthetic Metals*, 7Ax:05, Kyoto, 2010.

[240] M. A. Faist, S. Shoaee, S. Tuladhar, G. F. A. Dibb, S. Foster, W. Gong, T. Kirchartz, D. D. C. Bradley, J. R. Durrant, and J. Nelson. Understanding the reduced efficiencies of organic solar cells employing fullerene multiadducts as acceptors. *Adv. Ener. Mater.*, 3(6):744–752, 2013.

Appendix

A– List of Constants

These constants are adapted from the official CODATA set of internationally recommended values of fundamental physics constants maintained by NIST.[12]

Constant	Value	Unit	Description
h	$6.626\ 069\ 57(29) \cdot 10^{-34}$	J s	Planck constant
$\hbar = \frac{h}{2\pi}$	$1.054\ 571\ 726(47) \cdot 10^{-34}$	J s	Planck constant over 2 π
k_B	$1.380\ 648\ 8(13) \cdot 10^{-23}$	J K^{-1}	Boltzmann constant
ϵ_0	$8.854\ 187\ 817(00) \cdot 10^{-12}$	F m^{-1} = A s $(V\ m)^{-1}$	electric constant
e	$1.602\ 176\ 565(35) \cdot 10^{-19}$	A s	elementary charge
eV	$1.602\ 176\ 565(35) \cdot 10^{-19}$	V A s = J	electron volt
m_e	$9.109\ 382\ 91 \cdot 10^{-31}$	kg	electron mass

[12] Jan. 2013: http://physics.nist.gov/cuu/Constants/index.html

B– List of Abbreviations

Abbreviation	Description
A	electron acceptor
BO	Born Oppenheimer
CB	chlorobenzene
CF	chloroform
CT	charge transfer
CuPC	copper phtalocyanine
D	electron donor
DOS	density of states
EPIA	European photovoltaic industry association
EQE	external quantum efficiency
ESR	electron spin resonance
F-PL	field dependent photoluminescence
FET	field effect transistor
IEA	International Energy Agency
IPES	inverse photoelectron spectroscopy
IQE	internal quantum efficiency
IPCC	Intergovernmental Panel on Climate Change
ITO	indium tin oxyde
MeLPPP	ladder-type poly(para-phenylene)
MDMO-PPV	poly(2-methoxy-5(3',7'-dimethylloctyloxy)-1,4-phenylene-vinylene)
OLED	organic light emitting diode
OPV	organic photovoltaic
P3AT	poly(3-alkylthiophene)
P3HT	poly(3-hexylthiophene)
PADMR	photoinduced absorption detected magnetic resonance
PIA	quasi steady-state photoinduced absorption
PLDMR	photoluminescence detected magnetic resonance
PEDOT:PSS	poly(3,4-ethylenedioxythiophene):(polystyrenesulfonate)
PES	photoelectron spectroscopy
PDI	perylene-3,4:9,10-bis(dicarboximide)
PL	photoluminescence
PF	polyfluorene
PV	photovoltaic
PPV	poly(phenylene vinylene)

Abbreviation	Description
PCBM	[6,6]-phenyl-C_{61} butyric acid methyl ester
TA	transient absorption
TDI	terrylene-3,4:11,12-bis(dicarboximide)
TOF	time of flight
TRMC	time-resolved microwave (photo)conductance
UPS	ultraviolet photoelectron spectroscopy
XRD	X-rays diffraction

C– List of Figures

D– List of Tables

E– Acknowledgment

To conclude this work, I would like to express my gratitude to all those who have helped me in the course of the last years, and make it possible for an "artist" like me to go on having something to do with the field he likes, rather than with art. I would like to mention specially:

- Professor Vladimir Dyakonov, for one day coming with the odd idea of hiring a strange french guy, and to then share pieces of his life and research experience, in a courageous attempt to make of me an educated researcher.
- To Professor Carsten Deibel for his unfailing loyalty to support those who are under his responsibility, and for his extreme patience toward stupid french guys.
- To Prof. Hertel for accepting twice to review my dissertation.
- To those three again and to Professor Natasha Kirova and to Professor Tom Savenije also, and to lot of others again who contaminated me further with the passion of science, and helped me to understand so much.
- To the teams of Max Planck Institut für Polymer Forschung, Universidad Autónoma de Madrid, and the University of Wupperthal for sending me interesting materials to study.
- To Prof. Achim Schöll and the chair of experimental physics VII for fruitful collaboration.
- To Prof. Jens Pflaum and the Pflaumies for all the shared research discussion as well as the fun and for having made me discover Looping Louis, and more specially to Andy Steindamm and Krissie who put a roof over my head, each time I need to come back to Würzburg.
- To Daniel Mack, Mathias Gunz, Andy Kämpgen and Clemens Grünewald, who had the madness of becoming my master/diploma students, and yet, managed to be quite successful, and with whom I had so much fun working.
- To Moritz Liedtke and Johannes Krantz, who taught me the secrets of photoinduced absorption.
- To all the photophysics group with who I had so much fun and interest working.
- To Björn Giesieking, even if he stole my banana box.

- To Julia Kern, Manuel Ruf, Stefan Väth and all those who shared my office, and made life a bit more sunny.
- To Andy Baumann, Alex Förtig, Daniel Rauh, Jens Lorrmann, although they all beat me at tennis even when I practice regularly whereas they play just once in a while.
- To those ones already cited and also to Maria Hammer, to the Lorrmann brothers, to Julia Rauh, Clemens Feser and Stefan Geißendörfer, Christian Weber, Alexander Wagenpfahl, die Franzi, Vera Stehr, Johannes Erben, Björn Titze, Andres Fritze, to all my colleagues, who not only managed to cope with me at work, but even occasionally out of work, for events with lower scientific content.
- To Valentin Baianov for his incomparable kindness and ability to change a pack of lenses into an optimized optical setup, just like others change water into wine.
- To Andre Thiem Riebe whose restless work managed to keep the labs running in spite of the dangerously clumsy people such as I, working into it.
- To Diep and before her Monica who know everything and always have good anwers to any problem and helped me so much.
- To those who complained even more than I each time I was in a complaining mood, making me realize that, well, maybe it's ok.
- To my chemistry teacher, Frédéric Lahitete, who would probably never have though that I could work so much with chemists and whose lessons although "unfreiwillig gelernt", were in the end precious as far as up to now.
- To my wife who managed to force me out of work more often and more intensively that I would have done by myself.
- To Alfred, Alfred, Alfred, Alfred and Husuky for constant support.
- To my family.
- To the people in the street who just sometimes smile and make the good mood come back.
- To all those I forget and to who I apologize because I didn't intend to forget anyone.
- And of course to the European Project SolarNType for financial support.

F– Scientific Contributions

Full Papers in Peer-Reviewed Journals

- J. Gorenflot, M. C. Heiber, A. Baumann, J. Lorrmann, M. Gunz, A. Kämpgen, V. Dyakonov and C. Deibel. Nongeminate recombination in neat P3HT and P3HT:PCBM blend films. *The Journal of Applied Physics*, 114 (14):144502, 2014.

- J. Gorenflot, A. Sperlich, A. Baumann, D. Rauh, A. Vasilev, C. Li, M. Baumgarten, C. Deibel and V. Dyakonov. Detailed study of N,N'–(diisopropylphenyl)– terrylene-3,4:11,12-bis(dicarboximide) as electron acceptor for solar cells application. *Synthetic Metals*, 161(23–24):2669, 2012 (Cover page).

- T. J. Savenije, D. H. K. Murthy, M. Gunz, J. Gorenflot, L. D. A. Siebbeles, V. Dyakonov, and C. Deibel. Absence of postnanosecond charge carrier relaxation in poly(3-hexylthiophene)/fullerene blends. *The Journal of Physical Chemistry Letters*, 2(12):1368, 2011.

- C. Deibel, D. Mack, J. Gorenflot, A. Schöll, S. Krause, F. Reinert, D. Rauh, and V. Dyakonov Energy levels and exciton binding energy in the conjugated polymer poly(3-hexyl thiophene). *Physical Review B*, 81:085202, 2010.

Conference Talks

- **2011 DPG Frühjahrstagung 2011 Dresden, Germany**
  Talk HL 46.9: Influence of phase separation on the recombination dynamics of trapped charges in disordered organic semiconductors.
  J. Gorenflot, M. Gunz, A. Kämpgen,, J. Lorrmann, C. Deibel and V. Dyakonov.
  (`http://www.dpg-verhandlungen.de/2011/dresden/hl46.pdf`)

- **2010 ICSM 2010 Kyoto, Japan**
  Talk 7Ax-05: Energetics of Excited States in the Conjugated Polymer Poly(3-hexylthiophene).
  J. Gorenflot, D. Mack, D. Rauh, S. Krause, C. Deibel, A. Schöll, F. Reinert, and V. Dyakonov

- **2010 DPG Frühjahrstagung 2010 Regensburg, Germany**
  Talk CPP 20.10: Energetics of Excited States in the Conjugated Polymer

Poly(3-hexylthiophene).
J. Gorenflot, D. Mack, D. Rauh, S. Krause, C. Deibel, A. Schöll, F. Reinert, and V. Dyakonov
(http://www.dpg-verhandlungen.de/2010/regensburg/cpp20.pdf)

Conference Posters

- **2009 EMRS 2009 Strasbourg, France**
  Poster AP3-83: Limiting factors in phenyl-substituted rylenes as electron acceptors for bulk heterojunction solar cells.
  J. Gorenflot, A. Sperlich, A. Baumann, A. Vasilev, M. Baumgarten, C. Li, C. Deibel and V. Dyakonov.

- **2009 DPG Frühjahrstagung 2009, Dresden, Germany**
  Poster SYOP 4.47: Limiting factors in phenyl-substituted rylenes as electron acceptors associated with P3HT donor in bulk heterojunction solar cells.
  J. Gorenflot, M. Hammer, A. Sperlich, A. Baumann, A. Vasilev, M. Baumgarten, C. Li, C. Deibel and V. Dyakonov. (http://www.dpg-verhandlungen.de/year/2009/conference/dresden/part/syop/session/4/contribution/47/)